Development of Blast Resistant Panels and Wall Systems Made of Engineered Cementitious Composites and Light-Gauge Steel Sheets

By

Emre Insel

Thesis submitted to the

University of Ottawa

in partial fulfillment of the requirements

for the Doctorate in Philosophy degree in Civil Engineering

Department of Civil Engineering

Faculty of Engineering

University of Ottawa

Abstract

This thesis outlines experimental and numerical research that was performed for the fulfillment of doctoral requirements at the Civil Engineering Department of the University of Ottawa.

The thesis research is aimed at developing blast-resistant cementitious panels reinforced with light-gauge steel sheets and blast-resistant wall systems consisting of the panels and the supporting hollow steel sections (HSS) acting as studs. It consists of experimental and numerical components. The experimental research involves large-scale tests of panels and walls under simulated blast loading using the shock tube facility of the University of Ottawa. The numerical research involves finite element analysis (FEA) using LS-Dyna software to simulate blast loads and the behaviour of panels under these loads. The numerical research also includes a parametric study for investigating the blast resistance of various panel configurations that are not included in the experimental program.

Four different types of panels were included in 16 panel tests. They consisted of two layers of engineered cementitious composites (ECC) with either 1.5 mm or 3.0 mm thick steel sheets sandwiched in the middle. The panel layers were connected by means of self-drilling screws as shear connectors to ensure composite action, spaced at either 100 mm or 200 mm. Each panel was 510 mm (20 inches) wide, 2080 mm (82 inches) tall, and 15 mm (5/8 inch) thick to keep the weight approximately equal to 50 kilograms, which facilitates easy installation. The panels were tested in three different configurations: first, they were tested as panels only without any HSS studs; second, connected to vertically placed hollow steel sections (HSS) that were relatively flexible; third, they were connected to vertically placed HSS that were at the front and back of the panels for increased

strength and rigidity. A fifth set, consisting of only 1.5 mm and 3 mm steel sheets, was also tested to assess the contribution of ECC to panel behaviour.

The results of the shock tube tests indicated that the panels are suited for use as blast-resisting elements with significant ductility. The panels with 100 mm connector spacing performed better than those with 200 mm connector spacing due to the enhanced composite action. The wall systems consisting of the panels and the HSS studs resulted in increased blast resistance for use in increased threat scenarios.

In the analytical phase of research, the finite element models were first validated against shock tube test data. Using the validated models, a parametric finite element study was performed by varying the model parameters. This parametric study included specimens with HSS members and 3 mm steel sheets without the ECC layers; panel-only specimens with higher contact explosion strength; panel-only specimens with thicker ECC layers; partition wall type panel-HSS-panel specimens; and a ballistic penetration model for ECC-steel-ECC panels and steel sheet panels.

The results of the experimental and analytical research indicate that 15 mm thick panels with 3 mm thick steel sheets provide significant protection against blast loads when used in conjunction with HSS members. The partition wall type panels with HSS members as main vertical structural elements, enclosed by an ECC-Steel-ECC panels on both sides, provide an attractive alternative to existing blast mitigation strategies for creating a blast-resistant enclosure with the added advantage of ease and speed of installation stemming from their lightweight.

Acknowledgements

First and foremost, I would like to thank my supervisor, Dr. Saatçioğlu. He inspired me to pursue my passion, supported me financially, and, more importantly, mentally during this long journey. None of “this” would have been possible without him. I can’t thank him enough.

I would like to thank Dr. Eric Jacques, who developed the OverPressure and RCBlast software and shared them with the public, greatly improving the efficiency of my work in this research.

I would like to thank the administrative and technical staff at the University of Ottawa for their support. The facilities of the university and the services provided by them as a whole have been instrumental in this work.

I would like to thank my professors. They were there to always answer my questions and provide guidance, not only in a technical capacity, but also on a personal level.

I would like to thank my classmates and fellow students for making this experience fun.

I would like to thank Abdul Saboor Karzad; without his experience, guidance, support, and most importantly, friendship, I would not have been able to complete this work.

I would like to thank my family and friends. They provided me with purpose, they supported me and believed in me. I would have been lost without them.

I would like to thank the CBC Radio World Report and the CBC Ottawa Morning Show teams. Thanks to them, waking up at 5 am was something I looked forward to, and I was able to start working on my thesis early in the day.

Finally, my dear wife, Elvin and our precious children, Ates and Dolunay. I am endlessly sorry for not being there when I should have been. I will forever be sorry for the times I was not there, and

for my grumpiness while I was. You are my everything, and I thank you for loving me and supporting me during this journey.

Contents

Abstract ii

Acknowledgements iv

List of Figures x

List of Tables xxii

List of Equations xxiv

Chapter 1. Introduction 1

1.1 Background 1

1.2 Research Objectives and Scope 4

1.3 Original Contributions to Structural/Blast Engineering 5

1.4 Composition of Thesis 6

Chapter 2. Literature Review 8

2.1 Fundamentals of Blast Engineering 8

2.2 Literature Review on Engineered Cementitious Composites (ECC) and the Strain Rate Effects on Steel 24

2.3 Review of Literature on Blast Resistant Panels 40

2.4 Blast Testing Using the University of Ottawa Shock Tube 47

Chapter 3. Experimental Research 49

3.1 Test Specimens 54

3.1.1 ECC Mix Design 54

3.1.2 Specimen Preparation 58

3.2 Shock Tube as a Blast Simulator 63

3.3 Blast Test Configurations and Test Procedure 66

3.4 Shock Tube Test Results 76

3.5.1 First Set of Specimens 78

3.5.2 Second Set of Specimens 89

3.5.3 Third Set of Specimens 95

3.5.4 Fourth Set of Specimens 99

3.5.5 Fifth Set of Specimens 104

Chapter 4. Analytical Investigation 108

4.1 Finite Element Analysis 108

4.1.1 Selection of FEM Software and Background Information 109

4.1.2 Model Parameters 114

4.1.3 Mesh Sensitivity Analysis 123

4.2 Verification of Finite Element Models with Shock Tube Experiments 124

4.2.1 First Set of Specimens: Panels with HSS Members – 3mm Steel 124

4.2.2 Second Set of Specimens: Panels without HSS Members – 3 mm Steel 131

4.2.3 Third Set of Specimens: Panels without HSS Members – 1.5 mm Steel 138

4.2.4 Fourth Set of Specimens: Panels with HSS Members on Both Faces – 1.5 mm Steel 143

4.2.5 Fifth Set of Specimens: 1.5 mm and 3 mm Steel Sheets without ECC 148

4.3 Parametric Finite Element Analysis Study 152

4.3.1 HSS Member with 3 mm steel sheet without ECC layers 152

4.3.2 Panel-only specimens with higher contact strength 156

4.3.3 Panel-only specimens with 12 mm thick ECC layers 159

4.3.4 Partition Wall: Panel – HSS – Panel Specimens 162

4.3.5 Ballistic Protection Comparison 167

4.4 Single Degree of Freedom (SDOF) Approach 171

4.4.1 Tension Behaviour of Panel-only Specimens 172

4.4.2 Flexure-only Behaviour of Panels 176

Chapter 5. Design Recommendations 179

5.1 Effects of Design Parameters 179

5.1.1 Steel Sheet Thickness 179

5.1.2 ECC Layer Thickness 180

5.1.3 Connector Spacing 181

5.1.4 HSS Members 183

5.1.5 Support Stiffness and Movement 185

5.1.6 Ballistic performance 186

5.2 Design Recommendations 186

5.3 Design Example 190

Chapter 6. Summary and Conclusion 194

6.1 Summary 194

6.2 Conclusions 197

6.3 Limitations and Recommendations for Future Research 199

Chapter 7. Bibliography 201

Appendices 209

Appendix A 209

List of Figures

Figure 1: Blast parameters as a function of Scaled Distance, Z, as shown in Figure 2-15 of **(UFC 3-340-02, 2008)** 10

Figure 2: Response limits corresponding to different performance levels for reinforced concrete elements (CSA S850, 2023) 12

Figure 3: Triangular pressure vs time for front wall loading as defined in the ASCE 59-22 (2022) 13

Figure 4: Catchment system for non-load bearing masonry wall (Task Committee on Blast-Resistant Design, 2025) 14

Figure 5: Illustration of a strong column preventing progressive collapse **(FEMA-426/BIPS-06, 2011)** 16

Figure 6: Threat description and damage potential charts **(FEMA-428/BIPS-07, 2012)** 17

Figure 7: Flexural resistance, stiffness and support shears for one-way members **(SBEDS Methodology Manual, 2008)** 19

Figure 8: Additional moment resistance due to catenary action caused by tension membrane response **(SBEDS Methodology Manual, 2008)** 19

Figure 9: Cost vs level of protection **(Smith & Hetherington, 1994)** 20

Figure 10: Full-scale blast testing of buildings **(Dusenberry, 2010)** 21

Figure 11: Aircraft impact on deformable target **(Bangash and Bangash, 2006)** 23

Figure 12: Stress vs strain chart of ECC coupon specimen under direct tension **(Li, 2019)** 25

Figure 13: Compressive behaviour of ECC **(Li, 2019)**.......... 26

Figure 14: Effect of oiling agent on tensile stress-strain curve, 0%, 0.3%, 0.5%, 0.8%, 1.2% **(Li et al, 2002)**.......... 27

Figure 15: Column and link beam behaviour of R/C and ECC under reversed cyclic loading **(V. C. Li, 2009)** 28

Figure 16: Performance of high fly ash mix under tensile loading **(Yang & Li, 2012)**.......... 29

Figure 17: Impact performance of R/C vs R/ECC mix beams **(Yang & Li, 2012)**.......... 30

Figure 18: Performance of ECC mixes using various PVA fibre coatings **(Sun et al., 2018)**..... 31

Figure 19: Steel fibres distributed within the cementitious solid **(Drdlová et al., 2018)**.......... 33

Figure 20: Crack distribution on test specimen vs LS-Dyna model **(Drdlová et al., 2018)** 33

Figure 21: Change in ductility vs. age, fly ash, limestone replacement ratios **(Turk & Nehdi, 2021)** 34

Figure 22: Direct tension test results showing tensile stress vs strain **(Ranade et al., 2013)** 35

Figure 23: Compressive and Tensile stress-strain curves of UHP-ECC **(Yu et al., 2019)** 37

Figure 24: Fibre surface damage and fibre/matrix interface **(Yu et al., 2019)** 37

Figure 25: Variation of failure stress and failure strain vs water cement ratio **(Park et al., 2020)** 38

Figure 26: DIF values for grade 40, 60, and 75 ksi reinforcing steel **(Malvar, 1998)** 39

Figure 27: Comparison of experimental results and Johnson-Cook model **(Forni et al., 2016)** 40

Figure 28: Calculated and experimental resistance functions of panels **(Naito et al., 2014)**...... 41

Figure 29: Performance of Ductal panels under a 6-ton TNT blast **(Cavili & Rebentrost, 2006)** 42

Figure 30: Fibre reinforced panels after the contact charge tests **(Nam et al., 2017)** 44

Figure 31: Midspan deflection for 1, 0.75, and 0.5 m standoff distance **(Lim et al., 2025)** 45

Figure 32: 200 mm thick specimen tested under 5.5 kg TNT at 1.5 m standoff distance **(Giovino et al., 2014)** 47

Figure 33: Displacement vs time history of columns with axial load **(Kadhom, 2016)** 48

Figure 34: Multiple panels positioned for blast testing 50

Figure 35: Vertical HSS Studs and panel-stud composite wall system for blast resistance 51

Figure 36: Preliminary FEA using LS-Dyna – ECC panels supported on their short sides 53

Figure 37: Dimensions of tension coupon specimens 55

Figure 38: Direct tension test setup of ECC coupons, LVDTs on the right front and left behind 55

Figure 39: Alignment of U-shaped load application plates before tension tests 56

Figure 40: Stress-strain relationship of an ECC coupon in direct tension 57

Figure 41: HDPE sheet used as a formwork layer for ease of debonding and not damaging the panel surface 58

Figure 42: Self-drilling screw installation 59

Figure 43: Panels with 100 mm (left) and 200 mm (right) connector spacing 60

Figure 44: Fibres before (left) and after (right) air-tumbling 61

Figure 45: Two hand mixers are being used simultaneously for mixing in a plastic drum 62

Figure 46: Specimens immediately after pouring and covered with wet burlap, four hours later62

Figure 47: Panel specimens prior to installation on the shock tube for blast testing.................. 62

Figure 48: Driver and diaphragm (top) and expansion (bottom) sections of the shock tube....... 64

Figure 49: Aluminum sheets on either side of the diaphragm section.. 65

Figure 50: Pressure vs. time data of a simulated blast at the shock tube.................................... 66

Figure 51: A single panel and an HSS member behind at its left-hand side............................... 68

Figure 52: #14 x 2-1/2-inch-long hex head self-drilling screws attached 69

Figure 53: Support angles, HSS, and panel connection... 69

Figure 54: 3D rendering of the test setup for the first set of specimens 69

Figure 55: Each panel is connected to support angles using 12 mm bolts 70

Figure 56: Second set of wall specimens during installation... 70

Figure 57: Third set of wall specimens prior to testing 71

Figure 58: Set 4 specimens during preparation.. 72

Figure 59: Set 4 wall specimens prior to testing... 73

Figure 60: Set 5 steel sheets prior to testing 73

Figure 61: Displacement measurement locations on the panels 75

Figure 62: Checkerboard tape markings on wall specimens 75

Figure 63: Air pressure control device.. 76

Figure 64: Movement tracking of points before (left) and during (right) blast test..................... 77

Figure 65: Pressure, Impulse and Displacement vs Time chart for Set 1 - shot #6 – 82 kPa & 1066 kPa-ms (Scaled distance, Z = 5.5 m / kg$^{1/3}$) ... 79

Figure 66: Set 1 specimens before and during shot #6 ... 80

Figure 67: Set 1 specimens after failure, back side ... 82

Figure 68: Set 1 specimens after failure, front side ... 82

Figure 69: Set 1 specimens after failure, failed bolt (left), demolition (right) ... 83

Figure 70: Displacement vs Time graph showing all shots of Set 1 specimens ... 83

Figure 71: Pressure, Impulse and Displacement vs Time chart for set 1 - shot #1 – 21 kPa & 56 kPa-ms, 13.3 m/kg$^{1/3}$ ... 84

Figure 72: Pressure, Impulse and Displacement vs Time chart for set 1 - shot #2 – 48 kPa & 138 kPa-ms, 7.5 m/kg$^{1/3}$ ... 85

Figure 73: Pressure, Impulse and Displacement vs Time chart for set 1 - shot #3 – 58 kPa & 183 kPa-ms, 6.7 m/kg$^{1/3}$ ... 86

Figure 74: Pressure, Impulse and Displacement vs Time chart for set 1 - shot #4 – 58 kPa & 455 kPa-ms, 6.7 m/kg$^{1/3}$ ... 87

Figure 75: Pressure, Impulse and Displacement vs Time chart for set 1 - shot #5 – 76 kPa & 648 kPa-ms, 5.7 kg/m$^{1/3}$ ... 88

Figure 76: Set 2 Specimens - movement of support angle during the 3rd Shot ... 90

Figure 77: Set 2 shot #3 fragmentation at panels 2 and 4 (left), 309 mm additional deformation (right) ... 91

Figure 78: Pressure, Impulse and Displacement vs Time chart for set 2 - shot #1 – 30 kPa & 324 kPa-ms, 10.3 m/kg$^{1/3}$ 92

Figure 79: Pressure, Impulse and Displacement vs Time chart for set 2 - shot #2 – 60 kPa & 668 kPa-ms, 6.5 m/kg$^{1/3}$ 93

Figure 80: Pressure, Impulse and Displacement vs Time chart for set 2 - shot #3 – 85 kPa & 1048 kPa-ms, 5.4 m/kg$^{1/3}$ 94

Figure 81: Set 3 shot #2 fragmentation at panels 2, 3 and 4 (left), 414 mm maximum deformation (right) 96

Figure 82: Pressure, Impulse and Displacement vs Time chart for set 3 - shot #1 – 35 kPa & 320 kPa-ms, 9.2 m/kg$^{1/3}$ 97

Figure 83: Pressure, Impulse and Displacement vs Time chart for set 3 - shot #2 – 63 kPa & 577 kPa-ms, 6.4 m/kg$^{1/3}$ 98

Figure 84: Set 4 specimens following shot #3 100

Figure 85: Threaded rods after failure 100

Figure 86: Pressure, Impulse and Displacement vs Time chart for set 4 - shot #1 – 36 kPa & 402 kPa-ms, 9.0 m/kg$^{1/3}$ 101

Figure 87: Pressure, Impulse and Displacement vs Time chart for set 4 - shot #2 – 62 kPa & 714 kPa-ms, 6.4 m/kg$^{1/3}$ 102

Figure 88: Pressure, Impulse and Displacement vs Time chart for set 4 - shot #3 – 86 kPa & 1139 kPa-ms, 5.3 m/kg$^{1/3}$ 103

Figure 89: Buckling of steel sheets after shot #2 105

Figure 90: Pressure, Impulse and Displacement vs Time graph for set 5 - shot #1 – 32 kPa & 260 kPa-ms, 9.8 $m/kg^{1/3}$ 106

Figure 91: Pressure, Impulse and Displacement vs Time graph for set 5 - shot #2 – 62 kPa & 495 kPa-ms, 6.4 $m/kg^{1/3}$ 107

Figure 92: Inversion of a diagonal mass matrix........ 111

Figure 93: Eight-node solid hexahedron element (LSTC, 2025b)........ 115

Figure 94: LS-Dyna model showing solid elements........ 115

Figure 95: HSS Members modelled with shell elements in LS-Dyna........ 116

Figure 96: Beam elements used to model threaded rods and screws........ 117

Figure 97: ECC Stress vs. Strain in tension (top) and compression (bottom)........ 118

Figure 98: ECC coupon specimen undeformed (top), ECC coupon specimen before rupture (center), Stress vs time in the longitudinal direction (bottom) 119

Figure 99: Steel plate Stress vs. Strain 120

Figure 100: Active (left) and inactive (right) contact algorithm between support angles........ 121

Figure 101: Flexural yielding at the midspan of the HSS members........ 124

Figure 102: Movement of the supports observed in the shock tube (left) and in LS-Dyna (right) 126

Figure 103: Pressure vs. time, measured in the shock tube and applied in LS-Dyna for 1567 kg of TNT with a standoff distance of 64 metres, Z = 5.5 $m/kg^{1/3}$ (82 kPa and 1066 kPa-ms)127

Figure 104: Displacement vs time curve of Shot #1, 3.5 kg at 20 m, Z = 13.3 m/kg$^{1/3}$ (21 kPa and 56 kPa-ms) 128

Figure 105: Displacement vs time curve of Shot #2, 9 kg at 16 m, Z = 7.5 m/kg$^{1/3}$ (48 kPa and 138 kPa-ms) 128

Figure 106: Displacement vs time curve of Shot #3, 15 kg at 16 m, Z = 6.7 m/kg$^{1/3}$ (58 kPa and 183 kPa-ms) 129

Figure 107: Displacement vs time curve of Shot #4, 228 kg at 41 m, Z = 6.7 m/kg$^{1/3}$ (58 kPa and 455 kPa-ms) 129

Figure 108: Displacement vs time curve of Shot #5, 390 kg at 42 m, Z = 5.7 m/kg$^{1/3}$ (76 kPa and 648 kPa-ms) 130

Figure 109: Displacement vs time curve of Shot #6, 1567 kg at 64 m, Z = 5.5 m/kg$^{1/3}$ (82 kPa and 1066 kPa-ms) 130

Figure 110: Shock tube tested specimen with 200 mm connector spacing (left), and LS-Dyna modelled specimen (center, right) subjected to a blast load with the 1417 kg TNT weight and 60 metre standoff distance, Z = 5.4 m/kg$^{1/3}$ (85 kPa and 1048 kPa-ms)........ 132

Figure 111: Shock tube tested specimen with 100 mm connector spacing (left), and LS-Dyna modelled specimen (center, right) subjected to a blast load with the 1417 kg TNT weight and 60 metre standoff distance, Z = 5.4 m/kg$^{1/3}$ (85 kPa and 1048 kPa-ms)........ 133

Figure 112: Displacement vs time curve of Shot #1, 305 kg at 69 m, Z = 10.3 m/kg$^{1/3}$ (30 kPa and 324 kPa-ms) 136

Figure 113: Displacement vs time curve of Shot #2, 677 kg at 57 m, Z = 6.5 m/kg1/3 (60 kPa and 668 kPa-ms) 137

Figure 114: Displacement vs time curve of Shot #3, 1417 kg at 60 m, Z = 5.4 m/kg1/3 (85 kPa and 1048 kPa-ms) 137

Figure 115: Shock tube tested specimen with 100 mm connector spacing (left), and LS-Dyna modelled specimen (center, right) subjected to a blast load with the 398 kg TNT weight and 47 metre standoff distance, Z = 6.4 m/kg$^{1/3}$ (63 kPa and 577 kPa-ms) 140

Figure 116: Shock tube tested specimen with 200 mm connector spacing (left), and LS-Dyna modelled specimen (center, right) subjected to a blast load with the 398 kg TNT weight and 47 metre standoff distance, Z = 6.4 m/kg$^{1/3}$ (63 kPa and 577 kPa-ms) 141

Figure 117: Displacement vs time curve of Shot #1, 214 kg at 55 m, Z = 9.2 m/kg$^{1/3}$ (35 kPa and 320 kPa-ms) 142

Figure 118: Displacement vs time curve of Shot #2, 398 kg at 47 m, Z = 6.4 m/kg$^{1/3}$ (63 kPa and 577 kPa-ms) 142

Figure 119: Shock tube tested specimen with 100 mm connector spacing (left), and LS-Dyna modelled specimen (center, right) subjected to a blast load with the 1787 kg TNT weight and 65 metre standoff distance, Z = 5.3 m/kg$^{1/3}$ (86 kPa and 1139 kPa-ms)........ 144

Figure 120: Shock tube tested specimen with 200 mm connector spacing (left), and LS-Dyna modelled specimen (center, right) subjected to a blast load with the 1787 kg TNT weight and 65 metre standoff distance, Z = 5.3 m/kg$^{1/3}$ (86 kPa and 1139 kPa-ms)........ 145

Figure 121: Displacement vs time curve of Shot #1, 399 kg at 67 m, Z = 9.0 m/kg$^{1/3}$ (36 kPa and 402 kPa-ms) 146

Figure 122: Displacement vs time curve of Shot #2, 777 kg at 59 m, Z = 6.4 m/kg$^{1/3}$ (62 kPa and 714 kPa-ms) 147

Figure 123: Displacement vs time curve of Shot #3, 1787 kg at 65 m, Z = 5.3 m/kg$^{1/3}$ (86 kPa and 1139 kPa-ms).. 147

Figure 124: Shock tube tested 3 mm thick steel sheet (left), and LS-Dyna modelled specimen (center, right) subjected to a blast load with the 244 kg TNT weight and 40 metre standoff distance, Z = 6.4 m/kg$^{1/3}$ (62 kPa and 485 kPa-ms).. 149

Figure 125: Shock tube tested 1.5 mm thick steel sheet (left), and LS-Dyna modelled specimen (center, right) subjected to a blast load with the 244 kg TNT weight and 40 metre standoff distance, Z = 6.4 m/kg$^{1/3}$ (62 kPa and 485 kPa-ms).. 150

Figure 126: Displacement vs time curve of Shot #1, 138 kg at 51 m, Z = 9.8 m/kg$^{1/3}$ (32 kPa and 260 kPa-ms) 151

Figure 127: Displacement vs time curve of Shot #2, 244 kg at 40 m, Z = 6.4 m/kg$^{1/3}$ (62 kPa and 485 kPa-ms) 151

Figure 128: Deformed shape of LS-Dyna model with HSS member and 3 mm steel sheet without ECC layers (left), Set 1 specimen 3 mm steel sheet with ECC-Steel-ECC panel (right) under the blast effect of 1567 kg TNT at 64 m, Z = 5.5 m/kg$^{1/3}$ (82kPa, 1066 kPa-ms) 153

Figure 129: Required ductility ratio versus load duration to vibration period chart of elasto-plastic systems (UFC 3-340-02, 2008) 155

Figure 130: Deformed shape of LS-Dyna model with enhanced contact (left), Set 2 specimen representing 100 mm connector spacing (right) under the blast effect of 1417 kg TNT at 60 m, Z = 5.4 m/kg$^{1/3}$ (85 kPa and 1048 kPa-ms).. 157

Figure 131: Deformed shape of the enhanced panel (left), deformed shape showing the effective plastic strain (right) under the blast effect of 5666 kg TNT at 60 m, Z = 3.4 m/kg$^{1/3}$ (239 kPa and 2725 kPa-ms) 158

Figure 132: Deformed shape of the LS-Dyna model of the 27 mm thick specimen side (left) and front (right) using the contact formulation representing the 100 mm connector spacing, under 1417 kg TNT at 60 m blast load, Z = 5.4 m/kg$^{1/3}$ (85 kPa and 1048 kPa-ms).......... 159

Figure 133: Deformed shape of the LS-Dyna models of enhanced contact 27 mm thick specimen (left) and enhanced contact 15 mm thick specimen (right) under 1417 kg TNT at 60 m blast load, Z = 5.4 m/kg$^{1/3}$ (85 kPa and 1,048 kPa-ms).......... 160

Figure 134: Deformed shape of the LS-Dyna models of enhanced contact 27 mm thick specimen (left) and enhanced contact 15 mm thick specimen (right) under 5666 kg TNT at 60 m blast load, Z = 3.4 m/kg$^{1/3}$ (239 kPa and 2725 kPa-ms).......... 161

Figure 135: Undeformed view of the LS-Dyna model for the "Partition Wall" specimen........ 163

Figure 136: Deformed shape and plastic strain of the "Partition Wall" type specimen under the blast of 1567 kg TNT at 64 metres, Z = 5.5 m/kg$^{1/3}$ (82 kPa and 1066 kPa-ms). Protected side (top), blast side (bottom). 164

Figure 137: Deformed shape and plastic strain of the "Partition Wall" type specimen from the protected side under the blast of 10 kg TNT at 5 metres, Z = 2.3 m/kg$^{1/3}$ (674 kPa and 506 kPa-ms) 165

Figure 138: Deformed shape and plastic strain of the "Partition Wall" type specimen under the blast of 15 kg TNT at 5 metres, Z = 2.0 m/kg$^{1/3}$ (1,011 kPa and 687 kPa-ms). Protected side (top), blast side (bottom).......... 166

Figure 139: LS-Dyna model of a 9 mm bullet and a 3 mm thick steel plate 168

Figure 140: LS-Dyna model of a 9 mm bullet and a 15 mm thick ECC-steel-ECC panel........ 169

Figure 141: Change in kinetic energy 170

Figure 142: Bullet moving through ECC-Steel-ECC (left) and Steel (right) models............... 170

Figure 143: Span, length and sag of a cable with only axial stiffness 173

Figure 144: Resistance function of an ECC-steel-ECC panel with a 3 mm thick steel sheet ... 175

Figure 145: Displacement vs. Time obtained using RCBlast software 175

Figure 146: Moment-Curvature relationship for a 76 x 51 x 3.2 mm HSS member with ECC-Steel-ECC panel 177

Figure 147: Resistance-Curvature diagram for 76x51x3.2 mm HSS and ECC-steel-ECC panel 177

Figure 148: Resistance function for the 76x51x3.2 mm HSS and ECC-steel-ECC specimen.. 178

Figure 149: Deformation vs. Time relationship obtained from SDOF analysis 178

Figure 150: Moment-Curvature relationship for Panel-HSS-Panel section using 15 mm thick panels and HSS 152x152x6 mm 190

Figure 151: Resistance function of the Panel-HSS-Panel wall using 15 mm thick panels and HSS 152x152x6 mm 192

Figure 152: Deformation vs. Time relationship of the wall under 1011 kPa reflected pressure and 687 kPa-ms reflected impulse 193

Figure 153: Pressure-Impulse diagram for the 4-metre-high wall 193

List of Tables

Table 1: Mix proportions for the ECC by weight, (Lepech & Li, 2008) 55

Table 2: Types of panels included in the experimental program... 67

Table 3: Specimen testing matrix.. 67

Table 4: Blast load details for the first set of specimens.. 81

Table 5: Blast load details for the second set of specimens 91

Table 6: Blast load details for the third set of specimens... 96

Table 7: Blast load details for the fourth set of specimens 100

Table 8: Blast load details for the fifth set of specimens 105

Table 9: Unit system used in LS-Dyna models..113

Table 10: Mesh sensitivity analysis summary.. 123

Table 11: LS-Dyna Model vs. Shock Tube Specimen after the sixth shot................................ 125

Table 12: Shock tube 2nd Set of Specimens vs. LS-Dyna Models comparison for Shot #3....... 136

Table 13: Shock tube 3rd Set of Specimens vs. LS-Dyna Models comparison for shot #2....... 141

Table 14: shock tube 4th Set of Specimens vs. LS-Dyna Models comparison for shot #3 146

Table 15: Shock tube 5th Set of Specimens vs. LS-Dyna Models comparison for shot #2....... 150

Table 16: Deformation results for shock tube Set 1 Specimen, LS-Dyna Model for Set 1, LS-Dyna Model without ECC 153

Table 17: LS-Dyna results for panel with 100 mm connector spacing and enhanced contact panels 159

Table 18: LS-Dyna Model results for 27 mm and 15 mm thick enhanced contact specimens exposed to blast loads from 1417 kg and 5666 kg TNT at 60 m 162

Table 19: Summary of results for the "Partition Wall" type specimens 167

Table 20: Sag, length, support movement and resistance function values for an ECC-steel-ECC panel 174

List of Equations

Eq. 1....110

Eq. 2....110

Eq. 3....110

Eq. 4....110

Eq. 5....110

Eq. 6....110

Eq. 7....111

Eq. 8....111

Eq. 9....112

Eq. 10....112

Eq. 11....112

Eq. 12....112

Eq. 13.... 122

Eq. 14.... 173

Eq. 15.... 174

Chapter 1. Introduction

1.1 Background

The terrorist attack on the Alfred P. Murrah Federal Building in Oklahoma City on April 19, 1995, exposed the vulnerabilities of otherwise well-designed civilian structures to blast loading. As a result, engineers and government agencies focused their efforts on remedying these vulnerabilities. Design guidelines aiming to provide necessary design tools for structural engineers were developed by government agencies in the ensuing years (FEMA P-439B, 2010; FEMA-426/BIPS-06, 2011; FEMA-428/BIPS-07, 2012). These documents provide methods to mitigate risks involved with terrorist attacks against civilian buildings, including structural design strategies. Documents developed by the U.S. Department of Homeland Security provide comprehensive guidelines for designing building structures and the built environment in general. They emphasize the importance of blast-resistant design of individual elements, as well as load path continuity and redundancy, to prevent progressive collapse (FEMA/BIPS 05, 2011).

As a part of the continued effort to increase the resilience of structures against blast loads, structural design codes were modified to strengthen structures against progressive collapse. An example of such a modification is providing continuity reinforcement underneath reinforced concrete columns to provide positive moment resistance and tensile capacity (Canadian Standard Association, 2024a). Similar structural integrity requirements exist for steel (CSA S16:24, Cl. 6.1.2) and wood (CSA O86:24, Cl. 4.3.3) structures as well (Canadian Standard Association, 2024b; Canadian Standard Association, 2024c). These structural design provisions are intended to prevent a total or partial collapse of a structure; however, they do not address the non-structural components of a building.

Even though the provisions of modern structural design codes, especially those with seismic design requirements, may enable the structural elements of a building to remain intact in the event of an explosion (FEMA P-439B, 2010), non-structural elements, including unreinforced masonry walls or curtain wall glazing, remain vulnerable to blast loads. The failure of building envelope components could pose a significant threat to the inhabitants due to the very high velocities of fragments moving toward the interior space. Therefore, to protect the inhabitants of a building subjected to blast loads, it is necessary to ensure the integrity of non-structural exterior elements in addition to the overall structural stability. This requires a holistic approach to building design to achieve resiliency against blast loads.

The need for a standard specifically aimed at blast-resistant design of buildings in Canada was recognized by the Canadian Standards Association in 2010. Consequently, a concerted effort was made to put together a technical committee to develop a design standard for building structures exposed to blast loads. This resulted in the first Canadian standard, CSA S850, in 2012 (and updated in 2023 and 2025), to serve as a guide for assessing and designing buildings against blast loads in Canada (Canadian Standard Association, 2023). This Standard addresses blast-resistant design of structural and non-structural elements for new construction, as well as assessing and hardening of existing buildings. CSA S850-23 includes provisions for blast load calculations, design approaches for structural and non-structural elements, as well as blast analysis methodologies. The standard uses four performance objectives that limit progressive collapse, damage to structural components, damage to the building envelope and falling debris. Additionally, it includes methods for assessing and mitigating the vulnerability of existing buildings to mitigate blast risk through strengthening (hardening) of existing structural and non-structural elements, while promoting continuity and redundancy among members.

The process for mitigating blast risk in existing buildings differs from designing a new building. For new buildings, the designers have a wide range of options available that would allow them to choose resilient systems and materials for structural and non-structural components. On the other hand, with existing buildings, the structural system and materials are predetermined. While it may be possible to replace existing windows and doors with blast-resistant alternatives, it is generally not economically feasible to replace a structural element (especially in a cast-in-place concrete building). Therefore, existing structural elements that do not satisfy the performance requirements need to be hardened (strengthened) against blast loads (Dusenberry, 2010).

Hardening existing structural elements against blast loads aims to provide additional strength, ductility, and continuity to the strengthened members (Alsayed et al., 2016; Carriere et al., 2009; King et al., 2009; Z. Li et al., 2019). Although several methods are available for hardening existing structural elements (Alsayed et al., 2016; Cavili & Rebentrost, 2006; Ciornei & Saatcioglu, 2022; Jackson et al., 2022; King et al., 2009; Lacroix & Doudak, 2018) CSA S850-23 makes explicit reference to fibre-reinforced polymer (FRP) strengthening of existing reinforced concrete slabs, beams, columns, walls, and masonry walls. CSA S850-23 makes reference to CSA S806 (Canadian Standard Association, 2012) for the use of FRP as a strengthening technology. While FRP strengthening of reinforced concrete members provides additional strength and ductility against blast loads, it has limitations, as FRP failure modes of debonding and elastic rupturing (lack of ductility) are brittle types of failures (Jackson et al., 2022; Lacroix & Doudak, 2018). Additional blast hardening strategies have been developed in recent years and are summarized in Chapter 2 under “Literature Review.”

1.2 Research Objectives and Scope

The primary objective of the current research project is to develop a blast-resistant sandwich panel that consists of engineered cementitious composite (ECC) layers with a light-gauge steel sheet as reinforcement in between. The emphasis is placed on producing thin (~15mm) panels that are lightweight for easy handling while possessing sufficiently high strength against blast loads. High tensile capacity and ductility of ECC (3.0 MPa to 4.0 MPa in tension with up to 5% tensile strain), coupled with the inherently high tensile strength and ductility of steel sheets, provide flexural strength and energy absorption capacity under blast loads. These benefits are further enhanced by the ability of the panels to develop membrane behaviour under excessively high blast deformations for continued protection. The panels can also be used with attached vertical hollow steel sections (HSS), forming a blast-resistant wall system with further enhancement of blast resistance. These wall systems can be used as exterior or interior walls of buildings, providing a safe occupied space as the blast loads are transferred to the attached structural elements.

The scope consists of the following tasks:

- Review of available literature that consists of the fundamentals of blast engineering reflecting the current state of the art for designing blast-resistant elements, performance of the materials used with emphasis on ECC, and previous research on blast-resistant panels.
- Experimental research to develop blast-resistant ECC sandwich panels, as well as blast-resistant wall systems consisting of the panels and the attached HSS studs to validate the concept experimentally.
- Selection and design of test specimens that are representative of the panels and the wall systems to be developed for proposed applications in practice.

- Materials testing to verify the selected ECC mix design for use in the panels.
- Tests of selected specimens using the University of Ottawa Shock Tube Facility, and the analysis of test data.
- Numerical research involving the selection of appropriate software; discussion of the features of the software, modelling approach and construction of numerical models; as well as the validation of the numerical models against experimental results.
- Numerical parametric investigation to assess the significance of design parameters beyond those considered in the experimental phase.
- Analytical research to validate the use of single-degree-of-freedom dynamic analysis as an analytical design tool for use in practice while also developing resistance functions for the proposed panels.
- Development of a design procedure for use in engineering design practice.

1.3 Original Contributions to Structural/Blast Engineering

The current research project resulted in the following original contributions to the field of structural engineering in the area of blast risk mitigation through developing innovative hardening techniques:

- A new blast-resistant panel was developed utilizing engineered cementitious composite (ECC) material to mitigate blast risk in buildings. The panels can be used both as non-structural interior elements or exterior building envelope components. They can also be used as catchment elements against blast-induced fragmentation because of their ability to develop combined flexural and membrane actions.

- A new blast-resistant wall system was developed, consisting of the above blast-resistant panels and HSS studs as structural elements to protect building occupants against blast threats. They are intended to dissipate the effects of blast loads by transferring blast loads to supporting structural members, such as floor systems. They can be used as internal partition walls providing security against internal explosions, as well as building envelope elements.
- Extensive experimental data were generated on large-scale blast tests of the panels and wall systems developed above under simulated blast loads. The experimental phase of research makes original research data available to the profession for use in subsequent research projects, as well as in utilizing the new elements in practice.
- Numerical investigation was conducted to provide guidance for future research involving the use of ECC and HSS combinations as blast-risk mitigation strategies.
- Design and detailing procedures were developed for the new blast-resistant elements, utilizing single-degree-of-freedom (SDOF) dynamic analysis methodology.

It is noteworthy that the above research and development efforts had not been pursued prior to the current research project; hence, they do not exist in the existing literature.

1.4 Composition of Thesis

This thesis is composed of six chapters. In this first chapter, an introduction to the topic of blast-resistant panels is provided. The second chapter includes a review of the existing literature on blast loads, engineered cementitious composites, and panels used in blast-resistant design. The experimental part of the research carried out in the scope of this work is presented in the third chapter. The fourth chapter is dedicated to the analytical investigation that was performed as part of this research. The experimental and analytical research work presented in chapters 3 and 4 is discussed in the fifth chapter. This discussion is followed by design recommendations that outline a step-by-step approach to analyzing the behaviour of the panels using a single degree of freedom (SDOF) method and for designing the panels. Finally, the conclusions drawn from the research are provided in the sixth chapter.

Chapter 2. Literature Review

There is significant literature on the blast resistance of existing structures. Experiments performed by military engineers resulted in publications like the UFC 3-340-02, 2008, that are of foundational importance to blast engineering. There are several important works in the form of books that summarize this information in an effective way, including those authored by (Bangash & Bangash, 2006; Dusenberry, 2010; Krauthammer, 2008; Smith & Hetherington, 1994). Additionally, there are many scholarly publications that focus on the blast resistance of structures, some of which are summarized below.

The literature summarized below provides a gradual progression from a general blast engineering background to specific research related to cementitious blast-resistant panels. First, a background in blast engineering related to the calculation of blast loads, as well as analysis and design of existing and new structures, is provided. This is followed by a review of the literature on ECC and steel, which form the materials for the blast-resistant panels developed in the current research project. Subsequently, research related to the impact and blast resistance of panels, including sandwich panels, is reviewed.

2.1 Fundamentals of Blast Engineering

Codes and standards as well as best practice guidelines developed by military and civilian organizations provide much needed fundamental information on blast engineering. They provide insight into the blast phenomena as well as analysis, design and protection strategies for buildings against blast load effects. This information, initially developed through classified research conducted by the US Army researchers, was subsequently made available for civilian use and formed the basis of current blast engineering practice. The following paragraphs provide a brief review of the salient features of these documents.

Unified Facilities Criteria (UFC) (2008). *Structures to Resist the Effects of Accidental Explosions (UFC 3-340-02)*. U.S. Department of Defense

UFC 3-340-02 is a comprehensive document with over 1500 pages, which covers a wide range of topics, from blast pressures caused by various types of explosives on building surfaces to analysis of structural components under these loads. Based on explosives research conducted by the U.S. military and the U.S. Department of Defense, the data and charts included in this document provide a valuable foundation for blast engineers. Empirical charts, like the one shown in **Figure 1**, relate scaled distance, $Z = R / W^{1/3}$ (m / $kg^{1/3}$), to various blast parameters and are frequently used in determining design pressures. R is the stand-off distance between the explosive and the target surface, and W is the weight of the explosive specified as mass of equivalent trinitrotoluene (TNT). This scaling concept allows users of the document to relate various combinations of charge weight and distance, and enables a standardized approach for determining blast pressures. Essentially, UFC 3-340-02 provides the tools to estimate reflected pressure and reflected impulse values caused by an explosive detonated at a certain distance from the target. Additionally, a simplified yet reasonably accurate method of representing the blast pressure vs time relationship as a single triangular pulse is covered in detail in the document. This simplified triangular load approach allows the use of a single degree of freedom (SDOF) analysis for various structural and façade components under blast loads. The governing differential equations of a dynamic SDOF system under a triangular pulse load can be solved without engaging the complexities of the finite element method of analysis and related software. By applying certain factors and making some reasonable assumptions, the UFC 3-340-02 document provides charts and simple design tools for performing blast analysis of elastic-perfectly plastic structural members. In addition to the calculation of blast-induced pressures, this document has comprehensive guidelines for designing structural elements subjected to these loads. It provides information on practical reinforcement and connection detailing for building components, such as the use of lacing reinforcement for reinforced concrete members and connection details for steel elements.

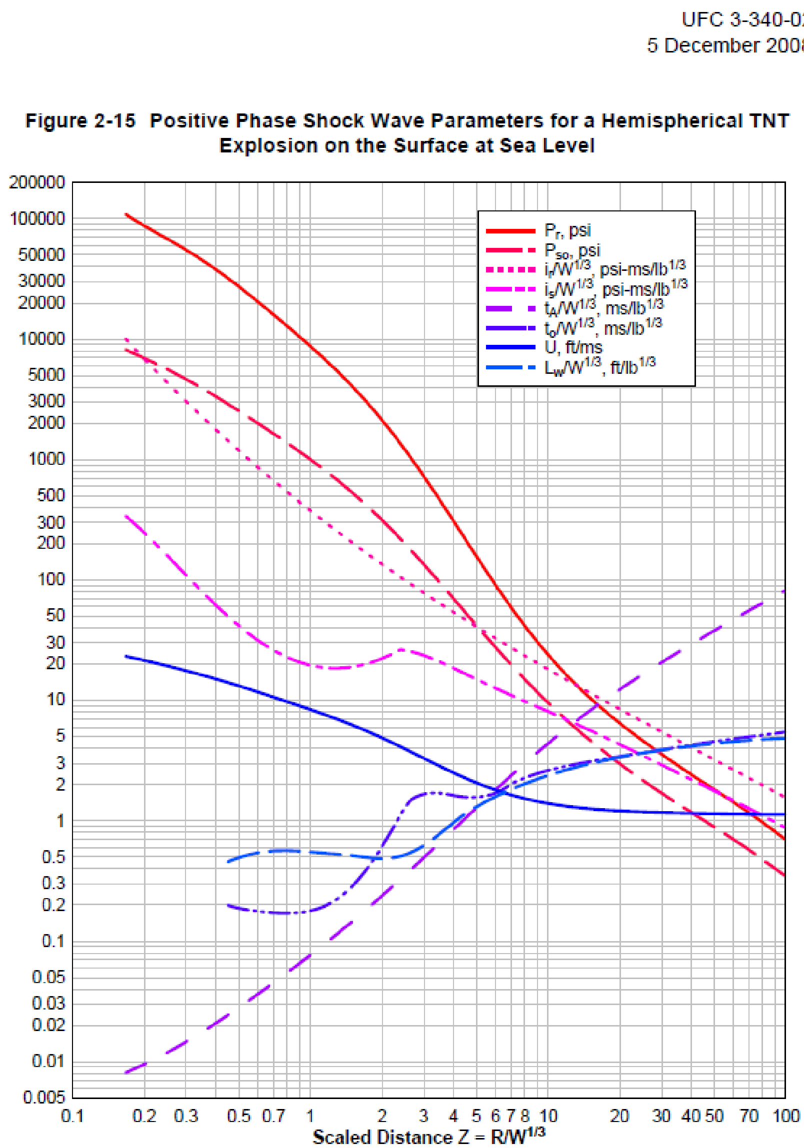

Figure 1: Blast parameters as a function of Scaled Distance, Z, as shown in Figure 2-15 of **(UFC 3-340-02, 2008)**

Canadian Standards Association. (2023). *CSA Standard S850:23: Design and assessment of buildings subjected to blast loads*. CSA Group.

CSA S850 is the national standard used in Canada for designing and assessing the blast resistance of buildings. This standard provides guidelines for enhancing building resilience against blast loads. The standard defines performance criteria for various structural and non-structural components with the goal of reducing structural damage and harm to building inhabitants, incorporating the use of different construction materials. An example of response limits for different performance levels for reinforced concrete elements is shown in **Figure 2**. CSA S850 addresses methods of calculating blast loads starting with design basis threats (DBT) and combining these loads with gravity loads for use in structural design. There are specific clauses regarding the design of walls, columns, and connections, with an emphasis on how each type of element shall be designed based on the material from which it is made. Strength increase factors (SIF) and dynamic increase factors (DIF) for various materials under blast conditions are provided to account for the rarity of the blast event and the higher strength associated with high strain rates under blast loads. It further details structural analysis techniques, including single-degree and multi-degree-of-freedom systems, finite element analysis, and computational fluid dynamics, to evaluate building responses to blast pressures.

Performance levels for structural and façade elements made of reinforced concrete, steel, wood, and masonry are provided to aid designers in achieving a well-calibrated design. Hardening (strengthening) methods of existing structures and components that require performance enhancement against blast loads are also given. These techniques allow designers to assess existing buildings using DBT and recommend solutions to building owners.

Table 4.4
Response limits for reinforced concrete*
(See Clauses 4.5.2.1, 4.5.2.2, 4.5.2.4, 4.5.2.5, 9.1.9, and A.4.5 and Table 4.3.)

Element type		B1		B2		B3		B4	
		μ_{max}	θ_{max}	μ_{max}	θ_{max}	μ_{max}	θ_{max}	μ_{max}	θ_{max}
Flexure	Single-reinforced slab or beam†	1	—	—	2°	—	5°	—	10°
	Double-reinforced slab or beam without shear reinforcement‡,§	1	—	—	2°	—	5°	—	10°
	Double-reinforced slab or beam with shear reinforcement‡	1	—	—	4°	—	6°	—	10°
	With tension membrane**	1	—	—	6°	—	12°		20°
Combined flexure and axial compression	Single-reinforced beam-column†	1	—	—	2°	—	2°	—	2°
	Double-reinforced beam-column without shear reinforcement‡,§	1	—	—	2°	—	2°	—	2°
	Double-reinforced beam-column with shear reinforcement‡	1	—	—	4°	—	4°	—	4°
	Wall or confined column††	0.9	—	1	—	2	—	3	—
	Unconfined column††	0.7	—	0.8	—	0.9	—	1	—

Figure 2: Response limits corresponding to different performance levels for reinforced concrete elements (CSA S850, 2023)

American Society of Civil Engineers. (2022). *Blast protection of buildings* (ASCE/SEI 59-22).

The ASCE 59-22 standard, first published in 2011, builds upon the data from other US-based guidelines and standards, incorporating analysis techniques and design methods for the blast resistance of building structures. As with many structural design standards, it defines minimum requirements for structural elements to ensure adequate performance under expected loading.

ASCE 59-22 provides users with valuable information on risk assessment, performance criteria, blast loading, fragmentation, structural system analysis and design, exterior envelope design, material detailing, and performance qualification. Blast load calculation procedure defined in this standard utilizes idealized bilinear and triangular loads in the form of blast pressure vs. time relationships, as shown in **Figure 3**. Unlike the CSA S850 standard, this standard provides useful guidelines for the effects of fragmentation caused by blast. In addition, the concept of a 'safe haven' is defined in the standard, which requires a specific part of the structure to be not only blast-resistant but also impact-resistant. This concept is of relevance to the panels discussed in the current research project, as the panels provide a certain amount of impact resistance in addition to blast resistance. The standard also emphasizes the importance of considering occupant protection and post-blast functionality when establishing performance objectives for protective structures.

The materials detailing section of this standard addresses the specific design and detailing requirements of frequently used materials, including reinforced concrete, steel, masonry, fibre-reinforced polymer composites, and steel-concrete composites. These provisions are particularly useful in that they address the detailing of open web steel joists and concrete slabs on metal deck systems, which are frequently used in North American industrial buildings. There is also guidance on 'steel-plate composite walls,' which utilize two exterior steel faceplates that behave as a composite element with a structural concrete core. Although detailing guidelines for aluminum, wood, and cold-formed steel are not explicitly addressed, the users are frequently referred to the relevant material design standards.

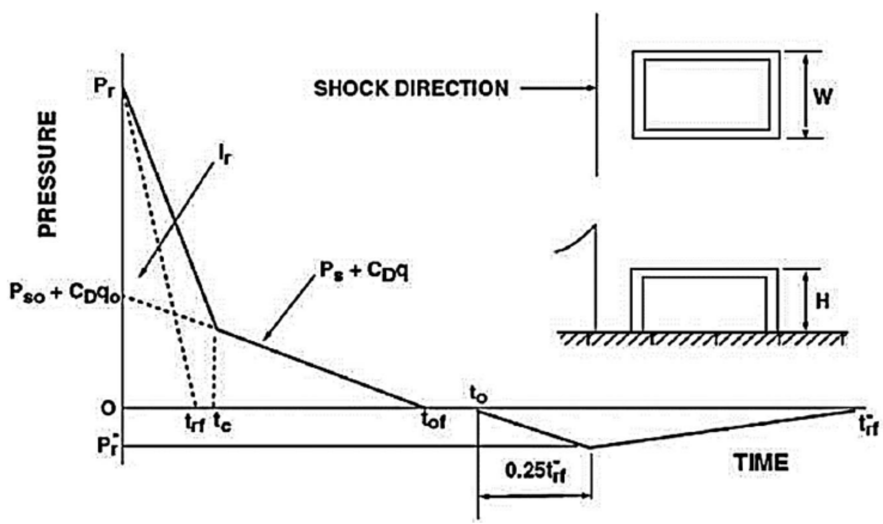

Figure 3: Triangular pressure vs time for front wall loading as defined in the ASCE 59-22 (2022)

Task Committee on Blast-Resistant Design. (2025). *Design of blast-resistant buildings in energy and industrial facilities* (3rd ed.). American Society of Civil Engineers. https://doi.org/10.1061/9780784485897

This extensive engineering report, prepared by the ASCE Petrochemical Energy Committee, is a valuable resource for researchers and practicing engineers alike. The report provides a comprehensive background on calculating blast pressures on various surfaces of building structures. The primary benefit of the report is that it is geared toward guiding practicing professionals and hence includes many realistic design details and examples. This report addresses the design and hardening of structural members like columns, beams, slabs, and shear walls in addition to non-structural members like windows, doors and non-load bearing façade elements. Furthermore, the theoretical background on these methods is provided along with useful references. **Figure 4** below shows a sample detail for a catchment system of a non-load-bearing masonry wall. In this detail, a geotextile fabric is wrapped around steel plates. Steel plates are connected to the slab above and below, and the geotextile serves as a catchment function through its membrane action. This particular method is similar to the panels proposed in this study, where flexible HSS sections replace the steel plates, and the panels replace the geotextile fabric.

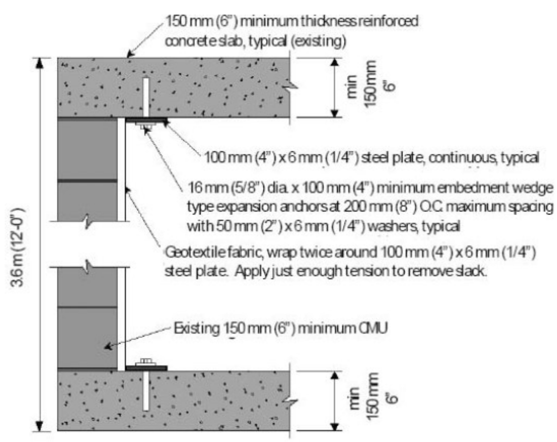

Figure 4: Catchment system for non-load bearing masonry wall (Task Committee on Blast-Resistant Design, 2025)

Federal Emergency Management Agency. (2011). *Reference Manual to Mitigate Potential Terrorist Attacks Against Buildings (Edition 2)* (FEMA-426/BIPS-06). Department of Homeland Security.

The FEMA-426 document is a reference manual for mitigating terrorist attack risks on buildings. This document aims to inform a wide range of readers, not limited to structural engineers and researchers, on the topic of blast resistance. Hence, valuable information is provided on enhancing the blast resistance of architectural, structural, and mechanical components of buildings. It also discusses the concepts of vulnerability and risk assessment, as well as the design of security systems. In terms of structural design, the approach in the document is more qualitative. Despite a lack of detailed technical guidance, this reference manual includes valuable design tips for a resilient and blast-resistant structural system of a building. Furthermore, design concepts and tips for various façade systems, elements, and their connections to structural members are discussed. The document also emphasizes the importance of an integrated design approach in which architectural, structural, mechanical, and security considerations are coordinated from the early stages of a project. In addition, practical recommendations are provided for reducing potential hazards associated with progressive collapse, flying debris, and glazing failure following an explosive event. An example of the type of information presented is shown in **Figure 5**, which illustrates the benefit of having strong columns in the case of the 1993 bombing of World Trade Center 1. This example highlights the importance of structural redundancy and robust load paths, which can significantly improve the ability of a building to withstand localized damage without experiencing disproportional collapse.

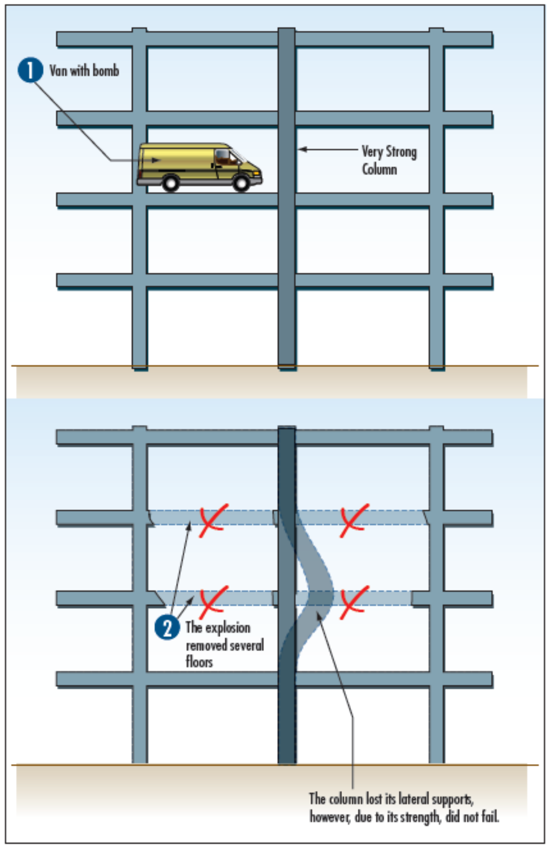

Figure 5: Illustration of a strong column preventing progressive collapse **(FEMA-426/BIPS-06, 2011)**

Federal Emergency Management Agency. (2012). *Primer to Design Safe School Projects in Case of Terrorist Attacks and School Shootings* (FEMA 428/BIPS-07). Department of Homeland Security.

This document provides design guidelines to enhance the blast resistance of school buildings, addressing potential terrorist attacks and active shooter scenarios. As is the case with other FEMA documents, the target audience for this document goes beyond structural engineers. Its contents are related to site planning, architectural requirements, and general risk planning. Due to its goal of serving a broader audience, this document includes sketches that serve as valuable teaching tools for explaining the threat levels associated with various sizes of explosives, the damage these explosions can cause, and the mechanism of damage progression in building structures (**Figure 6**).

FEMA 428 identifies that schools, especially those located in urban areas, are potential targets for blast-related threats due to their proximity to high-risk structures. The importance of a layered approach is emphasized, where, as a first line of defense, physical barriers are used to limit the distance between the school buildings and vehicle-borne explosive threats. Following the perimeter approach, designers are guided to focus on external walls, windows and doors to increase strength. Laminated glazing, which limits breaking and prevents shards from creating debris, is recommended.

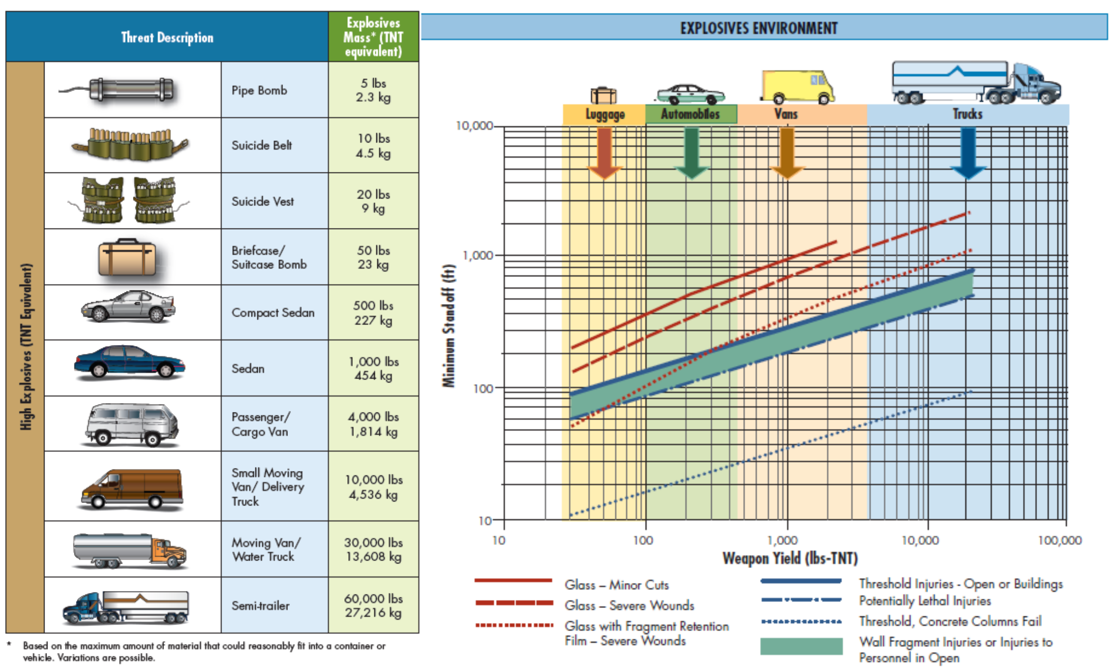

Figure 6: Threat description and damage potential charts **(FEMA-428/BIPS-07, 2012)**

U.S. Army Corps of Engineers. (2008). *Methodology Manual for the Single-Degree-of-Freedom Blast Effects Design Spreadsheets (SBEDS)* (PDC TR-06-01, Rev 1).

This technical manual is a comprehensive guide for using the Microsoft Excel-based SBEDS tool. As SBEDS is an easy-to-use tool that uses the SDOF approach for analyzing and designing structural elements subjected to blast loads, this manual is a critically important supporting document. It summarizes a wealth of information in a concise and targeted way. For example, components of the resistance function for various support conditions of one-way members are shown in **Figure 7**. Although these resistance function parameters are based on the load and mass factors for the SDOF analysis that was derived in Biggs (1964), the SBEDS manual summarizes this information along with an explanation of how the tool utilizes it. This tool can be used to calculate the resistance of the element based on its strength, stiffness, and support conditions, as well as its deflections under blast loads. In addition, the manual provides guidance on the interpretation of analysis results and the assessment of structural performance levels, allowing users to evaluate whether a structural element satisfies the desired blast-resistance criteria.

A concept addressed in this manual that is especially relevant to the topic of the experiments covered in current research is the tension membrane response of elements under blast loads. The large displacements experienced by the 15 mm thick panels developed in current research include catenary action. The force couple developed between the supports and the midspan of the member creates additional resistance, as illustrated in **Figure 8**. The contribution of this mechanism becomes increasingly important as the element undergoes large deformations and transitions from flexural behaviour to membrane-dominated response.

This manual also includes material-specific design documentation for reinforced concrete, structural steel, masonry and wood. As part of these design guidelines, it provides valuable information about strain rate effects and how the strength values of these materials increase under the high strain rates caused by blast-induced forces.

Support Conditions and Loading Diagrams	Elastic Resistance	Ultimate Flexural Resistance	Stiffness		Equivalent Support Shears
			Bending[1,2]	Shear[3]	
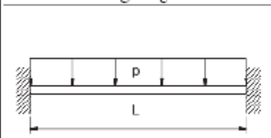	$r_e = \frac{12M_n}{L^2}$	$r_u = \frac{8\left(M_n + M_p\right)}{L^2}$	$k_e = \frac{384EI}{L^4}$ $k_{ep} = \frac{384EI}{5L^4}$ $k_E = \frac{307EI}{L^4}$	$k_e = k_{ep} = \frac{hE}{0.35L^2}$	$V = \frac{r_u L}{2}$
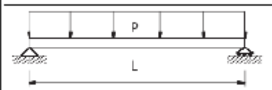	$r_e = r_u$	$r_u = \frac{8M_p}{L^2}$	$k_e = k_E = \frac{384EI}{5L^4}$	$k_e = \frac{hE}{0.35L^2}$	$V = \frac{r_u L}{2}$
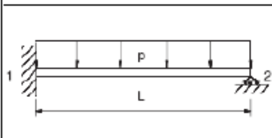	$r_e = \frac{8M_n}{L^2}$	$r_u = \frac{4\left(M_n + 2M_p\right)}{L^2}$	$k_e = \frac{185EI}{L^4}$ $k_{ep} = \frac{384EI}{5L^4}$ $k_E = \frac{160EI}{L^4}$	$k_e = k_{ep} = \frac{hE}{0.35L^2}$	$V_1 = \frac{5r_u L}{8}$ $V_2 = \frac{3r_u L}{8}$
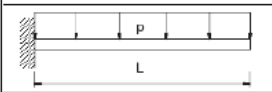	$r_e = r_u$	$r_u = \frac{2M_n}{L^2}$	$k_e = k_E = \frac{8EI}{L^4}$	$k_e = \frac{hE}{1.4L^2}$	$V = r_u L$
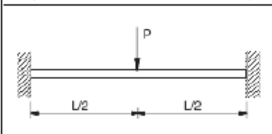	$r_e = \frac{8M_n}{L}$	$r_u = \frac{4\left(M_n + M_p\right)}{L}$	$k_e = \frac{192EI}{L^3}$ $k_{ep} = \frac{48EI}{L^3}$ $k_E = \frac{192EI}{L^3}$	$k_e = k_{ep} = \frac{hE}{0.7L}$	$V = \frac{R_u}{2}$
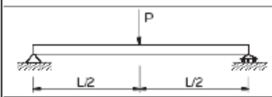	$r_e = r_u$	$r_u = \frac{4M_p}{L}$	$k_e = k_E = \frac{48EI}{L^3}$	$k_e = \frac{hE}{0.7L}$	$V = \frac{R_u}{2}$
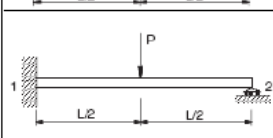	$r_e = \frac{16M_n}{3L}$	$r_u = \frac{2\left(M_n + 2M_p\right)}{L}$	$k_e = \frac{107EI}{L^3}$ $k_{ep} = \frac{48EI}{L^3}$ $k_E = \frac{106EI}{L^3}$	$k_e = k_{ep} = \frac{hE}{0.7L}$	$V_1 = \frac{11r_u}{16}$ $V_2 = \frac{5r_u}{16}$
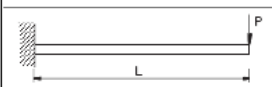	$r_e = r_u$	$r_u = \frac{M_n}{L}$	$k_e = k_E = \frac{3EI}{L^3}$	$k_e = \frac{hE}{2.8L}$	$V = r_u$

Figure 7: Flexural resistance, stiffness and support shears for one-way members **(SBEDS Methodology Manual, 2008)**

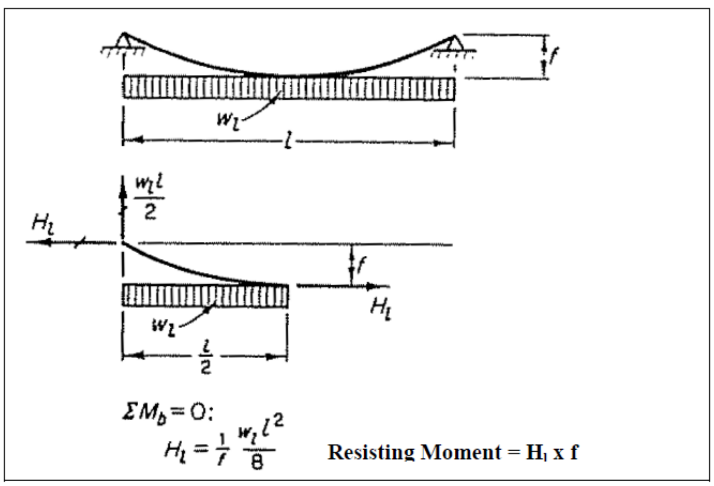

Figure 8: Additional moment resistance due to catenary action caused by tension membrane response **(SBEDS Methodology Manual, 2008)**

Smith, P. D., Hetherington, J. G. (1994). *Blast and Ballistic Loading of Structures*. Routledge, Taylor & Francis Group.

This book has valuable information regarding the detonation chemistry of explosives and the rapid expansion of the shockwave within various media (air, water and ground). Furthermore, the dynamic interaction between the shockwave and the building is investigated in depth. In addition, there is a high-level coverage of the protection of existing structures with an emphasis on cost. This part emphasizes the effectiveness of increasing the standoff distance by limiting access to buildings to be protected. Additionally, a compromise between the cost of loss and the cost of protection is recommended. **Figure 9** demonstrates this optimization concept.

The authors discuss analysis methods, including the SDOF approach and finite element analysis, to determine structural forces resulting from blast loads. The importance of ductility and energy absorption for structural resilience is mentioned. Smith and Hetherington also provide valuable information on the use of layered composites and their effectiveness in resisting ballistic impact. It is notable that utilizing a brittle exterior material with a high hardness value, which is backed up with a softer ductile material, is a method that provides a higher ballistic resistance than the sum of the resistances of each layer considered individually.

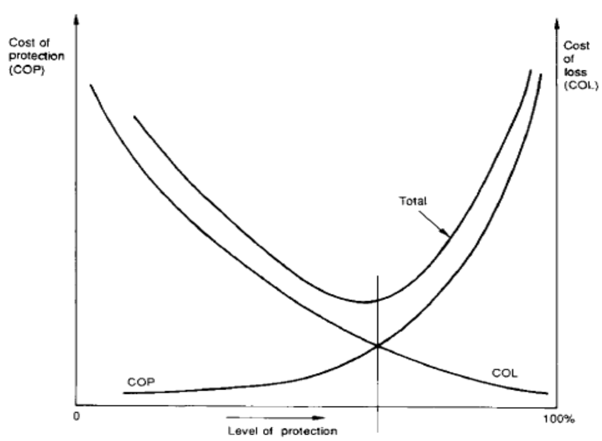

Figure 9: Cost vs level of protection **(Smith & Hetherington, 1994)**

Dusenberry, D. O. (Ed.). (2010). *Handbook for blast-resistant design of buildings*. J. Wiley.

In this handbook, the authors cover a wide range of topics related to blast-resistant design, from blast effect calculations to design considerations, structural system design and member detailing. The handbook provides valuable information on design methods for new structures and retrofitting (hardening) of existing structures. Full-scale blast testing data of buildings, as shown in **Figure 10**, are shared and discussed. Design methodologies for various structural elements and hardening methods are also discussed. The significant deformation capacity provided by carbon fibre reinforced polymer (CFRP) wrapping of reinforced concrete columns is discussed. An introduction to fragmentation protection methodologies for building envelopes is also given. The critical benefit of this book is the breadth of topics summarized in a clear, concise, and practical manner. It is a handbook for engineers and architects that provides critical knowledge to design safer and more resilient buildings against blast loads.

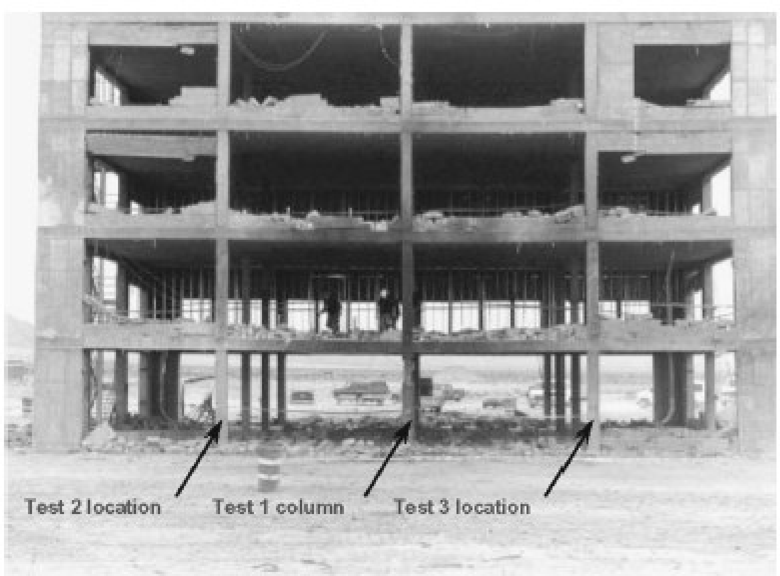

Figure 10: Full-scale blast testing of buildings **(Dusenberry, 2010)**

Bangash, M. Y. H., & Bangash, T. (2006). *Explosion-Resistant Buildings: Design, Analysis, and Case Studies.* Springer.

Bangash and Bangash present an important reference on blast resistance of buildings that also addresses fire resistance of buildings and their structural components. They provide a comprehensive treatment of blast loading phenomena, including blast wave propagation, shock reflection, scaling laws and the determination of pressure-time histories for structural analysis. Detailed discussions are also presented on the analytical and numerical methods used to evaluate the dynamic response of structures subjected to blast, impact and fire loading. In addition, they delve into the topic of structural resistance to aircraft impact, as illustrated in **Figure 11**, which includes the aircraft fuel fire–structure interaction topic that was experienced during the September 11th, 2001 attacks on the World Trade Center (WTC) buildings in New York City. A detailed analysis of the WTC attacks is also included. The authors provide several case studies of building damage analysis under large-scale damage scenarios. A significant exploration of the contact or gap elements and their governing algorithms used in various finite element software is also included. The software discussed in the publication includes DELFT, ANSYS, ABAQUS, and LS-DYNA.

This book is particularly valuable because it combines theoretical background, practical design guidance, computational modelling techniques, and numerous real-world case studies within a single reference. Furthermore, it addresses both component-level and global structural response, enabling a comprehensive understanding of the behaviour of buildings subjected to extreme loading conditions.

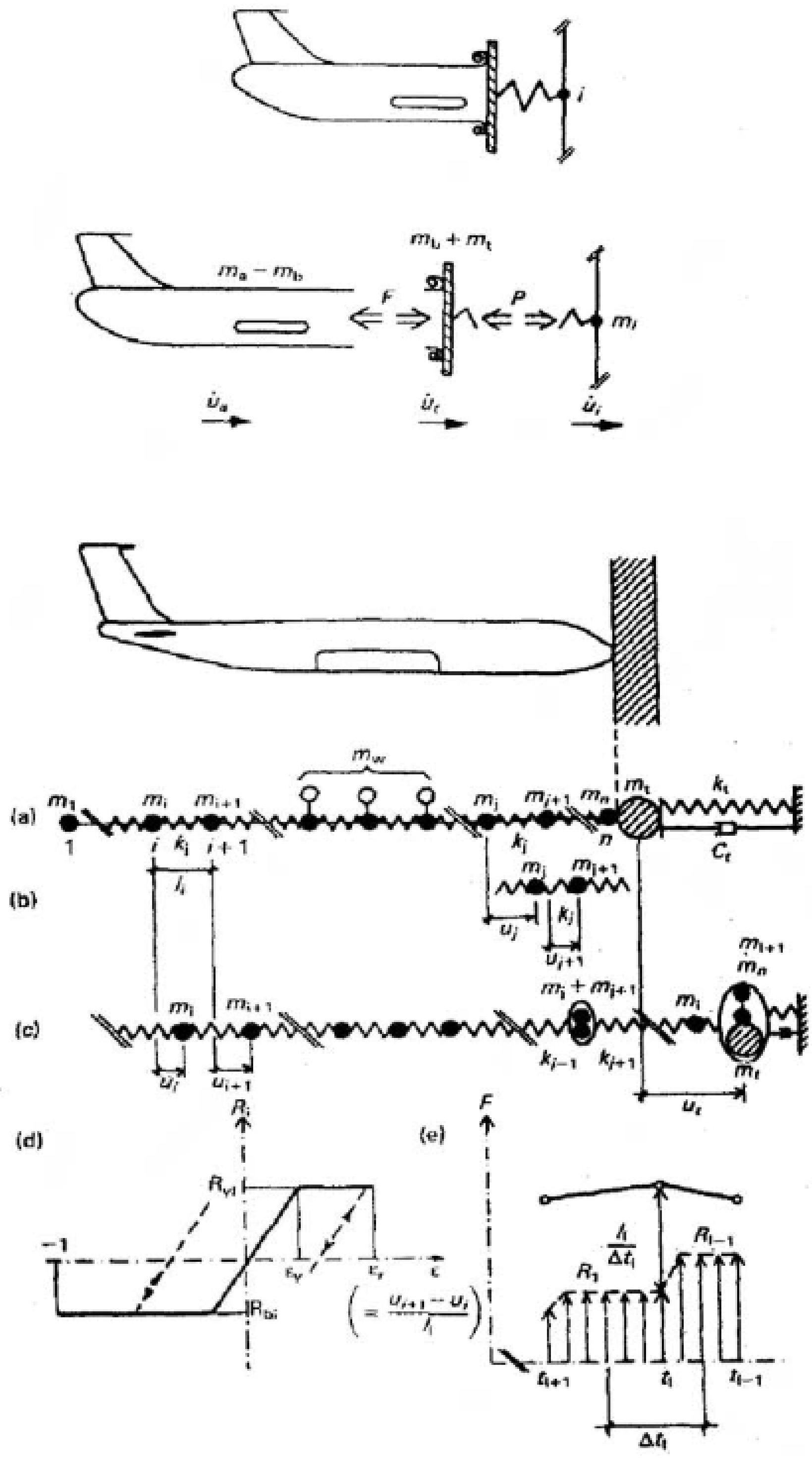

Figure 11: Aircraft impact on deformable target **(Bangash and Bangash, 2006)**

2.2 Literature Review on Engineered Cementitious Composites (ECC) and the Strain Rate Effects on Steel

ECC is a fibre-reinforced cementitious material developed in recent years for its high tensile strength and tensile strain capacity coupled with high ductility and excellent crack control. It utilizes microfibres, which improve the deformability of the material. The following publications were reviewed on the topic, and the findings of previous researchers are summarized in this section.

Li, V. C. (2019). *Engineered Cementitious Composites (ECC): Bendable Concrete for Sustainable and Resilient Infrastructure.* Springer Berlin Heidelberg. https://doi.org/10.1007/978-3-662-58438-5

Victor Li is an important member of the research community in the development of engineered cementitious composites (ECC). This book is the culmination of years of research, which includes background information on the development of ECC, the micromechanical tailoring approach, mechanical properties, resilience, durability, and sustainability of ECC. Additional information is also provided on constitutive modelling of ECC and its industrial applications. This book is unique in that it encompasses a depth of knowledge in material science and structural design. In relation to the current research project reported in this thesis, the most critical property of ECC is its strain hardening behaviour in tension due to the presence of distributed microcracks, as well as its high ultimate strain value in tension. This is illustrated in **Figure 12**. This figure shows that ECC exhibits a strain hardening behaviour in tension, similar to that of steel. In the specific ECC shown in Figure 14, the elastic tensile limit is approximately 3.3 MPa, with the first crack taking place at 3.8 MPa. As the loading continues, additional cracks are formed at other locations within the test coupon, resulting in decreases and increases in the stress level, while keeping an upward trend until the ultimate strength and failure are attained. The ultimate capacity in this case is 5.6 MPa, corresponding to a strain of 4.5%, which represents an almost 50% increase from the stress at the initiation of the first crack. This stress-strain behaviour can conveniently be idealized as a bi-linear material for use in finite element analysis.

The compression behaviour of ECC also offers a certain amount of ductile behaviour. The notable difference between the compression behaviour of ECC and normal concrete is that ECC retains approximately 40% of its peak stress up to a strain value of 1%, as shown in **Figure 13**.

The ductile behaviour of ECC in tension and compression, combined with high ultimate strain values, makes ECC particularly desirable for resisting blast loads, which require considerable energy absorption.

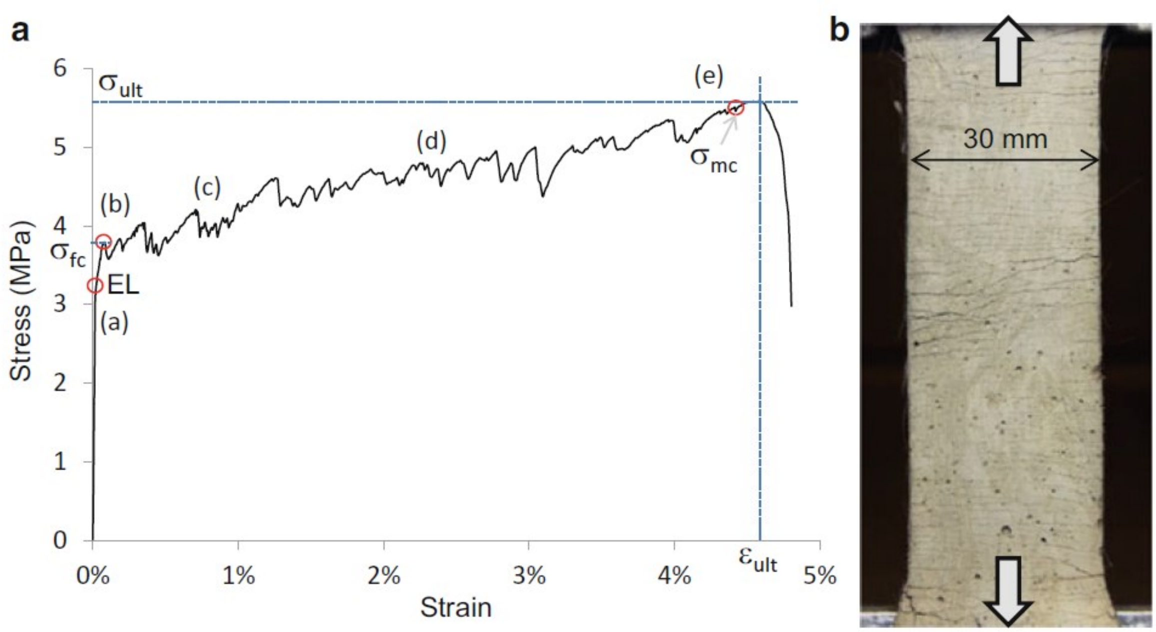

Figure 12: Stress vs strain chart of ECC coupon specimen under direct tension **(Li, 2019)**

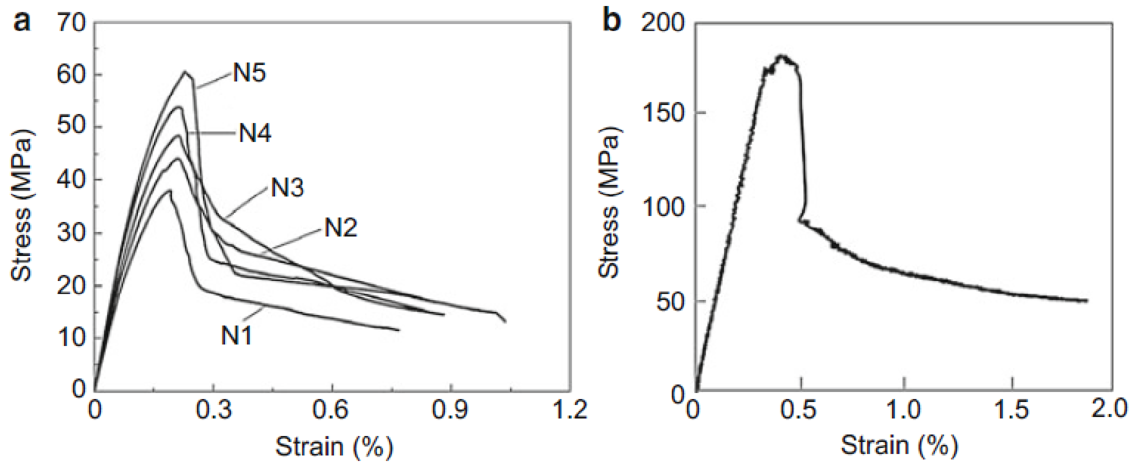

Figure 13: Compressive behaviour of ECC **(Li, 2019)**

Li, V. C., Wu, C., Wang, S., Ogawa A., Saito, T. (2002). Interface Tailoring for Strain-Hardening Polyvinyl Alcohol-Engineered Cementitious Composite (PVA-ECC). *ACI Materials Journal, 99(5)*. https://doi.org/10.14359/12325

This journal article outlines the use of Polyvinyl Alcohol (PVA) fibres to obtain Engineered Cementitious Composites (ECC) that exhibit strain-hardening behaviour. The results of this study indicate that ultimate tensile strains in the order of 4% can be achieved by using PVA fibres coated with an oiling agent that limits the bond stress between the fibres and the cementitious matrix. The critical hypothesis here is that reducing the bond stress between the fibres and the ECC matrix allows fibre slippage to occur prior to fibre rupture. This slip creates a microcrack, but ensures the fibre remains intact. The slipped fibre bridges the crack while sustaining the tensile load it carries. This sustained load and increased deformation allow a similar slip to occur at different sections, hence creating the distributed tension cracking behaviour of ECC. The significance of this research lies in its mathematical prediction that a reduced slip resistance between the PVA fibres and the cementitious paste would enable the formation of distributed cracks along the tensile coupon specimen. The PVA fibres coated with an oiling agent do, in fact, allow the formation of distributed cracks, coupled with a strain-hardening behaviour and a very high tensile strain capacity of up to 4%. The interaction between the amount of oiling agent and the tensile stress-strain curve of ECC in **Figure 14** clearly shows that fibres coated with 1.2% oiling agent have the highest tensile strain capacity. The percentage of oiling agent is the weight of the oiling agent divided by the weight of the fibres.

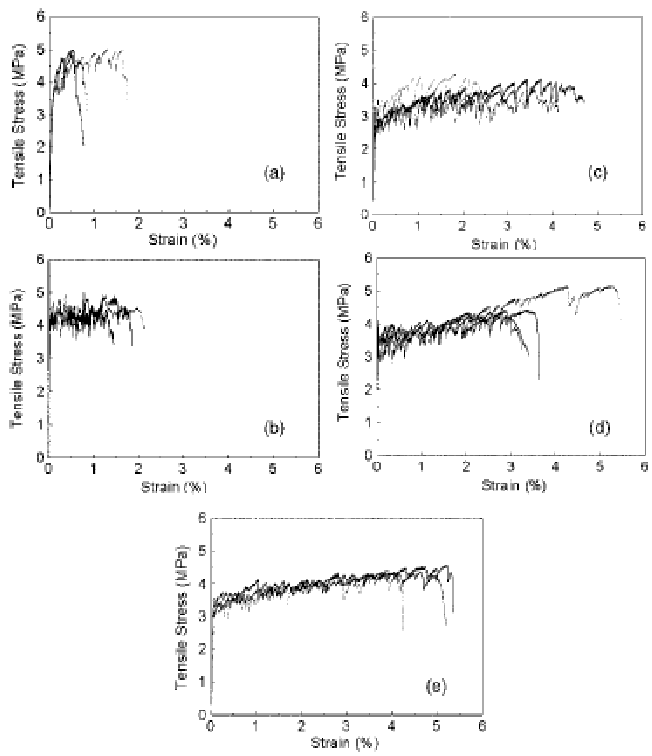

Figure 14: Effect of oiling agent on tensile stress-strain curve, 0%, 0.3%, 0.5%, 0.8%, 1.2% **(Li et al, 2002)**

Li, V. C. (2009). Damage Tolerant ECC for Integrity of Structures Under Extreme Loads. *Structures Congress 2009.*

In this paper, the author summarizes the benefits of the high ultimate tensile capacity of ECC and its strain hardening behaviour in tension. The researcher discusses the potential benefits of utilizing the material in various structural applications that demand a high degree of ductility. The author concentrates on large-scale applications of ECC and provides examples of experiments that demonstrate its superior performance. The author further provides a comparison of reverse cyclic testing of T-shaped columns performed on a reinforced concrete column with ties detailed for high seismic performance and an ECC column without ties. The results show that the reinforced concrete column with seismic detailing reaches a lateral drift ratio of 9% without much deterioration in strength and a drift ratio of 10% with 50% strength deterioration. On the other hand, the ECC column reaches a drift ratio of 15% without strength loss, while achieving 20% higher overall strength. The researcher also discusses a similar performance enhancement for shear beams or link beams that connect two shear walls. These link beams are under high levels of shear stress due to their typically shallow depths as dictated by architectural requirements. Hence, the reinforcement detailing for these beams is challenging and proves to be difficult to implement on site. By using ECC in these elements, not only is the shear reinforcement reduced, but the shear strength is sustained without degradation. The hysteretic behaviour of the ECC specimens is shown in **Figure 15**.

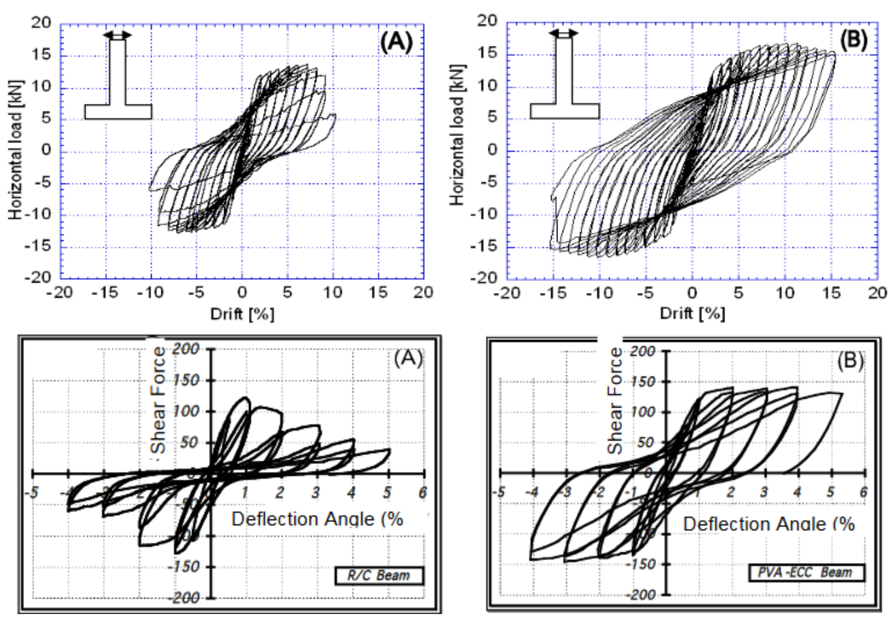

Figure 15: Column and link beam behaviour of R/C and ECC under reversed cyclic loading **(V. C. Li, 2009)**

Yang, E.-H., & Li, V. C. (2012). Tailoring engineered cementitious composites for impact resistance. *Cement and Concrete Research, 42*(8), 1066–1071. https://doi.org/10.1016/j.cemconres.2012.04.006

In this study, the authors explored the performance of ECC mixes under loads with various strain rates. The authors argue that an increase in fly ash content in the mix design lowers the tensile strength for lower strain rates (quasi-static), but the tensile strain capacity increases under high strain rates. As a control mix, they use the M45 mix that has a fly ash to cement ratio of 1.2 by weight. The alternative mixes used by the authors have a fly ash to cement ratio of 2.8 and 1.6, and use PVA fibres and PE fibres, respectively. They found that the alternative mix with PVA fibres and a fly ash to cement ratio of 2.8 has the highest ultimate tensile strain capacity under high strain rates. This is depicted in **Figure 16**.

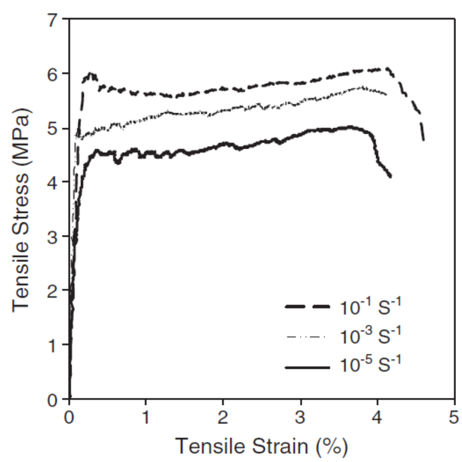

Figure 16: Performance of high fly ash mix under tensile loading **(Yang & Li, 2012)**

The authors performed additional impact testing on 305 mm x 76 mm x 51 mm-sized beam specimens made of a no-fibre regular cementitious mix and high-fly-ash ECC mix reinforced with a 5 mm diameter steel bar. The results show that the beam made of the regular mix failed after the first impact, whereas the ECC mix beam only experienced distributed microcracks after 10 impacts. The impact performance is shown in **Figure 17**.

Figure 17: Impact performance of R/C vs R/ECC mix beams **(Yang & Li, 2012)**

Sun, M., Chen, Y., Zhu, J., Sun, T., Shui, Z., Ling, G., & Zhong, H. (2018). Effect of Modified Polyvinyl Alcohol Fibers on the Mechanical Behavior of Engineered Cementitious Composites. *Materials*, *12*(1), 37. https://doi.org/10.3390/ma12010037

The authors compared in the paper the performance of tension coupons made from ECC mixes using PVA fibres coated with different oiling agents. They investigated the effects of using butadiene-styrene emulsion, vinyl acetate emulsion (VAE), and boric anhydride in the preprocessing of uncoated PVA fibres. The results are compared to using PVA REC15 fibres, which are the type of fibres used in studies by Li, V. C. (2019). As the PVA REC fibres are proprietary products and the details of the oiling agent application process are not publicly available, this research aims to achieve similar performance by testing known coating agents. The authors conclude that VAE-processed fibres exhibit satisfactory behaviour, achieving high values of tensile strength and ultimate tensile strain, along with strain hardening in tension (**Figure 18**).

No.	Water-Binder Ratio	Others	First Crack Strength (MPa)	Ultimate Tensile Strength (MPa)	Ultimate Tensile Strain (%)
G1	0.35	Domestic PVA	2.22	2.86	0.46
G2	0.35	Domestic PVA + VAE	2.26	2.79	0.97
S1	0.3	-	2.67	3.52	3.79
S2	0.35	VAE	2.67	3.33	4.05
S3	0.35	Boric anhydride + butylbenzene emulsion	2.5	2.83	2.02
S4	0.35	-	2.63	3.3	3.21

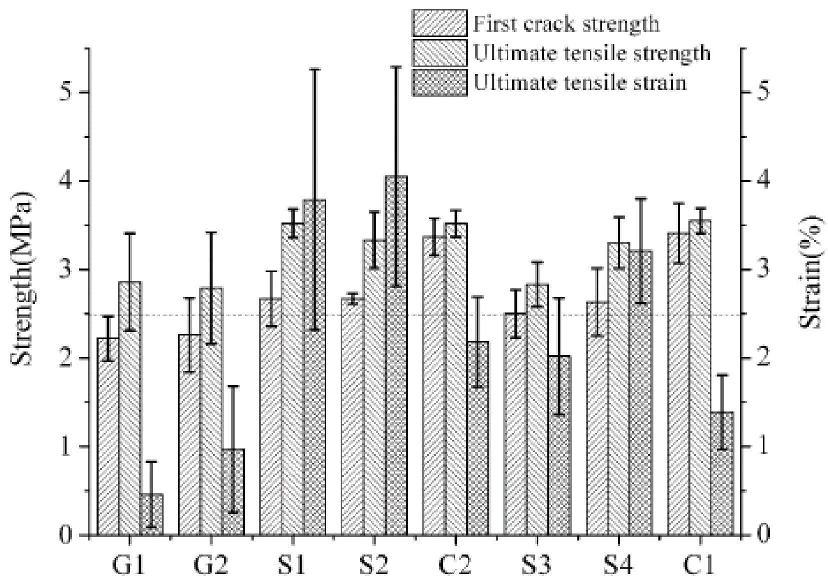

Figure 18: Performance of ECC mixes using various PVA fibre coatings **(Sun et al., 2018)**

Drdlová, M., Popovič, M., & Koutný, O. (2018). Blast resistance of hybrid fibre-reinforced concrete containing polyvinyl alcohol, polypropylene, and steel fibres with various shape parameters. *The European Physical Journal Special Topics, 227(1–2), 111–126*. https://doi.org/10.1140/epjst/e2018-00061-y

In this article, the authors investigate the performance of using a combination of two different types of fibres in the mix design against blast loading. This study involves using a combination of steel, polyvinyl alcohol (PVA) and polypropylene (PP) fibres to obtain a high-performance cementitious mix against blast loads. The authors argue that a hybrid fibre regime results in a cementitious mix with a superior performance against blast and impact compared to mono-fibre reinforced cementitious mixes. They postulated that shorter, thinner fibres would bridge microcracks, whereas longer, thicker fibres would resist the opening of macrocracks. To test their hypothesis, they prepared one mix with no fibres and ten mixes with fibres having a 3% fibre volume ratio. Of the ten mixes with fibres, two were with steel fibres only, and eight mixes were with 70% steel, 30% PVA or PP fibres. The authors conducted live blast tests using 150 g and 100 g Semtex 10 plastic high explosives on 500 x 500 x 40 mm specimens with a standoff distance of 100 mm. They measured the displacement of the panels, the weight of fragments that separate from the panels and the ultrasonic wave travel time from the center of the panel to the corners. The increase in transit time indicates a higher degree of internal damage. Finite element modelling using LS-Dyna was performed for four panels, including two steel-only panels and one panel with PVA and one with PP fibres. The steel fibres were modelled as linear elements randomly distributed within the solid geometry of the cementitious solid depicted in **Figure 19**. The PVA or PP fibres were implicitly modelled by adjusting the material properties of the cementitious matrix. Due to the proximity of the explosive charge to the specimen (a scaled distance of 0.2 m/kg$^{1/3}$) the blast was simulated as an interaction of an Euler mesh of air and a Lagrange mesh of the solid specimen. The results indicate that panels with 50 mm long steel and 12 mm long PVA fibres showed superior performance compared to other panels. These panels only showed 2.9 mm of permanent deformation under a 100 g charge, with the amount of fragments limited to 8 grams (0.03% by weight of the panel). The behaviour of the panels and the results of the finite element simulation showed good agreement, where the measured permanent deformation of 2.9 mm was 20% higher than the calculated value of 2.3 mm. The finite element model predicted the cracking pattern with accuracy, as shown in **Figure 20**.

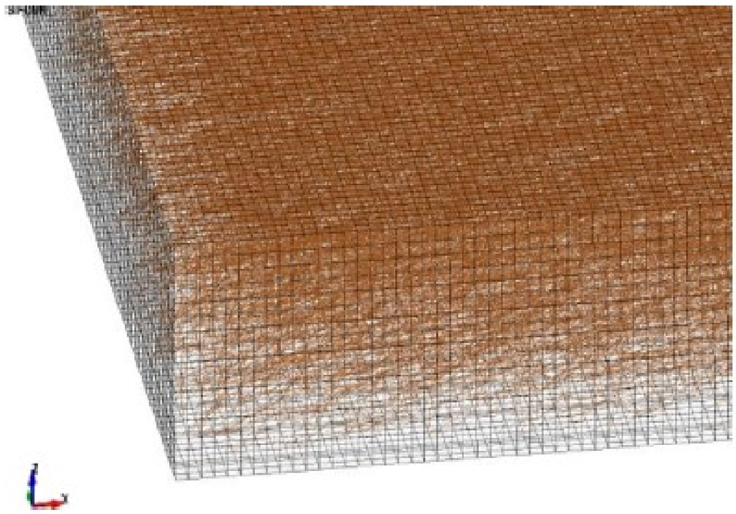

Figure 19: Steel fibres distributed within the cementitious solid **(Drdlová et al., 2018)**

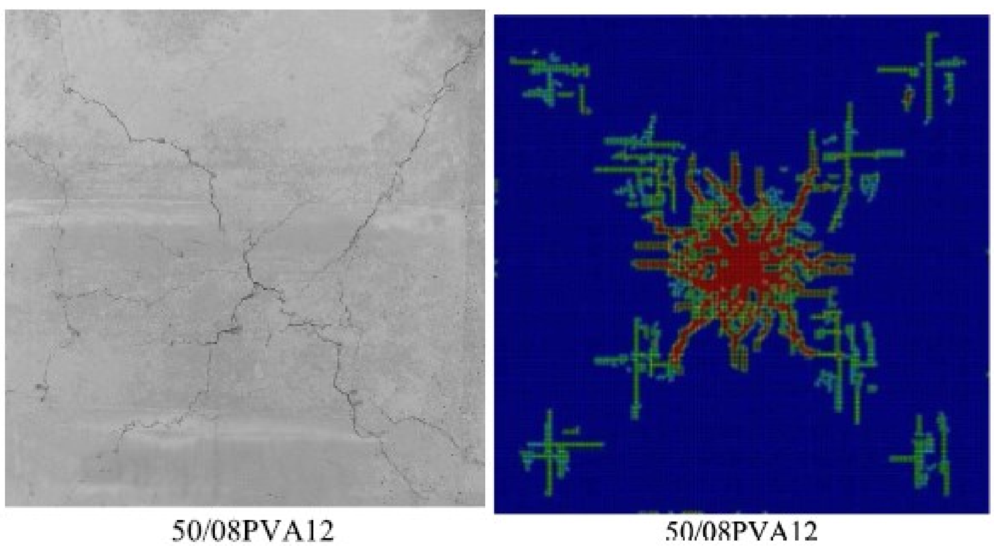

Figure 20: Crack distribution on test specimen vs LS-Dyna model **(Drdlová et al., 2018)**

Turk, K., & Nehdi, M. L. (2021). Flexural toughness of sustainable ECC with high-volume substitution of cement and silica sand. *Construction and Building Materials, 270*, 121438. https://doi.org/10.1016/j.conbuildmat.2020.121438

In this study, the authors evaluated flexural toughness and flexural ductility of ECC made by partially replacing cement with fly ash and partially or completely replacing silica sand with limestone filler material. They compared the performance of nine mixes that have a fly ash to cement ratio of 1.2, 2.2 and 3.2, along with 0%, 50%, and 100% limestone filler to silica sand replacement ratios. They utilized three methods, ASTM C1609, JSCE and Post-Crack Strength methods to evaluate the performance of various ECC mixes at 3, 28 and 90 days.

The researchers found that the 3-day strength of limestone filler mixes was higher than that of the silica sand only mixes. However, this tendency reversed at 28 and 90 days. They have also found that the deflection capacity of the mix that had a fly ash to cement ratio of 1.2 and 0% limestone filler was the highest. They concluded that the ductility and flexural toughness of ECC mixes are time dependent, and that for durability performance studies, this time-dependent behaviour must be considered**. Figure 21** illustrates the change in ductility with age for different fly ash-replacement ratios.

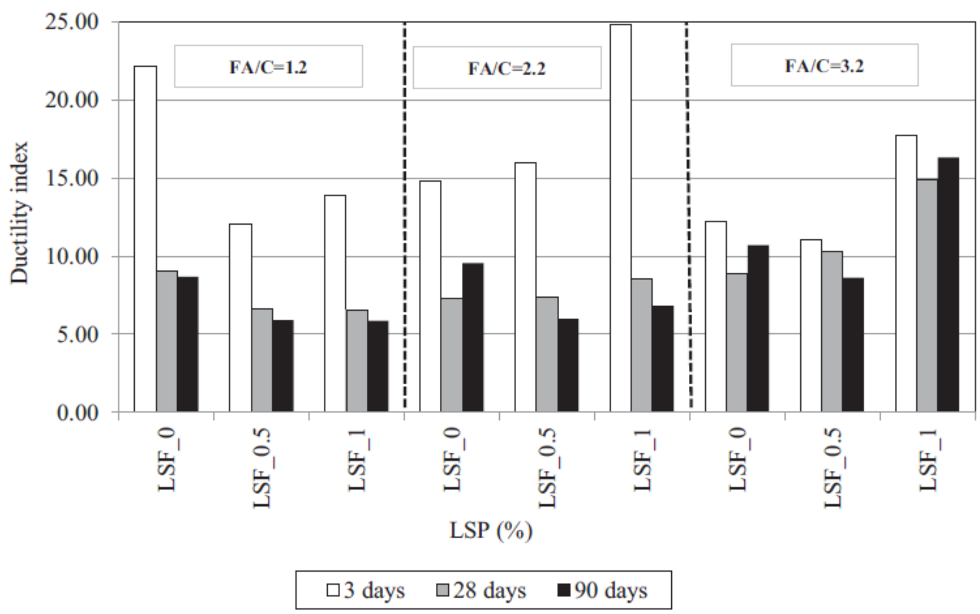

Figure 21: Change in ductility vs. age, fly ash, limestone replacement ratios **(Turk & Nehdi, 2021)**

Ranade, R., Li, V. C., Stults, M. D., Rushing, T. S., Roth, J., & Heard, W. F. (2013). Micromechanics of high-strength, high-ductility concrete. *ACI Materials Journal, 110*(4), 375–385.

In this study, the authors report the results of their experiments that resulted in a very high strength (166 MPa) and high tensile ductility (3.4%) cementitious composite. The authors utilized single-fibre pullout tests to determine the interaction between each fibre and the cementitious matrix. As a result of the fibre pullout tests, they proposed a new "inclined-bridging" mechanism for cementitious matrix-fibre micromechanical interaction. Using this new mechanism to calculate the necessary parameters for achieving the strain hardening behaviour of normal-strength ECC, the authors determined that ultra-high-molecular-weight-polyethylene (UHMWPE) fibres were required. Furthermore, they used a significant amount of silica fume, which has a much smaller particle size compared to cement, to increase the fracture toughness of the cementitious matrix.

Using this new mix design, the authors were able to achieve the tensile stress-strain relationships shown in **Figure 22**.

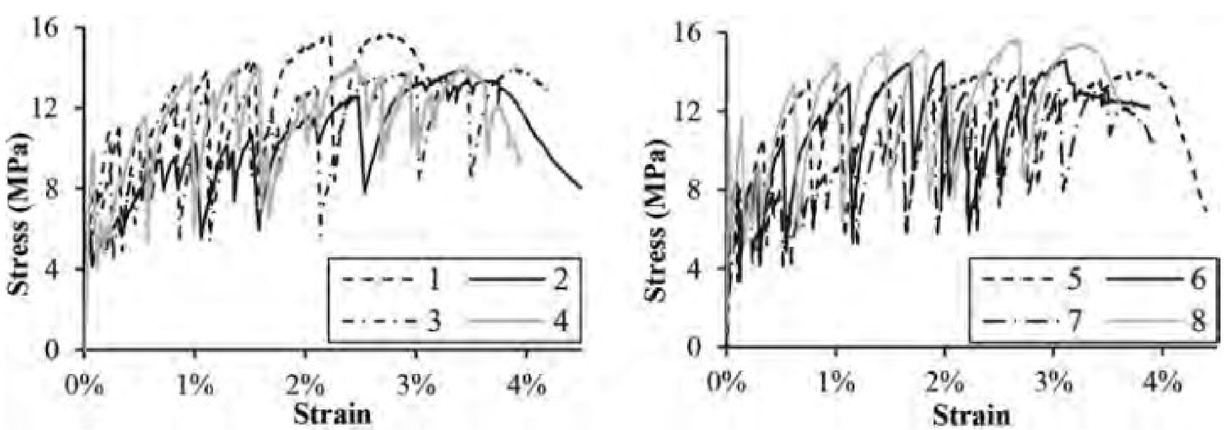

Figure 22: Direct tension test results showing tensile stress vs strain **(Ranade et al., 2013)**

Yu, K.-Q., Yu, J.-T., Dai, J.-G., Lu, Z.-D., & Shah, S. P. (2018). Development of ultra-high performance engineered cementitious composites using polyethylene (PE) fibres. *Construction and Building Materials, 158*, 217–227. https://doi.org/10.1016/j.conbuildmat.2017.10.040

In this study, the authors developed an ultra-high-performance engineered cementitious composite mix, which achieved a tensile strength of 17 MPa and a tensile elongation of 8.7%. Several important modifications were made to the mix design to obtain such results. First, they utilized ultra-high-molecular-weight polyethylene (UHMWPE) fibres to achieve these exceptionally high values. Second, they used very fine silica sand with a mean size of 135 μm and a maximum size of 180 μm. This small-sized fine aggregate was used to reduce the fracture toughness of the cementitious matrix to allow the initiation of micro-cracks and steady-state crack propagation. Third, part of the cement was replaced with silica fume and ground granulated blast furnace slag, both of which are considerably finer than cement and have much higher specific surface area. Finally, they also utilized a mixing procedure that is different from the typical procedure in the literature to ensure proper dispersion of the fibres within the cementitious matrix. As a result, the authors report that they achieved ultimate tensile strength and strain results that are superior to previously reported ultra-high-performance ECC mixes, as shown below in **Figure 23**. The average compressive strength of these mixes was 121 MPa, with an average modulus of elasticity of 44 GPa. The authors also reported that the inclusion of the silica fume and ground granulated blast furnace slag contributed to a very dense microstructure for the cementitious matrix, which led to very low porosity. This dense matrix increased the bond between the fibres and the matrix and resulted in the fracture of some of the fibres (**Figure 24**).

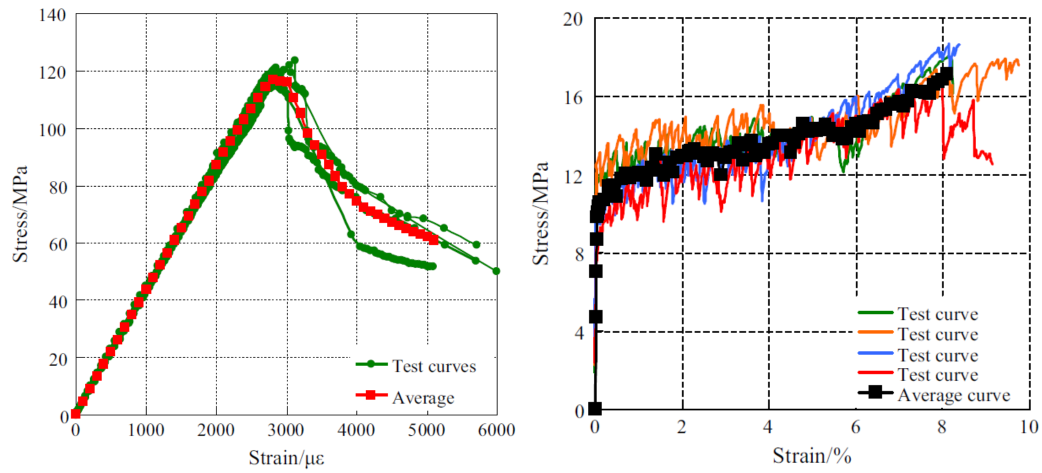

Figure 23: Compressive and Tensile stress-strain curves of UHP-ECC **(Yu et al., 2019)**

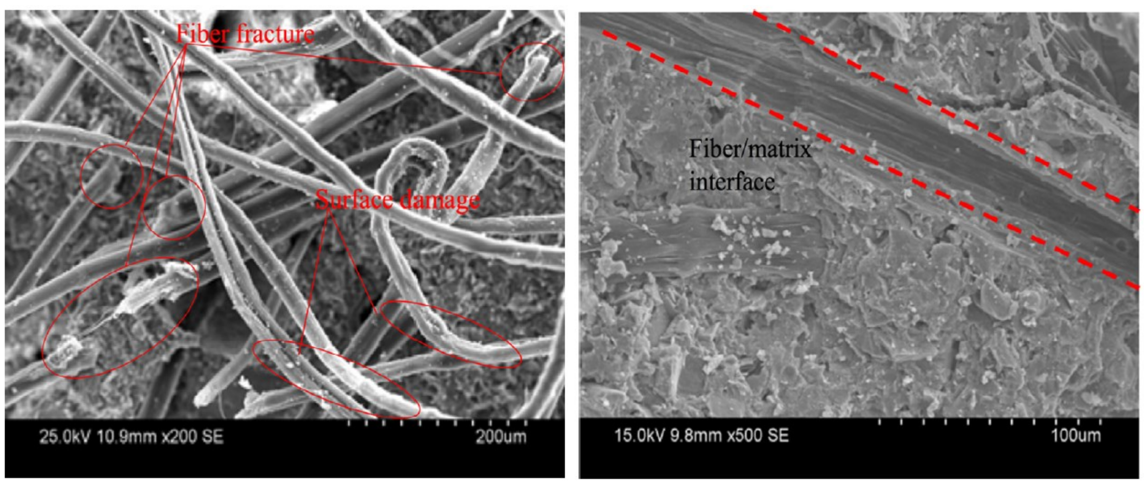

(a) Fiber fracture and surface damage

(b) Fiber/matrix interface

Figure 24: Fibre surface damage and fibre/matrix interface **(Yu et al., 2019)**

Park, P., Jones, R., Castillo, L., Vallangca, M., & Cantu, F. (2020). *Engineered Cementitious Composites (ECC) for Applications in Texas* (Report No. 0-7030-1). Texas Department of Transportation.

This report, prepared by the University of Texas for the Texas Department of Transportation, presents valuable information on the practical application of ECC in infrastructure components. A unique feature of this report is that it includes a detailed chapter on meta-analysis of ECC behaviour. This meta-analysis is performed using more than 70 datasets from published research. The authors conclude that a wide scatter exists in the results and emphasize that good quality control is crucial for achieving consistent ECC performance, as illustrated in **Figure 25**. They also found that the most frequently used ECC mixture was M45, which uses 55% fly ash as binder.

In addition, this report includes a life cycle assessment (LCA) study of using ECC as a pavement overlay material. This LCA study considers several parameters, including material, distribution, the effect of pavement on fuel consumption, and the necessity for repairs and maintenance. Their findings indicate that ECC has lower CO_2 emissions compared to conventional concrete overlays.

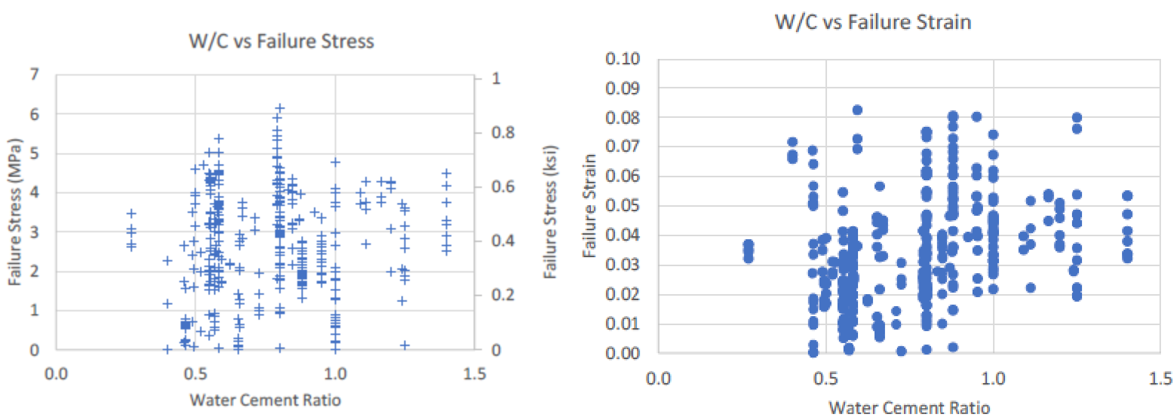

Figure 25: Variation of failure stress and failure strain vs water cement ratio **(Park et al., 2020)**

Malvar, L. J. (1998). Review of static and dynamic properties of steel reinforcing bars. *ACI Materials Journal, 95*(5), 609-614.

Malvar provided a comprehensive review of the dynamic and static properties of various grades of reinforcing steel. The ASTM A615 grade 60 is the most commonly used grade of reinforcement today, and therefore, the effect of high strain rates on the yield and ultimate stress values of this material is of critical importance. Moreover, this review paper also includes data on grades of reinforcing steel that were used prior to ASTM A615. Therefore, the data presented in this paper proves to be a useful guide for engineers investigating the resistance of existing buildings subjected to high-strain-rate loads (blast, impact or earthquakes). The author proposes a Dynamic Increase

Factor (DIF) formulation to express the amount of increase in the yield and ultimate stress values at various strain rates. The DIF is the ratio of the yield or ultimate stress value measured under high strain rates to the yield or ultimate stress value measured under quasi-static loading. As shown in **Figure 26**, the tendency for reinforcing steel is an increase in the DIF for decreasing nominal yield stress.

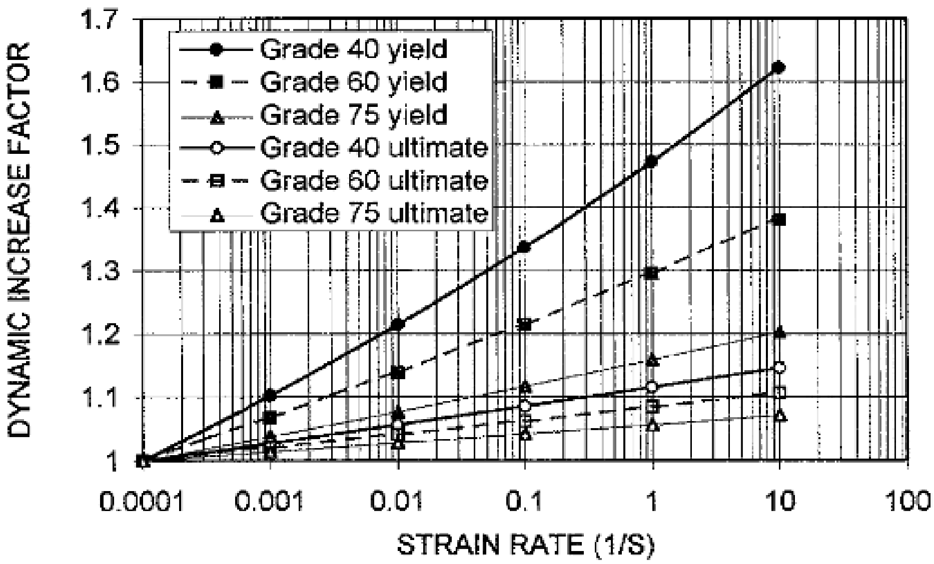

Figure 26: DIF values for grade 40, 60, and 75 ksi reinforcing steel **(Malvar, 1998)**

Forni, D., Chiaia, B., & Cadoni, E. (2016). Strain rate behaviour in tension of S355 steel: Base for progressive collapse analysis. *Engineering Structures, 119,* 164–173. https://doi.org/10.1016/j.engstruct.2016.04.013

In this paper, the authors performed experimental testing using a modified Split Hopkinson Tensile Bar (SHTB) to obtain tensile stress-strain data of S355 grade structural steel under very high strain rates. They compared the experimental results with Johnson-Cook and Cowper-Symonds constitutive models and validated the accuracy of these models. As S355 and its North American equivalent, 50 ksi steel, are commonly used in steel construction, the validation of these constitutive models is important for the analysis of this material under high strain rates. This is particularly relevant as finite element software like LS-Dyna incorporates these models for high-strain rate analysis. This stress increase model eliminates the necessity for the use of the Dynamic Increase Factor (DIF) for the finite element analysis. The good agreement found between the test results and the Johnson-Cook model is shown in **Figure 27**.

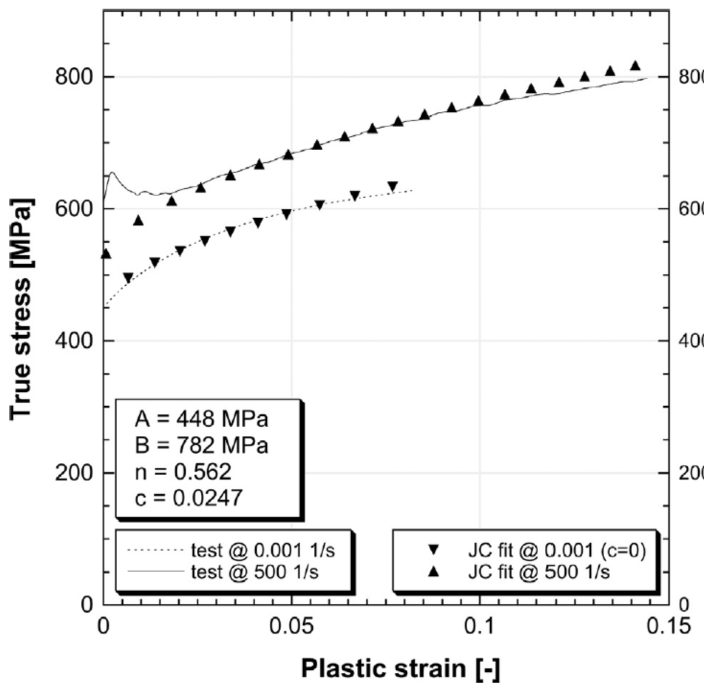

Figure 27: Comparison of experimental results and Johnson-Cook model **(Forni et al., 2016)**

2.3 Review of Literature on Blast Resistant Panels

Because the primary objective of current research is the development of a new blast-resistant panel for use in buildings, the literature review in this section concentrated on previous research on this specific topic. The following presents a summary of previous research on blast-resistant panels.

Naito, C., Beacraft, M., Hoemann, J., Shull, J., Salim, H., & Bewick, B. (2014). Blast performance of single-span precast concrete sandwich wall panels. *Journal of Structural Engineering, 140*(12), 04014096. https://doi.org/10.1061/(ASCE)ST.1943-541X.0001020

The authors reported the results of a comprehensive testing program in which they evaluated the blast resistance of various configurations of precast concrete sandwich wall panels. These types of panels are commonly used in industrial and military buildings, and their blast resistance is of critical importance. The thickness of the panels tested ranged between 200 mm and 230 mm, with a 76 mm (3 inches) thick insulating foam layer in the middle, with outer concrete layers. Prestressed and non-prestressed concrete layers were connected with a variety of connectors, and the combined performance of prestressing, connector type and insulation material was evaluated. The results indicated that both prestressed and non-prestressed panels were able to achieve the desired levels of strength. However, only prestressed panels were able to satisfy the deflection criteria. Using the single degree of freedom (SDOF) analysis method, the resistance functions of the panels were calculated and compared with the resistance functions calculated using the experimental data. The resistance functions of various panel types considered are shown in **Figure 28**.

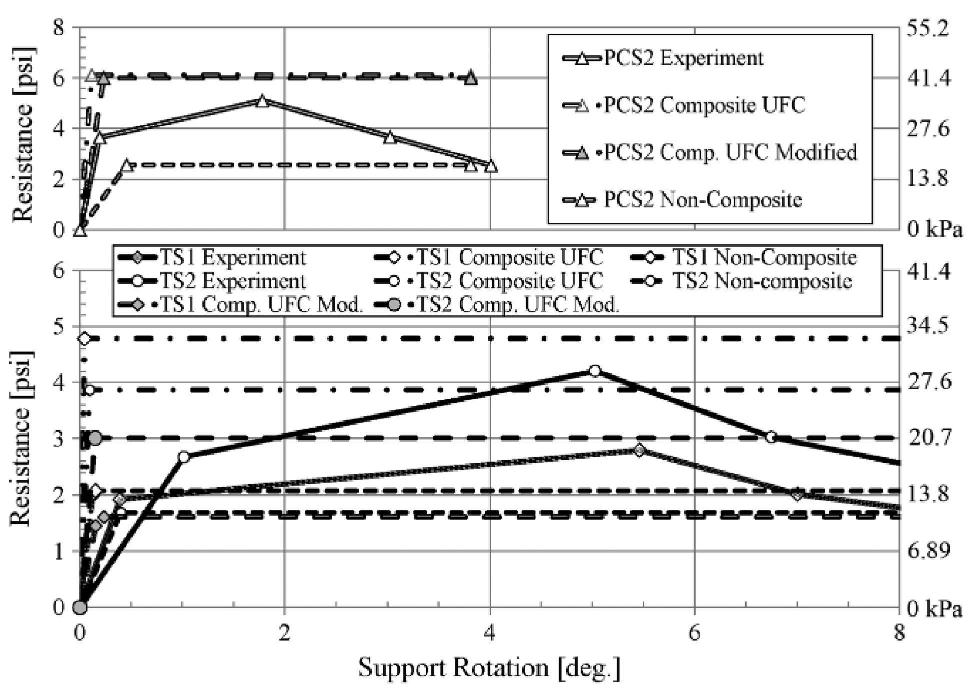

Figure 28: Calculated and experimental resistance functions of panels **(Naito et al., 2014)**

Cavill, B., & Rebentrost, M. (2006). Ductal – A High-Performance Material for Resistance to Blasts and Impacts. *Australian Journal of Structural Engineering, 7*(1), 37–45.

Ductal® panels are one of the earlier concrete panel products that were introduced for blast resistance. These panels were made of very high compressive strength (160 to 200 MPa) and high flexural strength (30 to 40 MPa) concrete, with high ductility. The exact composition of the material was not provided; however, the presence of silica fume and silica flour suggests a highly packed mixture that also shows very low porosity. Very fine high-strength steel fibres were used as reinforcement. In addition, some panel variants incorporated prestressing, which further increased the out-of-plane resistance of the panels. A total of eight panels were tested under the blast load of 6 tons of TNT at standoff distances ranging from 30 metres to 50 metres, which corresponds to a reflected pressure and impulse of 1,900 kPa and 6600 kPa-ms to 420 kPa and 3600 kPa-ms. The authors report that the prestressed variants of the panels behaved virtually elastically under the blast load. The summary of results obtained is shown in **Figure 29**.

Panel type	Stand-off Distance R	Recorded Deflection	Main observations
Stressed 100mm	30m	50mm in 37mm out 0mm	Virtually undamaged, no permanent deflection. Several vertical hairline cracks in front face of 0.1 to 0.2mm width. No fragmentation.
Stressed 100mm	40m	Laser No record 0mm	Basically undamaged, no permanent deflection. No fragmentation.
Stressed 75mm	40m	72mm in 55mm out 18mm in	Intact, cracked with small permanent deflection, no fragmentation.
Stressed 50mm	50m	Laser No record 0mm	Intact, shallow crack, no permanent deflection, no fragmentation.
Unreinforced 50mm	50m	>300mm	Fractured, no fragmentation
Stressed 75mm	30m	>300mm	Fractured, no fragmentation
Unreinforced 100mm	40m	280mm	Fractured, no fragmentation
Reinforced conventional concrete (f″c=40MPa) 100mm	40m	>300mm	Fractured, severe damage, fragmentation from back face

Figure 29: Performance of Ductal panels under a 6-ton TNT blast **(Cavili & Rebentrost, 2006)**

Nam, J., Kim, G., & Kim, H. (2017). Experimental investigation on the blast resistance of fibre-reinforced cementitious composite panels subjected to contact explosions. *International Journal of Concrete Structures and Materials, 11*(1), 29–43. https://doi.org/10.1007/s40069-016-0179-y

The authors reported their findings for the contact charge blast resistance of 100 mm thick 1 metre by 1 metre cementitious composite panels containing various fibre types. They conducted blast tests using contact charges on seven different panel types, with two panel types being non-fibre reinforced, and five being reinforced with fibres. The weights of the charges used were 50, 75, 100, 200, 400, and 800 grams for non-fibre reinforced panels. As expected, non-fibre reinforced panels failed at 50 grams by breaking and were completely destroyed under the effect of 800 grams. The fibre reinforced panels were tested under 100 and 200 grams of contact charges. They showed much higher resistance to contact charges, and none of the five types of panels were perforated. The best performance was shown by panels that had a hybrid fibre regime that had 50% steel and 50% polymer (PVA or PE) fibres. The improved performance of the hybrid fibre mixture was attributed to the complementary behaviour of the two fibre types. Steel fibres enhanced crack bridging and energy absorption at larger cracks, and the polymer fibres controlled the propagation of microcracks. The resulting elements were able to maintain their integrity under the severe localized forces due to the contact charges. This experimental study demonstrated that fibre reinforcement can significantly improve the capability of cementitious panels to resist localized blast damage and reduce fragmentation. The photographs illustrating the results of the tests are shown in **Figure 30**, with the bottom two rows corresponding to the hybrid fibre mixes.

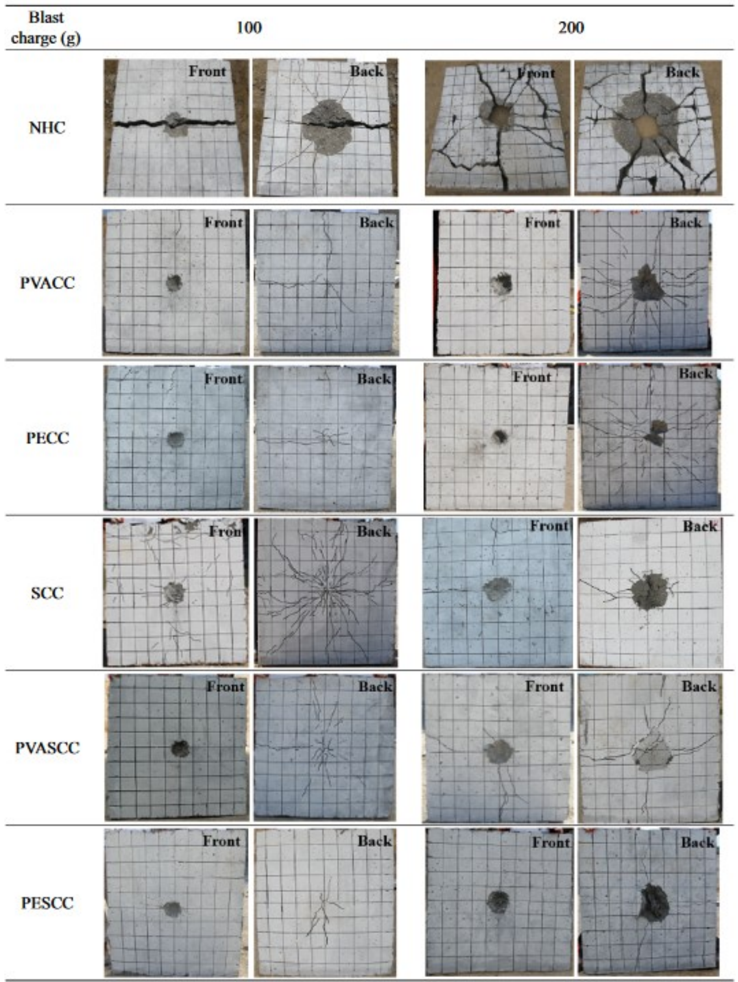

Figure 30: Fibre reinforced panels after the contact charge tests **(Nam et al., 2017)**

Lim, J. Y., Goh, C. Y. M., Kang, K. W., Li, J., & Wu, C. (2025). Structural response of steel-concrete composite panels to near-field simultaneous blast and fragmentation loading. *International Journal of Impact Engineering, 195,* 105142. https://doi.org/10.1016/j.ijimpeng.2024.105142

In their recently published study, Lim et al (2025) reported the results of experimental and analytical studies of steel-concrete-steel sandwich panels under blast loads. The blast testing was conducted using a pipe-shaped charge with an equivalent TNT weight of 2 kg. The explosive effects of the shaped charge were characterized by test explosions on pressure gauges. The peak reflected pressure and impulse were determined to be 410 kPa and 400 kPa-ms. The unique feature of these experiments was that they included the effects of the impact of fragments in addition to the shockwave resulting from the explosion. The test specimens were comprised of 3 mm thick outer steel plates and a 50 mm thick concrete layer in the middle. 50 x 50 x 3 mm U-shaped stiffener beams were used at 330 mm spacing to provide additional rigidity to the panels. The results of the tests indicate that all panels were able to resist the blast loads and fragments without any perforation; however, they all suffered significant permanent deformations. The displacement-time relationship for the panels is shown in **Figure 31**.

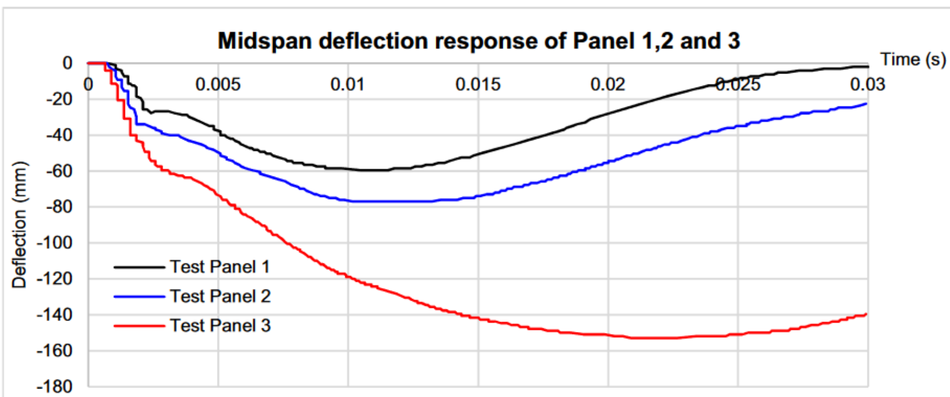

Figure 31: Midspan deflection for 1, 0.75, and 0.5 m standoff distance **(Lim et al., 2025)**

Giovino, G., Olmati, P., Garbati, S., & Bontempi, F. (2014). Blast resistance assessment of concrete wall panels: Experimental and numerical investigations. *International Journal of Protective Structures, 5*(3), 349–366. https://doi.org/10.1260/2041-4196.5.3.349

In their 2014 study, Giovino et al. (2014) tested 150 mm and 200 mm thick reinforced concrete precast panels with a length of 3500 mm and a width of 1500 mm, using 3.5 kg and 5.5 kg TNT charges at a standoff distance of 1.5 metres to the center of the panels. The 3.5 kg TNT at 1.5 metres corresponds to a scaled distance of 0.99 m/kg$^{1/3}$ or 2.49 ft/lb$^{1/3}$, whereas the 5.5 kg TNT at the same distance corresponds to a scaled distance of 0.85 m/kg$^{1/3}$ or 2.14 ft/lb$^{1/3}$. These explosion configurations create pressures equivalent to approximately 130 kg and 200 kg of TNT detonated at a 5-metre standoff distance. The panels were simply supported in the long direction (3.5 metres) and not supported in the short direction, hence behaving in one-way bending along the longer span. The 150 mm thick panel had a longitudinal reinforcement ratio of 0.15%, and the 200 mm thick panels had a longitudinal reinforcement ratio of 0.31%. Both types of panels had only a single layer of reinforcement in the middle. The average value of concrete compressive strength was 34 MPa, and the average yield strength and tensile strength of reinforcement were 543 MPa and 647 MPa, respectively. The results indicated that under 3.5 kg TNT, the 150 mm thick panel with 0.15% reinforcement deflected 108 mm at the midspan, whereas the 200 mm thick panel with 0.31% reinforcement deflected 70 mm with a residual deflection of 35 mm. The 200 mm thick specimen had a maximum crack width of 3 mm. Under 5.5 kg TNT, only the 200 mm thick specimen was tested, and it deflected 122 mm with a residual deflection of 82 mm. This specimen had a maximum crack width of 10 mm, which indicates excessive yielding of the reinforcement in the middle. The experimental results clearly show the benefits of increasing the thickness of the concrete panel and the amount of reinforcement. The reduction in both peak and residual deflections demonstrates the significant influence of flexural stiffness on the blast response of reinforced precast concrete panels. Furthermore, the increased area of reinforcement at the mid-height has also contributed to the enhanced performance of the 200 mm thick panel. Despite being subjected to a more severe loading condition, the 200 mm thick panel remained intact and did not experience catastrophic failure. The photographs from the results of these experiments are shown in **Figure 32**.

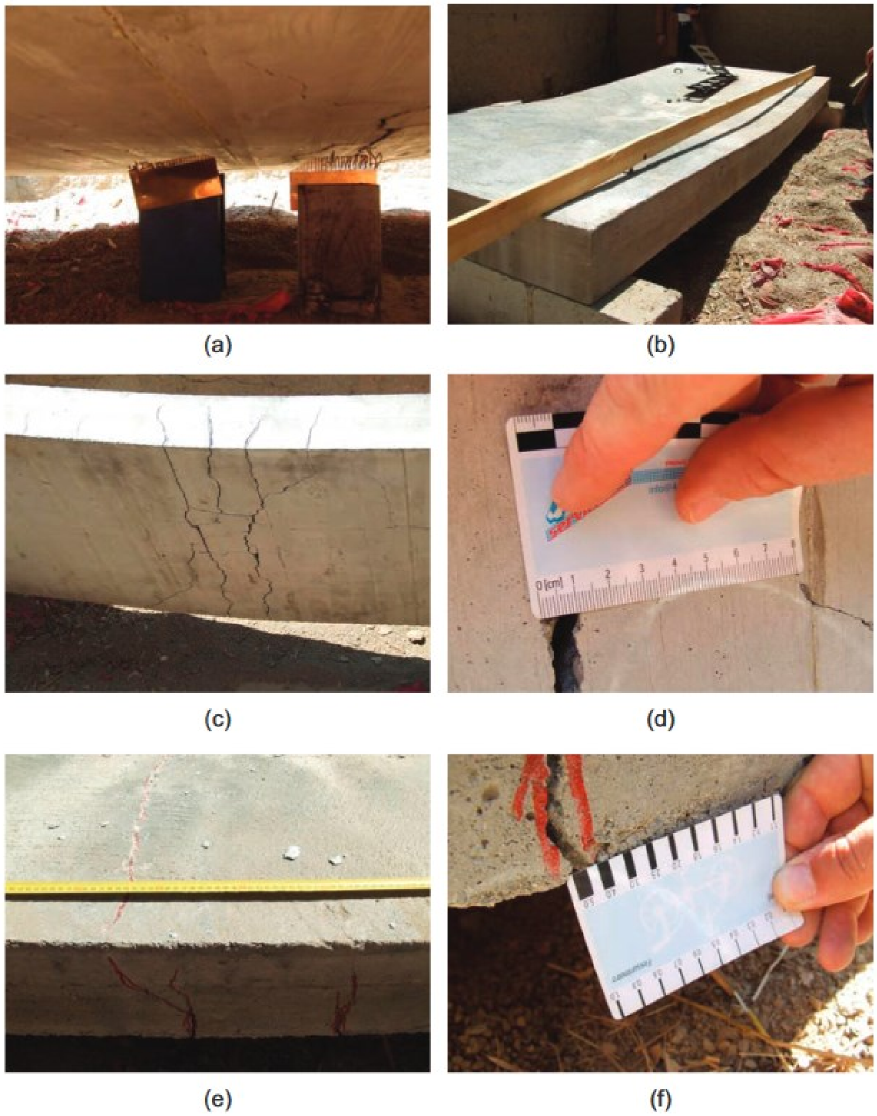

Figure 32: 200 mm thick specimen tested under 5.5 kg TNT at 1.5 m standoff distance (Giovino et al., 2014)

2.4 Blast Testing Using the University of Ottawa Shock Tube

The shock tube facility at the University of Ottawa has been used by previous researchers to conduct blast simulation tests since its installation. Blast research that has been published in the literature since 2009 includes applications of reinforced concrete columns, slabs and walls; masonry walls, timber, and glazing (Alameer & Saatcioglu, 2023; Algassem et al., 2017; Burrell et al., 2015; Hammoud et al., 2021; Jacques et al., 2014; McGrath & Doudak, 2021; Saatcioglu et al., 2009; Sherif et al., 2023; Viau & Doudak, 2016). These contributions have collectively shown that the shock tube can be used reliably to produce blast shock waves, and the resulting pressure vs. time history relationships accurately represent blast load effects as those generated by the detonation of high explosives. A particularly important feature of the shock tube is its short turnaround time between tests and repeatability of blast loads, which allows application of multiple shots to the same specimen in a single day. This feature allows researchers to start with low levels of blast pressure and gradually increase the pressure until the specimen fails. On the other hand, the application of multiple shots on the same specimen causes accumulated damage. The effects of this accumulation on reinforced concrete columns were investigated by Kadhom (2016). The researcher concluded that reinforced concrete columns that were subjected to multiple shots experienced higher residual displacements. This increase in residual displacements due to damage accumulation was significant in columns tested without any axial load; however, it was less pronounced in axially loaded columns. This is shown in **Figure 33**. Further discussion of the shock tube capabilities and use is discussed in Chapter 3.

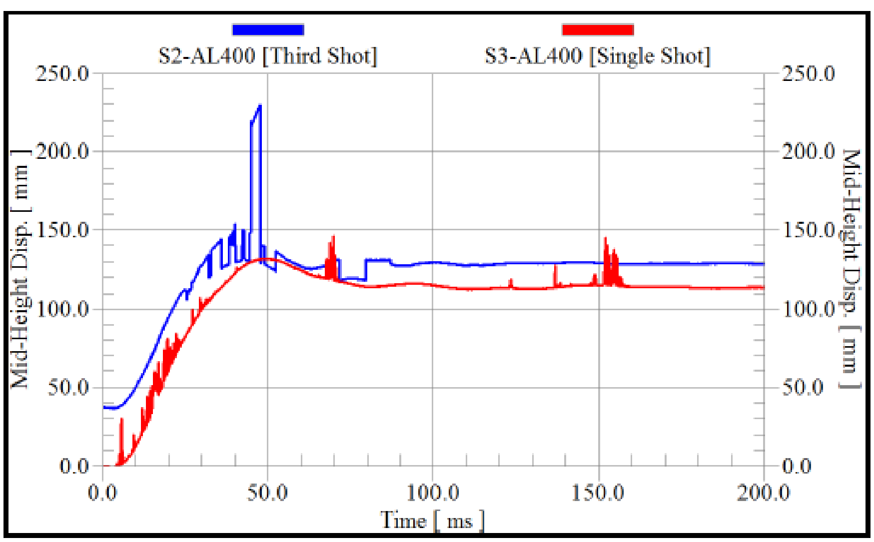

Figure 33: Displacement vs time history of columns with axial load **(Kadhom, 2016)**

Chapter 3. Experimental Research

Experimental research was conducted to develop blast-resistant panels and wall systems. This phase of research is presented under three main headings: i) fabrication of test panels, ii) blast test procedure, and iii) blast testing and discussion of test results. A preliminary investigation was first carried out to explore the feasibility of the concept. Two guiding principles lead to the development of the concept: i) achieving high blast load capacity stemming from combined flexural and membrane resistances of panels, as well as the wall systems, and ii) light weight for easy handling/assembly.

The panels consisted of two layers of engineered cementitious composites (ECC) with a light-gauge steel sheet in between. This resulted in a total panel thickness of 15 mm for the test specimens. The thickness of the steel sheet selected was either 1.5 mm or 3 mm. The test panels were designed to meet geometric and pressure capacity limitations of the shock tube used for blast testing. Each test panel had a 510 mm width and a 2080 mm height. This panel size kept the weight of individual panels to around 50 kilograms and allowed manual installation of specimens without using a forklift or other lifting devices. Four panels were placed side by side for testing. **Figure 34** shows the panels placed in front of the shock tube for blast testing. Further details and the manufacturing process are discussed in **Section 3.1.2 Specimen Preparation.** Additional tests were conducted on steel sheets alone as panels without the ECC layers to assess the contribution of the ECC layers to blast response.

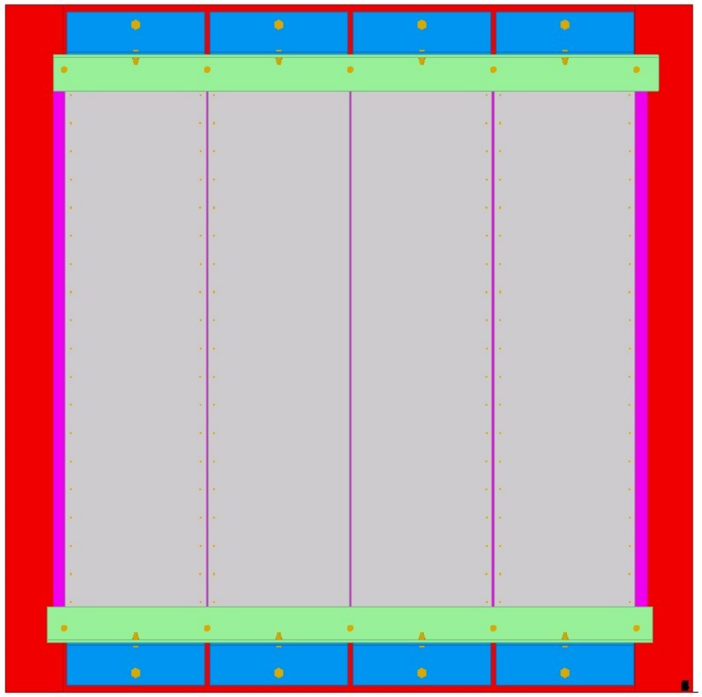

Figure 34: Multiple panels positioned for blast testing

In addition to the panels for their individual use, blast-resistant wall systems were also developed by connecting the panels to vertical HSS sections for enhanced blast resistance. The HSS sections were secured to the panels along their vertical joints as studs to transfer blast loads to the supporting structural elements, such as the top and bottom floor slabs of a building. HSS sections having dimensions of 76 mm x 51 mm x 3 mm were used for the laboratory testing. They were connected to the panels either at the back of the panels, providing support against blast loads, or on both sides (front and back) for increased blast load resistance. **Figure 35** shows a schematic view of wall specimens for testing. More detailed explanations of the panel preparation process, panel types, and the test matrix are given in Sections **3.1.2** Specimenand **3.3.**

The choice of ECC for use in the panels was due to its high tensile strain capacity (~5%) and tension-hardening behaviour (V. C. Li, 2019). ECC is a cementitious mortar that utilizes polyvinyl alcohol (PVA) or polyethylene (PE) fibres tailored to generate multiple cracks in the critical tension region as opposed to a single crack at maximum stress locations. This phenomenon of multiple crack formation enables tension hardening (tensile stress increase after the first crack) and a very high ultimate tensile strain (5%). The tension hardening behaviour has been validated by tensile coupon specimens that were tested in uniaxial tension as part of the preliminary materials investigation. Further details of ECC and material testing are provided in the following section. The high energy absorption capacity of ECC in tension makes it an ideal candidate for blast applications.

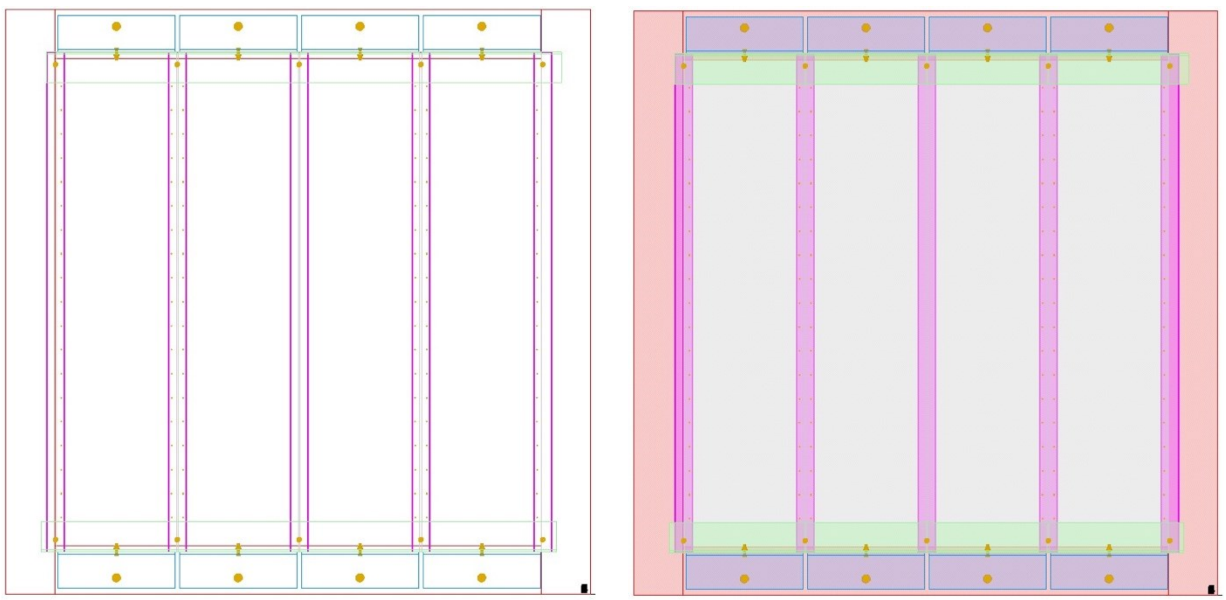

Figure 35: Vertical HSS Studs and panel-stud composite wall system for blast resistance

The use of steel sheets was aimed at utilizing the inherently high tensile strength and ductility of the material. On average, the yield strength of the steel selected in tension was approximately 80 times higher than that of ECC, and the ultimate tensile strain capacity was on average four times that of ECC, i.e., 20% (Canadian Standard Association, 2014) (20%). It is important to note that a 1-metre-wide, 1.5-mm-thick steel sheet provides 1,500 mm² area of steel. To put this into perspective, this amount of reinforcement would be adequate to provide the minimum reinforcement ratio 0.2% for a 750 mm thick concrete slab (Canadian Standard Association, 2024a). Therefore, the additional tensile strength provided by the steel sheets was significant.

The use of thin panels reduces flexural stiffness (due to the small moment of inertia); therefore, a significant amount of deformation is expected at relatively low loads. Following the formation of cracks and further reduction of the panels' effective moment of inertia, membrane behaviour is expected to dominate the panel response under blast loads. The high tensile strain capacity of ECC and steel is expected to provide the anticipated tensile deformation capacity and permit large out-of-plane deformations without rupture.

A preliminary FEA was performed prior to selecting the test specimens using LS-Dyna (LSTC, 2025b) software. The same software was also used to conduct a numerical investigation, subsequently with the applicable material constitutive models, and the results of the numerical analysis are discussed in Chapter 4. The preliminary results indicated that ECC-only panels with pin supports along their short sides (top and bottom) were able to resist a low-intensity blast shock wave resulting from a 50 kg of TNT at a 20 m standoff distance, which is equal to a scaled distance of 5.4 m / kg$^{1/3}$. This shock wave caused 83 kPa (12 psi) reflected pressure and 341 kPa-ms (50 psi-ms) reflected impulse. The maximum out-of-plane deformation of the panel under such loading was obtained to be 70 mm, as illustrated in **Figure 36**. The residual mid-span deflection was 33 mm. This preliminary analysis provided confidence that it is feasible to produce the panels as planned for use in blast-resistant construction.

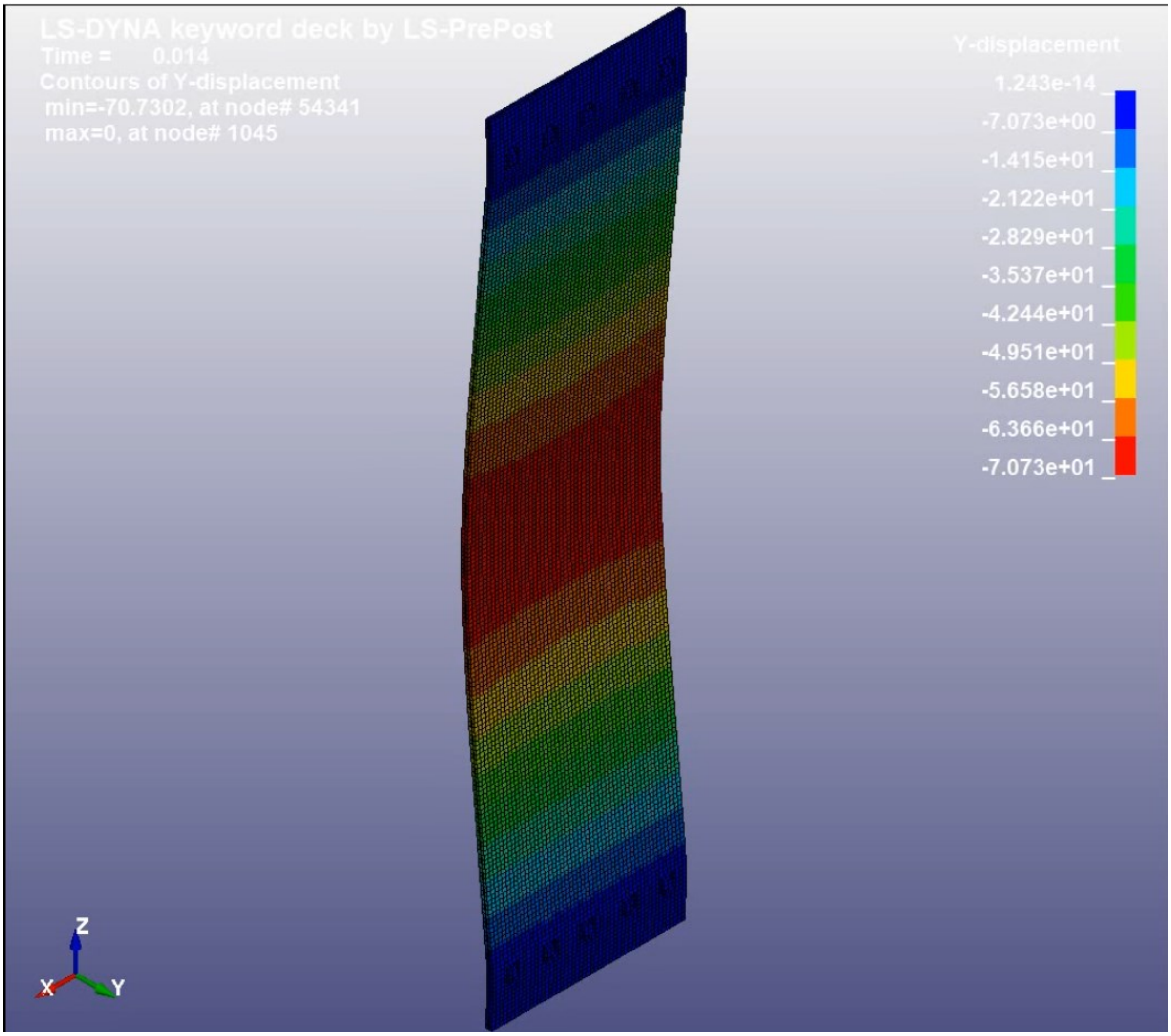

Figure 36: Preliminary FEA using LS-Dyna – ECC panels supported on their short sides

There are several advantages of using such thin and lightweight cementitious panels for hardening against blast loads. When they are used to harden an existing building element, they can be connected through mechanical connectors, i.e. self-drilling screws and a handheld drill. This ease of installation allows the installation to be completed quickly, causing less disruption to day-to-day activities. Furthermore, as these panels do not contain any toxic or volatile chemicals, it is not necessary to utilize respiratory protection during the application, unlike some of the other hardening materials (ex, FRP, Polyurea). They can also be used as multiple layers for areas that require higher protection. For example, multiple layers of panels could be utilized for the first few floors of a building, where blast load effects are higher due to smaller standoff distances, and a single layer could be utilized on the upper floors, where the loads become lower. Finally, as these materials are all readily available and do not require special handling during fabrication or application stages, the cost of procuring and installation is expected to be relatively low.

3.1 Test Specimens

The main objective of experimental research was the development of blast-resistant ECC-steel composite panels. The premise of the research was that a thin composite panel made of ECC–steel–ECC layers would be a cost-effective and versatile blast-resistant member. These panels provide protection by combining flexural resistance and tension membrane behaviour. The initial emphasis was placed on material development, as presented in the next section. Further improvement of blast resistance was explored by combining the panels with HSS studs. This resulted in the development of stronger blast-resistant wall systems.

3.1.1 ECC Mix Design

The mechanical properties of ECC, especially its high tensile capacity and ductility, directly influence the blast performance of panels. Therefore, it is paramount to use an appropriate ECC mix to achieve the required mechanical properties. ECC is a high-performance engineered cementitious material consisting of cement, fly ash, sand, water, microfibres, and water reducer. A large number of mix designs were tried before it was decided to adopt the mix design developed by Lepech and Li (2008) because of the favourable resulting tensile strength and toughness. Only the selected mixture is reported here, as the other mixtures had much higher variability in tensile strength and ductility parameters. The fibre type used was randomly placed polyvinyl alcohol

(PVA). **Table 1** gives the mix design employed. Tension coupon tests were performed to establish the stress-strain relationships of ECC. Dumbbell-shaped specimens were made for coupon testing. The elongation of the narrow segment of the specimens within a gauge length of 80 mm was measured using LVDT's placed symmetrically on both sides of the specimen (right-front and left-behind). The dimensions of a typical coupon specimen and a photograph of the test setup are shown in **Figure 37** and **Figure 38**.

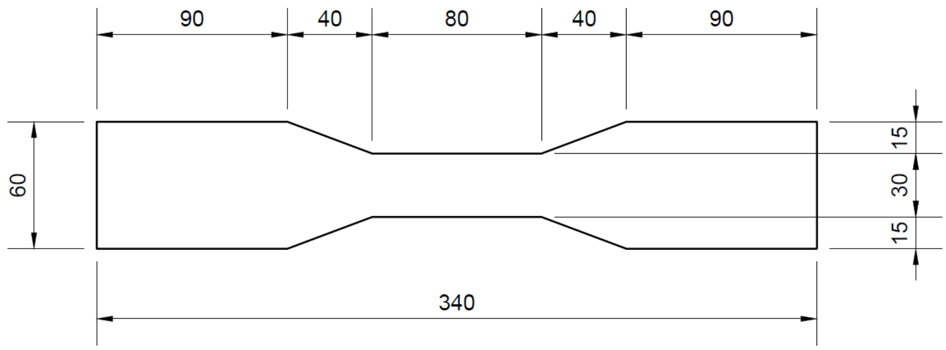

Figure 37: Dimensions of tension coupon specimens

Table 1: Mix proportions for the ECC by weight, **(Lepech & Li, 2008)**

Cement	Fly ash	Sand	Water	HRWR	Fibre, volume %
1	1.2	0.8	0.56	0.012	0.02

Figure 38: Direct tension test setup of ECC coupons, LVDTs on the right front and left behind

The tension coupon test setup was prepared such that the LVDT support frames were separated from the U-shaped load application plates. This separation allowed the elongation of the narrow portion of the dumbbell specimen to be measured independently of the applied force. The LVDT support frames were fabricated from aluminum to reduce their weight. Each frame was connected to the specimen using two screws at the front of the specimen and two screws at the back. The tips of the screws were ground to obtain a flat surface to avoid damaging the coupons and were hand-tightened to push on the surface of the coupon specimen. The friction force created by the normal force applied by the screws on the specimen prevented the movement of the frames with respect to the specimen. The U-shaped load application plates had sloped interior surfaces that matched the slope of the sides of the coupon specimens. This allowed a relatively uniform application of the force on the specimen. To eliminate any internal moment that could develop within the specimen, due to small eccentricities between the top and bottom plates, the plates were aligned before each test, as shown in **Figure 39**.

Figure 39: Alignment of U-shaped load application plates before tension tests

In addition, the load application plates were connected to the machine grips via 12mm diameter threaded rods. The free length of these rods between the U-shaped plates and the machine grips was kept at a minimum of 150 mm to reduce the flexural rigidity of the rods. To further decrease the flexural rigidity and transfer of moments, the thread engagement of the rods into the U-shaped load transfer plates and at the machine grips was limited to 6 mm (1/2 of the rod diameter). This reduction allowed a small amount of unresisted movement of the rod, resembling a flexural hinge. By creating a pseudo-hinge immediately above and below the U-shaped plates, moments due to eccentricities that may be caused by misalignment were reduced. This method facilitated pure uniaxial tension loading, resulting in the stress-strain relationship shown in **Figure 40**.

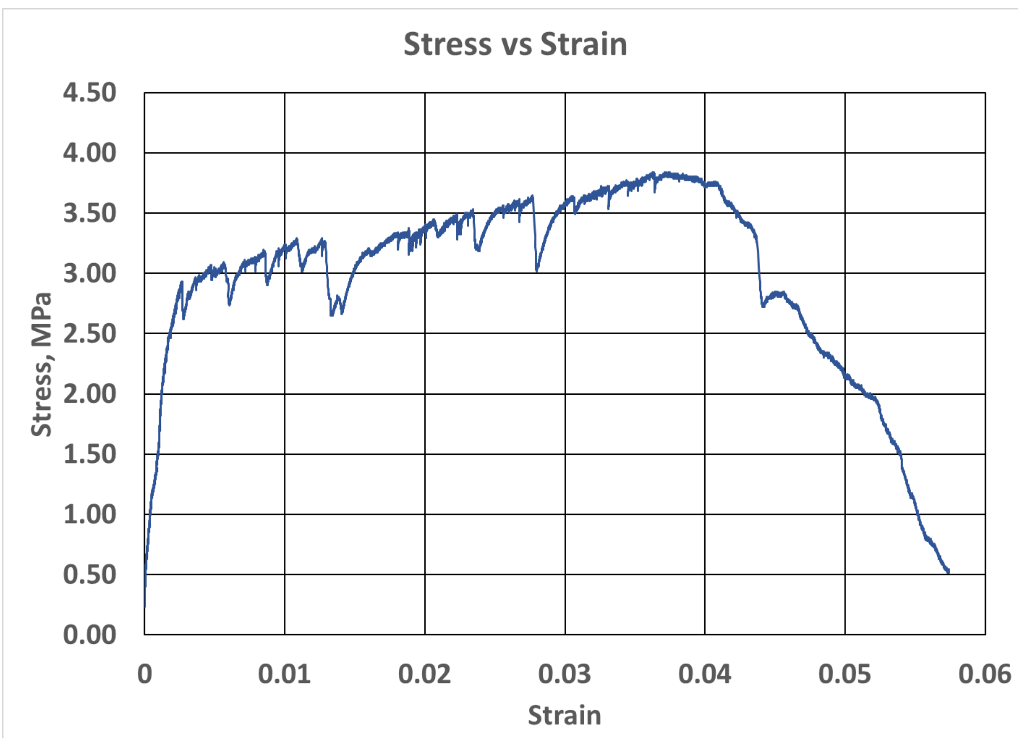

Figure 40: Stress-strain relationship of an ECC coupon in direct tension

3.1.2 Specimen Preparation

The panels were cast using a formwork placed horizontally on a flat surface in the laboratory. To ensure the flatness of the floor, it was cleaned of any existing debris. Once the formwork was placed on the floor, its flatness was verified via a level ruler. To ensure a smooth surface of the bottom layer of the ECC and to reduce adhesion to the formwork, high-density polyethylene (HDPE) sheets, commonly known as "puck board", were placed above the plywood as shown in **Figure 41**. It was observed that the HDPE sheets provided a smooth and glossy finish with a mirror-like appearance.

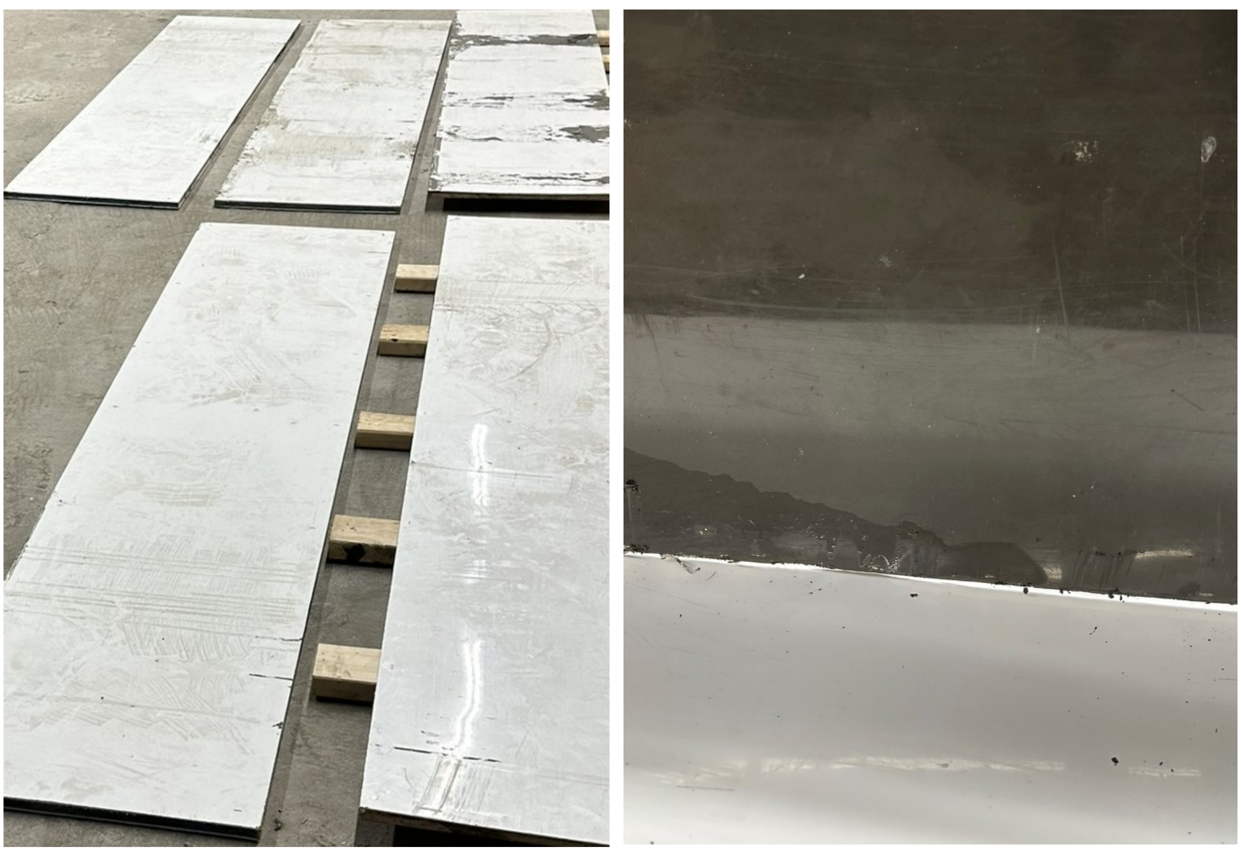

Figure 41: HDPE sheet used as a formwork layer for ease of debonding and not damaging the panel surface

Composite behaviour between the layers of ECC and the steel sheet was attained by means of #10 self-drilling screws with a diameter of 4.8 mm used as shear connectors (**Figure 42**). These shear connectors provided a mechanical connection between the layers. The connectors were spaced at 100 mm or 200 mm (**Figure 43**). These two spacings were selected to compare the effectiveness of connector spacing in providing the composite behaviour. The length of the connectors was limited to 6 mm on either side of the steel sheets to limit the variability of the thickness of ECC layers.

Figure 42: Self-drilling screw installation

The ECC mix for each panel was prepared using the previously selected mix design shown in **Table 1**. This mix was the same as the M45 mix reported by Lepech & Li, (2008) and V. C. Li, (2019). The mixing procedure was modified to account for the required volume of approximately 80 litres. It is important to note that the ECC mix requires higher speed mixing than traditional concrete mixers to ensure uniformity. Hence, standard laboratory equipment used for concrete mixing, including drum and pan mixers, was not suitable for this mix. For smaller batch sizes, a high-speed mortar mixer with a leaf-shaped mixing attachment may be used. However, for the relatively larger batch size of 80 litres, the mixing was performed inside the lower half of a plastic storage drum. This drum provided the necessary volume while allowing ease of access for the mixing equipment. In order to achieve the necessary mixing speeds, two 10-ampere capacity corded drills with 1/2-inch diameter mortar mixing attachments were used. Using two mixers minimized the clumping of the fibres, while allowing better control of the mixing depth (**Figure 45**). Due to the low water-to-binder ratio (0.25), a high dosage of high-range water reducer (HRWR) was used to obtain the necessary workability. Once the mixing started, both mixers were used at the highest speed setting until the completion of mixing.

Figure 43: Panels with 100 mm (left) and 200 mm (right) connector spacing

The mixing procedure employed is summarized below:

1. Add all the mixing water into the mixing drum,
2. Add all the sand, mix for 1 minute,
3. Add all the flyash, mix for 1 minute,
4. Add 1/3 of cement, add 100% of HRWR and mix for 1 minute,
5. Add 1/3 of cement, and mix for 1 minute,
6. Add the final 1/3 of cement, and mix for 3 minutes,
7. Add PVA fibres gradually by hand in 5 minutes while continuously mixing,
8. Mix for an additional 5 minutes after all fibres are added.

Before the mixing, the fibres were tumbled in pails using pressurized air to separate them and prevent clumping, as shown in **Figure 44**. This step was observed to be critical in obtaining uniform fibre dispersion within the ECC. The viscosity of the fresh ECC mix allowed it to self-consolidate and did not require additional compaction. During casting, the initial layer of ECC was poured into the formwork. Once the desired thickness was achieved uniformly throughout the formwork, the steel plate was placed on top of the fresh layer of ECC. The second layer of ECC was poured on top of the steel plate until the total specimen thickness of 15 mm was reached. After four hours, when the top layer of ECC had set, the panels were covered with wet burlap and polyethylene sheets until they were 7 days old (**Figure 46**). After 7 days, they were removed from the formwork and stored under wet burlap until they became 90 days old. Due to the high proportion of fly ash in the mix and the high dosage of HRWR, the setting time of the mix was longer than typical. In this case, a setting time of four hours was observed.

Figure 44: Fibres before (left) and after (right) air-tumbling

Figure 45: Two hand mixers are being used simultaneously for mixing in a plastic drum

Figure 46: Specimens immediately after pouring and covered with wet burlap, four hours later

Figure 47: Panel specimens prior to installation on the shock tube for blast testing

3.2 Shock Tube as a Blast Simulator

The University of Ottawa's Shock tube facility was used as a blast simulator to test the panels under simulated blast loads. The shock tube generates a shockwave using pressurized air, which resembles the overpressure created by the detonation of high explosives. At the location of the specimen to be tested, the shock tube can create reflected pressures of up to 100 kPa with a blast duration that varies between approximately 5 milliseconds (ms) and 50 ms. There are three essential components of the shock tube: the driver, the diaphragm, and the expansion sections (**Figure 48**). The expansion section ends at the opening where the test specimens are placed. The size of the opening as a test is 2032 mm by 2032 mm (80 inches by 80 inches). The driver component is comprised of 800 mm diameter steel pipe sections of various lengths, where the air is accumulated under high pressure. Additional pipe sections may be added or removed to control the volume of pressurized air. Longer driver sections allow more air to be accumulated, resulting in longer duration blasts (greater impulse). For the experimental program of this research, the shortest length of the driver was 305 mm (1 foot), which was then increased to 1830 mm (6 feet), and then to 3353 mm (11 feet).

The driver section can be pressurized up to 100 psi (689 kPa) of air using the pressurized air supply system, either supplied by a dedicated compressor for the shock tube or the central compressor that exists in the laboratory. The pressurized air in the driver section is separated from the diaphragm section via aluminum sheets of varying thickness (**Figure 49**). The thickness of the aluminum sheets is adjusted according to the desired driver pressure to be used for the test. For example, a single 0.01-inch-thick grade 1100 aluminum sheet typically resists a pressure of 15 psi (103 kPa). The second component of the shock tube is the diaphragm, which is a 100 mm long steel pipe of the same diameter as the driver. It performs the function of a trigger by allowing the user to control the occurrence of the blast. Typically, the aluminum sheets on either side of the diaphragm have the same total thickness to provide them with the same capacity against overpressure.

Figure 48: Driver and diaphragm (top) and expansion (bottom) sections of the shock tube

Figure 49: Aluminum sheets on either side of the diaphragm section

During the pressurization phase of testing, the diaphragm section overpressure is maintained at half the value of the driver section overpressure to achieve balance. When the desired driver pressure is reached, the diaphragm section is drained to ambient pressure. This causes the overpressure on the driver section to exceed the capacity of the aluminum sheets on the driver side of the diaphragm and burst. The pressurized air on the driver side expands very rapidly, causing the bursting of the aluminum sheets on the expansion side of the diaphragm. Following the burst of the second layer of aluminum sheets, the mass of pressurized air moves into the expansion section at a supersonic velocity, creating a shock front. This shock wave hits the specimens at the opening and creates a reflected pressure-time history similar to the one shown in **Figure 50**. As this shock wave travels within the expansion section, its pressure decreases significantly. An approximate rule of thumb for an 11-foot-long driver section is that the numerical value of the pressure in psi inside the driver will be measured at the piezoelectric pressure sensors at the opening of the shock tube in kPa. In other words, an 85-psi (586 kPa) driver pressure will create a shockwave with approximately an 85 kPa pressure on the test specimen, corresponding to a reduction ratio of about 1:7.

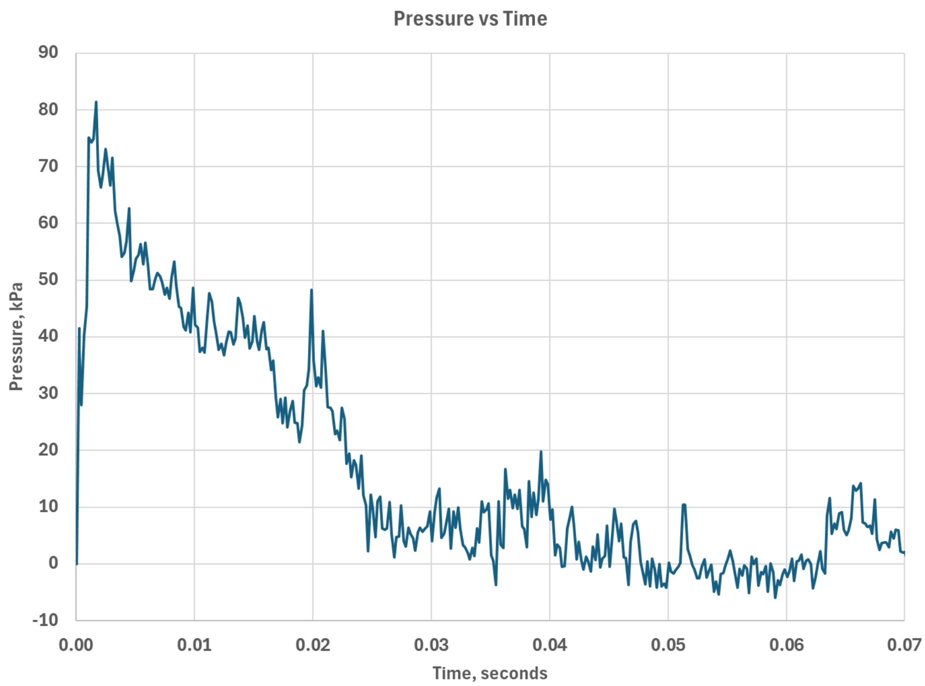

Figure 50: Pressure vs. time data of a simulated blast at the shock tube

3.3 Blast Test Configurations and Test Procedure

Wall specimens were tested in groups of four. Each group had a different test parameter to simulate an application in practice. While Sets 1 and 4 involved tests of blast-resistant wall systems, consisting of wall panels strengthened with HSS studs, Sets 2 and 3 involved tests of panels without the HSS studs. Set 5 was devoted to tests of steel sheets without the ECC. Tables 2 and 3 summarize the properties of test specimens and the test matrix considered. The details of each set of tests are presented below with a discussion of specimen performance provided in Section 3.4. This section also provides the test procedure and the instrumentation used to record primary test variables, which include measurements of reflected pressure, panel deflections, and high-speed camera videos.

Table 2: Types of panels included in the experimental program

Panel Type	Panel Size	Outer layer material and thickness	Inner layer material and thickness	Outer layer material and thickness	Total thickness	Connector Spacing
1a	2080 x 510 mm	ECC 6 mm	Steel 3 mm	ECC 6 mm	15 mm	100 mm
1b	2080 x 510 mm	ECC 6 mm	Steel 3 mm	ECC 6 mm	15 mm	200 mm
2a	2080 x 510 mm	ECC 6.75 mm	Steel 1.5 mm	ECC 6.75 mm	15 mm	100 mm
2b	2080 x 510 mm	ECC 6.75 mm	Steel 1.5 mm	ECC 6.75 mm	15 mm	200 mm
3a	2080 x 510 mm	-	Steel 3 mm	-	3 mm	-
3b	2080 x 510 mm	-	Steel 1.5 mm	-	1.5 mm	-

Table 3: Specimen testing matrix

Specimen Set	Wall #1 panel type	Wall #2 panel type	Wall #3 panel type	Wall #4 panel type	HSS used at walls
1	1a	1b	1a	1b	76x51x3 behind
2	1a	1b	1a	1b	-
3	2a	2b	2a	2b	-
4	2a	2b	2a	2b	76x51x3 front and behind
5	3a	3b	3a	3b	-

The first set of wall specimens consisted of four panels with 3 mm thick steel, two of which had connectors with 100 mm spacing (Panel Type 1a in **Table 2** and **Table 3**) and two panels with 200 mm spacing (Panel Type 1b). This group was tested as representative of a blast-load resistant wall system that included 76 x 51 x 3 mm (3 x 2 x 1/8 inch) HSS sections. In these tests, five HSS sections were placed vertically at 510 mm spacing, and the panels were oriented such that the long edges of each panel were parallel to the longitudinal axis of the HSS sections. This is illustrated in **Figure 51**. The panels were connected to the HSS sections using #14 x 2-1/2-inch self-drilling screws as depicted in **Figure 52** at a spacing of 100 mm. A washer was placed between the screws and the ECC layer for better distribution of pressure on the surface of the panel. The HSS sections were supported at the top and bottom by 4 x 4 x 1/4-inch angles, which were attached using 12 mm diameter (1/2 inch) bolts. The support angles were connected to 6 x 6 x 3/8-inch angles that were bolted to the shock tube frame, as shown in **Figure 53**. It is important to note that the 4x4x1/4 inch support angles and the panels are not connected. The panels are mechanically connected to the HSS sections, and the HSS sections are connected to the 4x4x1/4 inch support angles. The finished assembly before testing is shown in **Figure 61**, and a 3D rendering of the test setup is shown in **Figure 54**.

Figure 51: A single panel and an HSS member behind at its left-hand side

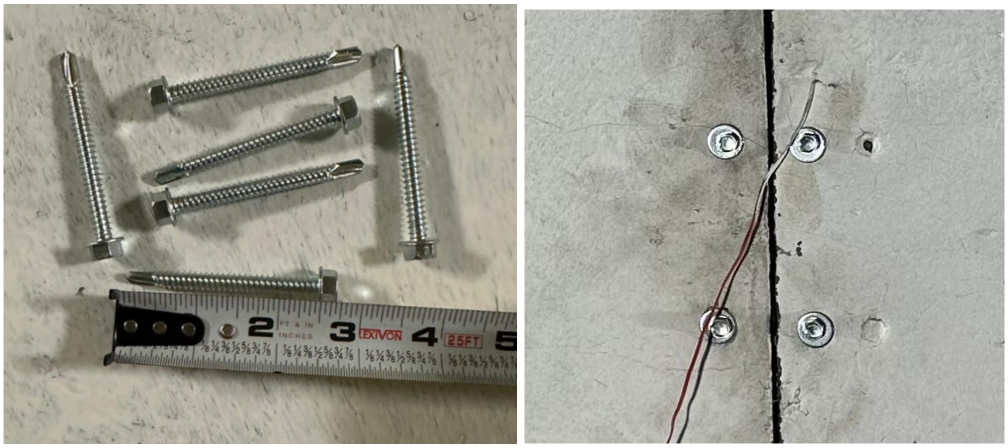

Figure 52: #14 x 2-1/2-inch-long hex head self-drilling screws attached

Figure 53: Support angles, HSS, and panel connection

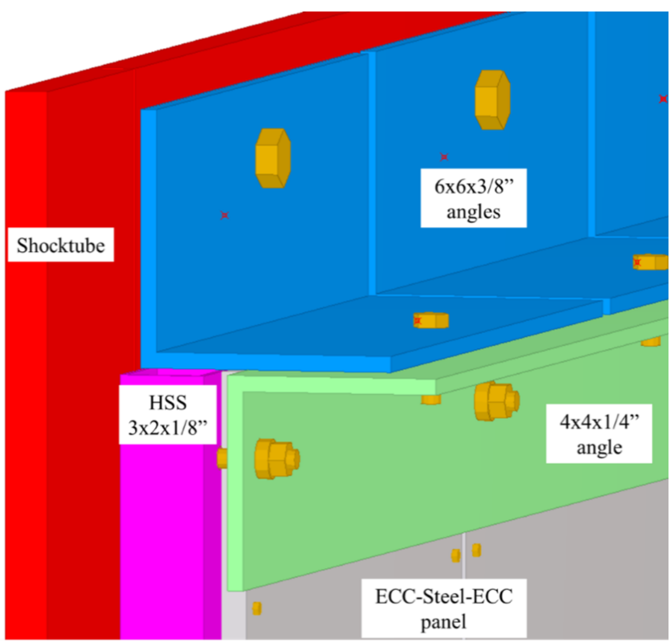

Figure 54: 3D rendering of the test setup for the first set of specimens

The second set of specimens also included 3 mm thick steel plates. Two panels had 100mm connector spacing (Panel Type 1a), and the other two panels had a 200 mm spacing (Panel Type 1b). This group was tested without the HSS sections. Each panel was connected with four 12 mm diameter (1/2 inch) bolts at the top and bottom to support angles, as illustrated in **Figure 55**. These support angles were bolted to the shock tube frame in the same way as Set 1 specimens. **Figure 56** shows Set 2 panels prior to testing.

Figure 55: Each panel is connected to support angles using 12 mm bolts

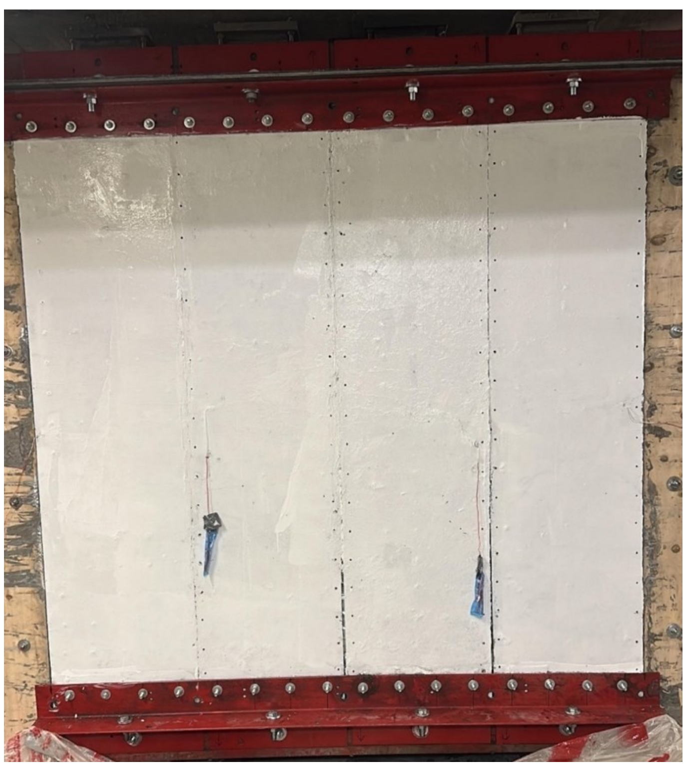

Figure 56: Second set of wall specimens during installation

The third set of specimens included 1.5 mm thick steel plates with half of the panels using connectors at 100 mm (Panel Type 2a) and the other half using connectors at 200 mm (Panel Type 2b). This group was also tested without the HSS sections. These panels were connected to the support angles using four 12 mm diameter (1/2 inch) bolts at the top and bottom, similar to the second set of specimens as depicted in **Figure 57**.

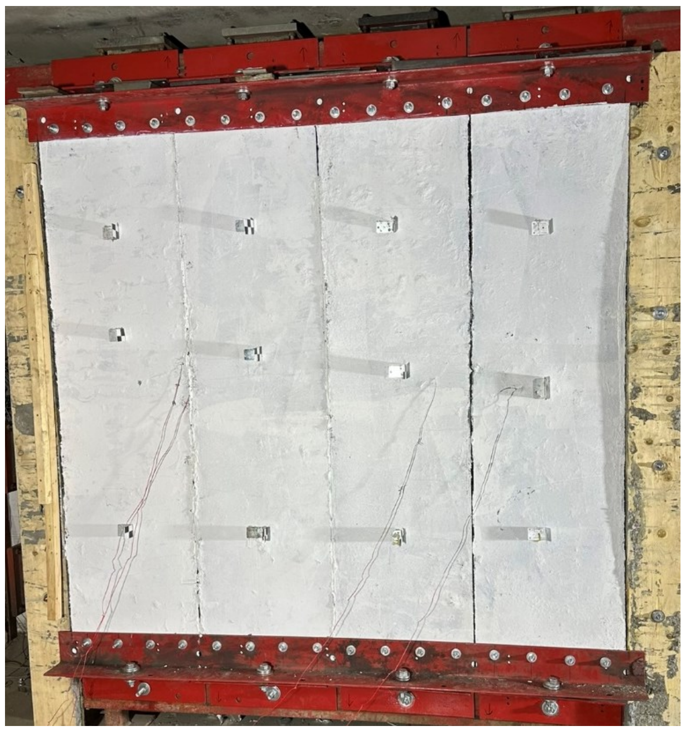

Figure 57: Third set of wall specimens prior to testing

The fourth set of wall specimens utilized HSS members at the front and back of the panels for increased blast resistance. The panels consisted of 1.5 mm thick steel plates. The connector spacing was 100 mm for two panels (Panel Type 2a) and 200 mm (Panel Type 2b) for the other two. These specimens were connected to 76 x 51 x 3 mm HSS sections along their long edges, with one HSS placed behind the panel (towards the shock tube side, i.e. the threat side) and one HSS placed in front of the panel (protected side) as illustrated in **Figure 58** and **Figure 59**. In this set, a sandwich wall system was created such that the HSS sections formed the outer layers and the panels formed the inner layer. The connection between the HSS sections and the panels was provided via 6 mm (1/4-inch) diameter threaded rods that had washers and nuts at both ends. The threaded rods were spaced at 200 mm. **Figure 58** and **Figure 59** illustrate Set 4 specimens during and after the assembly. For this set of specimens, the HSS member behind the panel (shock tube side) was connected to the 4x4x1/4-inch support angle at the top and bottom in a similar manner as Set 1, using 12 mm (1/2 inch) bolts.

Figure 58: Set 4 specimens during preparation

The fifth set of specimens was tested as benchmark tests to assess the performance of steel sheets alone. This set consisted of either 3.0 mm or 1.5 mm thick steel sheets. Two of each thickness of steel sheets were tested as indicated in Tables 1 and 2. The rationale for testing steel sheets without the ECC layers was to isolate the performance of steel sheets, without the composite action. In this set of tests, steel sheets were connected directly to the 4x4x1/4 steel angles at the top and bottom using 12 mm (1/2 inch) bolts. Specimen set five, prior to testing, is shown in **Figure 60**.


Figure 59: Set 4 wall specimens prior to testing

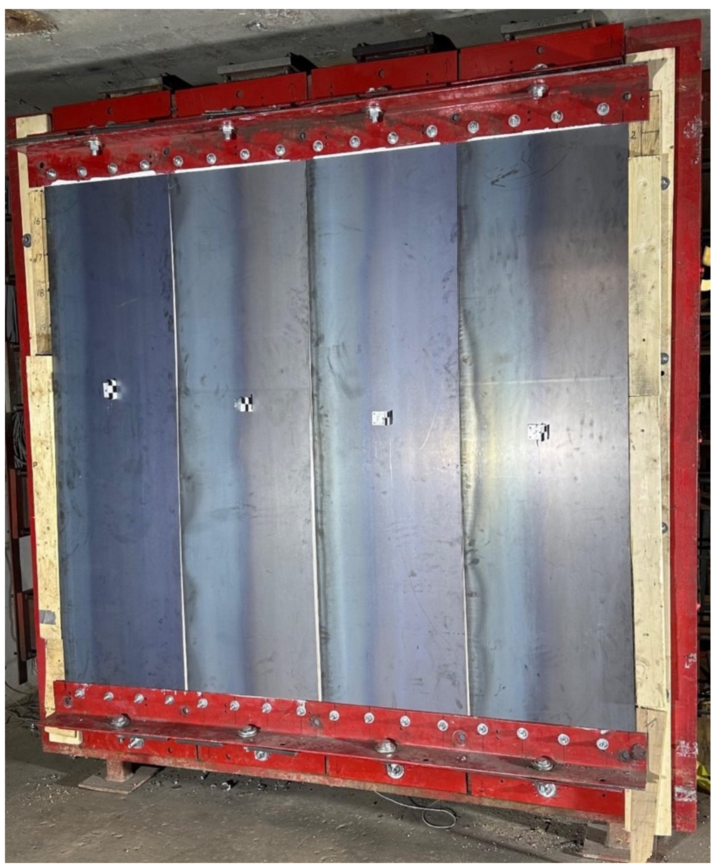
Figure 60: Set 5 steel sheets prior to testing

The specimens were well instrumented to record the required test data. The reflected pressure was recorded by means of two piezoelectric pressure sensors, one located at the bottom end of the test area in the middle, and the other on the right side (when facing the shock tube) at mid-height of the test area near the end (next to the specimens) to capture the reflected pressure. The displacement of each panel at mid-height was measured using the video images recorded by the Phantom® VEO 410L high-speed cameras used during each test. These cameras have the capability of recording 4000 frames per second with a resolution of 1280x800 pixels. For these tests, the videos were recorded at 2000 frames per second using a resolution of 1280x800 pixels. The video post-processing software, Phantom Camera Control (PCC), developed by the high-speed camera manufacturer, was used to analyze the videos and determine the displacement of points of interest. The points of interest were marked using black and white checkerboard tape, as shown in **Figure 61** and **Figure 62**, which created a single point with a high contrast that the software could track. The tests were controlled on the floor above the shock tube level through a controller. **Figure 63** illustrates the pressure control device with digital indicators for the driver and spool (diaphragm) pressures. The test was monitored and recorded by a computer and a data acquisition system. The results are discussed in the next section. The data acquisition system recorded data at a 100 kHz rate, which satisfactorily captured the high rate of change of pressure observed during each blast.

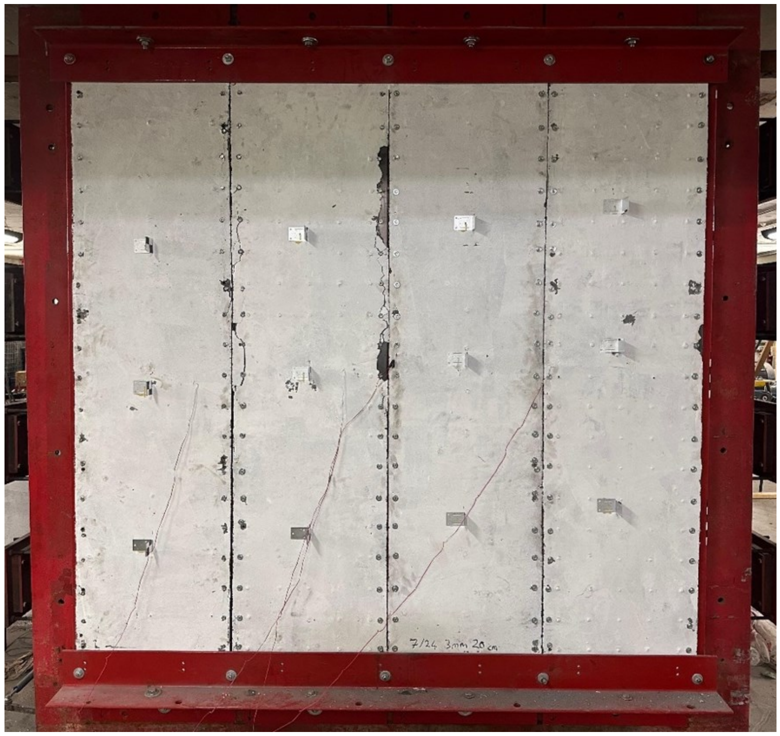

Figure 61: Displacement measurement locations on the panels

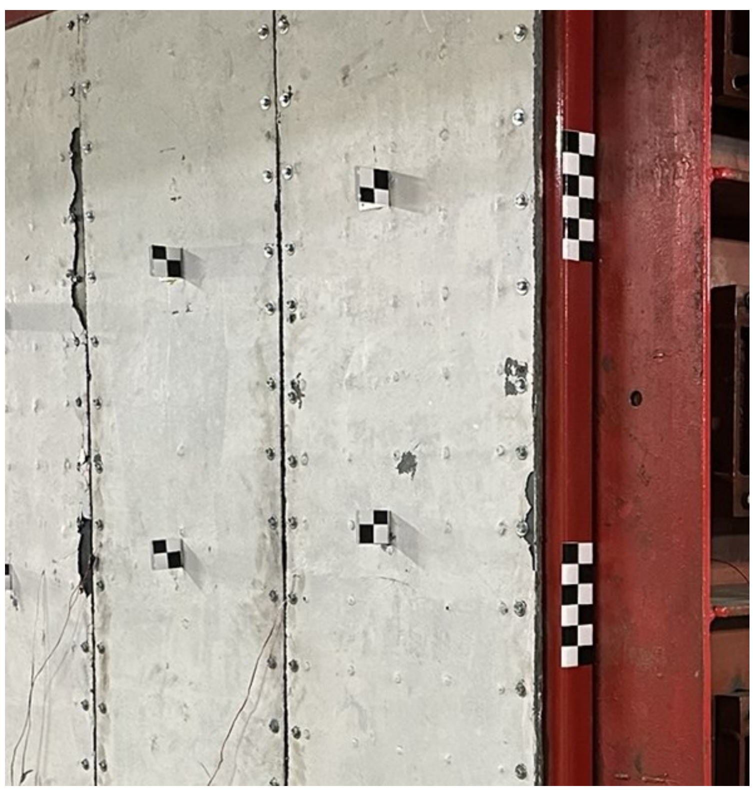

Figure 62: Checkerboard tape markings on wall specimens

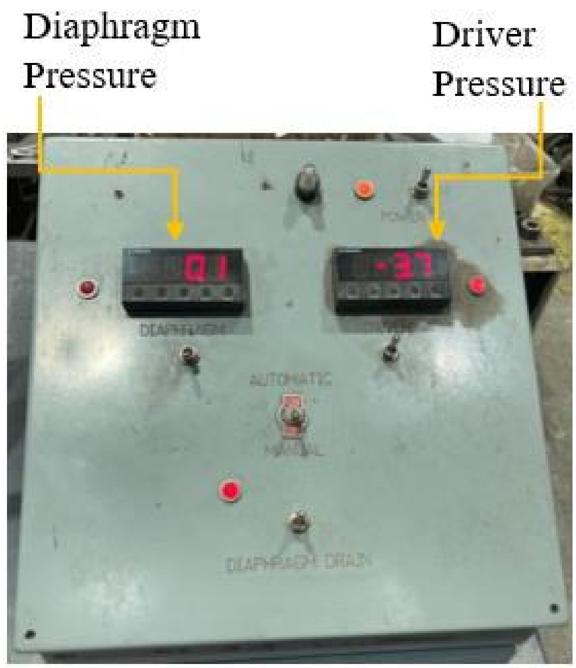

Figure 63: Air pressure control device

3.4 Shock Tube Test Results

The results of shock tube tests are provided in this section. The pressure vs time relationship for each blast test – referred to as “shot” – was recorded in the shock tube control data acquisition system. This data was exported in comma-separated value (CSV) format and converted to a native Microsoft Excel format (XLSX). In each file, a data point is recorded every 100,000th of a second (0.01 milliseconds), corresponding to a data acquisition rate of 100 kHz. The pressure values from the bottom and side piezoelectric pressure sensors were plotted against time. Numerical integration was utilized to calculate the positive impulse for each shot by multiplying the pressure value by the selected time increment and accumulating the products.

The peak displacement at the mid-height of each specimen was obtained from high-speed camera recordings. The checkerboard pattern tape attached to the specimens creates a high-contrast point at the intersection of black and white squares, which allows the point-tracking feature of the

Phantom Camera Control software to track these points (**Figure 64**). The software can track and record the X and Y coordinates of each tracked point at each video frame. These coordinate data may be exported as a "CSV" file to be processed in MS Excel.

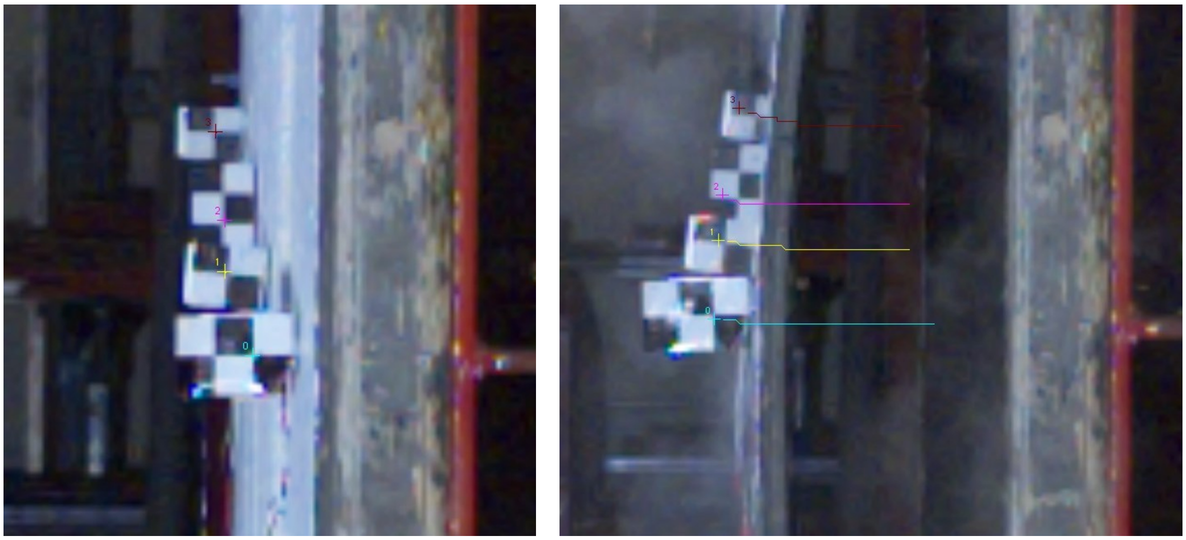

Figure 64: Movement tracking of points before (left) and during (right) blast test

For every specimen, for each shot, the peak pressure value, the positive impulse, maximum mid-height deformation, and the residual mid-height deformation are reported below. With the intention of providing a reference, the charge weight in kilograms of TNT and the standoff distance in metres corresponding to each shot are also provided. Multiple shots were applied until failure.

The back calculation of the blast threat was performed using the software OverPressure that was developed at the University of Ottawa (**Jacques, 2013**). This software uses the charts available in (UFC 3-340-02, 2008) to correlate the equivalent TNT charge weight, reflected pressure, and reflected impulse values. The reflected impulse calculation in OverPressure utilizes Figures 2-194(a) and 2-194(b) of the UFC document, which correlate the reflected scale impulse with the angle of incidence. For an angle of incidence of 0 degrees (frontal blast), the scaled reflected impulse value shown in the charts 2-194(a) and (b) is approximately 20% less than the value shown in Figure 2-15 of the UFC document. However, for the back calculation of threats, the software validation indicates errors that are less than 5% for all validation cases. Accurate calculation of back-calculated threat parameters was significant because they were used in LS-Dyna to simulate the pressure-time history of the shock tube tests.

3.5.1 First Set of Specimens

This first set of specimens displayed a flexure-dominant behaviour. The HSS members and the panels were connected using the self-drilling screws, which provided adequate shear transfer between the panels and the HSS. This shear transfer mechanism enabled the specimens to behave similarly to a T-beam, where the HSS members were the “web,” and the panels were the “flange”. This composite behaviour of HSS members and panels increased the system's overall stiffness, limiting displacement during lower-intensity shots. As the peak pressure and shot duration increased, the observed maximum displacements and residual displacements increased, indicating flexural yielding of the HSS members at mid-height. The failure of the specimen occurred during the sixth shot (**Figure 65**) via the formation of a flexural hinge at the mid-height of the HSS member, followed immediately by the failure of the top support. The top support failure was due to the failure of the bolted connection, specifically the bending of the bolts and rupturing of the washers (**Figure 69**). Frames from the high-speed video recording of the final shot for the first set of specimens are shown below in **Figure 66**. The displacement vs. time graph showing all shots is provided in **Figure 70**. The pressure, impulse and displacement vs. time graphs of shots 1, 2, 3, 4, and 5 are shown individually in **Figure 71** to **Figure 75**.

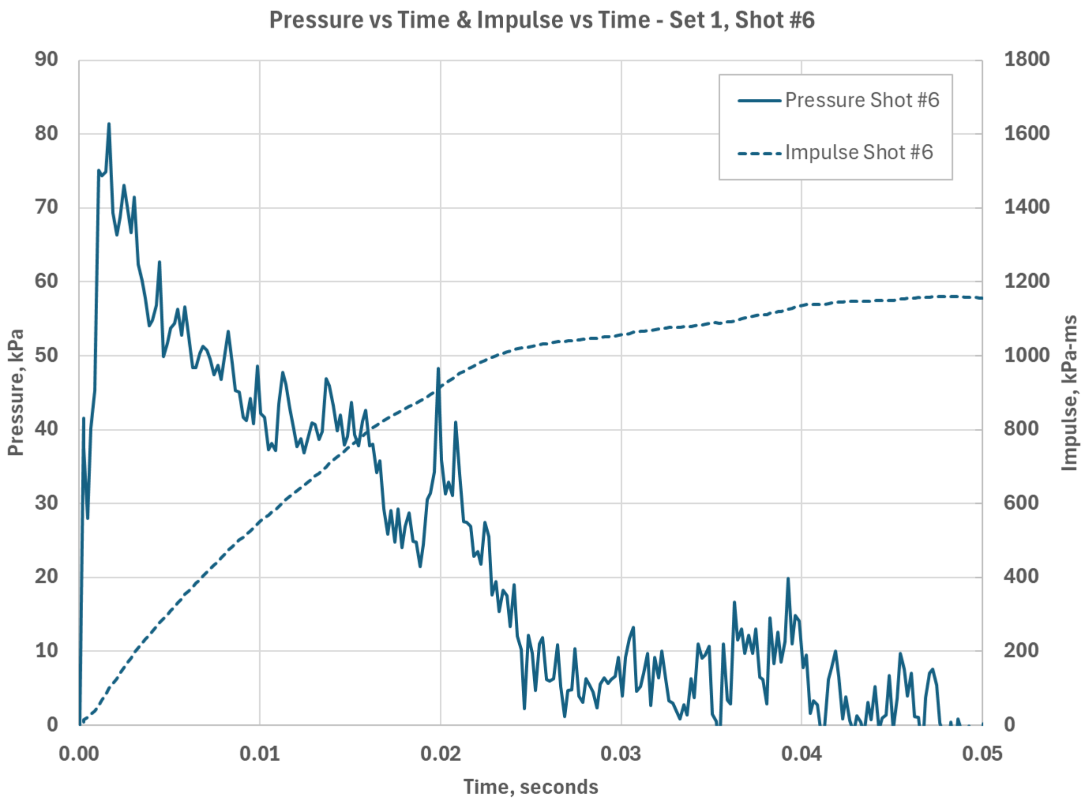

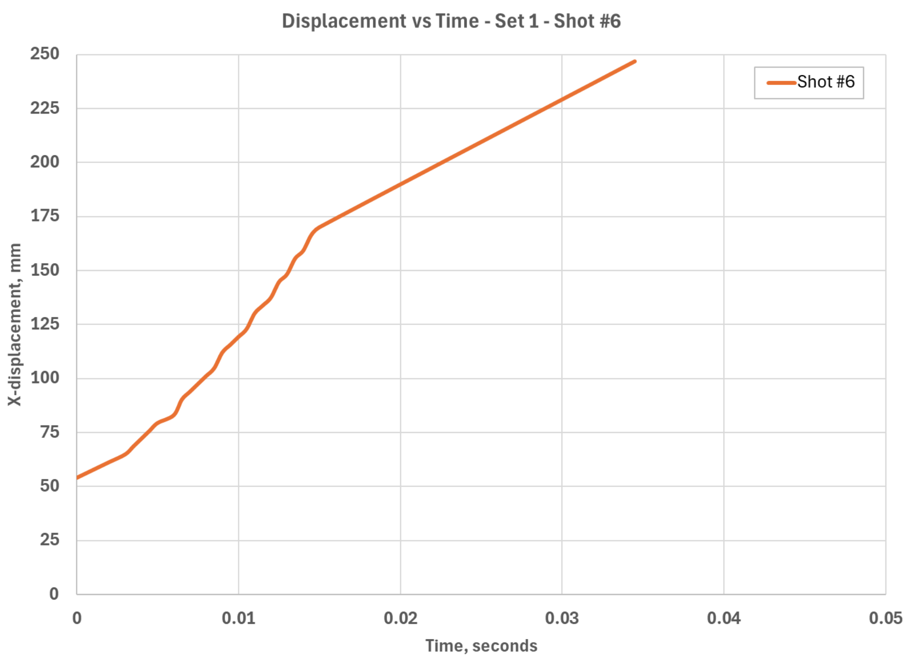

Figure 65: Pressure, Impulse and Displacement vs Time chart for Set 1 - shot #6 – 82 kPa & 1066 kPa-ms (Scaled distance, Z = 5.5 m / kg$^{1/3}$)

Figure 66: Set 1 specimens before and during shot #6

As can be observed from the image frames, the displacement capacity of the panels and the specimen assembly was significant. Prior to the failure of the top connection, the mid-height deflection of the panels was measured as 235 mm. Considering that the distance between the horizontal legs of the support angles was 2082 mm, a displacement value of 235 mm corresponds to a deflection of L/9. Post failure investigation of the specimen indicated no crushing on the back side of the panels (**Figure 67**). At the front side, distributed cracks, a signature property of ECC, were observed (**Figure 68**). Furthermore, no delamination of the ECC-steel-ECC layers was evident. This high displacement capacity, coupled with the structural integrity of the specimens, was considered to prove the existence of composite action of the ECC-steel-ECC panels. It was notable that the specimens remained structurally intact even after falling due to support failure. A combined effect of a demolition crowbar and multiple hits with a 12 lbs (5.5 kg) sledgehammer was necessary to separate the panels and the HSS, as shown in **Figure 69**. The peak reflected pressure, impulse of the shots and corresponding maximum deformation values of the first set of specimens are shown in **Table 4** below. The equivalent TNT charge weight (W) and standoff distance (R), along with the scaled distance ($Z = R / W^{1/3}$), are also shown in the table.

Table 4: Blast load details for the first set of specimens

	Shot #1	**Shot #2**	**Shot #3**	**Shot #4**	**Shot #5**	**Shot #6**
Peak Pressure, kPa	21	48	58	58	76	82
Impulse, kPa-ms	56	138	183	455	648	1066
Maximum Deformation, mm	7	10	18	63	105	247
Residual Deformation, mm	0	0	3	12	54	-
Additional Deformation, mm	-	10	18	60	93	193
Equivalent Charge Weight (kg) and Distance (m)	3.5 kg, 20 m	9 kg, 16 m	15 kg, 16 m	228 kg, 41 m	390 kg, 42 m	1567 kg, 64 m
Scaled Distance ($m/kg^{1/3}$)	13.3	7.5	6.7	6.7	5.7	5.5

Figure 67: Set 1 specimens after failure, back side

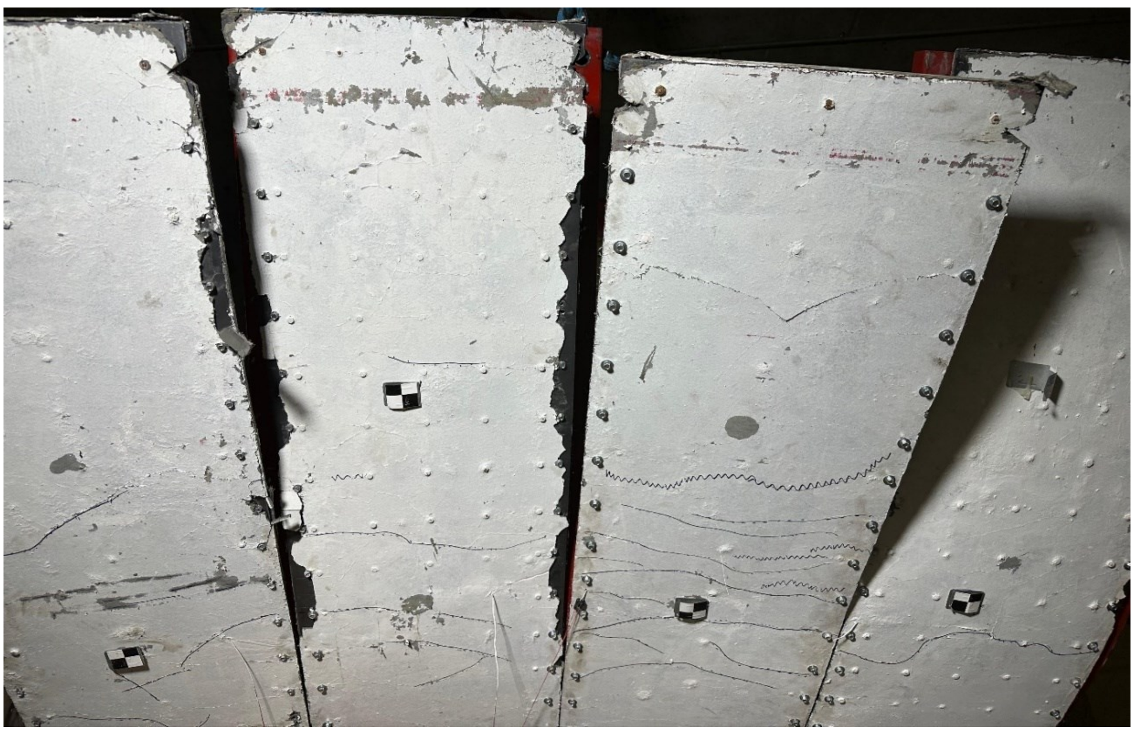

Figure 68: Set 1 specimens after failure, front side

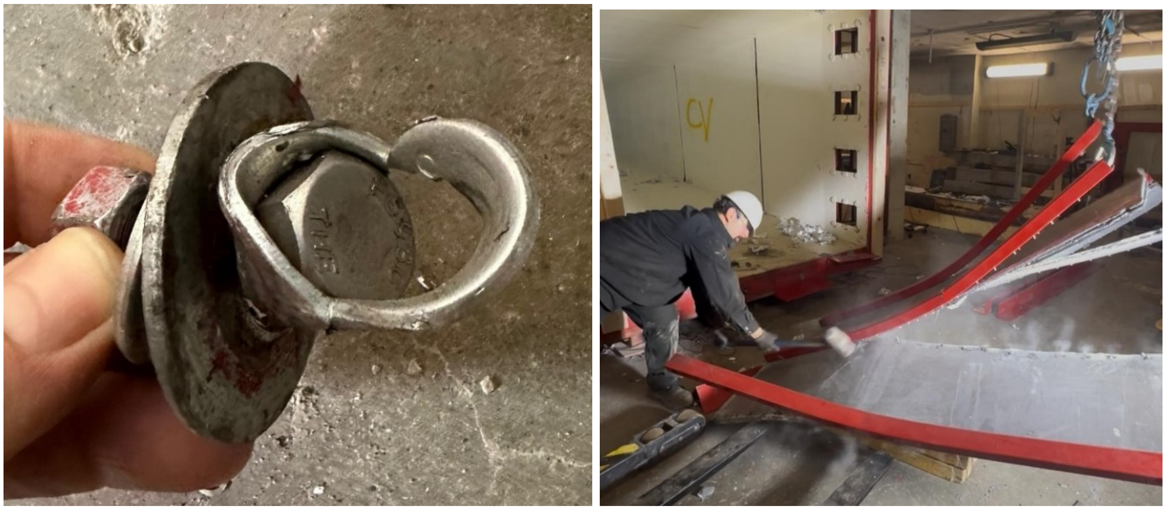

Figure 69: Set 1 specimens after failure, failed bolt (left), demolition (right)

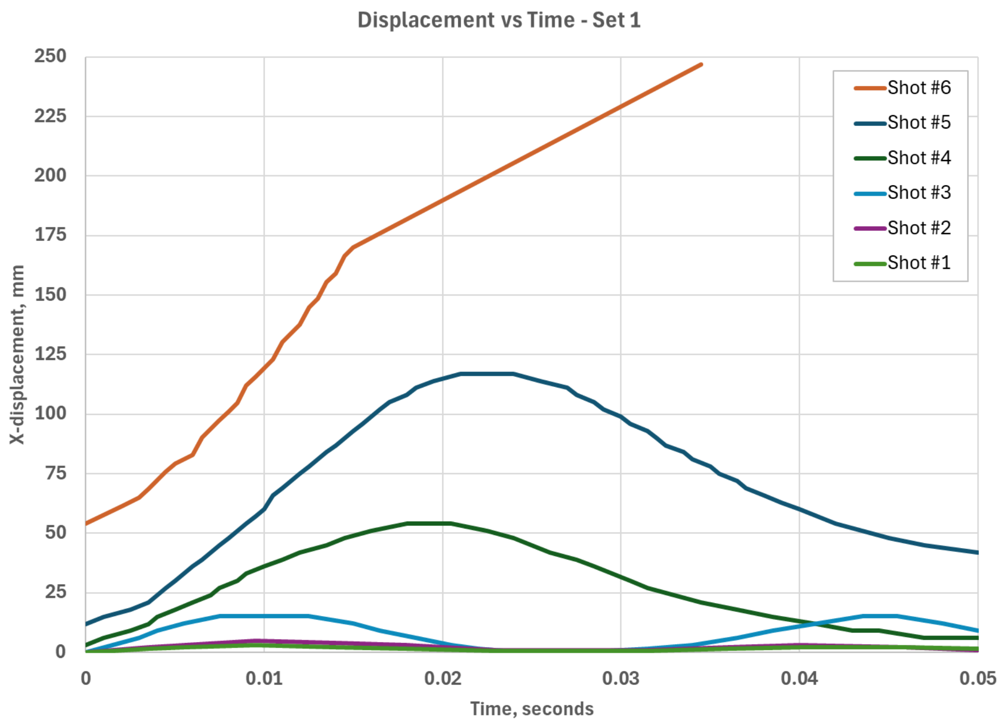

Figure 70: Displacement vs Time graph showing all shots of Set 1 specimens

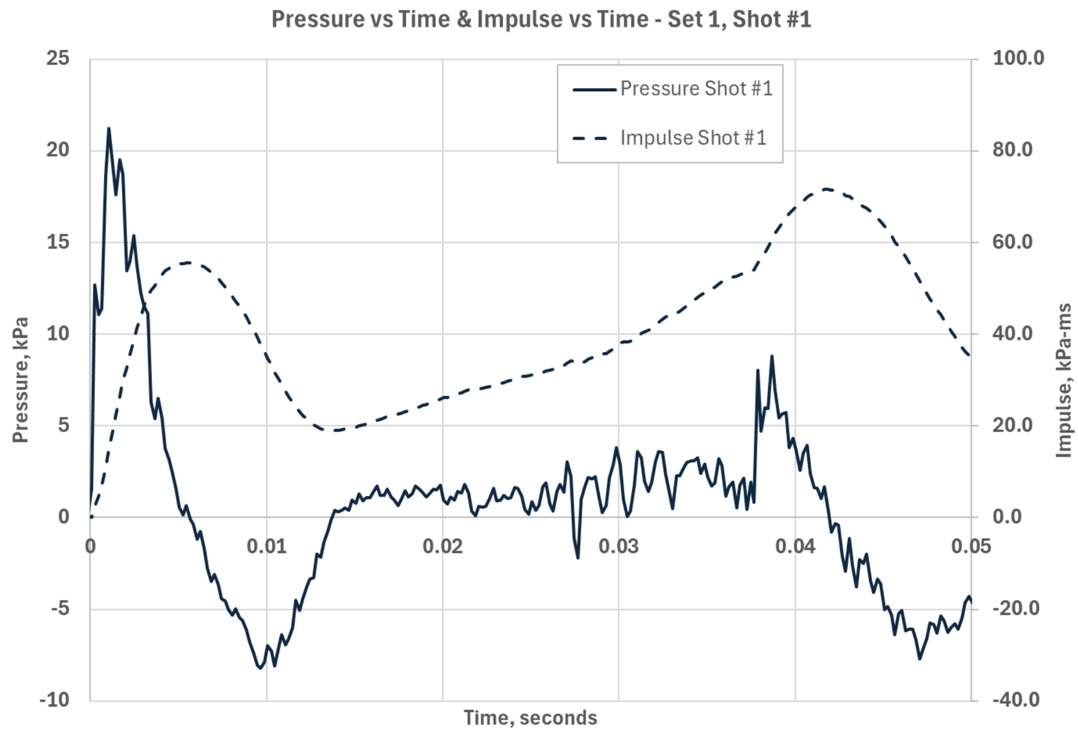

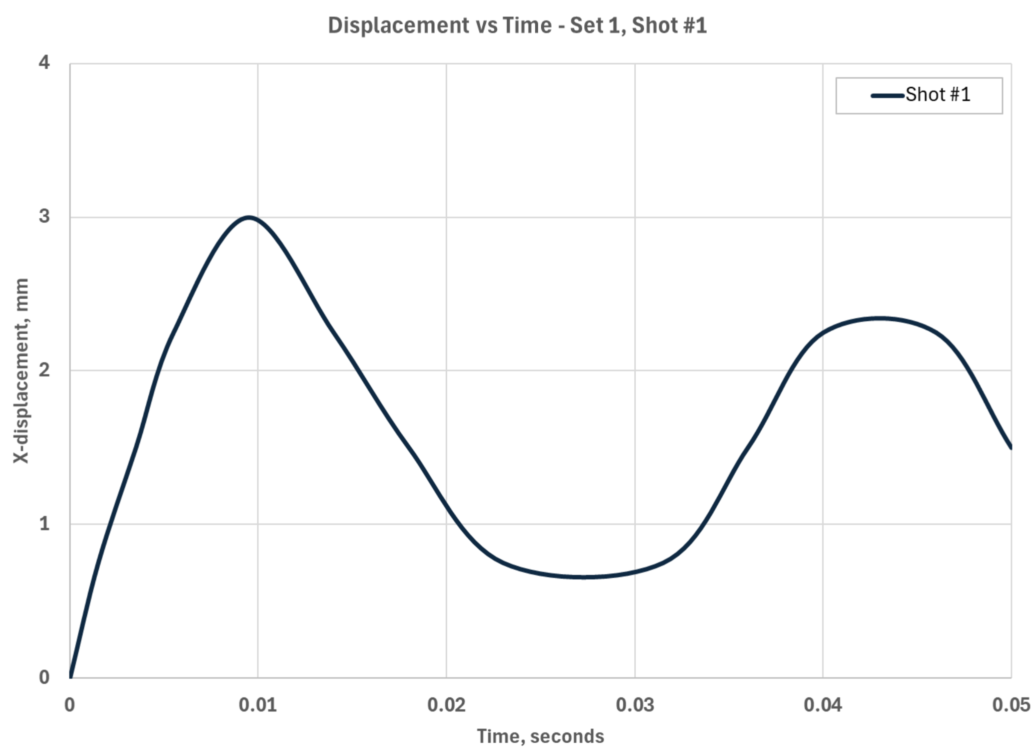

Figure 71: Pressure, Impulse and Displacement vs Time chart for set 1 - shot #1 – 21 kPa & 56 kPa-ms, 13.3 m/kg$^{1/3}$

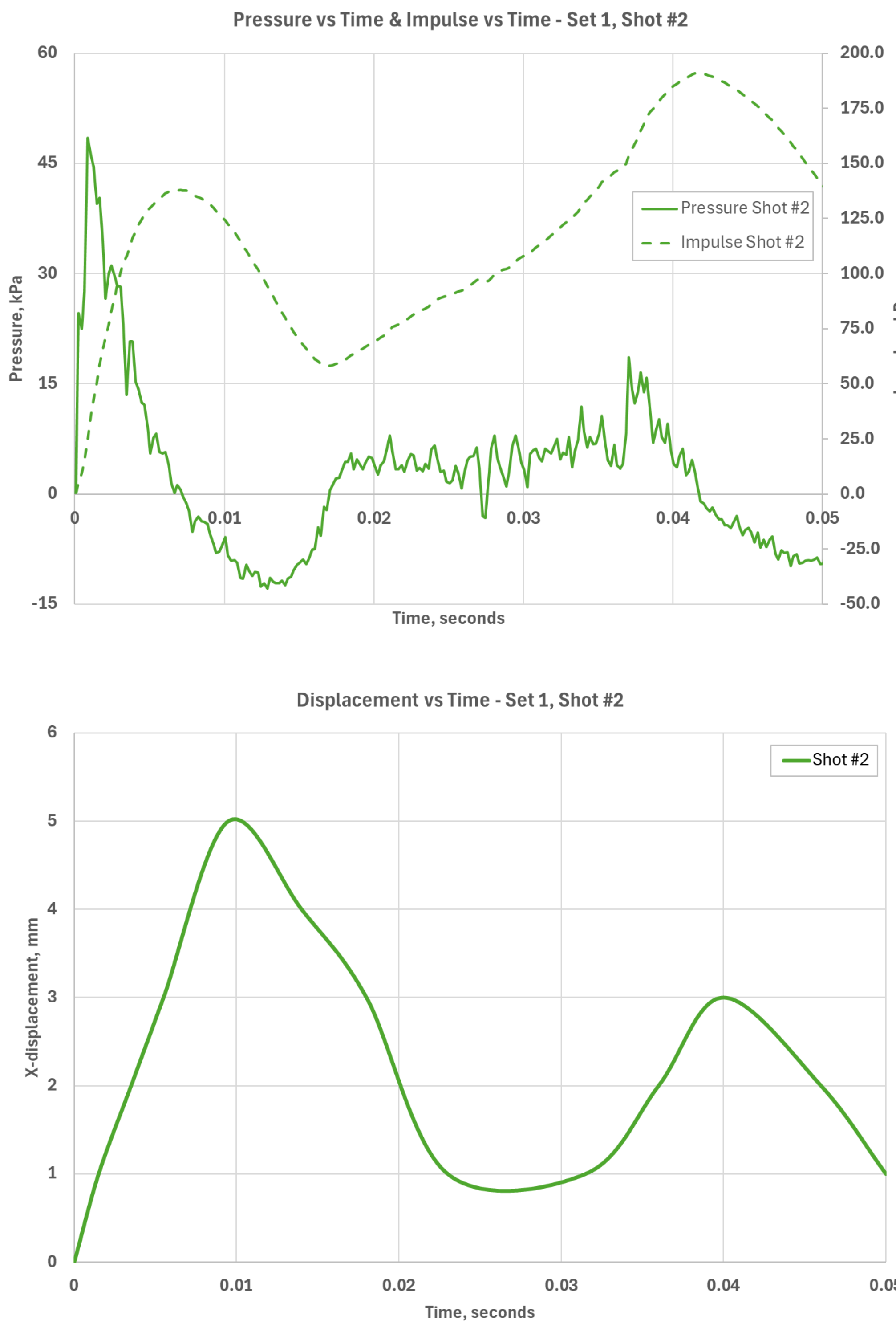

Figure 72: Pressure, Impulse and Displacement vs Time chart for set 1 - shot #2 – 48 kPa & 138 kPa-ms, 7.5 m/kg$^{1/3}$

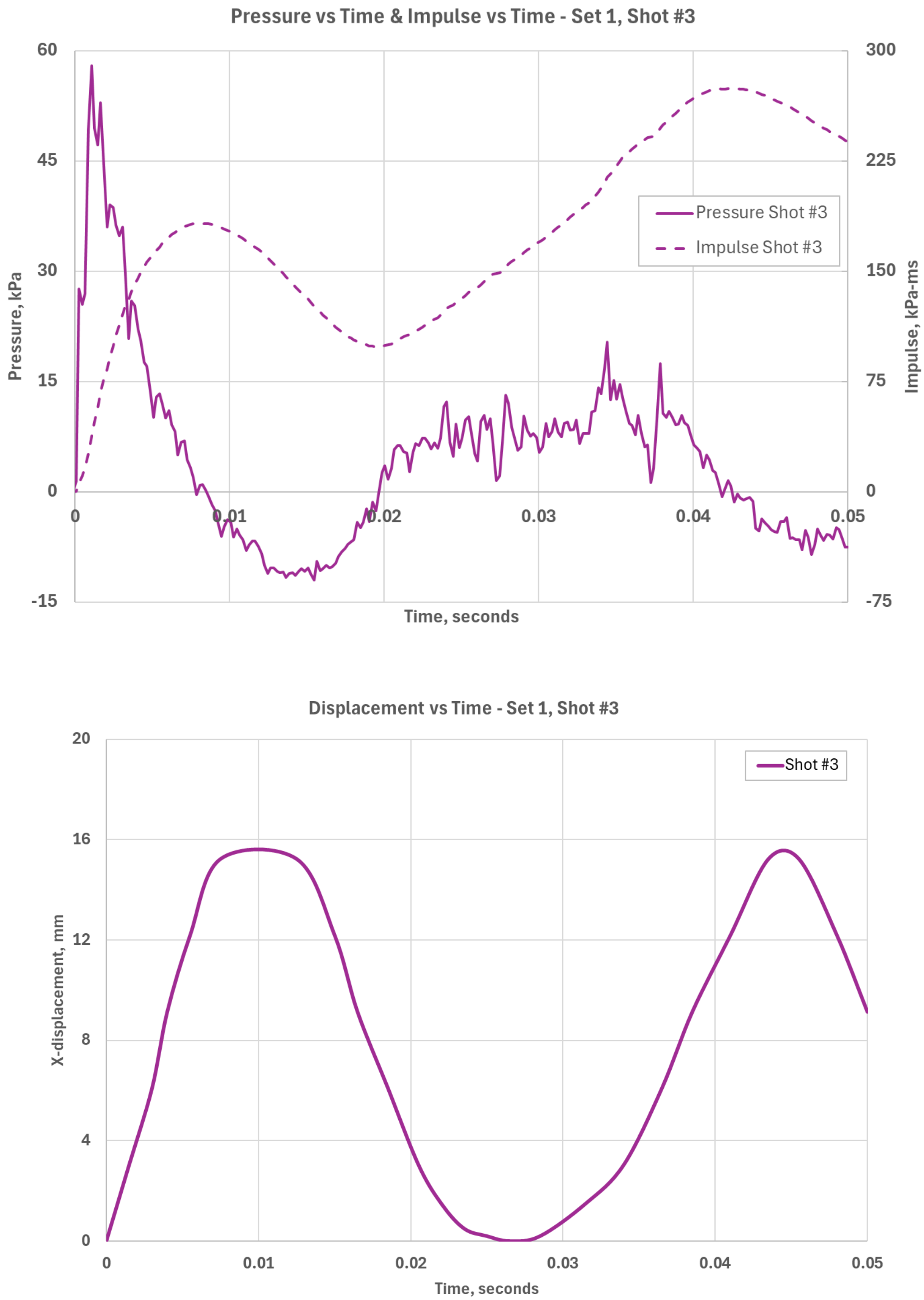

Figure 73: Pressure, Impulse and Displacement vs Time chart for set 1 - shot #3 – 58 kPa & 183 kPa-ms, 6.7 m/kg$^{1/3}$

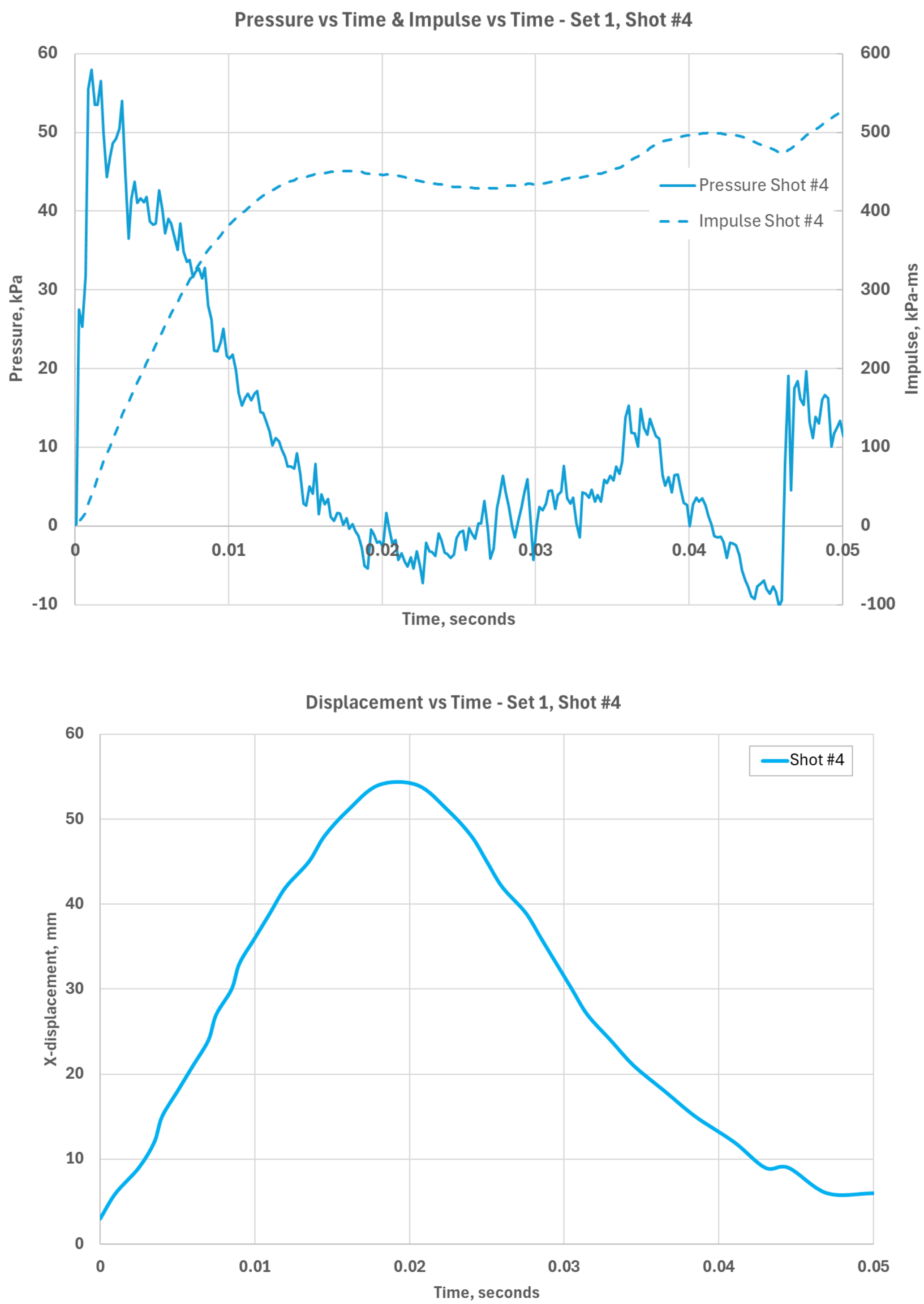

Figure 74: Pressure, Impulse and Displacement vs Time chart for set 1 - shot #4 – 58 kPa & 455 kPa-ms, 6.7 m/kg$^{1/3}$

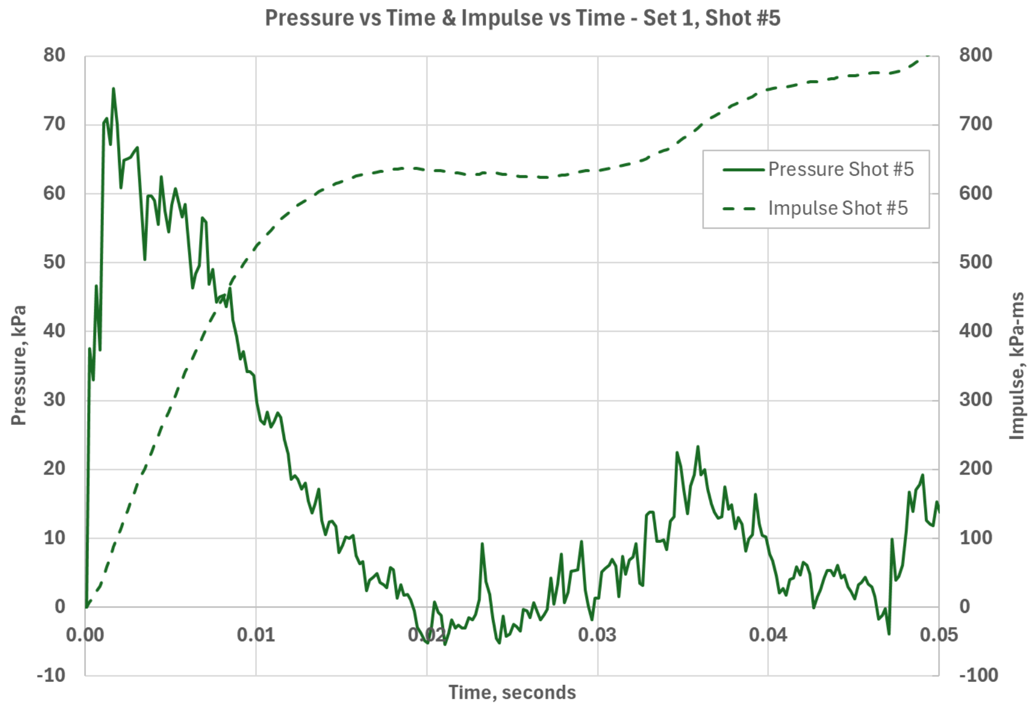

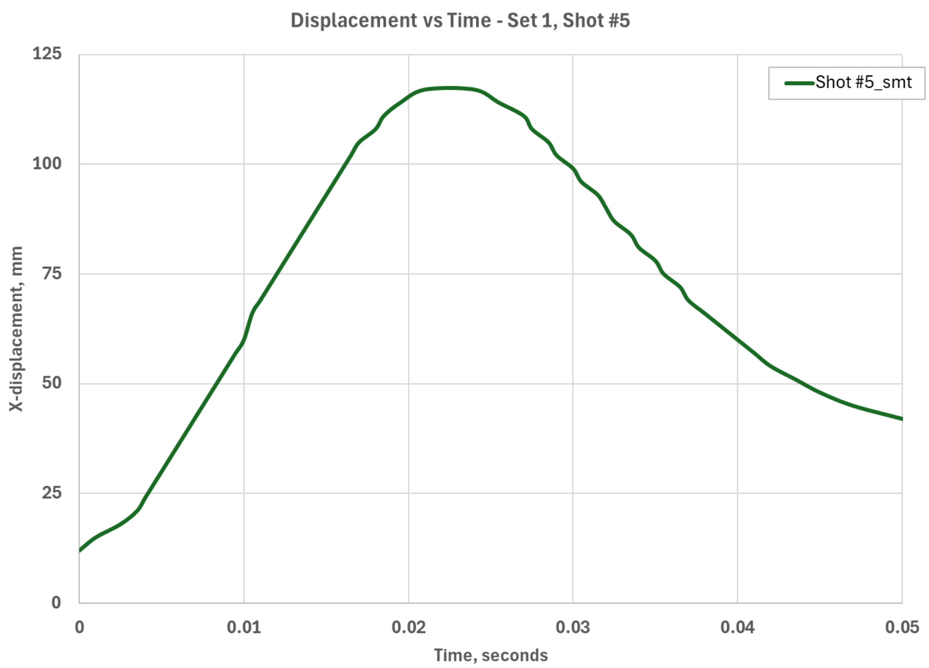

Figure 75: Pressure, Impulse and Displacement vs Time chart for set 1 - shot #5 – 76 kPa & 648 kPa-ms, 5.7 kg/m$^{1/3}$

3.5.2 Second Set of Specimens

The second set of specimens was subjected to three shots (**Table 5**), the third of which corresponded to a TNT charge weight of 1417 kg detonated at 60 metres (shot #3 = 85 kPa & 1048 kPa-ms, Scaled distance = 5.4 m/kg$^{1/3}$).

The dominant behaviour of this set of specimens was tension membrane. Due to being supported only at the top and bottom, and not at the sides, this tension membrane behaviour was similar to that of a cable under distributed load. Cables under a uniformly distributed load assume the shape of a catenary. The details of this catenary behaviour are discussed further in the analytical study chapter, where a single degree of freedom approach is used to predict the behaviour of the panels under blast loads.

The resistance provided by the tension catenary action is dependent on the out-of-plane deflection of the panel. As the deflection increases, the total length of the cable must also increase. Hence, the combined axial stiffness of ECC and steel in tension resists the deflection. The value of this tension force is calculated to be approximately 400 kN when both steel and ECC reach their yield stresses. This level of force is sufficient to cause movement at the supports through the bending of steel bolts and angles. For each shot of the second set of specimens, these support movements were observed. The movement of the support angle with respect to a reference point is shown in **Figure 76**. In this figure, the left image shows the support before the test, while the right image shows the support when the out-of-plane displacement of the panel was maximum.

Figure 76: Set 2 Specimens - movement of support angle during the 3rd Shot

It is important to note that the flexural stiffness of these panels is two orders of magnitude less than the stiffness provided by the tension membrane action. This is mainly due to the relatively small thickness of the specimens (15 mm) compared to the span (2000 mm). With a span to depth ratio of 133, the panels are well beyond the usual limits of flexural design using steel and concrete, which are approximately 20 and 10. Hence, for this set of specimens, the resistance provided by flexural behaviour is relatively small compared to the resistance provided by the tension catenary action. Therefore, the behaviour is considered tension-controlled.

In the third shot of this set of specimens, delamination of the front layer of ECC from the steel sheet was observed in panels 2 and 4 (panel type 1b), which had a connector spacing of 200 mm. The fragments from these specimens were disconnected from the main body of the panels with very high velocities and hit the wall across the shock tube (**Figure 77**). On the other hand, panel 1 (type 1a) did not have any fragmentation, while panel 3 had a single fragment with no horizontal residual velocity. That single fragment fell vertically without any horizontal movement. It is presumed that the difference between panels 1 and 3 (limited damage) and panels 2 and 4 (significant damage) is due to connector spacing. Based on the experimental results, it is evident that 100 mm spacing, which corresponds to 5% of the span, provided adequate composite behaviour.

The maximum and additional displacement observed at the midspan were measured as 369 mm and 309 mm, respectively, for the third shot. This significant displacement capacity is an indication of the ductility of the ECC-steel-ECC composite panels. A notable achievement of this set of specimens is that, despite being only 15 mm thick, panels 1 and 3 had mostly retained their integrity and would have provided sufficient protection against blast pressures and fragmentation.

Table 5: Blast load details for the second set of specimens

	Shot #1	**Shot #2**	**Shot #3**
Peak Pressure, kPa	30	60	85
Impulse, kPa-ms	324	668	1048
Maximum Deformation, mm	183	321	369
Residual Deformation, mm	57	60	-
Additional Deformation, mm	-	264	309
Equivalent Charge Weight (kg) and Distance (m)	305 kg, 69 m	677 kg, 57 m	1417 kg, 60 m
Scaled distance (m/kg$^{1/3}$)	10.3	6.5	5.4

Figure 77: Set 2 shot #3 fragmentation at panels 2 and 4 (left), 309 mm additional deformation (right)

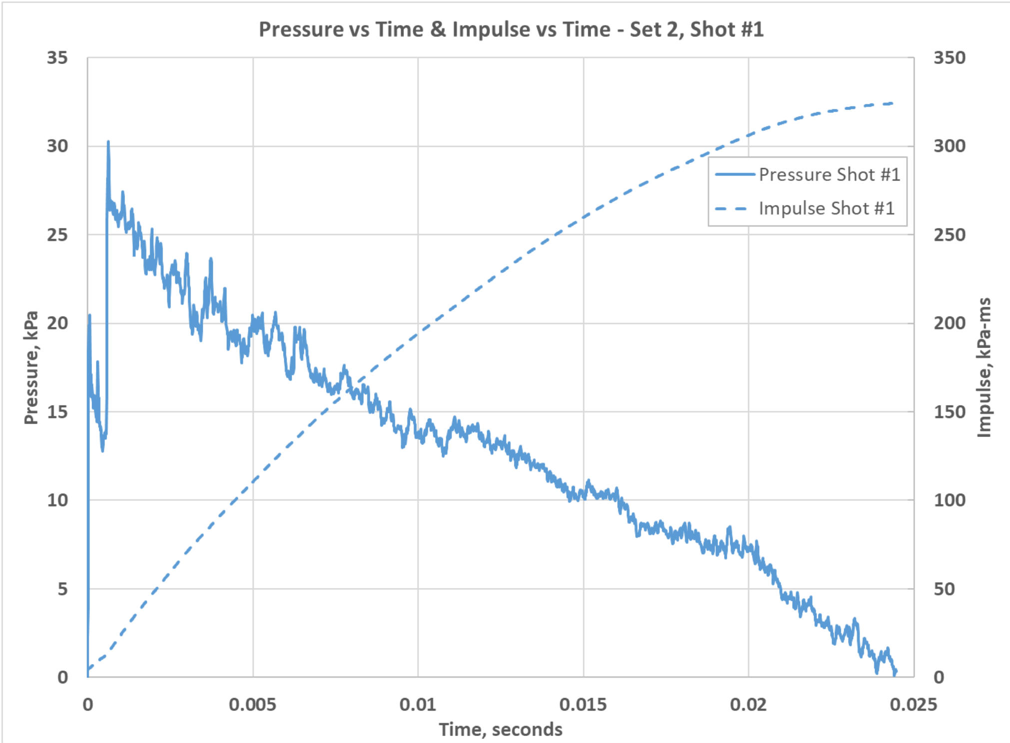

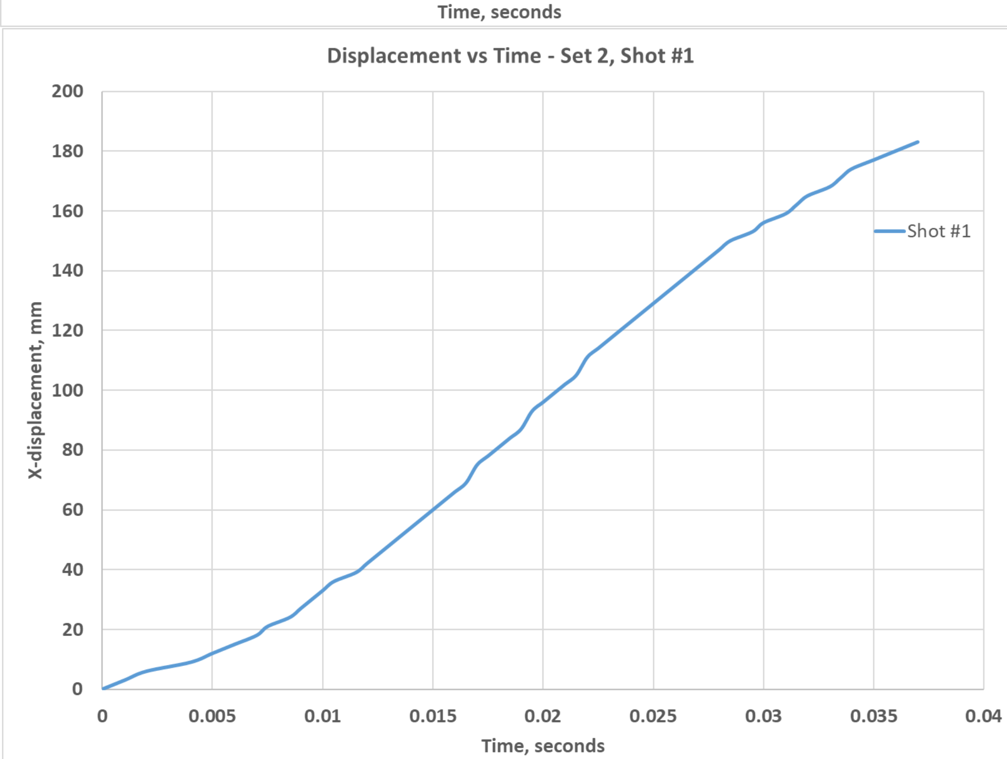

Figure 78: Pressure, Impulse and Displacement vs Time chart for set 2 - shot #1 – 30 kPa & 324 kPa-ms, 10.3 m/kg$^{1/3}$

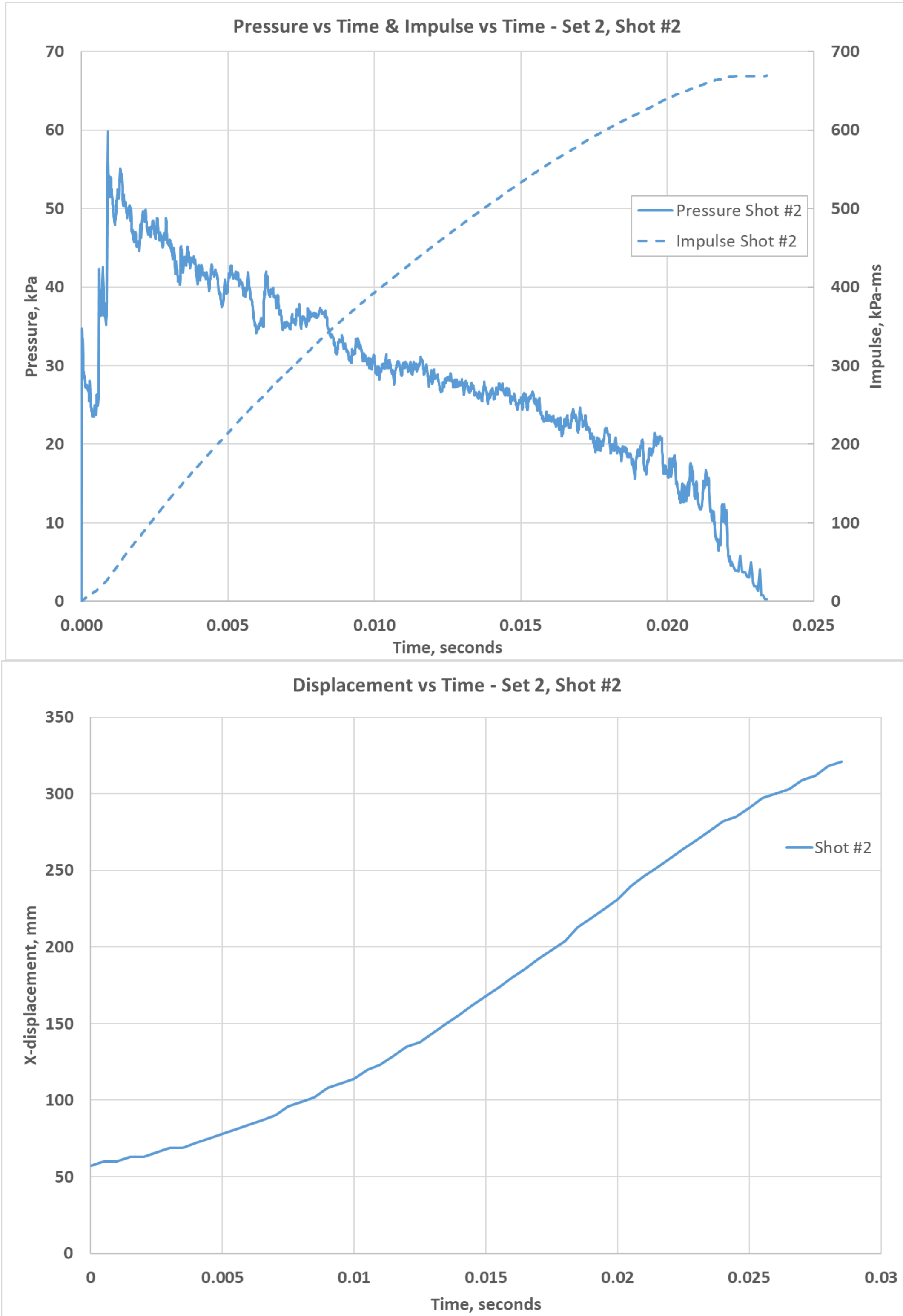

Figure 79: Pressure, Impulse and Displacement vs Time chart for set 2 - shot #2 – 60 kPa & 668 kPa-ms, 6.5 m/kg$^{1/3}$

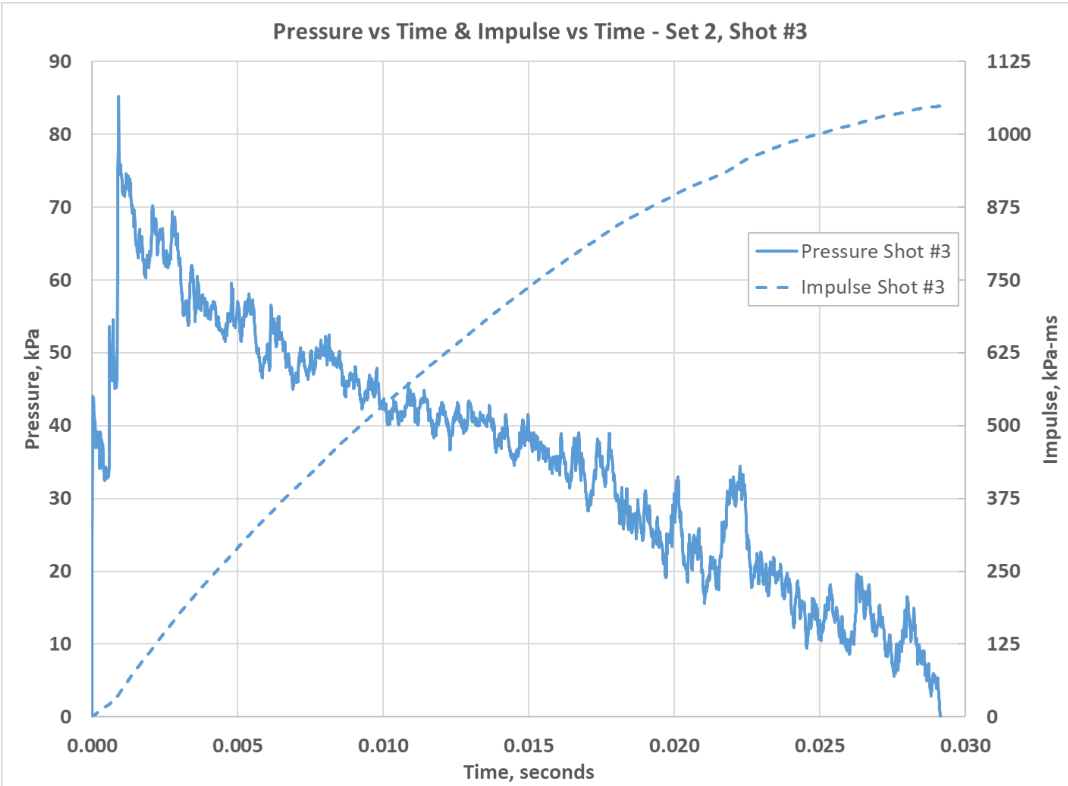

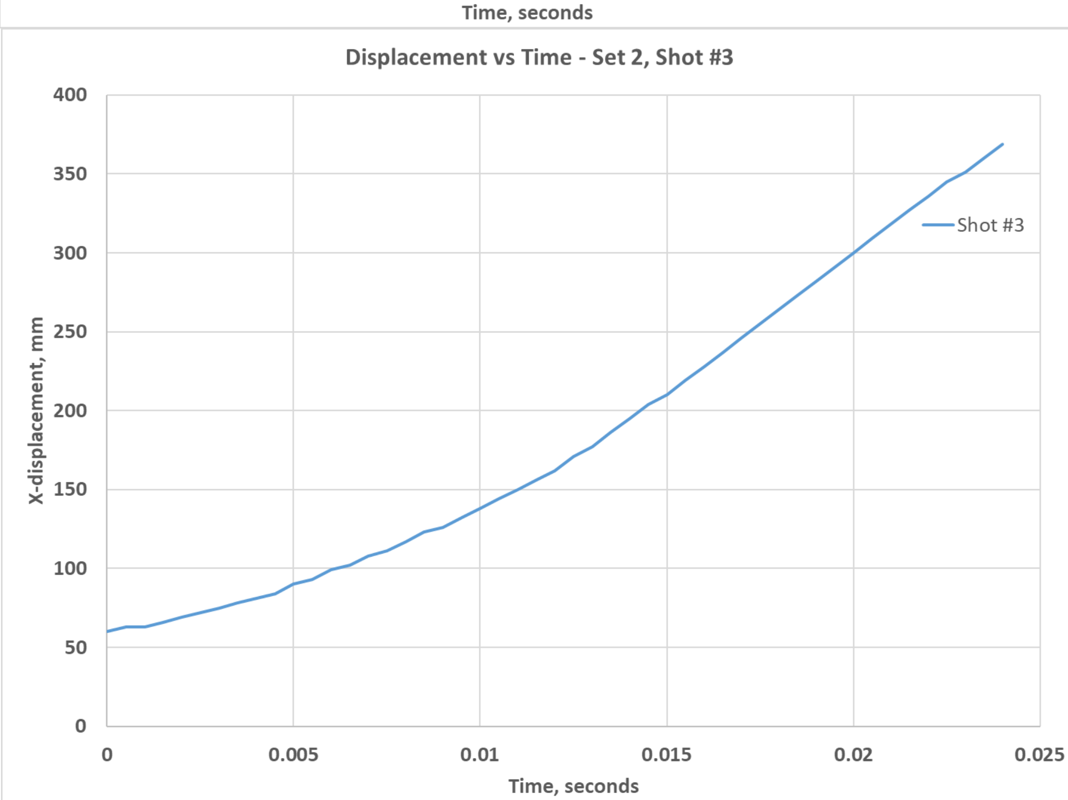

Figure 80: Pressure, Impulse and Displacement vs Time chart for set 2 - shot #3 – 85 kPa & 1048 kPa-ms, 5.4 m/kg$^{1/3}$

3.5.3 Third Set of Specimens

The third set of specimens, which utilized 1.5 mm thick steel sheets, was subjected to two shots (shot #2 = 63 kPa & 577 kPa-ms) before fragmentation failure occurred. This blast corresponded to a charge weight of 398 kg of TNT detonated at a standoff distance of 47 metres and a scaled distance of 6.4 m/kg$^{1/3}$.

After the first shot (35 kPa & 320 kPa-ms, Z = 9.2 m/kg$^{1/3}$), significant cracking was observed in panels 2 and 4 (type 2b), along with rupture and delamination, but the specimens were intact without any fragmentation. Cracks along the horizontal direction were also observed in panels 1 and 3, without delamination or rupture. This lack of delamination in panels with 100 mm connector spacing was in alignment with the observation of the second set of specimens.

Following the second and final shot (shot #2 = 63 kPa & 577 kPa-ms, Z = 6.4 m/kg$^{1/3}$), panel 1 (type 2a with 100 mm connector spacing) retained its integrity and did not experience any delamination or fragmentation. However, panel 3, which had the same connector spacing, failed due to fragmentation of the ECC layer facing the protected side. This difference in performance could be due to the fact that edge specimens allow some of the shockwave to dissipate from the free edge (wrap-around effect). The interior specimens did not experience a similar dissipation and therefore experienced a more intense shock.

Panels 2 and 4 (type 2b with 200 mm connector spacing) had already experienced rupture and delamination after the first shot. As expected, both of these specimens failed due to the fragmentation of the ECC layer that had already been delaminated. The ECC fragments detached from the panels had various velocities, with the highest measured velocity being 7 metres per second, whereas other fragments had negligible horizontal velocity and fell vertically. The front and side views of the third set of specimens during the second shot are shown below in **Figure 81**.

As expected, panels with 1.5 mm thick steel plates had lower resistance compared to the specimens with 3 mm thick steel plates due to the lower strength provided by the steel. It is important to note that these panels experienced higher deformation values compared to the panels with 3 mm thick plates. The maximum deformation observed in the second shot of was 414 mm, whereas for the second shot of the second set of specimens, the maximum displacement was 321 mm. The pressure, impulse, and displacement time history graphs for both are shown in **Figure 82** and **Figure 83**.

Table 6: Blast load details for the third set of specimens

	Shot #1	**Shot #2**
Peak Pressure, kPa	35	63
Impulse, kPa-ms	320	577
Maximum Deformation, mm	300	414
Residual Deformation, mm	186	-
Additional Deformation, mm	-	228
Equivalent Charge Weight (kg) and Distance (m)	214 kg, 55 m	398 kg, 47 m
Scaled Distance (m / kg$^{1/3}$)	9.2	6.4

Figure 81: Set 3 shot #2 fragmentation at panels 2, 3 and 4 (left), 414 mm maximum deformation (right)

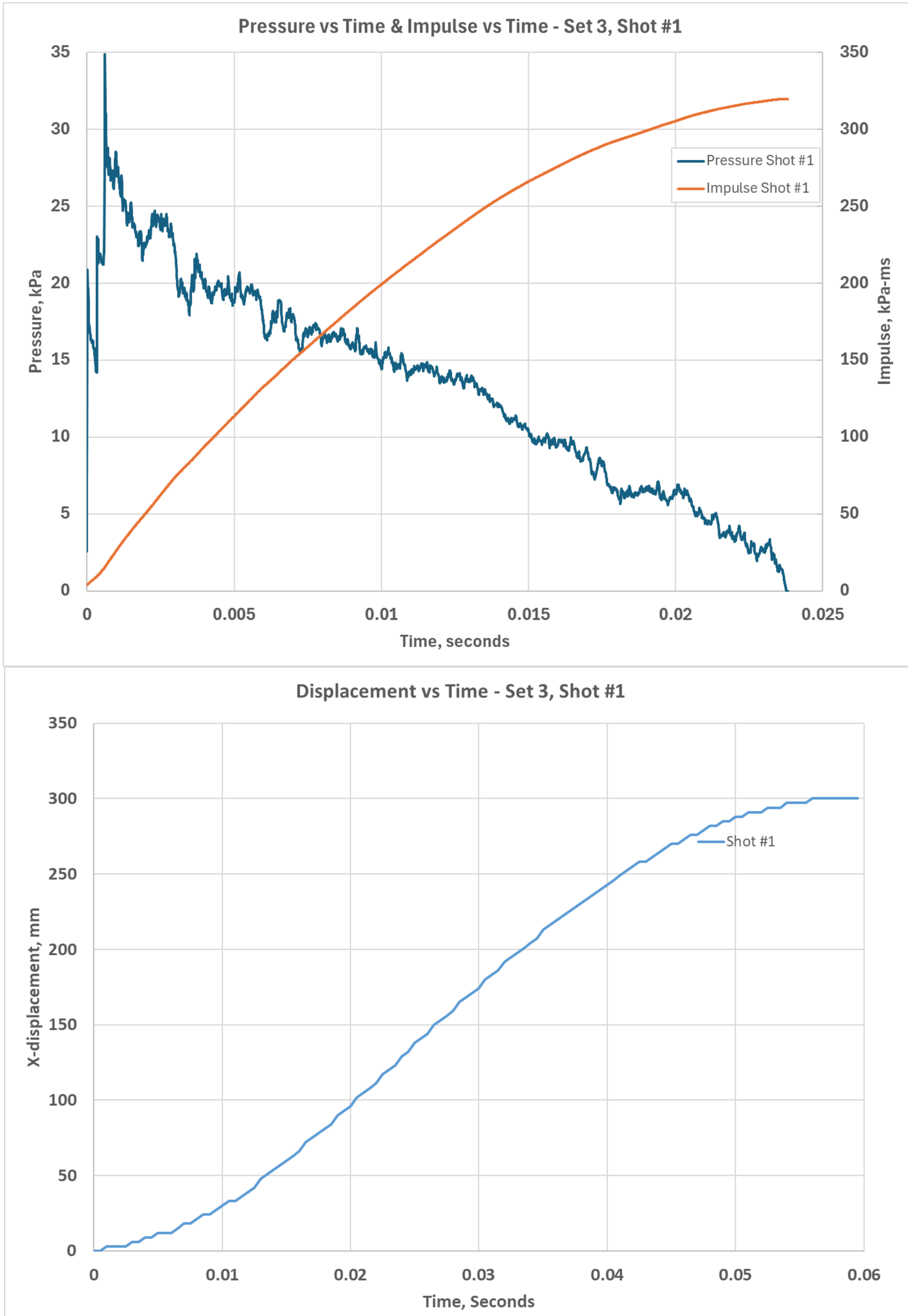

Figure 82: Pressure, Impulse and Displacement vs Time chart for set 3 - shot #1 – 35 kPa & 320 kPa-ms, 9.2 m/kg$^{1/3}$

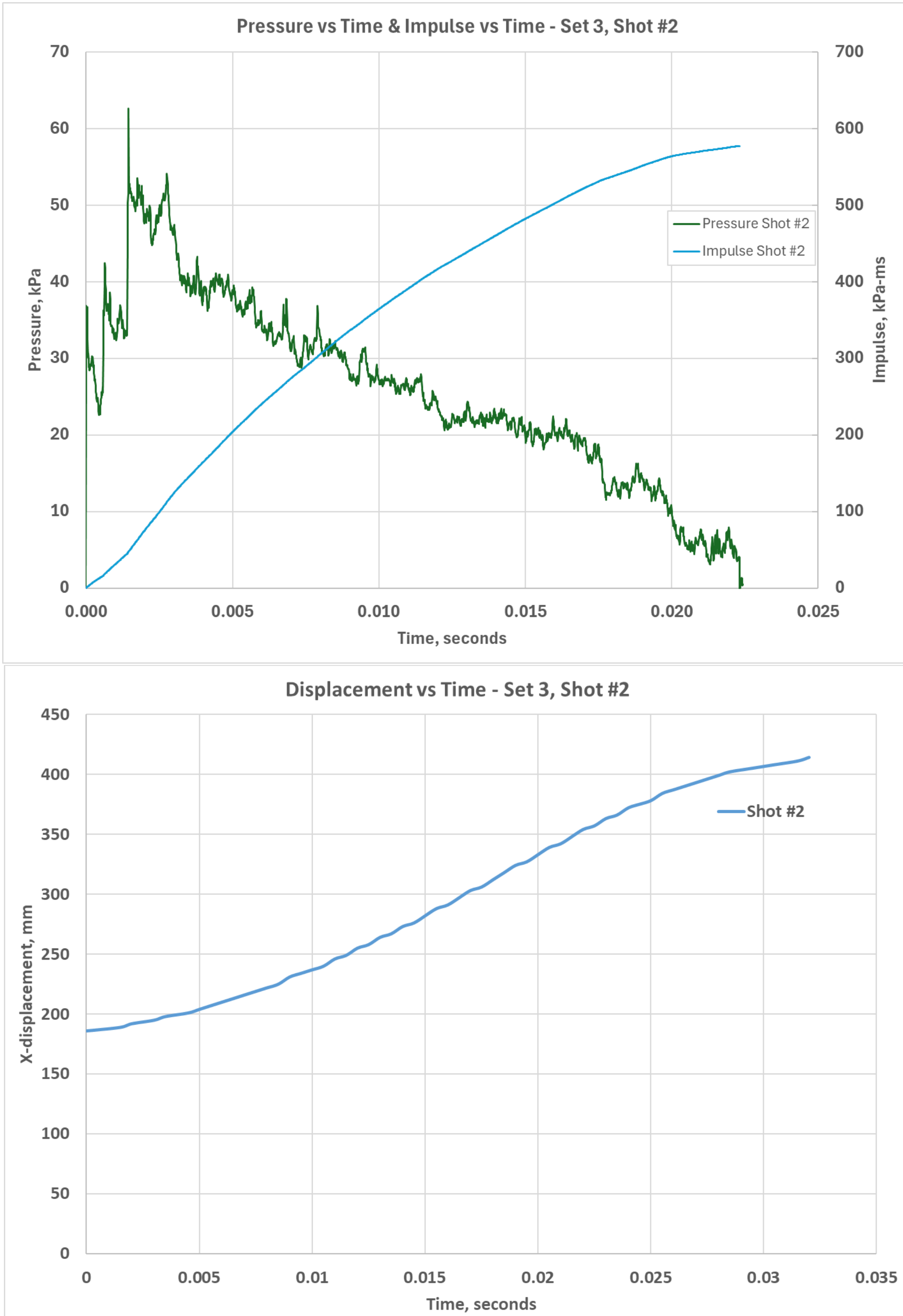

Figure 83: Pressure, Impulse and Displacement vs Time chart for set 3 - shot #2 – 63 kPa & 577 kPa-ms, 6.4 m/kg$^{1/3}$

3.5.4 Fourth Set of Specimens

The fourth set of specimens was subjected to three shots (Shot #3, 86 kPa and 1139 kPa-ms). This pressure and impulse combination corresponded to a TNT charge weight of 1787 kg detonated at 65 metres, and a scaled distance of 5.3 m/kg$^{1/3}$. The pressure, impulse and displacement time history graphs for all three shots are shown in **Figure 86** to **Figure** 88.

This set of specimens was unique because there were HSS members on both sides of the ECC-steel-ECC panels. The additional flexural rigidity provided by the HSS members increased the flexural stiffness of the overall system, and the observed behaviour was flexural dominant. Failure was observed in the HSS members as plastic hinges at the mid-span and at the through-bolt connectors that connected both HSS members at the panels. Although horizontal cracks were observed at the ECC layer on the front side, delamination of the ECC-steel-ECC layers was not evident. Although the HSS members failed in flexure, the ECC layers exhibited residual capacity.

The permanent deformation in panels 2 and 3 (the interior panels) and the HSS members connected to them was significantly greater than the permanent deformation in panels 1 and 4 (exterior panels), as shown in **Figure 84**. This is due to the fact that the HSS members on the exterior side of the exterior panels had a smaller tributary area than the HSS members at the interior. Due to the increased flexural stiffness of the double HSS members and the overall flexural dominant behaviour, this difference in tributary area had a more pronounced effect than previously tested specimens. The failure of the threaded rods was notable in these specimens. The shear flow resisted by the rods was maximum at the support locations, and their failure was observed near the supports. The threaded rods that failed by tension rupture or by thread failure are shown in **Figure 85**.

Table 7: Blast load details for the fourth set of specimens

	Shot #1	Shot #2	Shot #3
Peak Pressure, kPa	36	62	86
Impulse, kPa-ms	402	714	1139
Maximum Deformation, mm	30	68	211
Residual Deformation, mm	5	33	127
Additional Deformation, mm	-	63	178
Equivalent Charge Weight (kg) and Distance (m)	399 kg, 67 m	777 kg, 59 m	1787 kg, 65 m
Scaled Distance (m / kg$^{1/3}$)	9.0	6.4	5.3

Figure 84: Set 4 specimens following shot #3

Figure 85: Threaded rods after failure

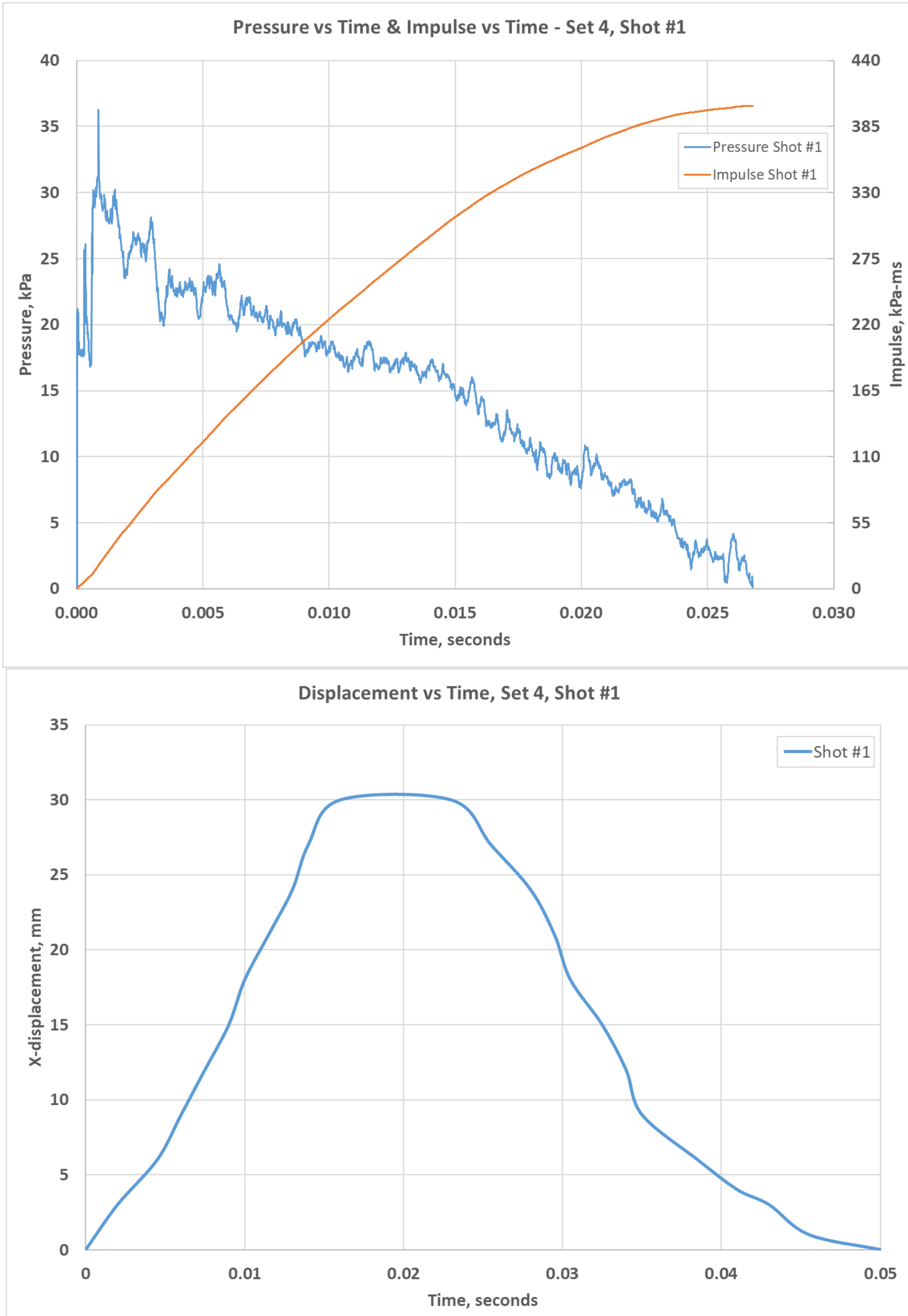

Figure 86: Pressure, Impulse and Displacement vs Time chart for set 4 - shot #1 – 36 kPa & 402 kPa-ms, 9.0 m/kg$^{1/3}$

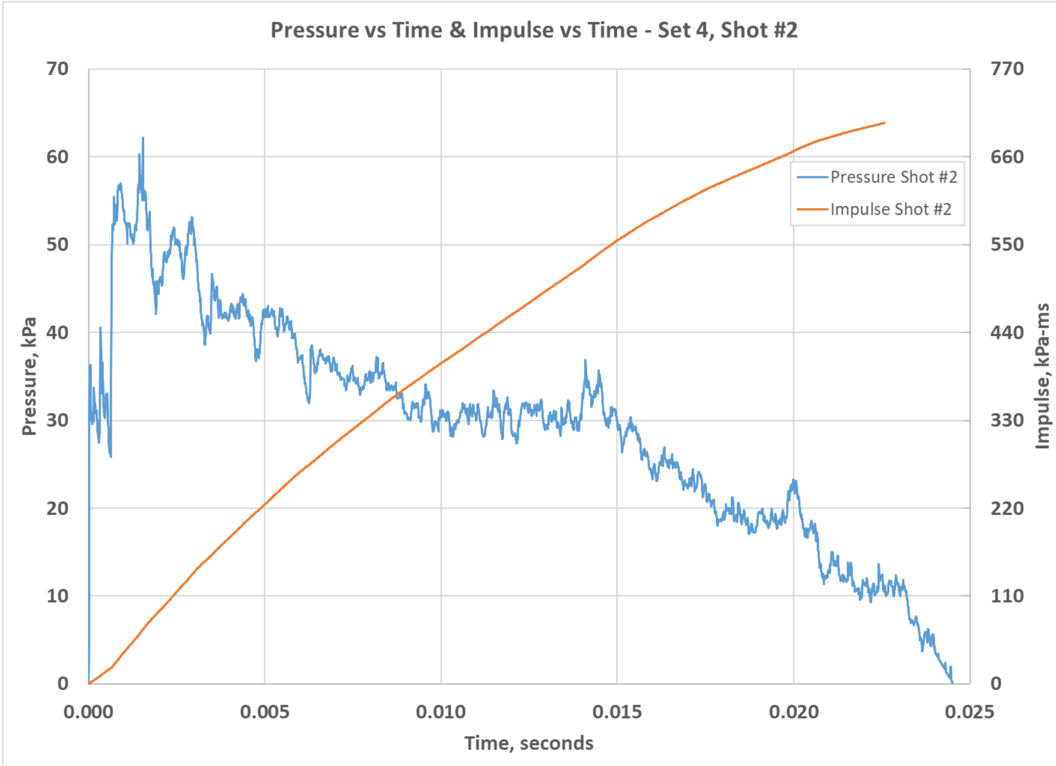

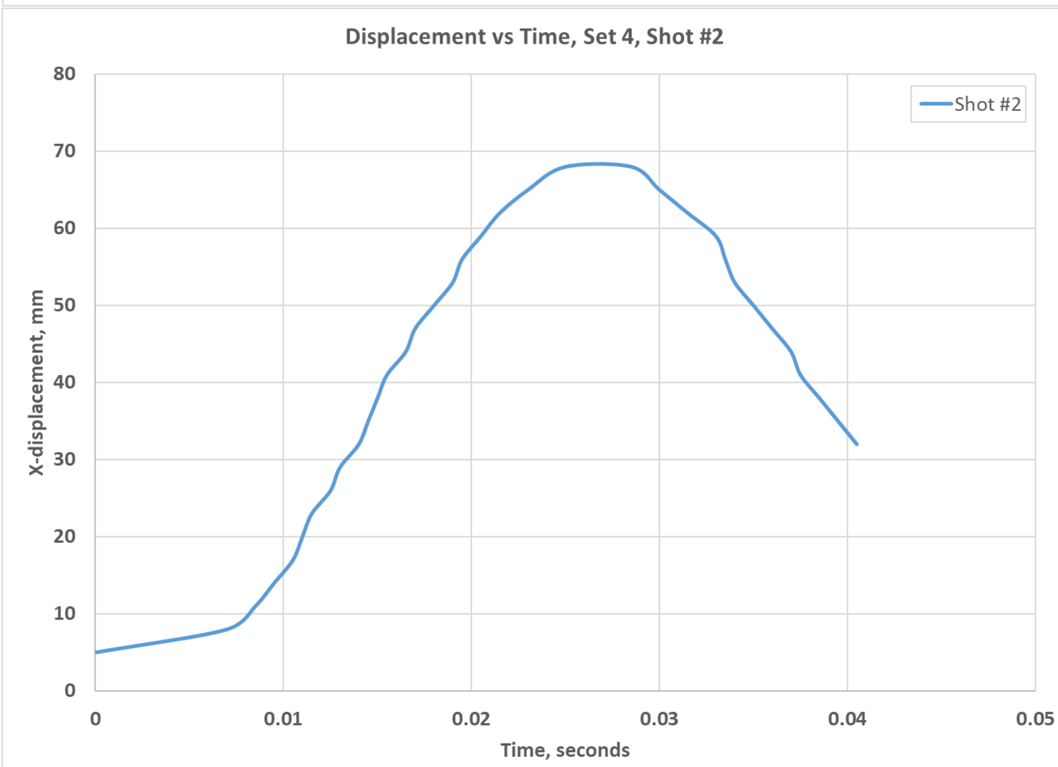

Figure 87: Pressure, Impulse and Displacement vs Time chart for set 4 - shot #2 – 62 kPa & 714 kPa-ms, 6.4 m/kg$^{1/3}$

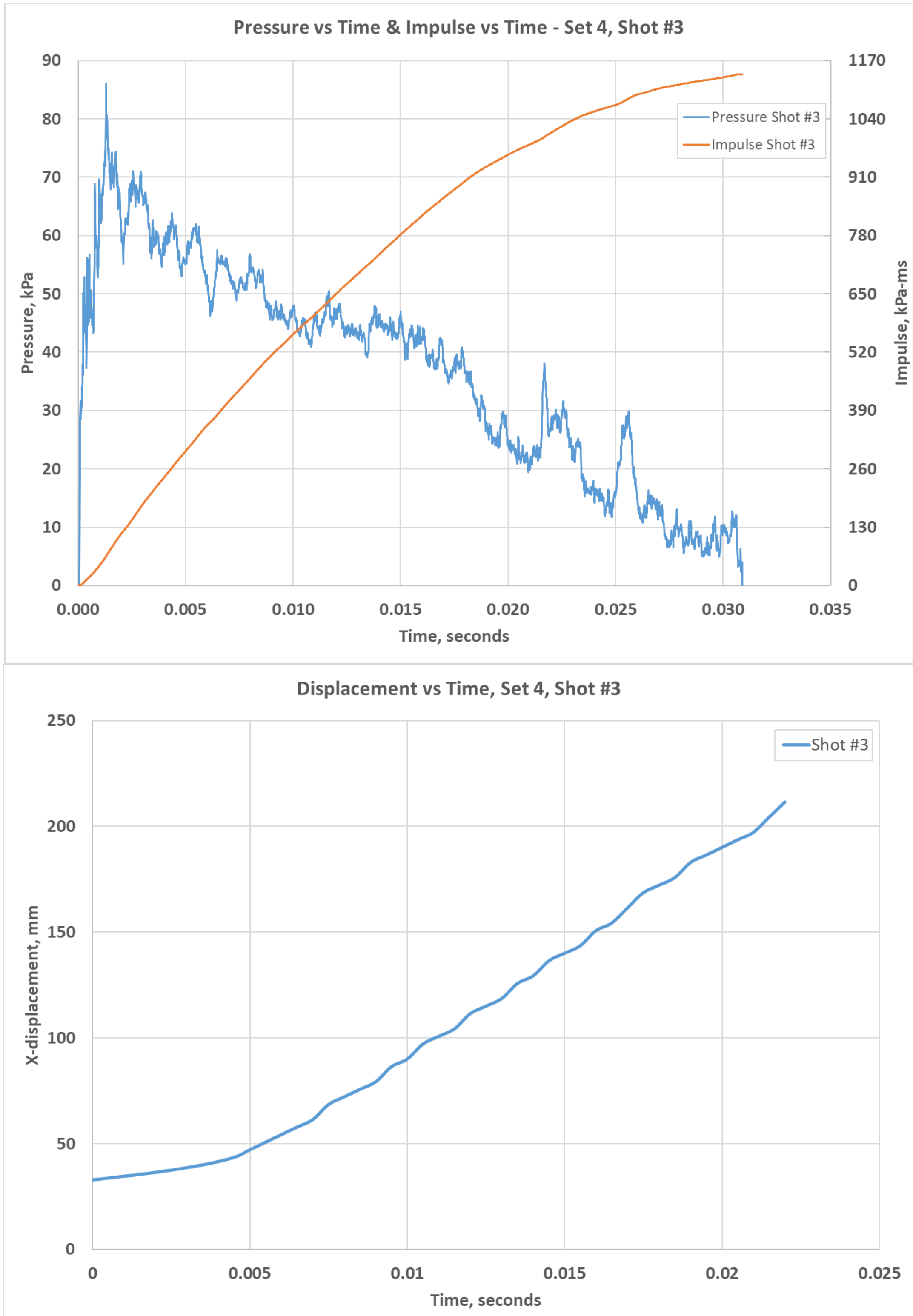

Figure 88: Pressure, Impulse and Displacement vs Time chart for set 4 - shot #3 – 86 kPa & 1139 kPa-ms, 5.3 m/kg$^{1/3}$

3.5.5 Fifth Set of Specimens

The fifth set of specimens was subjected to two shots. The second shot had a peak pressure of 62 kPa and a positive impulse of 495 kPa-ms, corresponding to a TNT charge weight of 244 kg, detonated at 40 metres, and a scaled distance of 6.4 m/kg$^{1/3}$. The failure mechanism was the buckling of the steel sheets.

The purpose of testing this set of specimens was to observe the resistance of steel sheets without the benefits of the ECC layers. The results of prior experiments had already demonstrated that panels could behave in a composite manner, providing additional mass, strength and stiffness. However, a valid follow-up question was whether the performance improvement provided by the ECC layers justified the extra effort and cost associated with them. The failure mode of this set of specimens provided valuable insights regarding the behaviour of steel sheets without the additional mass, strength and stiffness provided by the ECC layers.

Under blast loads, the steel sheets have predominantly experienced tension membrane behaviour and undergone permanent elongation and reached their maximum displacement. As the shockwave dissipated and the positive pressure phase ended, the steel sheets started to return to their undeflected state. However, due to the permanent elongation, the panels were now longer than the distance between the supports, which had remained constant. As a result, axial compression started to act on the steel sheets, which caused them to buckle due to their extreme slenderness. This buckling failure was only observed in this set and has not been observed in the other sets where ECC-steel-ECC panels were used. Therefore, it may be concluded that the ECC layers, in addition to providing strength and stiffness, also brace the steel sheets against out-of-plane buckling. The deflected state of set 5 after the second shot is shown in **Figure 89** below. The pressure, impulse, and displacement time history graphs for both shots are shown in **Figure 90** and **Figure 91**.

Table 8: Blast load details for the fifth set of specimens

	Shot #1	**Shot #2**
Peak Pressure, kPa	32	62
Impulse, kPa-ms	260	495
Maximum Deformation, mm	288	406
Residual Deformation, mm	10	87
Additional Deformation, mm	-	396
Equivalent Charge Weight (kg) and Distance (m)	138 kg, 51 m	244 kg, 40 m
Scaled Distance (m/kg$^{1/3}$)	9.8	6.4

Figure 89: Buckling of steel sheets after shot #2

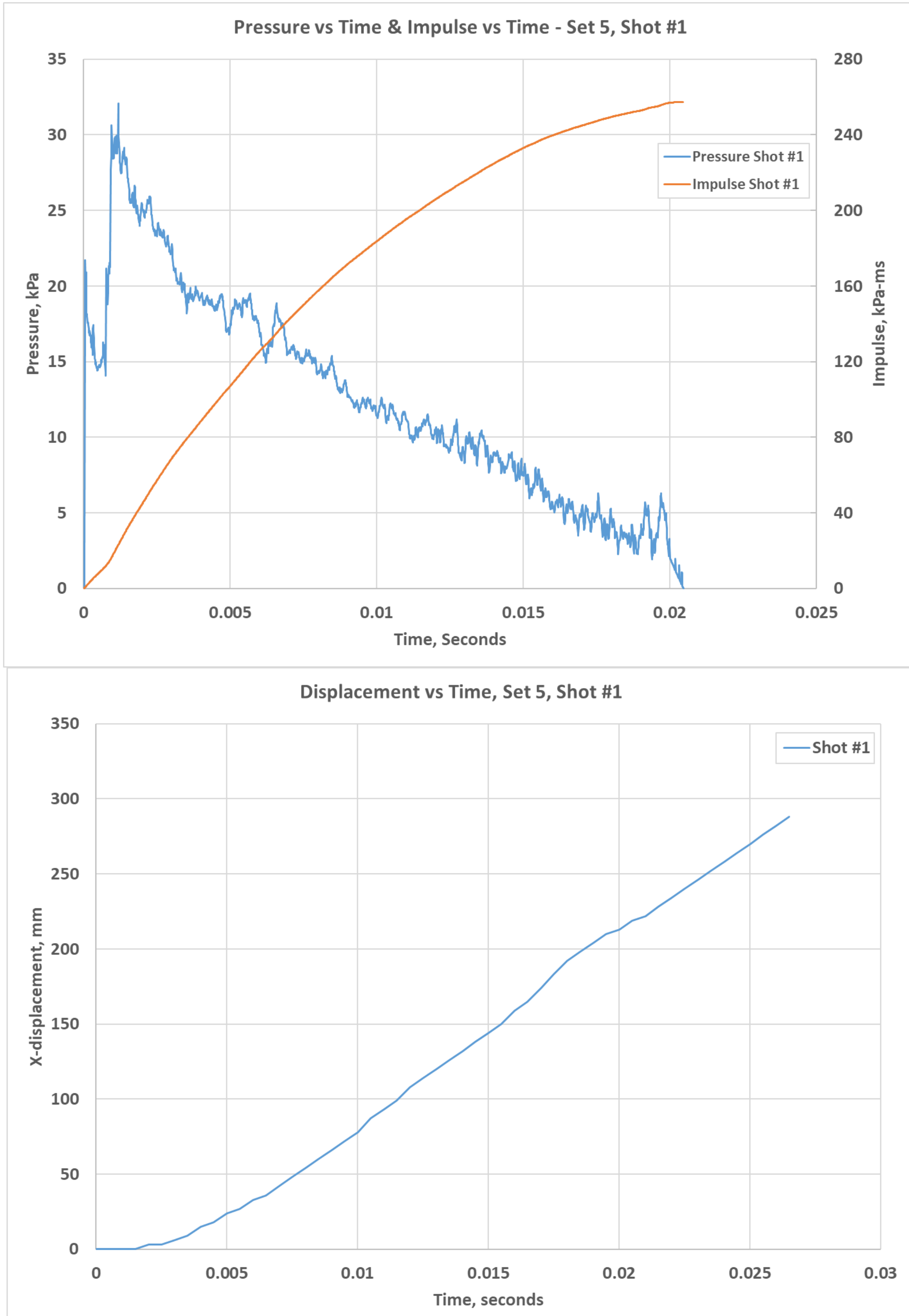

Figure 90: Pressure, Impulse and Displacement vs Time graph for set 5 - shot #1 – 32 kPa & 260 kPa-ms, 9.8 m/kg$^{1/3}$

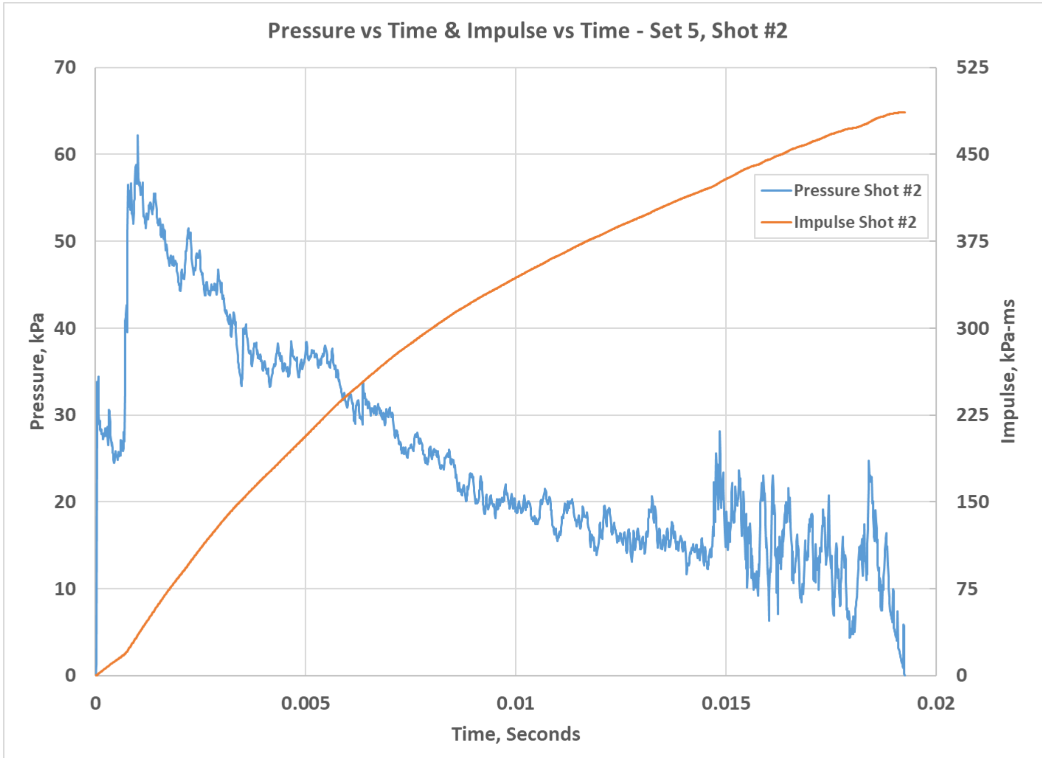

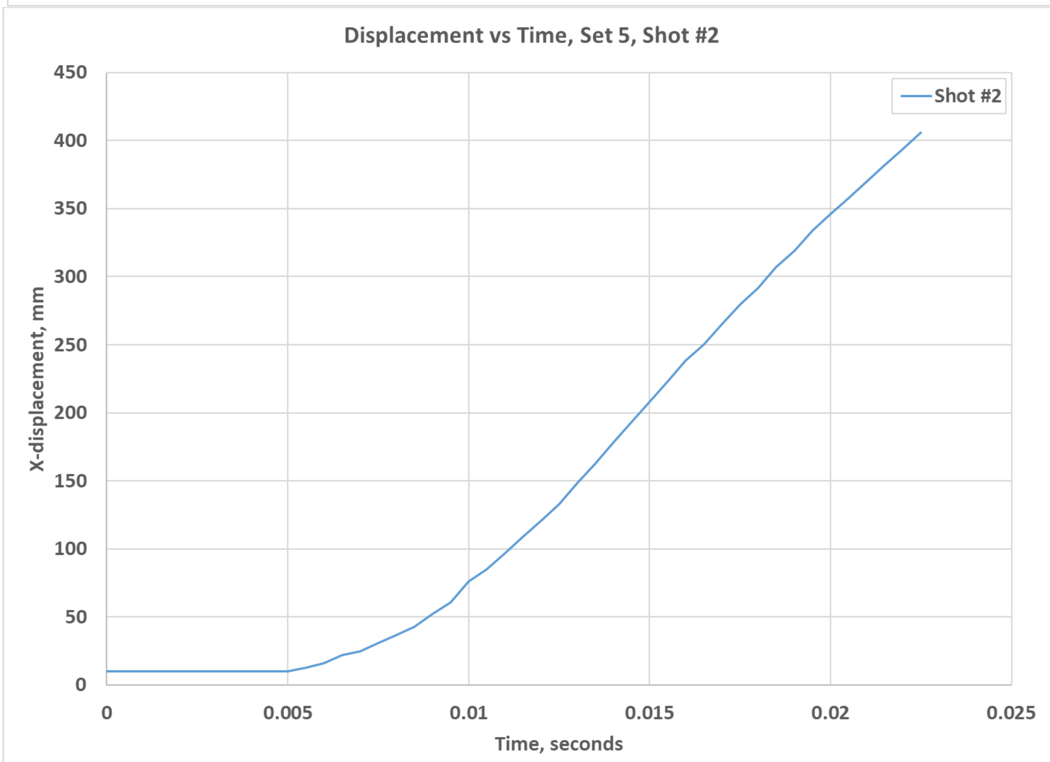

Figure 91: Pressure, Impulse and Displacement vs Time graph for set 5 - shot #2 – 62 kPa & 495 kPa-ms, 6.4 m/kg$^{1/3}$

Chapter 4. Analytical Investigation

This chapter presents the analytical phase of research. It consists of the finite element method (FEM) of analysis of the panels and the wall systems developed in the current investigation. The selection of the software and the constitutive models used in the analytical research is presented. FEM models constructed for the ECC coupons, test panels, and the wall systems are discussed. This is followed by the validation of the FEM models against the test data reported in Chapter 3. A parametric finite element investigation was performed to examine the effects of selected design parameters, and the results are presented. This task enabled controlled variation of the modelling and design parameters to expand the results obtained from the test panels and wall systems to a wider scope of application in engineering practice.

The final section of the chapter includes the use of a single degree of freedom (SDOF) approach for the analysis of the panels and walls with a view to exploring the possibility of its use as a design tool. This SDOF approach provides a relatively simple analysis methodology of the panels with different configurations and offers a strong potential for use as a sufficiently accurate design tool.

4.1 Finite Element Analysis

The finite element analysis of current research had two main components: verification of modelling parameters against the experimental results and a parametric study to expand the results of the experimental research by considering design parameters beyond those considered in the tests.

4.1.1 Selection of FEM Software and Background Information

The finite element analysis part of this research was performed using LS-Dyna **(LSTC, 2025b)**, software intended for analyzing the large deformation response of structures. This software was selected as it is considered an industry standard for blast load analysis, incorporating computational fluid dynamics (CFD) and FEM features. Developed as DYNA3D in the 1970s at the Lawrence Livermore National Laboratory, as of 2025, LS-Dyna is owned by ANSYS, Inc. Over the years, the capabilities of the software have evolved significantly to include four-node tetrahedron, eight-node solid, two-node beam, three and four-node shell, eight-node solid shell, truss, membrane, and discrete elements, as well as rigid bodies. Although an implicit solver is available, LS-Dyna is more commonly known for its use of the explicit time integration method to analyze complex dynamic problems **(LSTC, 2025b)**. A detailed development history and the theoretical background are provided in the LS-Dyna theory manual: R16 by Livermore Software Technology Corporation. In this thesis, only the relevant properties of LS-Dyna used in the current research are discussed.

The explicit time integration solver is suitable for nonlinear dynamic problems involved in this thesis. This suitability stems from two self-reinforcing factors: the inherently short duration of blast phenomena, and the fact that the explicit solver of LS-Dyna does not require the inversion of the global stiffness matrix at every time step if sufficiently small time steps are used. In other words, the explicit solver is efficient for short-duration dynamic problems and blast phenomena that in general require the solution of short-duration dynamic problems.

LS-Dyna uses the explicit central difference scheme to integrate the equation of motion at each time step. The central difference method that is used to solve the equation of motion is described in the LS-Dyna theory manual **(LSTC, 2025b)**, and it is included here for completeness.

$$Ma^n = P^n - F^n + H^n \qquad \textbf{Eq. 1}$$

$$a^n = M^{-1}\left(P^n - F^n + H^n\right) \qquad \textbf{Eq. 2}$$

$$v^{n+1/2} = v^{n-1/2} + a^n \Delta t^n \qquad \textbf{Eq. 3}$$

$$u^{n+1} = u^n + v^{n+1/2} \Delta t^{n+1/2} \qquad \textbf{Eq. 4}$$

$$\Delta t^{n+1/2} = \frac{\left(\Delta t^n + \Delta t^{n+1}\right)}{2} \qquad \textbf{Eq. 5}$$

$$x^{n+1} = x^0 + u^{n+1} \qquad \textbf{Eq. 6}$$

In **Eq. 1** above, **M** is the diagonal mass matrix, $\mathbf{a^n}$ is the acceleration, $\mathbf{P^n}$ denotes the external forces and body forces, $\mathbf{F^n}$ is the stress divergence vector, and $\mathbf{H^n}$ is the hourglass resistance, where the superscript "**n**" denotes the time. Within the $\mathbf{P^n}$ term, the external forces consist of externally applied forces that act at the boundary of the element, for example, blast pressures or contact forces. The body forces act on the entire volume of the finite element, a common example of which is the gravity forces. The stress divergence vector, $\mathbf{F^n}$, represents the forces that arise due to variations in the internal stresses within the element. For example, bending of the panels causes tensile stresses on one surface and compressive stresses on the other surface, causing a stress gradient between the panel surfaces. The hourglass resistance term, $\mathbf{H^n}$, represents the computational stability term required to eliminate the hourglass modes of the finite elements.

In **Eq. 2**, the force terms are multiplied by the inverse of the global mass matrix, $\mathbf{M^{-1}}$, to obtain the acceleration term, $\mathbf{a^n}$, at the relevant time step. The mass matrix is a diagonal matrix, and its inversion is performed by reciprocating its diagonal elements, as shown in **Figure 92**. Compared to the calculation of the inverse of the global stiffness matrix of a 100,000-node model, the inversion of the mass matrix is computationally trivial.

$$M = \begin{bmatrix} m_1 & 0 & 0 \\ 0 & m_2 & 0 \\ 0 & 0 & m_3 \end{bmatrix} \overset{-1}{\Rightarrow} M^{-1} = \begin{bmatrix} 1/m_1 & 0 & 0 \\ 0 & 1/m_2 & 0 \\ 0 & 0 & 1/m_3 \end{bmatrix}$$

Figure 92: Inversion of a diagonal mass matrix

The subsequent Eq**. 3** and Eq**. 4** are used to compute the velocity and displacement of the element by relating them to the acceleration, $\mathbf{a^n}$, and the time step, $\mathbf{\Delta t}$. The position of the element at the next time step, **n+1**, is computed by adding the initial geometry $\mathbf{x^0}$ and the displacement, $\mathbf{u^{n+1}}$, as shown in **Eq. 6**. The value of the central time step, $\mathbf{\Delta t^{n+1/2}}$, is calculated as an average of $\mathbf{\Delta t^n}$ and $\mathbf{\Delta t^{n+1}}$, as shown in **Eq. 5**, because the value of the time step at any given point in the analysis is related to the size of the smallest finite element within the model. This relationship between the time step and the smallest finite element is explained below.

The computational efficiency of the central difference method mentioned above is conditional. It requires the integration time step to be smaller than the critical time step, $\mathbf{\Delta t_e}$. The critical time step size is related to wave propagation within that element and is calculated differently for each element type. For truss and beam elements, the critical time step is a function of the smallest element length, $\mathbf{L_e}$ and the sound wave speed, **c**, within that element (**Eq. 7**). The sound wave speed, **c**, is a function of the modulus of elasticity, **E**, and mass density, **ρ** (**Eq. 8**).

$$\Delta t_e = \frac{L_e}{c} \qquad \textbf{Eq. 7}$$

$$c = \sqrt{\frac{E}{\rho}} \qquad \textbf{Eq. 8}$$

For solid elements, the critical time step, Δt_e, is dependent on the characteristic length of the element, L_e, the adiabatic speed of sound, **c**, and the bulk viscosity of the element, **Q** (**Eq. 9**). The bulk viscosity term, **Q**, is a function of quadratic (Q_1) and linear (Q_2) viscosity coefficients and is equal to zero when the volumetric strain rate, $\dot{\varepsilon}_{kk}$, is positive (the element is in tension) when the volumetric strain rate is negative (the element is in compression) (**Eq. 10**). The characteristic length of the element, L_e, is calculated by dividing the volume of the element by the area of its largest side (**Eq.** 11). The adiabatic speed of sound is a function of the material stiffness and mass density, and it can be simplified as shown below in **Eq. 12** for elastic materials with a constant bulk modulus.

$$\Delta t_e = \frac{L_e}{\left[Q + \left(Q^2 + c^2\right)^{1/2}\right]} \qquad \textbf{Eq. 9}$$

$$Q = \begin{cases} Q_2 c + Q_1 L_e \left|\dot{\varepsilon}_{kk}\right| & \text{for } \dot{\varepsilon}_{kk} \leq 0 \\ 0 & \text{for } \dot{\varepsilon}_{kk} > 0 \end{cases} \qquad \textbf{Eq. 10}$$

$$L_e = \frac{v_e}{A_{e_{\max}}} \qquad \textbf{Eq. 11}$$

$$c = \sqrt{\frac{E(1-\nu)}{(1+\nu)(1-2\nu)\rho}} \qquad \textbf{Eq. 12}$$

The calculation of the critical time step, Δt_e, is performed inherently by LS-Dyna to ensure stability of results. For the end user, it is important to be mindful that as the mesh size is reduced, the smallest characteristic length is also reduced. This will invariably increase the computational effort involved in the analysis. Furthermore, the speed of sound is linearly proportional to the modulus of elasticity of the solid object. Therefore, higher values of modulus of elasticity result in a greater value of speed of sound, which in turn further reduces the value of the critical time step.

For reference, the calculation of the critical time increment for a single solid element made of steel with dimensions 3 mm by 10 mm by 10 mm is shown below for both negative and positive volumetric strain rates. For the quadratic and linear viscosity coefficients, the default values of LS-Dyna (**Q_1=1.5**, **Q_2=0.06**) were used. The effect of the strain rate term in the total value of Q is negligible in this calculation. The value of Q for a volumetric strain rate of 10^{-5} (static loading) is only 1.5% lower than the Q value for an extremely high volumetric strain rate of 1000 ($Q_{0.00001}$=302853 & Q_{1000}=307353). A volumetric strain rate of 1 was used in this calculation. It is worth noting that the difference in **Δt_e** between the tension (Q=0) and compression volumetric strain rates is only 6.2%.

$$c_{steel} = \sqrt{\frac{E_{steel}}{\rho_{steel}}} = \sqrt{\frac{200,000\, N/mm^2}{7.85*10^{-9}\ tonne/mm^3}} = 5,048,000\, mm/\text{sec} \qquad L_e = \frac{v_e}{A_{e_{\max}}} = \frac{3mm*10mm*10mm}{10mm*10mm} = 3mm$$

$$Q_{compression} = Q_2 c + Q_1 L_e \left|\dot{\varepsilon}_{kk}\right| = 0.06\,\text{sec}/mm * 5,048,000\ mm/\text{sec} + 1.5/mm * 3mm * 1 = 302,857$$

$$\Delta t_e = \frac{L_e}{\left[Q + \left(Q^2 + c^2\right)^{1/2}\right]} = \frac{3mm*1/mm}{\left[302857 + \left(302857^2 + 5,048,000^2\right)^{1/2}\right]} = 5.598*10^{-7}\ \text{sec}$$

$$\Delta t_{e\_tension} = \frac{L_e}{\left[0 + \left(0^2 + c^2\right)^{1/2}\right]} = \frac{3mm*1/mm}{\left[0 + \left(0 + 5,048,000^2\right)^{1/2}\right]} = 5.943*10^{-7}\ \text{sec}$$

It is important to note that LS-Dyna uses sets of units that are consistent with Newton's second law of motion. In the above calculation, and in the models that were created as a part of this study, the unit system used and corresponding values for steel are shown below.

Table 9: Unit system used in LS-Dyna models

Length	millimetre, mm
Time	second, sec
Mass	tonne
Force	Newton, N
Modulus of Elasticity of Steel	200,000 N/mm^2
Density of Steel	7.85*10^{-9} tonne/mm^3

4.1.2 Model Parameters

In this section, various element formulations, material models, and contact algorithms used in the LS-Dyna models are presented. The element formulations section includes relevant information about one, two, and three-dimensional finite elements used in the models. The material models section explains the various material models that were used for steel sheets, bolts, angles, and ECC layers. The contact algorithms section provides detailed information about the modelling methodology used to define the relationship between ECC layers and steel sheets, in addition to the interaction relationship between all solid elements.

Element Formulations

LS-Dyna has many different types of elements to facilitate accurate representation for analysis. Those used in the current analytical investigation are listed in the following paragraphs.

8-Node Fully Integrated Solid Element

In LS-DYNA, there are numerous solid elements that could be used. For the current research, the "ELFORM = 3" card, which corresponds to a fully integrated quadratic 8-node element with nodal rotations, was used (**LSTC, 2025a**). Because of its fully integrated formulation, this element does not require hourglass control, as long as the Poisson's ratio does not approach 0.5 (**LSTC, 2025b**). A material with a Poisson's ratio of 0.5 corresponds to an incompressible material; this limitation is not relevant to this model, where all solid materials are compressible. This element was used to model the ECC layers, steel sheets, support angles, and bolts, as shown in **Figure 94** below. These solid elements were preferred for panel layers due to their solid geometry, which better represents the contact and the stresses and strains arising from this contact between layers, compared to shell elements.

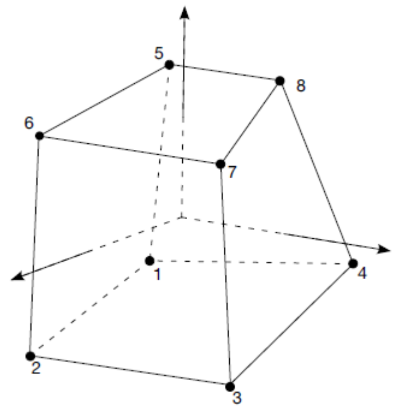

Figure 93: Eight-node solid hexahedron element **(LSTC, 2025b)**

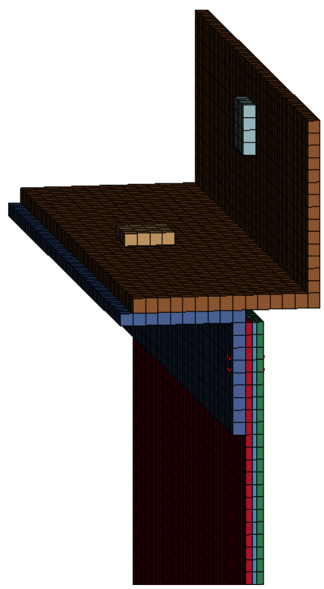

Figure 94: LS-Dyna model showing solid elements

Shell Elements (Belytschko–Tsay, ELFORM = 2)

In LS-Dyna, the Belytschko–Tsay shell element (ELFORM = 2) is the default shell element. This element card was used for the shell elements used in the models due to its computational efficiency and robustness in explicit solutions. Due to its reduced integration formulation, this element has an embedded hourglass control (**LSTC, 2025b**). These shell elements were used in modelling the HSS members that were connected to the ECC-steel-ECC panels, as shown in **Figure 95**. Although these elements are much less computationally demanding, they do not capture the interactive stresses between layers as solid elements do. This is the primary reason for not using these elements for the ECC and steel layers of the panels.

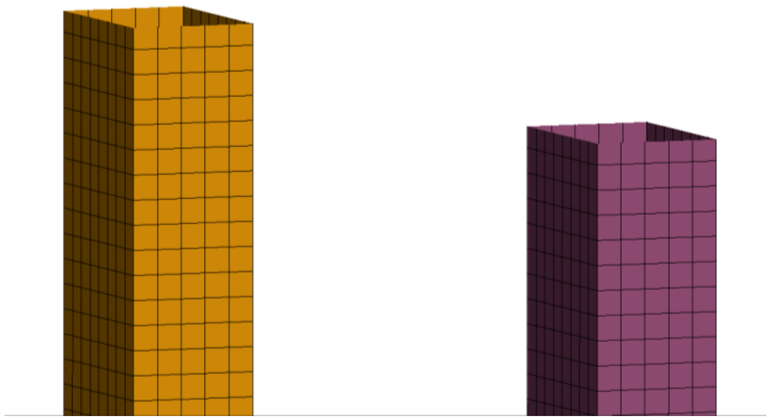

Figure 95: HSS Members modelled with shell elements in LS-Dyna

Beam Elements (Hughes–Liu Formulation, ELFORM = 1)

The Hughes–Liu beam formulation (ELFORM = 1) is the default beam element in LS-Dyna. This element was used in the models as it is a robust formulation that is also compatible with two and three-dimensional elements. The primary use of the beam elements in the models was in threaded rods that connect various layers of the panels together. Therefore, the compatibility with other element types was a critical feature (**LSTC, 2025b**). These elements were used to model the threaded rods and self-drilling screws that connected the ECC-steel-ECC panels with HSS members, as shown in **Figure 96**.

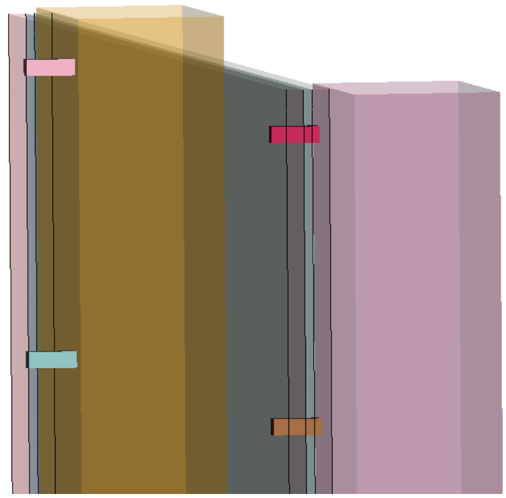

Figure 96: Beam elements used to model threaded rods and screws

Material Properties

Material Model: MAT_PLASTICITY_COMPRESSION_TENSION (MAT_124)

The MAT_PLASTICITY_COMPRESSION_TENSION formulation (MAT_124) was used in this research to represent the mechanical behaviour of Engineered Cementitious Composites (ECC). This material model allows the user to define distinct stress-strain relationships for tension and compression. Therefore, the behaviour of ECC can be accurately represented by inputting separate tension and compression relationships, as shown in **Figure 97**. The material model allows the definition of a failure strain and deletes the finite element when this strain value is reached. This feature is useful for capturing the tension rupture behaviour of ECC layers.

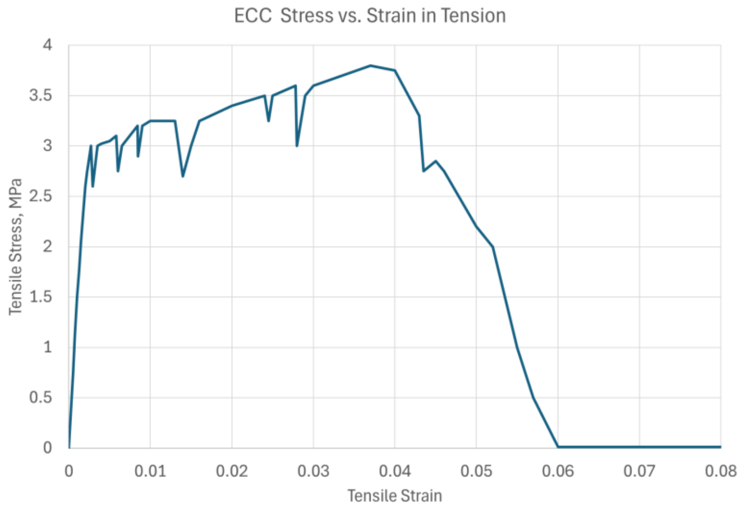

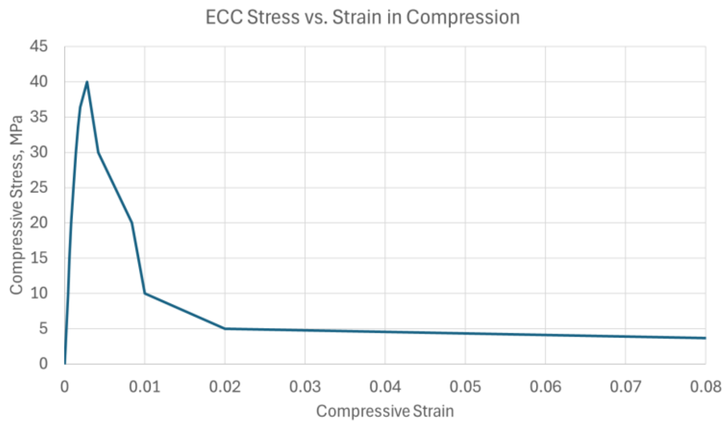

Figure 97: ECC Stress vs. Strain in tension (top) and compression (bottom)

A verification of the material model was performed by modelling a coupon specimen resembling the ECC coupons that were tested under uniaxial tension loading. This modelled coupon specimen was loaded under uniaxial tension to verify the behaviour of the solid elements using the MAT_124 formulation. The stress distribution within individual finite elements and the overall reaction forces at the boundaries are in agreement with the results of the laboratory experiments. This was considered to be the confirmation of the suitability of MAT_124 to accurately capture the tension behaviour of ECC elements (**Figure 98**).

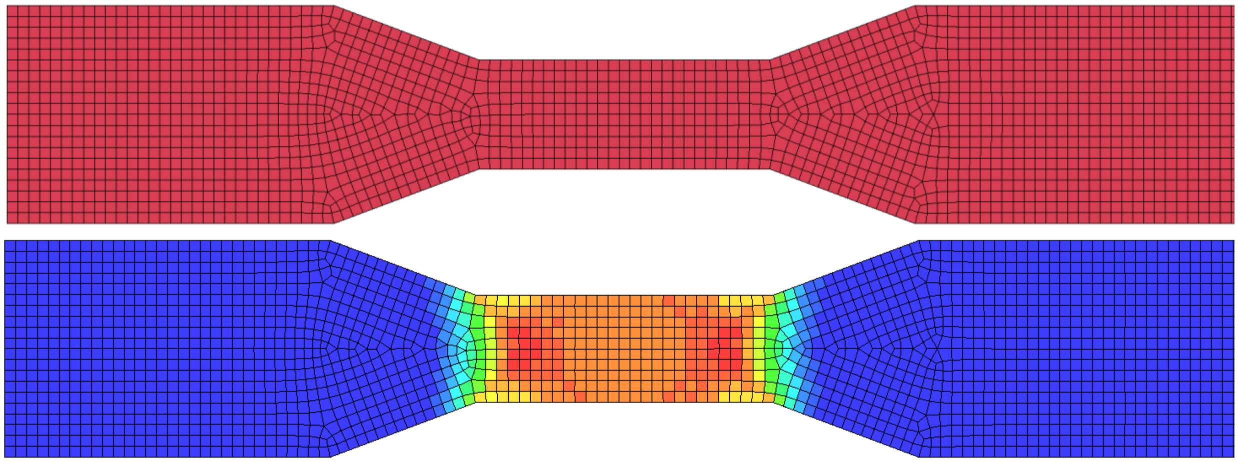

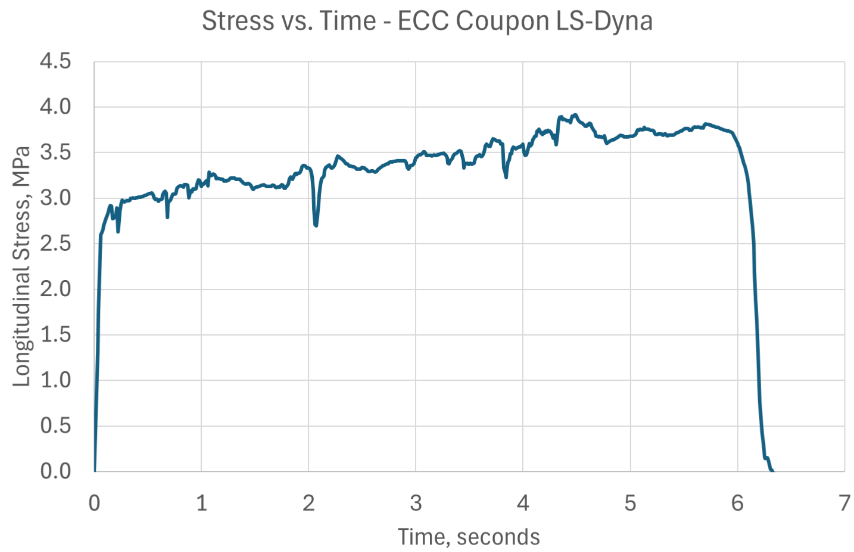

Figure 98: ECC coupon specimen undeformed (top), ECC coupon specimen before rupture (center), Stress vs time in the longitudinal direction (bottom)

Material Model: MAT_PIECEWISE_LINEAR_PLASTICITY (MAT_024) The steel plate located between the two ECC layers was modelled using the MAT_024 material formulation. This material card allows the user to input an isotropic elastic–plastic stress versus strain behaviour. The failure strain option of this material property enables the finite element to be deleted when the failure strain is reached. The stress-strain graph of the steel sheets used in the models is shown in **Figure 99**. In addition, the HSS members, which were modelled using shell elements, used this material type. This is due to the fact that MAT_024 is compatible with solid, shell and beam type elements, as opposed to MAT_013, which is compatible with solid elements only.

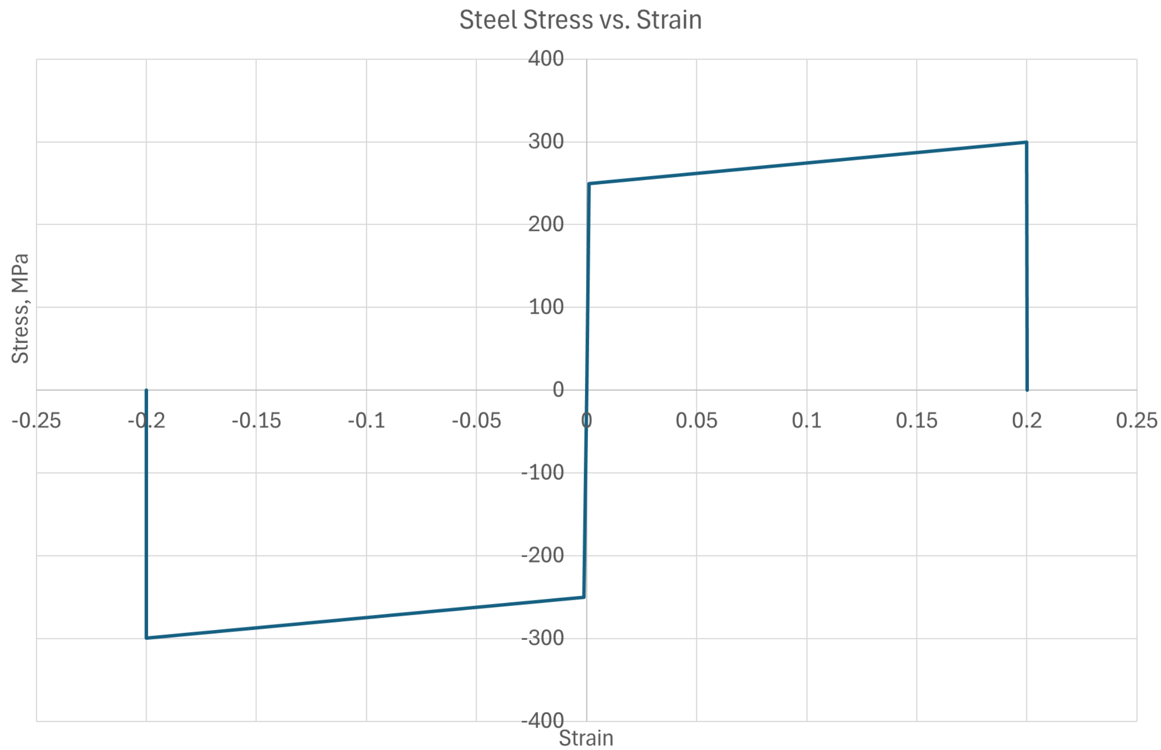

Figure 99: Steel plate Stress vs. Strain

Material Model: *MAT_ISOTROPIC_ELASTIC_PLASTIC* with Plastic Strain Failure (MAT_013)

The structural steel support angles in this research were modelled using MAT_ISOTROPIC_ELASTIC_PLASTIC with Plastic Strain Failure (MAT_013). This is a simple and computationally efficient model that is compatible with solid elements.

Contact Algorithms

In LS-Dyna, contact algorithms are used to prevent interpenetration between components and to correctly represent the transfer of forces across interfaces. In this work, two contact formulations were used: Automatic Surface-to-Surface Contact and Automatic Surface-to-Surface Tiebreak Contact.

Automatic Surface to Surface Contact

The automatic surface-to-surface contact algorithm is a versatile feature of LS-Dyna that can be used to define the rules of interaction between solid, shell, beam elements or sets of nodes. The primary function of this algorithm is to prevent the penetration of one element by another element that does not share its nodes. For example, two distinct objects moving towards each other would be able to travel through each other without any resistance if this contact algorithm is not used. This formulation is penalty-based, meaning that springs normal to the surface of an element apply a contact force, penalizing movement, against the nodes of the penetrating element.

This algorithm was used to ensure that elements in the models, including support angles, panel layers, and HSS members, do not share the same volume. **Figure 100** below shows the interaction between two support angles when the contact algorithm is active (left) and inactive (right).

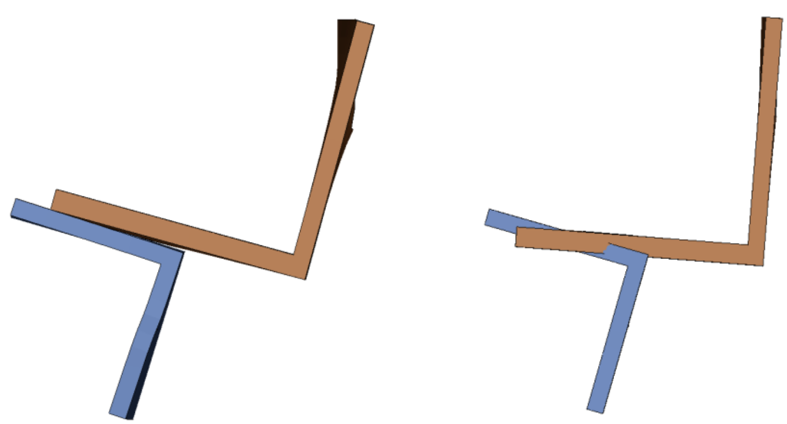

Figure 100: Active (left) and inactive (right) contact algorithm between support angles

Automatic Surface to Surface Contact Tiebreak

The automatic surface-to-surface tiebreak contact algorithm is an effective feature of LS-Dyna that is used to model elements that are tied together via a contact stress. This feature could be used to model the adhesion between multiple plies of composites or layers of plywood. This algorithm provides a rigid interface between the layers until the tiebreak stress is reached. Once the tiebreak stress between the layers is reached, the adhesion fails, and the two layers start to act as separate elements.

In the models developed for this research, this algorithm was used to connect the layers of the ECC-steel-ECC panels, in lieu of the connectors that were used in the specimens tested in the Shock tube. For specimens with 100 mm connectors, a shear contact stress of 1.1 MPa was used. This value was changed to 0.55 MPa for specimens with connectors at 200 mm spacing. These values were obtained as shown below in **Eq. 13**. The chemical adhesion stress of 0.4 MPa was assumed to be present on all surfaces, whereas the concentrated shear resistance due to the connectors were assumed to be distributed uniformly within their tributary area.

Eq. 13

$$\tau_{connector} = \frac{V_{connector}}{spacing^2} + \sigma_{adhesion} \quad where\, \sigma_{adhesion} = 0.4 MPa$$

$$V_{connector} = 6.9\, kN \;\; for\;\; a\;\; 4.8\, mm\;\; diameter\, screw$$

$$\tau_{connector,100mm} = 1.09\, MPa$$

$$\tau_{connector,200mm} = 0.57\, MPa$$

4.1.3 Mesh Sensitivity Analysis

A mesh size of 10 mm was used for the solid and shell elements in the LS-Dyna models. This value was obtained as a result of an iterative analysis process of a 500 mm by 2080 mm panel with 6 mm ECC, 3 mm Steel and 6 mm ECC layers. The iteration was started with a 30 mm mesh size, then subsequently decreased to 25mm, 20 mm, 15 mm, 10 mm and 8 mm. The maximum deformation value of each model was compared to assess the difference between each model.

Maximum deformation at the panel midpoint versus mesh size is shown in **Table 10** below. A trend is evident that the maximum deformation increases with decreasing mesh size. The difference between the maximum deformations of 10 mm and 8 mm mesh size specimens was 4.4%. This difference was considered sufficiently small, and a mesh size of 10 mm was chosen for subsequent analyses to achieve an acceptable level of accuracy while maintaining a reasonable analysis time.

Table 10: Mesh sensitivity analysis summary

Mesh Size (mm)	30	25	20	15	10	8
Number of Nodes	7,680	10,680	16,404	28,632	64,050	100,320
Maximum Deformation (mm)	34.9	35.5	36.5	38.0	41.3	43.2
Difference with 8 mm %	19.3	17.9	15.6	12.0	4.4	0
Difference with the next mesh size %	1.7	2.7	3.9	8.0	4.4	0
Analysis Duration (minutes)	5	7	13	20	45	68

4.2 Verification of Finite Element Models with Shock Tube Experiments

4.2.1 First Set of Specimens: Panels with HSS Members – 3mm Steel

For the first set of specimens, panels with 3 mm steel with HSS members on the shock tube side, the failure mode was flexural failure of the HSS members. Horizontal cracks were observed on the ECC layer of the panels on the tension side; however, rupture was not observed. Plastic hinges at the midspan of the HSS members were formed after the third shot (**Figure 101).** As a result of the same shot, the bolts of the connection of the top steel angles to the shock tube failed, causing the specimen to fall to the ground.

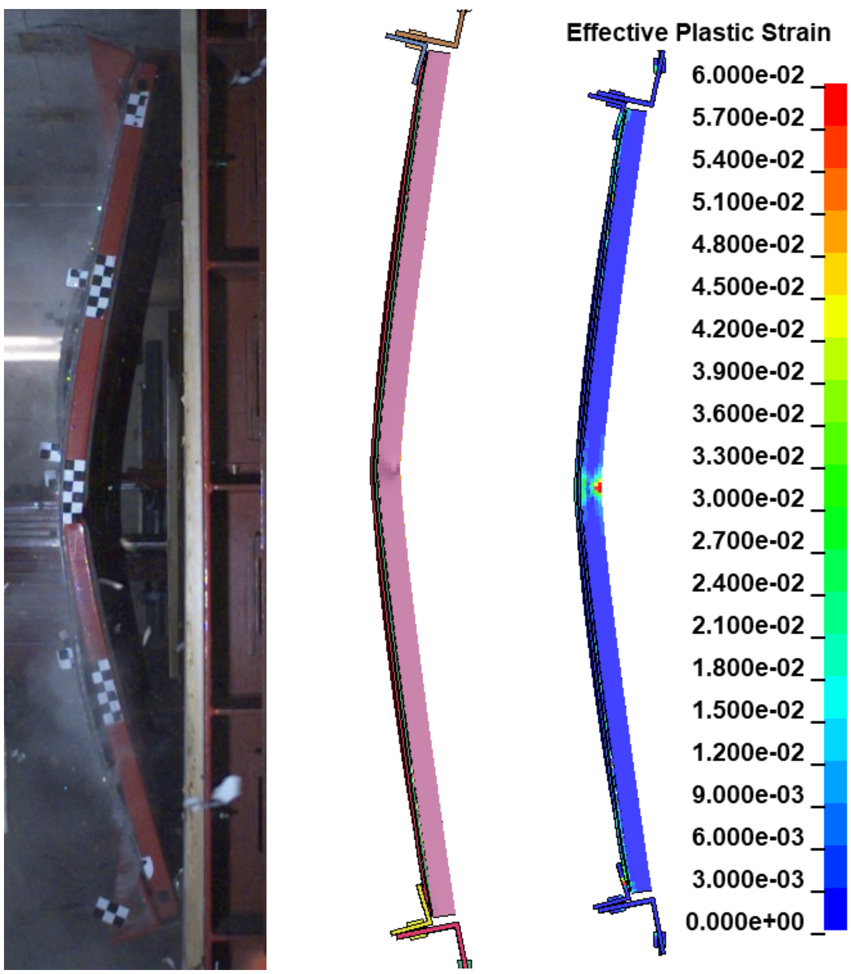

Figure 101: Flexural yielding at the midspan of the HSS members

In LS-Dyna, the model was separately loaded with the blast load representing each individual shot. It is important to note that the LS-Dyna model was loaded from an undeflected, unloaded state, whereas only the first shock tube specimen was loaded from an unloaded state. Subsequent shock tube shots had been performed on the specimen after the completion of the previous shot. Hence, with each shot, there was an increasing amount of residual deformation. The residual deformation after the fifth shot, prior to the sixth and final shot, was 42 mm. The maximum deflection obtained in the LS-Dyna model for the sixth shot was 175 mm, which is approximately 9% less than the 193 mm maximum deflection observed in the shock tube specimen. The midspan deformation of the LS-Dyna model and the shock tube specimen after the sixth shot is shown in **Table 11** below.

Table 11: LS-Dyna Model vs. Shock Tube Specimen after the sixth shot

	LS-Dyna Model	**shock tube Specimen**
Initial Deformation, mm	0 mm	54 mm (Shot #5)
Maximum Deformation, mm	175 mm	247 mm (Shot #6)
Additional Deformation, mm	175 mm	193 mm
Equivalent Charge Weight (kg) and Standoff Distance (m) (reflected pressure, impulse)	1567 kg, 64 m (82 kPa, 1066 kPa-ms)	1567 kg, 64 m (82 kPa, 1066 kPa-ms)
Scaled Distance (m / kg$^{1/3}$)	5.5	5.5

The steel angles and the bolts in the LS-Dyna model were included to accurately replicate the support conditions. In the shock tube experiments, significant bending of the steel angles was observed, which contributed to the overall deformed shape of the specimens. The angles and bolts were modelled using solid elements as they exhibited bending deformation similar to the shock tube specimen supports (**Figure 102**). In the LS-Dyna model, the movement of the support angles contributed to the midspan deflection of the panels in the same manner as the shock tube experiments. The solid element representing the bolt connected to the shock tube frame was constrained on its vertical surface to accurately capture the rigidity of the shock tube frame. This constraint was the only constraint applied to the model as a boundary condition and prevented movement in the X, Y, and Z axes.

The mid-height displacement of the LS-Dyna model during each shot is given below in **Figure 104** to **Figure 109**. For comparison purposes, the displacement vs time curve of the corresponding shock tube experiment is also included in the same figure. For the first shot, both the LS-Dyna model and the shock tube experiment start from an undeformed state. For the subsequent shots, the residual deformation that exists in the shock tube shots does not exist in the LS-Dyna model. For the first three shots, for which the maximum displacement values were small, the LS-Dyna models overpredict the maximum displacement significantly. For shots four, five, and six, the LS-Dyna and shock tube results are in better agreement. Although the initial displacement of the shock tube specimens for these shots was nonzero, the overall shapes of the curves for both LS-Dyna and the shock tube specimens agree well. Furthermore, the additional deformation experienced by the shock tube specimen is within 10% of the deformation value simulated by LS-Dyna. These results were considered to validate the ability of the LS-Dyna model to predict the failure accurately.

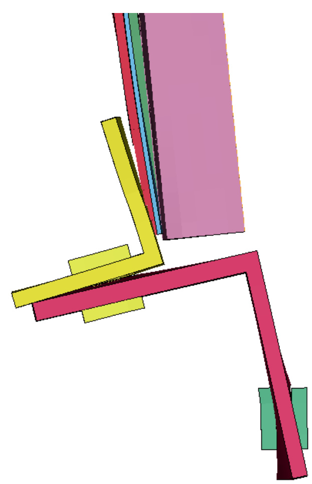

Figure 102: Movement of the supports observed in the shock tube (left) and in LS-Dyna (right)

The blast loading in LS-Dyna was applied using the Blast Force Enhanced keyword, which allows the user to enter the equivalent TNT weight and stand-off distance. This keyword calculates the pressure shockwave based on the UFC 3-340-02, 2008 document. Using the back-calculated blast parameters as an input in LS-Dyna, the pressure-time relationship shown in **Figure 103** was obtained. The measured pressure-time relationship in the shock tube and the applied pressure-time history in LS-Dyna show good agreement. This agreement was observed for the loading curves of all the shock tube experiments. The individual pressure vs time graphs for each shot were not provided in this text for brevity.

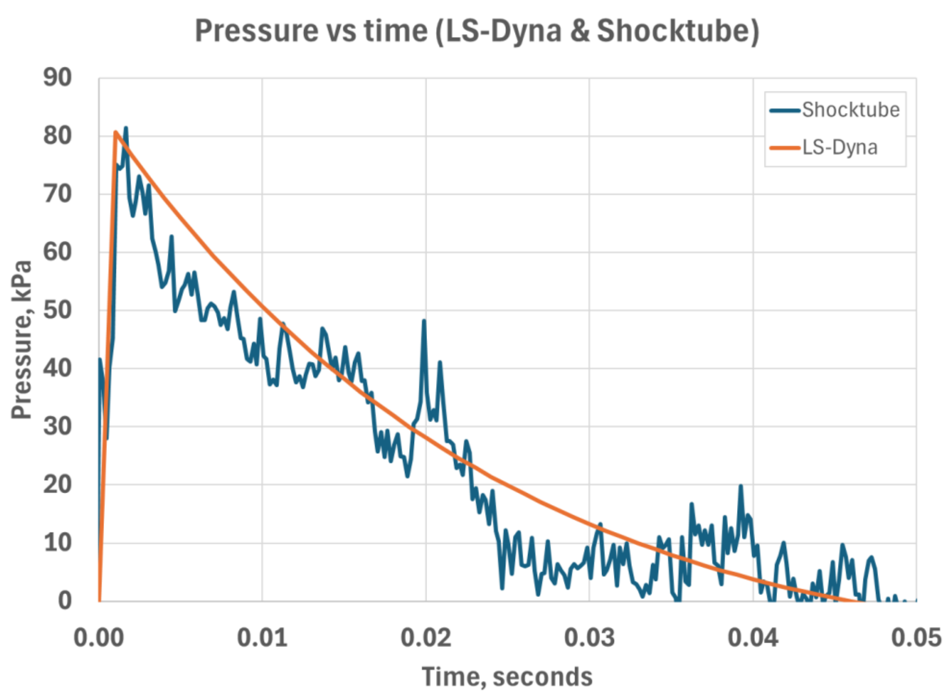

Figure 103: Pressure vs. time, measured in the shock tube and applied in LS-Dyna for 1567 kg of TNT with a standoff distance of 64 metres, Z = 5.5 m/kg$^{1/3}$ (82 kPa and 1066 kPa-ms)

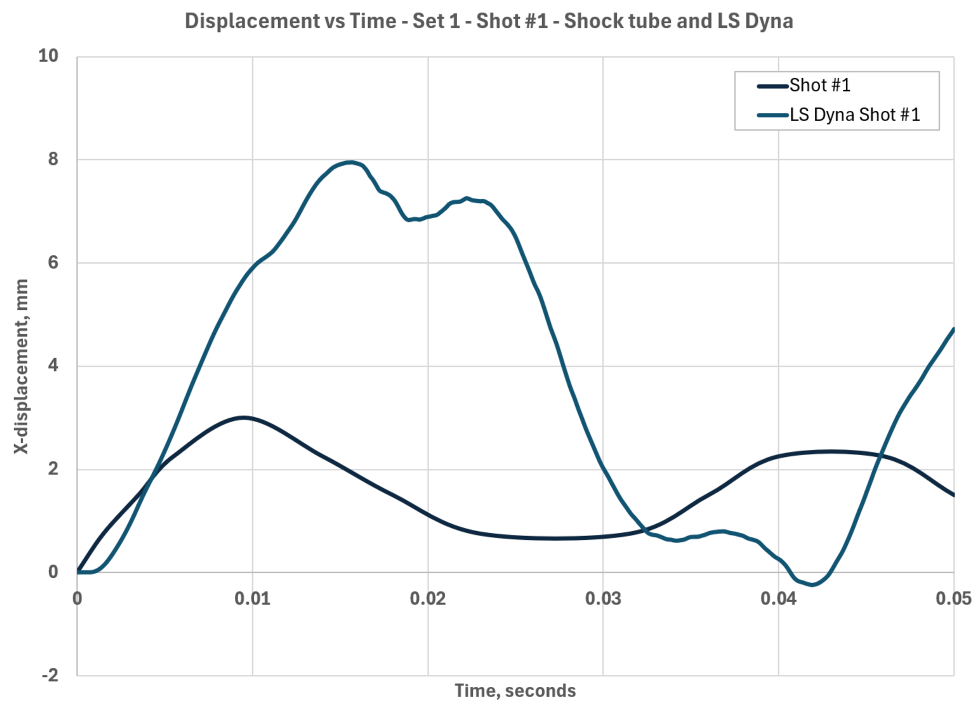

Figure 104: Displacement vs time curve of Shot #1, 3.5 kg at 20 m, Z = 13.3 m/kg$^{1/3}$ (21 kPa and 56 kPa-ms)

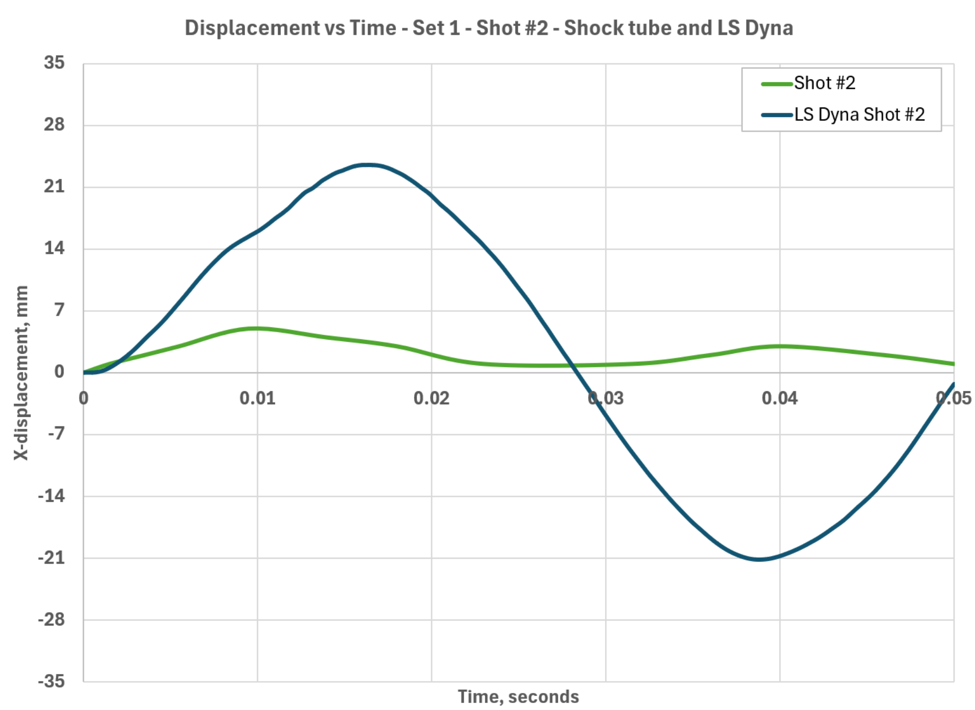

Figure 105: Displacement vs time curve of Shot #2, 9 kg at 16 m, Z = 7.5 m/kg$^{1/3}$ (48 kPa and 138 kPa-ms)

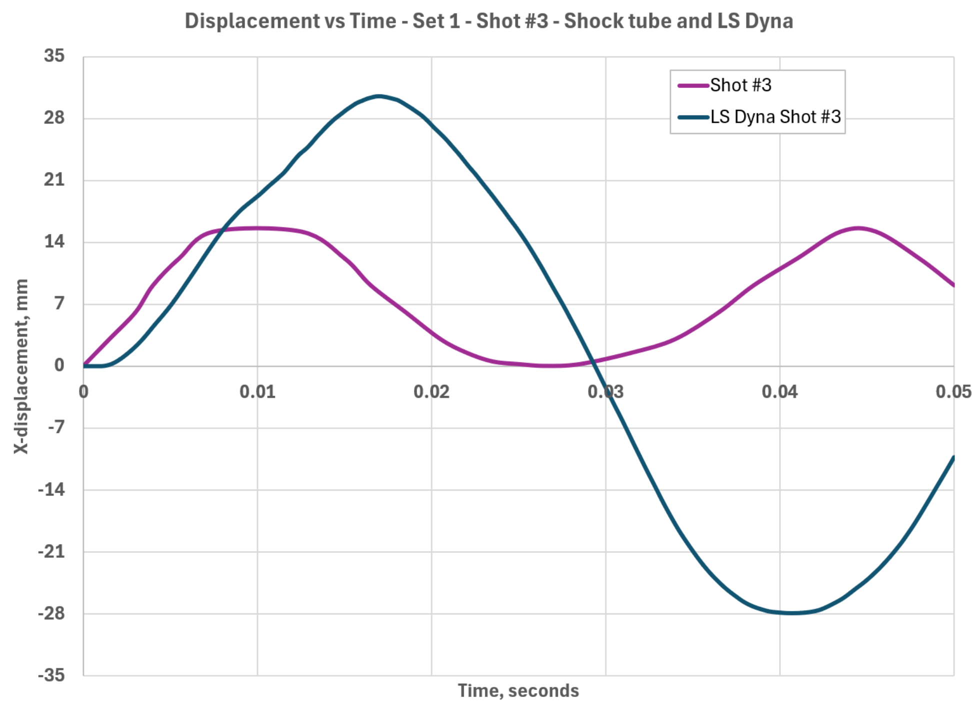

Figure 106: Displacement vs time curve of Shot #3, 15 kg at 16 m, Z = 6.7 m/kg$^{1/3}$ (58 kPa and 183 kPa-ms)

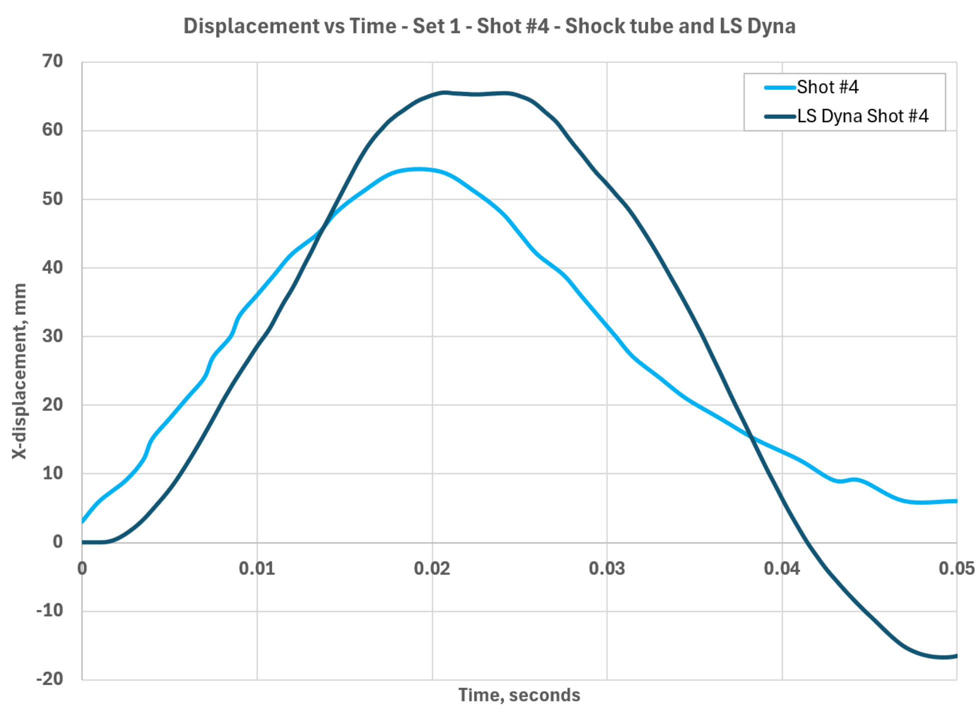

Figure 107: Displacement vs time curve of Shot #4, 228 kg at 41 m, Z = 6.7 m/kg$^{1/3}$ (58 kPa and 455 kPa-ms)

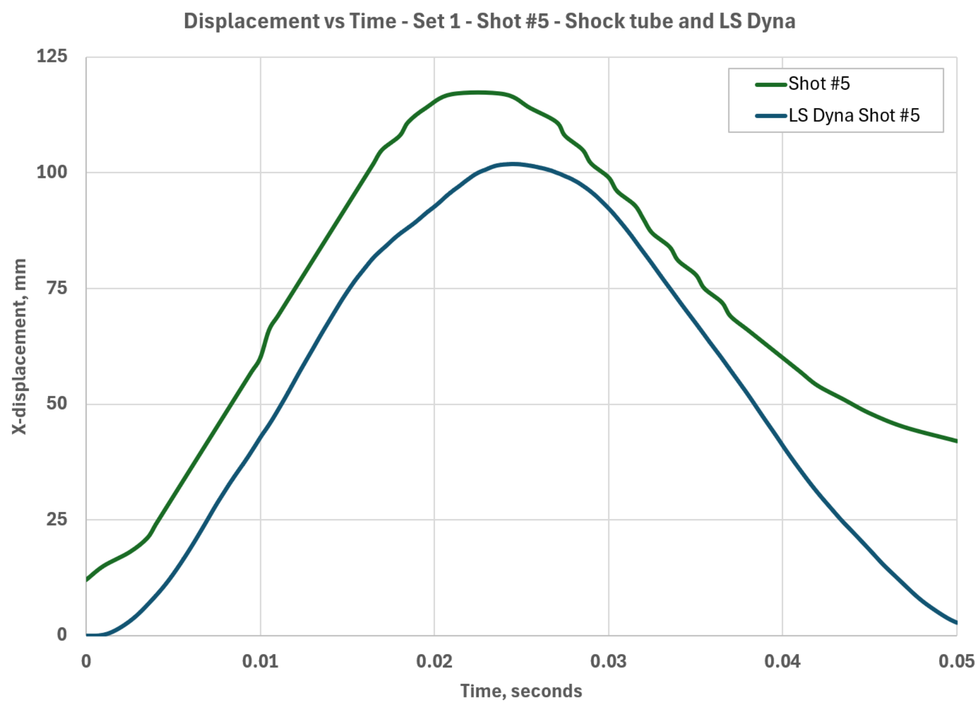

Figure 108: Displacement vs time curve of Shot #5, 390 kg at 42 m, Z = 5.7 m/kg$^{1/3}$ (76 kPa and 648 kPa-ms)

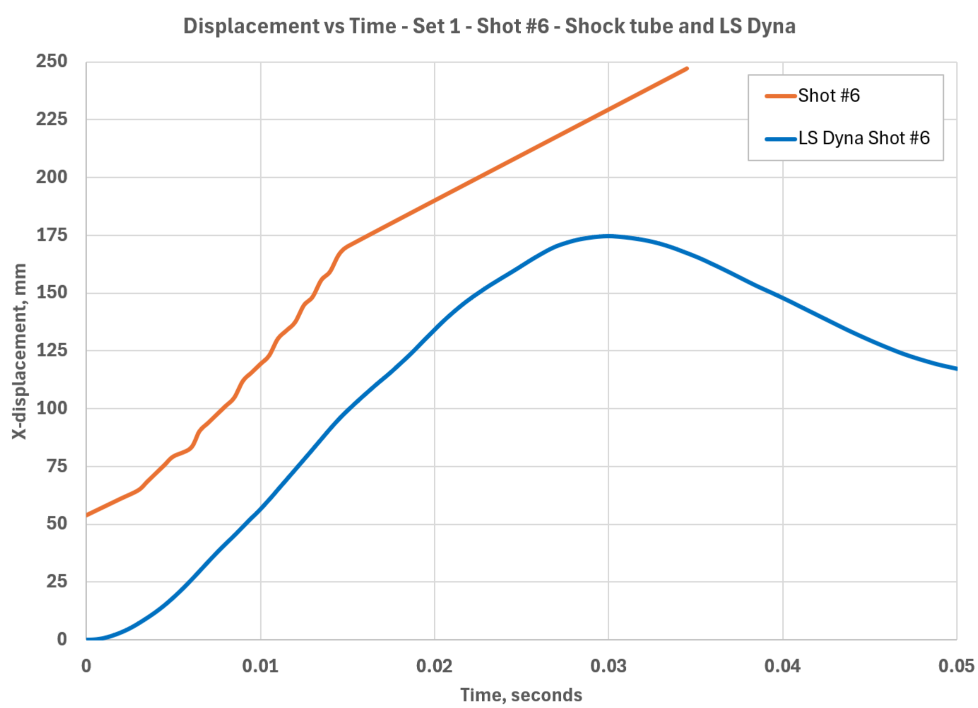

Figure 109: Displacement vs time curve of Shot #6, 1567 kg at 64 m, Z = 5.5 m/kg$^{1/3}$ (82 kPa and 1066 kPa-ms)

4.2.2 Second Set of Specimens: Panels without HSS Members – 3 mm Steel

For the second set of specimens, panels with 3 mm steel without HSS members, the failure mode in the shock tube tests was the delamination of the ECC layer on the protected side and the subsequent tension rupture of this layer. For both specimens with 200 mm connector spacing, delamination and tension rupture of ECC occurred (**Figure 110**, **left**). For the modelled version of the same specimen, the delamination and tension rupture failure was also observed (**Figure 110, right**).

In the shock tube, one of the specimens with 100 mm connector spacing failed with delamination and rupture of ECC, with minor defragmentation. The other specimen with 100 mm connector spacing experienced cracking, but delamination and tension rupture were not observed. For the modelled version of this specimen, cracking and partial delamination were observed in the front ECC layer without a complete rupture. This behaviour was representative of the specimen that cracked without rupturing (**Figure 111**).

In LS-Dyna, a variation of the automatic surface-to-surface tiebreak contact algorithm was used to represent the specimens with 100 mm and 200 mm connector spacings. For the 100 mm connector spacing, a higher tiebreak shear stress value, 1.10 MPa, was used. For the 200 mm connector spacing, 0.55 MPa tiebreak shear stress was used. Both of these models were subjected to all three blast loads applied in the shock tube. The corresponding blast parameters and maximum displacement data at rupture for shot 3 are shown in **Table 12** below.

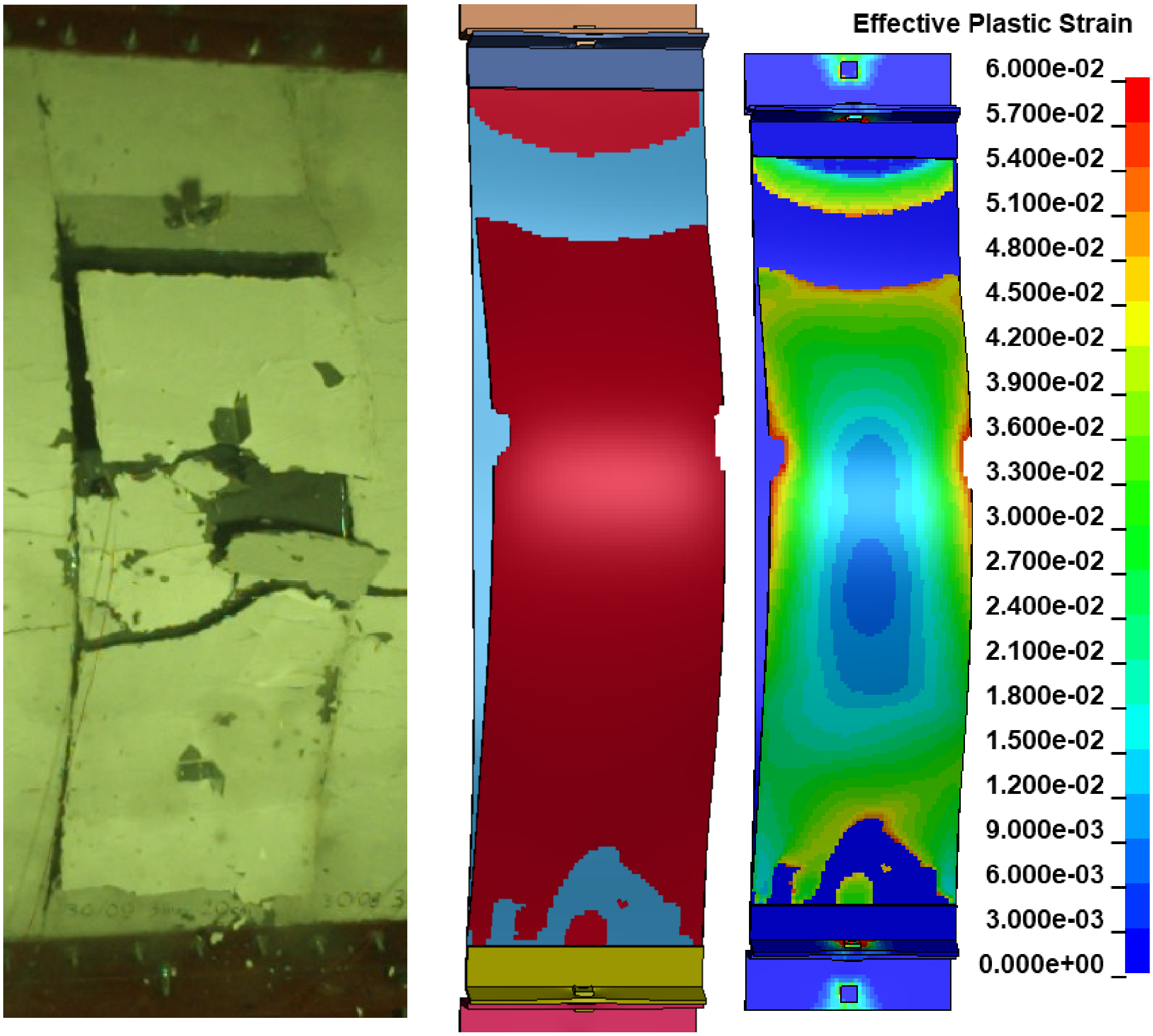

Figure 110: Shock tube tested specimen with 200 mm connector spacing (left), and LS-Dyna modelled specimen (center, right) subjected to a blast load with the 1417 kg TNT weight and 60 metre standoff distance, Z = 5.4 m/kg$^{1/3}$ (85 kPa and 1048 kPa-ms)

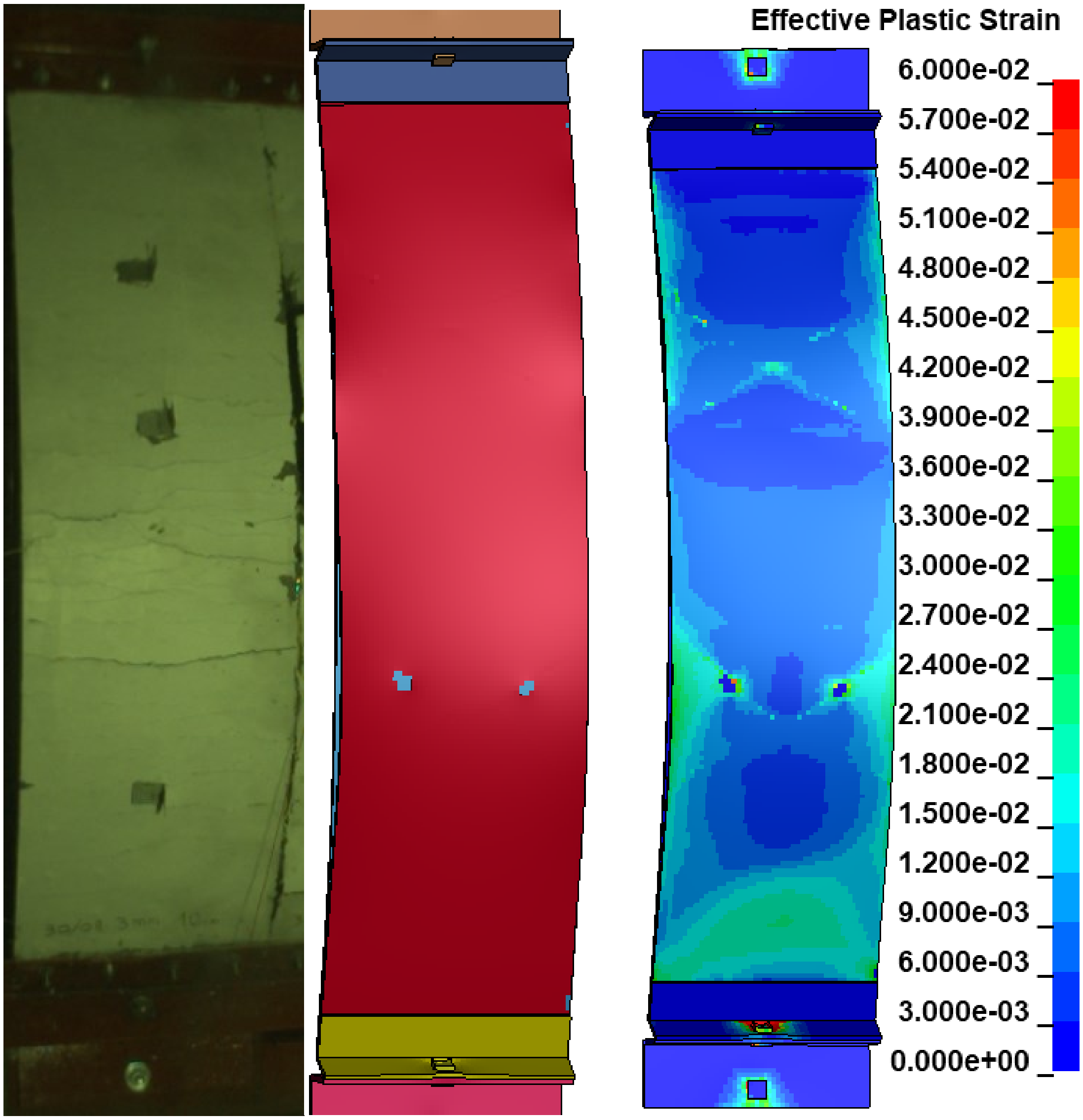

Figure 111: Shock tube tested specimen with 100 mm connector spacing (left), and LS-Dyna modelled specimen (center, right) subjected to a blast load with the 1417 kg TNT weight and 60 metre standoff distance, Z = 5.4 m/kg$^{1/3}$ (85 kPa and 1048 kPa-ms)

For model 1, which represents the 100 mm connector spacing, under the loading representing the third shot, the maximum deformation (295 mm) was 20% less than the maximum deformation (369 mm) and 5% less than the additional deformation (309 mm) measured for the shock tube specimen. For model 2, which represents the 200 mm connector spacing, under the loading representing the third shot, the maximum deformation, before rupture (365 mm), was 1% less than the maximum deformation (369 mm) and 18% more than the additional deformation (309 mm) of the shock tube specimen. Although the LS-Dyna models underestimate the maximum deformation at rupture, they represent the failure modes accurately.

The mid-height displacement vs time curves of both LS-Dyna models are shown in **Figure 112** to **Figure 114**. In each figure, the corresponding shock tube test results are also given. It is important to note that the LS-Dyna models are loaded from an undeformed state. Although the initial deformation of the models differs from that of the shock tube specimens for shots 2 and 3, the slope of the displacement vs time curve indicates agreement of dynamic properties.

The LS-Dyna and shock tube displacement curves for the first shot both start from the undeformed state, with zero initial displacement. All three curves for the first shot show good agreement in maximum deformation and the time to reach the maximum deformation. Both LS-Dyna curves match almost identically in the ascending branch. However, the model for the 200 mm connector spacing experiences partial delamination of the front ECC layer as it approaches its maximum deformation. This partial delamination causes the maximum deformation of the 200 mm connector spacing model to be higher than that of the 100 mm connector spacing model.

For the second shot, similar to the first shot, both LS-Dyna models are almost identical to each other until maximum deformation is reached. The model with 200 mm connector spacing experiences partial delamination, which results in a higher maximum deformation. The time to reach maximum deformation and the slope of the ascending branch of both LS-Dyna curves agree well with the shock tube specimen curve. The curve for the shock tube specimen has a higher maximum deformation value due to the initial deformation of 57 mm. At 25 ms, the deformations are 233 mm (LS-Dyna Model 1), 237 mm (LS-Dyna Model 2), and 291 mm (Shock tube), corresponding to differences of 58 mm and 54 mm, which compare well with the 57 mm initial deformation.

For the third shot, the ascending branch slopes and the time to reach maximum deformation of the LS-Dyna curves match the shock tube curve well. The shock tube specimen reached maximum deformation of 369 mm at 24 ms, at which time the displacement values were 294 mm (Model 1) and 317 mm (Model 2) for the LS-Dyna models. Considering that the initial deformation of the shock tube specimen was 60 mm, the deformation values of the LS-Dyna curves are within 5% of that of the shock tube. It is important to note that for the LS-Dyna Model 2, the displacement was recorded even after failure, and the failed element continued to move even though it had separated from the steel sheet. For model 2, delamination occurs at 21 ms, and the subsequent rupture of the ECC layer occurs at 26 ms, when the mid-height deformation was 365 mm.

Based on the comparison of the LS-Dyna displacement vs time curves with those of the shock tube explained above, it was concluded that the LS-Dyna model behaviour was representative of the shock tube specimens. Specifically, these models were found to accurately predict the time and displacement corresponding to the front ECC layer at the time of rupture. Therefore, these models, and the material and blast load modelling parameters utilized therein, could be used to predict the blast loads that would cause panel failure due to rupture of the front ECC layer.

Table 12: Shock tube 2nd Set of Specimens vs. LS-Dyna Models comparison for Shot #3

	LS-Dyna Model 1	Shock tube Specimen 1	LS-Dyna Model 2	Shock tube Specimen 2
Contact Capacity / Connector Spacing	1.1 MPa	100 mm	0.55 MPa	200 mm
Initial Deformation, mm	0 mm	60 mm	0 mm	60 mm
Maximum Deformation, mm	295 mm (before rupture)	369 mm	365 mm (before rupture)	369 mm (before rupture)
Additional Deformation, mm	295 mm (before rupture)	309 mm	365 mm (before rupture)	309 mm (before rupture)
Equivalent Charge Weight (kg), Standoff Distance (m) (Reflected Pressure, Impulse)	1417 kg, 60 m (85 kPa, 1048 kPa-ms)	1417 kg, 60 m (85 kPa, 1048 kPa-ms)	1417 kg, 60 m (85 kPa, 1048 kPa-ms)	1417 kg, 60 m (85 kPa, 1048 kPa-ms)
Scaled Distance ($m / kg^{1/3}$)	5.4	5.4	5.4	5.4

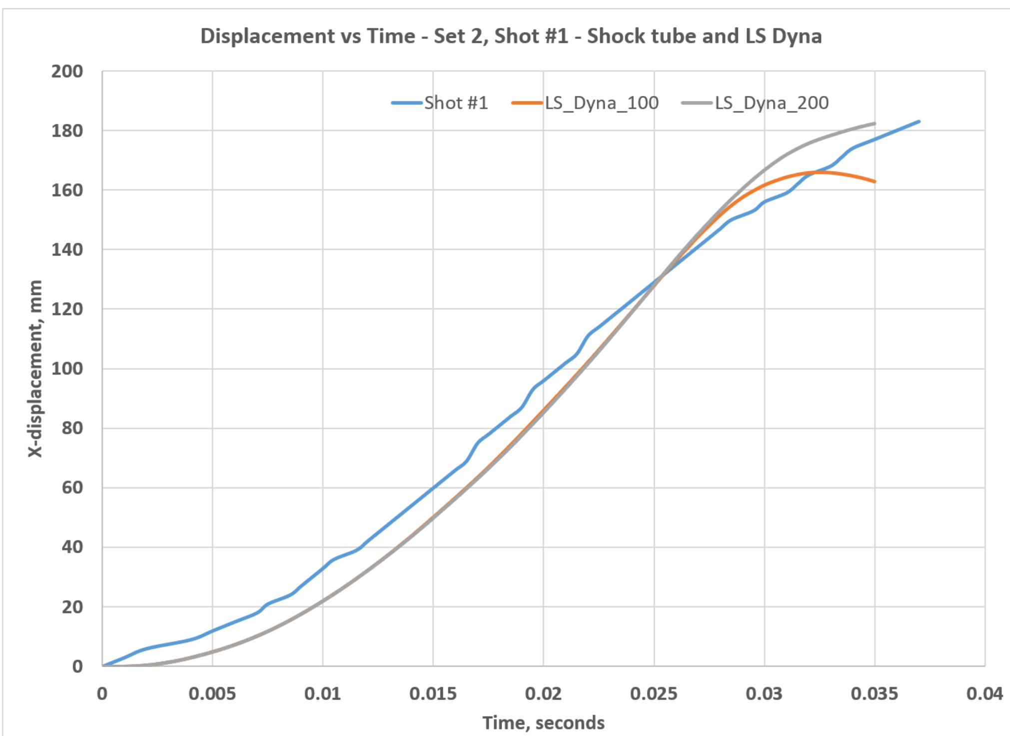

Figure 112: Displacement vs time curve of Shot #1, 305 kg at 69 m, Z = 10.3 $m/kg^{1/3}$ (30 kPa and 324 kPa-ms)

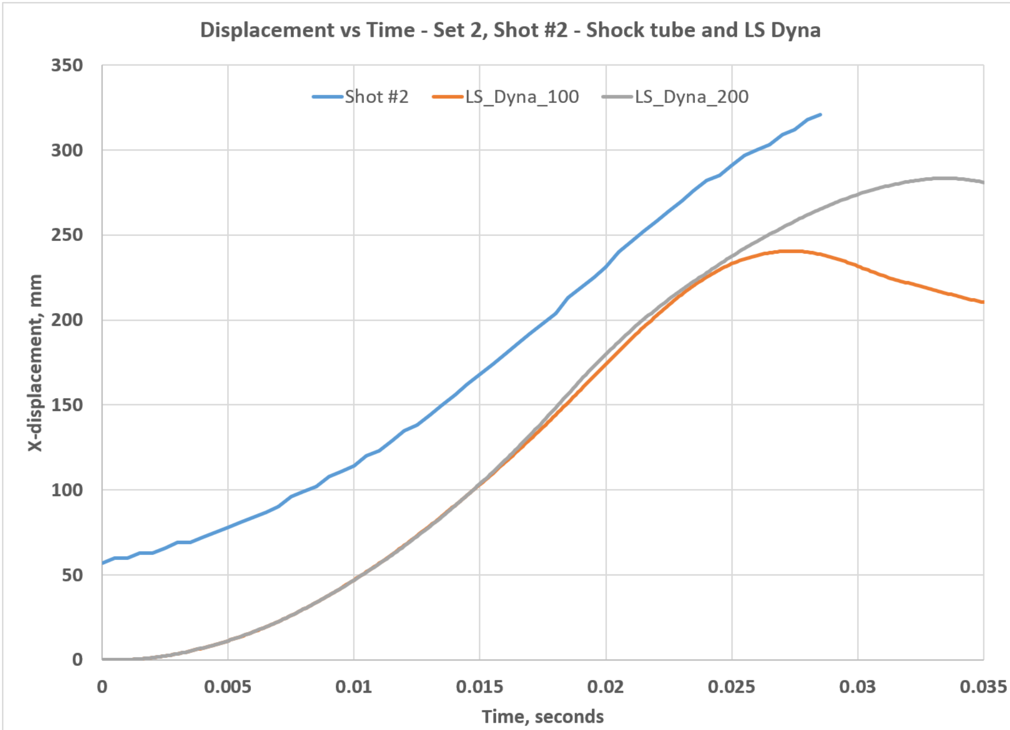

Figure 113: Displacement vs time curve of Shot #2, 677 kg at 57 m, Z = 6.5 m/kg1/3 (60 kPa and 668 kPa-ms)

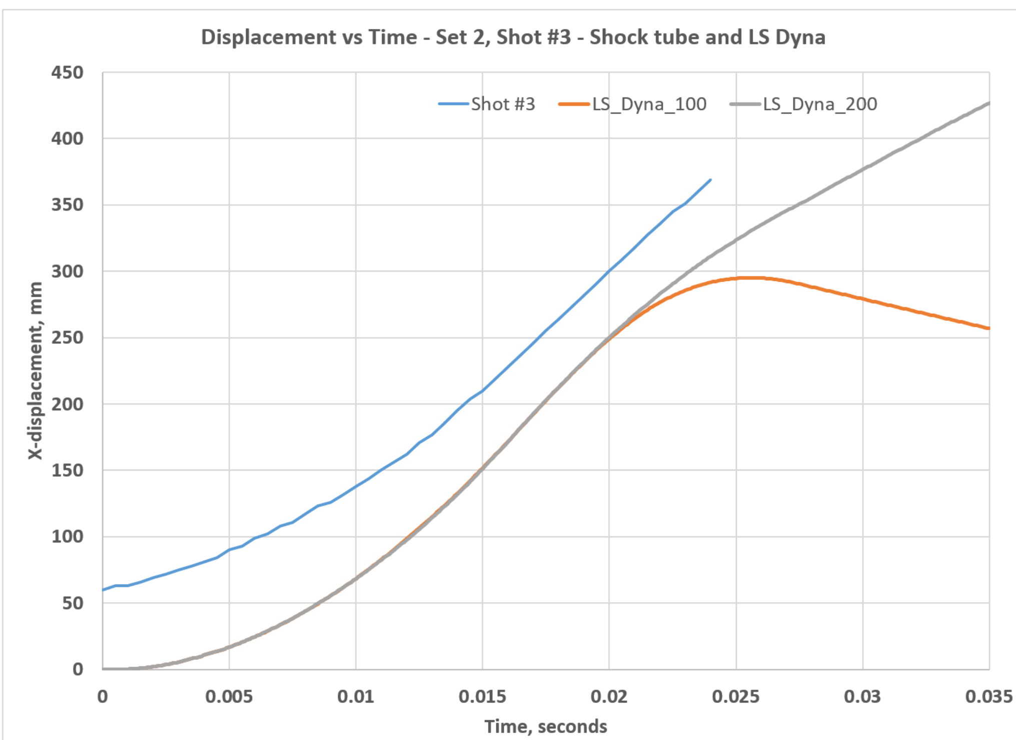

Figure 114: Displacement vs time curve of Shot #3, 1417 kg at 60 m, Z = 5.4 m/kg1/3 (85 kPa and 1048 kPa-ms)

4.2.3 Third Set of Specimens: Panels without HSS Members – 1.5 mm Steel

The third set of specimens had the same setup as the second set of specimens. However, in this set of specimens, the thickness of the steel plate between the ECC layers was 1.5 mm. Due to the smaller thickness of the steel plate, the capacity of the panels was lower compared to the panels with a 3 mm thick plate. This reduction in resistance was observed in the shock tube test results, as well as in the modelled specimens.

For the shock tube specimens, two of the specimens had connectors spaced at 100 mm and two at 200 mm. Both specimens that had a 200 mm connector spacing cracked in the first shot and failed by rupture and delamination. During the second and final shot, for both specimens, fragmentation of the delaminated pieces was observed. Of the two specimens that had 100 mm connector spacing, one failed by delamination and tension rupture of the ECC layer, while the other one did not fail. The specimen that did not fail exhibited tension cracks; however, delamination, rupture and fragmentation were absent.

The LS-Dyna models of these specimens had two variations of the contact algorithm to represent the 100 mm and 200 mm connector spacing. The same contact algorithm definition as the models used for the second set of specimens was used for these models. The LS-Dyna models exhibited behaviour that is similar to the shock tube specimens. The model representing the 100 mm connector spacing experienced cracking and tension rupture failure under the blast effects of the final shot of the shock tube specimens (**Figure 115**). This was considered to be an accurate representation of the behaviour of the shock tube specimen. Additionally, the maximum deformation of the panel before rupture (217 mm) is within 5% of the additional deformation (228 mm) measured for the shock tube specimen.

The model representing the 200 mm connector spacing also experienced delamination and rupture similar to the shock tube specimens (**Figure 116**). The measured deformation of the shock tube specimen before delamination and rupture, and the LS-Dyna model 2 deformation before the initiation of element deletion, differed by approximately 3% (233 mm vs 228 mm). This was considered to be a good correlation. The blast parameters of the LS-Dyna models and the shock tube specimens, along with the maximum deformation, are shown in **Table 13**.

The mid-height displacement versus time curves of both LS-Dyna models under the first and second shots are shown in **Figure 117** and **Figure 118** below. In both figures, the displacement of the shock tube specimens is also shown. It is important to note that LS-Dyna models were loaded from an undeformed state.

For the first shot, the slope of the ascending branch of the curves for both models matches the shock tube specimen curve up to 14 milliseconds. Beyond this time, the slope for the shock tube specimen curve is lower compared to the LS-Dyna model curves. Moreover, the maximum deformation values of the LS-Dyna curves are approximately 35% lower than the maximum deformation value of the shock tube specimen curve. Although the maximum deformation value calculated by LS-Dyna does not accurately represent the shock tube experiment result for this shot, the ascending stiffness showed good agreement.

For the second shot, similar to the first shot, LS-Dyna models predicted the ascending slope accurately. Furthermore, the additional deformation experienced by the shock tube specimens before failure was within 5% of the maximum deformation calculated by the LS-Dyna models before the front ECC layer ruptured. For LS-Dyna model 1, simulating the 100 mm connector spacing, rupture of the front ECC layer occurs at 22 ms with a mid-height deformation of 217 mm.

For the LS-Dyna model 2, simulating the 200 mm connector spacing, the ruptured portion of the ECC layer continues to move after its detachment from the panel, causing the displacement value to continue increasing. The rupture of the ECC layer had occurred at 23 ms, when the mid-height deformation was 233 mm. Due to the good agreement of the maximum deformation value of the LS-Dyna models with the additional deformation value of the shock tube specimens, and the mode of failure, these LS-Dyna models were considered to accurately represent the failure of the shock tube specimens.

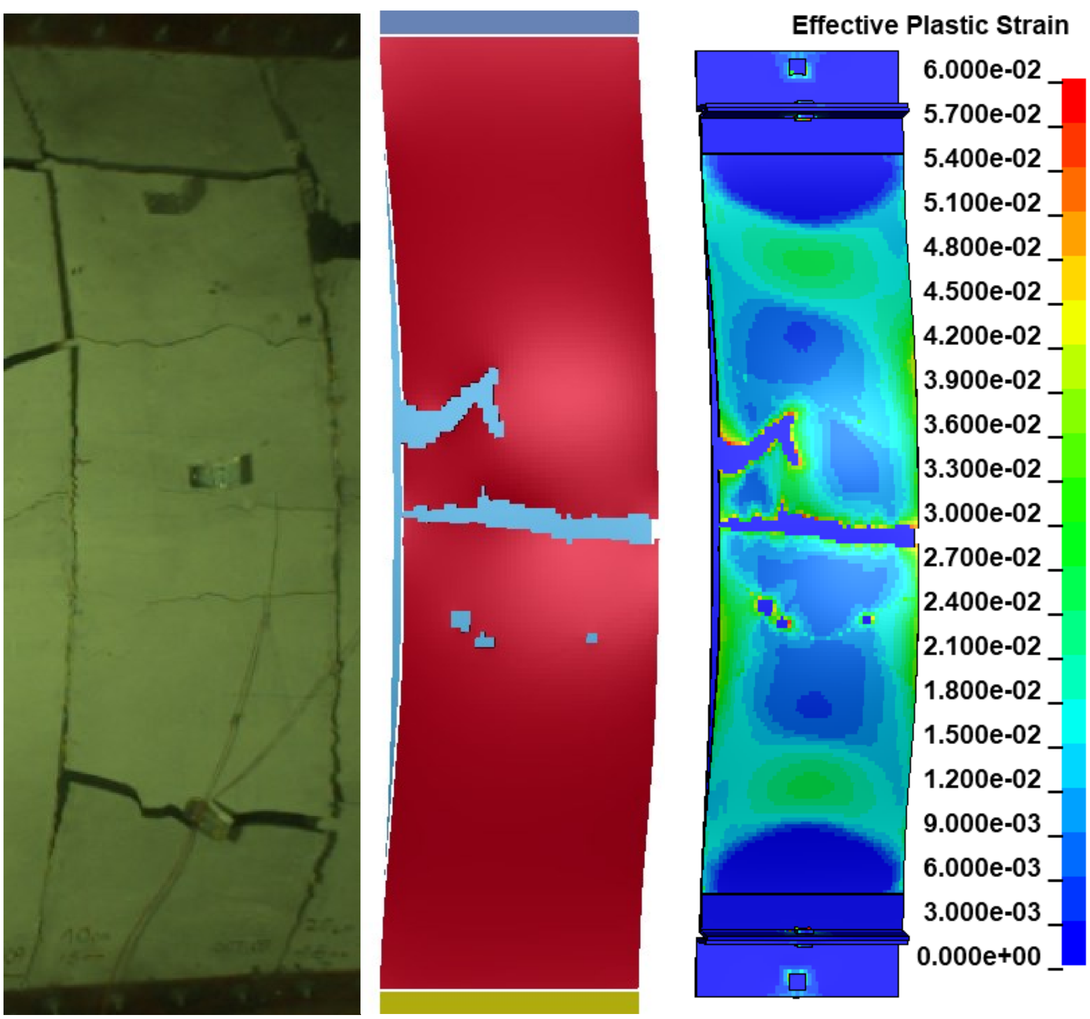

Figure 115: Shock tube tested specimen with 100 mm connector spacing (left), and LS-Dyna modelled specimen (center, right) subjected to a blast load with the 398 kg TNT weight and 47 metre standoff distance, Z = 6.4 m/kg$^{1/3}$ (63 kPa and 577 kPa-ms)

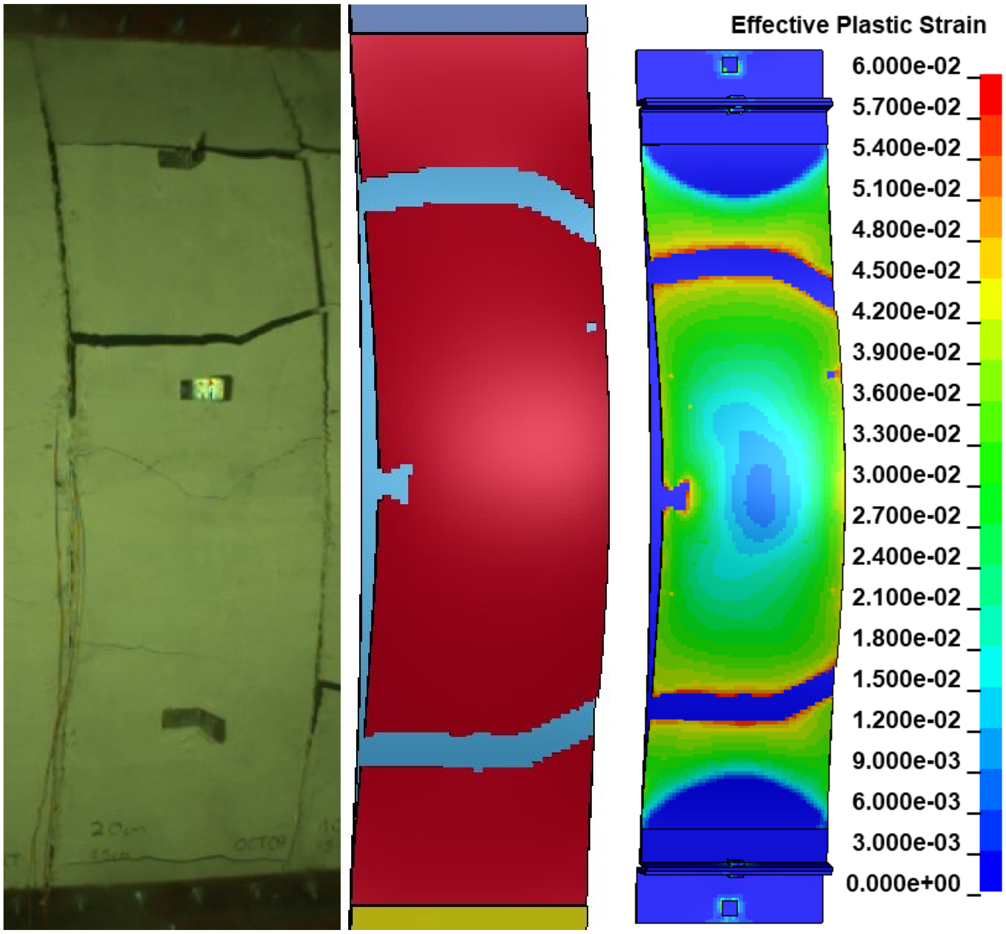

Figure 116: Shock tube tested specimen with 200 mm connector spacing (left), and LS-Dyna modelled specimen (center, right) subjected to a blast load with the 398 kg TNT weight and 47 metre standoff distance, Z = 6.4 m/kg$^{1/3}$ (63 kPa and 577 kPa-ms)

Table 13: Shock tube 3rd Set of Specimens vs. LS-Dyna Models comparison for shot #2

	LS-Dyna Model 1	**Shock tube Specimen 1**	**LS-Dyna Model 2**	**Shock tube Specimen 2**
Contact Capacity / Connector Spacing	1.1 MPa	100 mm	0.55 MPa	200 mm
Initial Deformation, mm	0 mm	186 mm	0 mm	186 mm
Maximum Deformation, mm	217 mm (before rupture)	414 mm	233 mm (before rupture)	414 mm (before rupture)
Additional Deformation, mm	217 mm (before rupture)	228 mm	233 mm (before rupture)	228 mm (before rupture)
Equivalent Charge Weight (kg), Standoff Distance (m) (Reflected Pressure; Impulse)	398 kg, 47 m (63 kPa, 577 kPa-ms)	398 kg, 47 m (63 kPa, 577 kPa-ms)	398 kg, 47 m (63 kPa, 577 kPa-ms)	398 kg, 47 m (63 kPa, 577 kPa-ms)
Scaled Distance (m / kg$^{1/3}$)	6.4	6.4	6.4	6.4

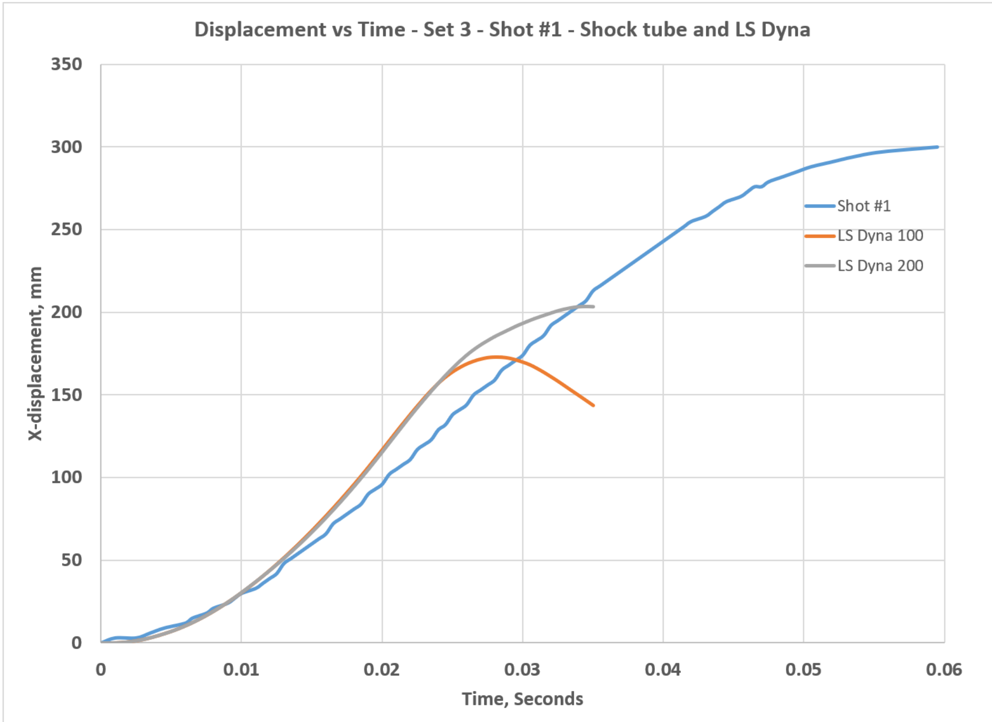

Figure 117: Displacement vs time curve of Shot #1, 214 kg at 55 m, Z = 9.2 m/kg$^{1/3}$ (35 kPa and 320 kPa-ms)

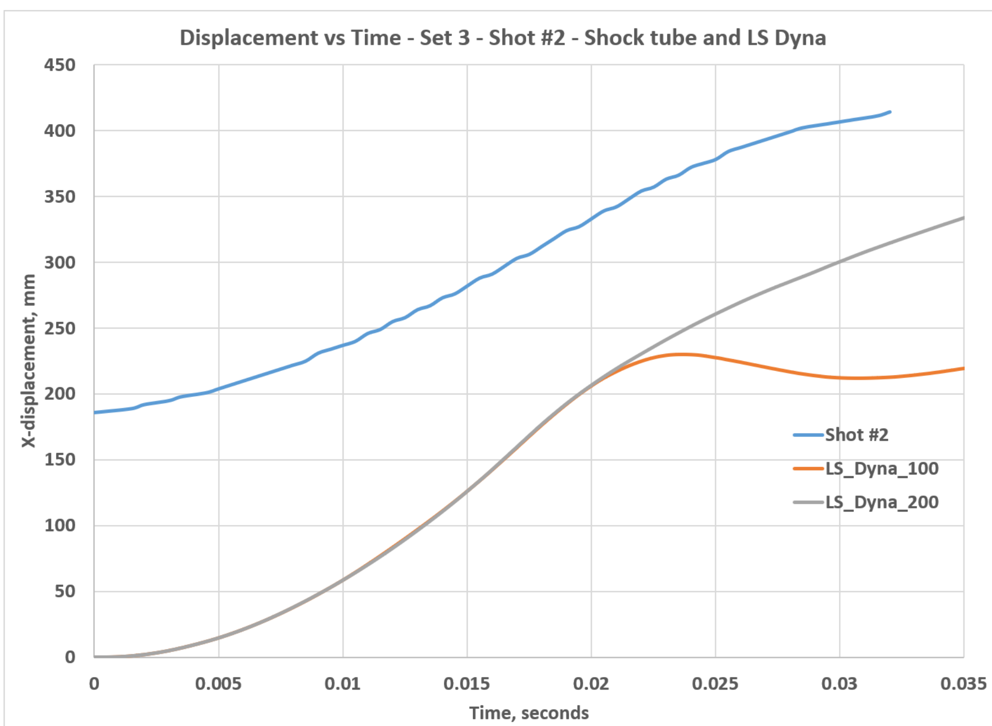

Figure 118: Displacement vs time curve of Shot #2, 398 kg at 47 m, Z = 6.4 m/kg$^{1/3}$ (63 kPa and 577 kPa-ms)

4.2.4 Fourth Set of Specimens: Panels with HSS Members on Both Faces – 1.5 mm Steel

The fourth set of specimens in the shock tube had an HSS member at the front and back of the ECC-Steel-ECC panels. There were threaded rods that connected all layers between the exterior face of the HSS at the front to the exterior face of the HSS at the back. These screws prevented the edges of the ECC layers under the HSS members from delaminating. Therefore, in the shock tube specimens, ECC delamination was not observed. However, tension cracks at the mid-height of the ECC layer were observed after the third and final shot (86 kPa, 1139 kPa-ms, $Z = 5.3\ m/kg^{1/3}$) for specimens both having a connector spacing of 100 mm and 200 mm.

The LS-Dyna models representing this set of specimens had the same contact formulation as the previously reported specimens. Contact stresses of 1.1 MPa and 0.55 MPa were used to represent specimens with 100 mm and 200 mm connector spacing, respectively.

Under the blast load corresponding to the third shot, the deformation pattern of the LS-Dyna Model 1, which represented the 100 mm connector spacing specimen, was similar to the shock tube specimen (**Figure 119**). The panel experienced flexural behaviour in both the long and short spans. The short span bending occurred between the HSS members, and the long span bending occurred along the HSS members.

The LS-Dyna Model 2, which represented the 200 mm connector spacing specimen, exhibited a similar behaviour to Model 1 under the loading of the third shot. Delamination of the ECC was not observed; the panel and HSS deformed under flexure. The HSS members exhibited flexural bending behaviour, and the panels experienced bending along the short and long spans. The behaviour of this LS-Dyna model was consistent with the behaviour of the shock tube specimen

(**Figure 120**). The deformation values of the LS-Dyna models and the shock tube specimens for the third shot are provided in **Table 14**.

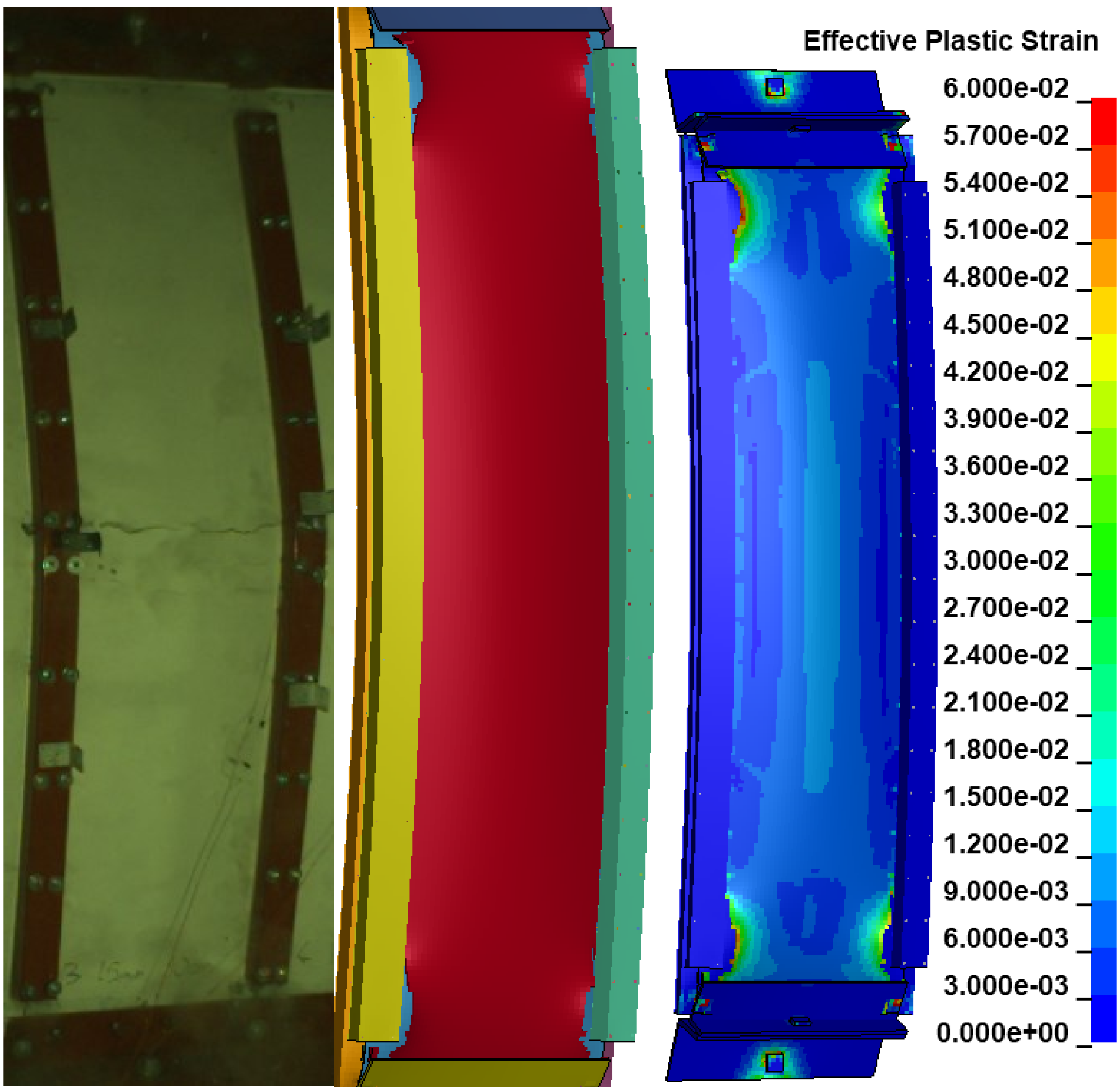

Figure 119: Shock tube tested specimen with 100 mm connector spacing (left), and LS-Dyna modelled specimen (center, right) subjected to a blast load with the 1787 kg TNT weight and 65 metre standoff distance, Z = 5.3 m/kg$^{1/3}$ (86 kPa and 1139 kPa-ms)

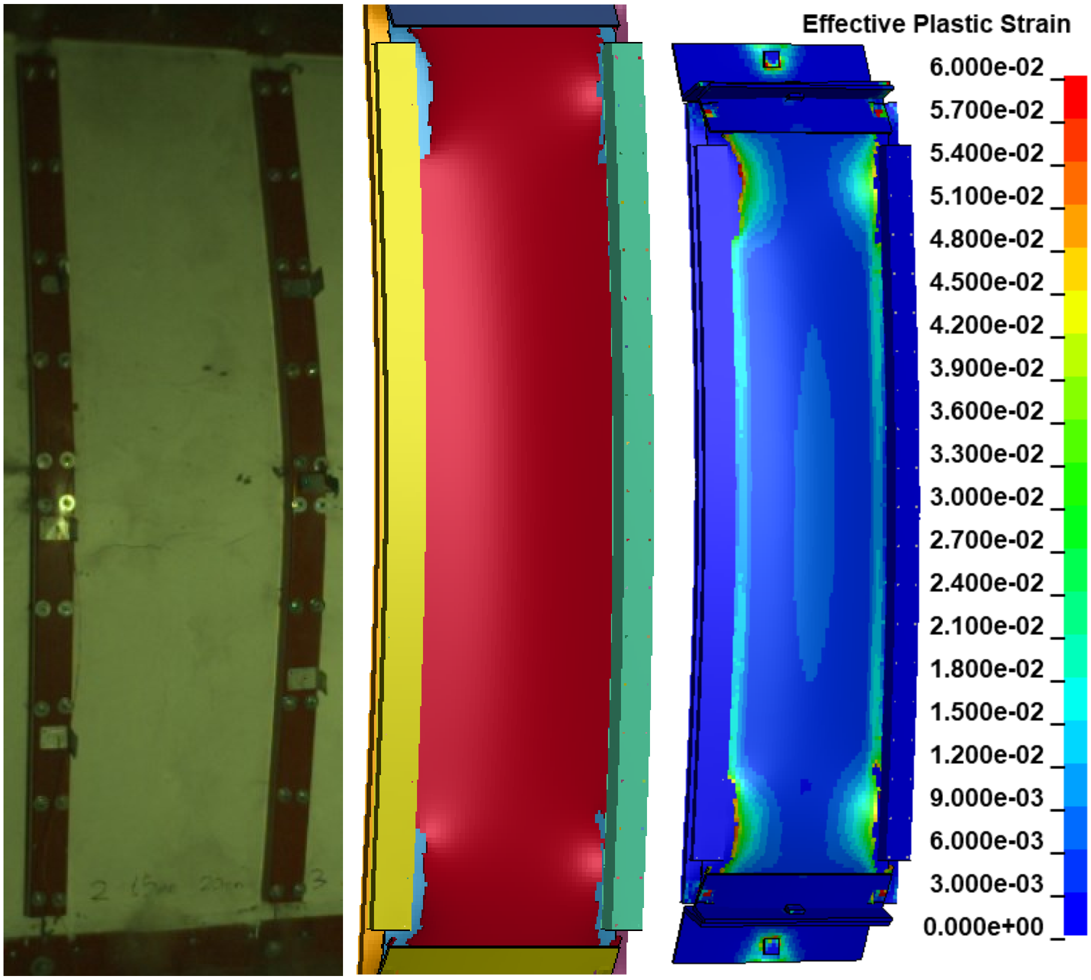

Figure 120: Shock tube tested specimen with 200 mm connector spacing (left), and LS-Dyna modelled specimen (center, right) subjected to a blast load with the 1787 kg TNT weight and 65 metre standoff distance, Z = 5.3 m/kg$^{1/3}$ (86 kPa and 1139 kPa-ms)

The mid-height displacement vs time curves of both LS-Dyna models under the blast load representing all three shots are shown in **Figure 121** to **Figure 123**. The displacement of the corresponding shock tube specimen is also provided. It is important to note that LS-Dyna models were loaded from an undeformed state and do not have residual deformation. However, the slope of the curves shows good agreement. Furthermore, the time to reach the maximum deformation agrees well between the shock tube specimen and the LS-Dyna models. This agreement is considered to indicate a match of the dynamic properties of the model and the shock tube specimen.

Table 14: shock tube 4th Set of Specimens vs. LS-Dyna Models comparison for shot #3

	LS-Dyna Model 1	Shock tube Specimen 1	LS-Dyna Model 2	Shock tube Specimen 2
Contact Capacity / Connector Spacing	1.1 MPa	100 mm	0.55 MPa	200 mm
Initial Deformation, mm	0 mm	33 mm	0 mm	33 mm
Maximum Deformation, mm	116 mm	211 mm	116 mm	211 mm
Additional Deformation, mm	116 mm	178 mm	116 mm	178 mm
Equivalent Charge Weight (kg), Standoff Distance (m) (Reflected Pressure, Impulse)	1787 kg, 65m (86 kPa, 1139 kPa-ms)	1787 kg, 65 m (86 kPa, 1139 kPa-ms)	1787 kg, 65 m (86 kPa, 1139 kPa-ms)	1787 kg, 65 m (86 kPa, 1139 kPa-ms)
Scaled Distance (m / kg$^{1/3}$)	5.3	5.3	5.3	5.3

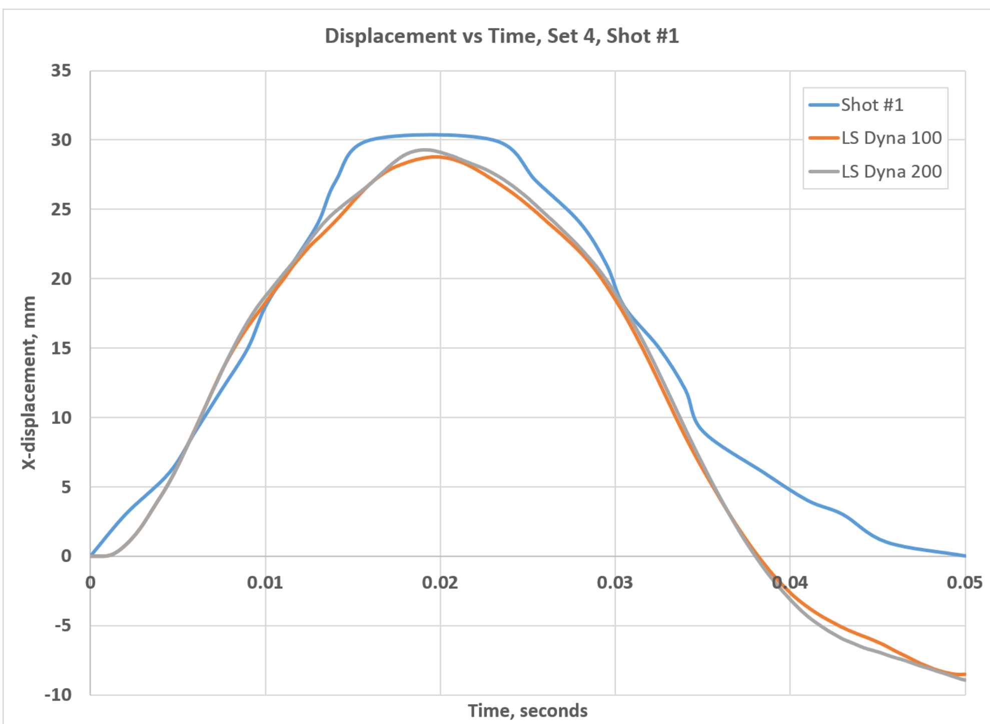

Figure 121: Displacement vs time curve of Shot #1, 399 kg at 67 m, Z = 9.0 m/kg$^{1/3}$ (36 kPa and 402 kPa-ms)

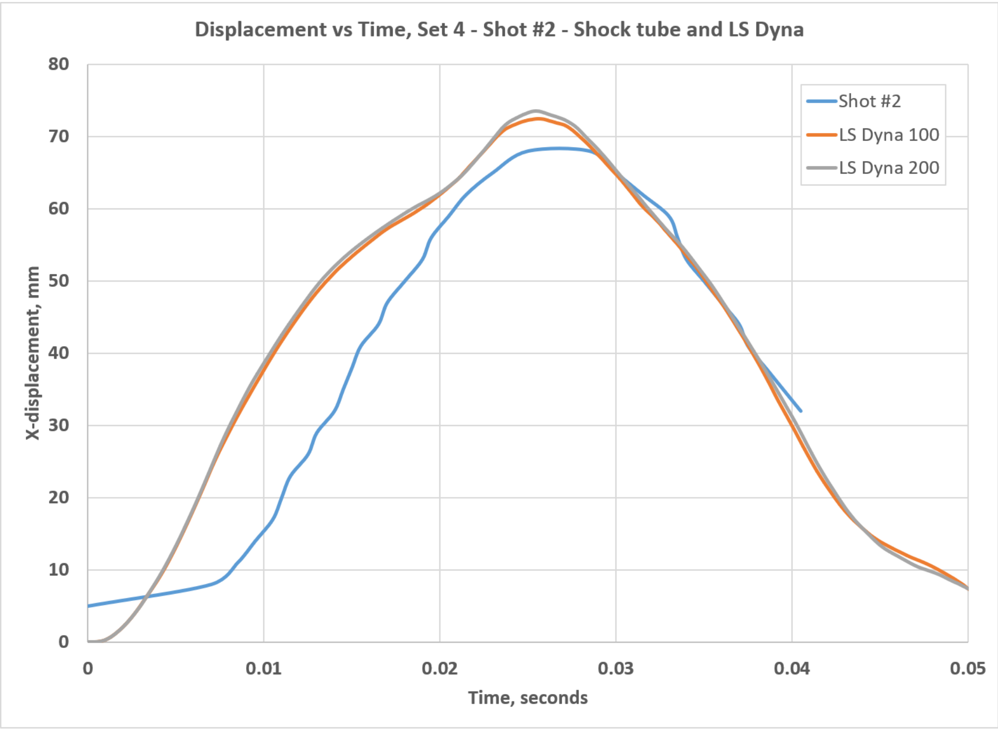

Figure 122: Displacement vs time curve of Shot #2, 777 kg at 59 m, Z = 6.4 m/kg$^{1/3}$ (62 kPa and 714 kPa-ms)

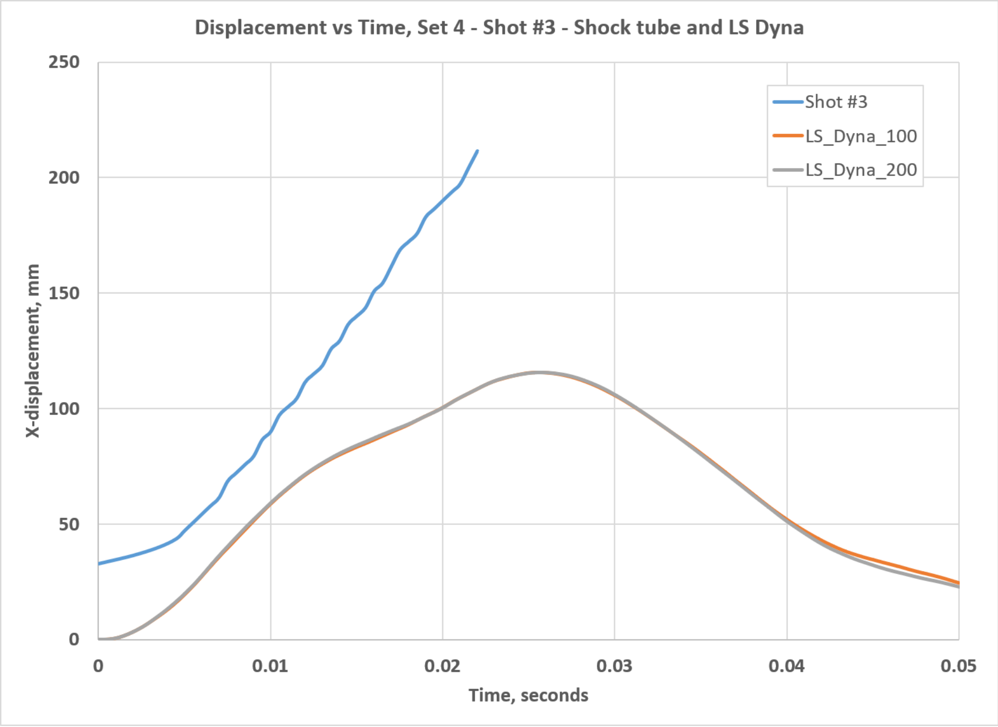

Figure 123: Displacement vs time curve of Shot #3, 1787 kg at 65 m, Z = 5.3 m/kg$^{1/3}$ (86 kPa and 1139 kPa-ms)

4.2.5 Fifth Set of Specimens: 1.5 mm and 3 mm Steel Sheets without ECC

The fifth set of specimens consisted of 1.5 mm and 3 mm thick steel sheets, without the ECC layers. This set of specimens was tested to observe the effects of the absence of ECC layers and compare the results with those of ECC-Steel-ECC panel specimens.

The LS-Dyna models for these specimens were similar to those of the second set of specimens. The ECC layers were removed from the model, and the steel sheets were connected to the support angles.

During the shock tube experiments, the steel sheets had failed by buckling. This behaviour was observed due to the steel sheet yielding under tension loads during the loading phase and becoming longer than its initial length. As the distance between the supports had not changed, the elongated sheets experienced compression forces when they returned to their original positions. Due to the extreme slenderness of the sheets, under the compression forces, they buckled.

In the LS-Dyna models, the yielding of the sheets in tension was also observed. The maximum deformation of the steel sheets was observed to be similar to that measured during the shock tube experiments. The deformed shape of the LS-Dyna Model 1, representing the 3 mm thick steel sheet, is shown below in **Figure 124**. The deformed shape of the 1.5 mm thick steel sheet tested in the shock tube and its corresponding LS-Dyna modelled representation are shown **Figure 125**.

The measured deformations of the shock tube specimens and the modelled specimens, along with the blast parameters, are shown in **Table 15** below. The displacement vs time curve of the LS-Dyna models under each shot, along with the displacement of the shock tube specimens, is shown in **Figure 126** and **Figure 127**. For the first shot, the ascending branch of the displacement vs time curve of the LS-Dyna models is within 10% of the shock tube specimen curve. The maximum displacement value predicted by the LS-Dyna models is approximately 35% less than the maximum deformation measured for the shock tube specimen. For shot 2, the LS-Dyna models indicate higher stiffness compared to the shock tube specimen. The maximum deformation values of the LS-Dyna models are within 20% of the value measured for the shock tube specimens. Based on the overall agreement of the displacement vs time curve of the LS-Dyna models with the shock tube specimen results, the LS-Dyna models were considered to predict the failure accurately.

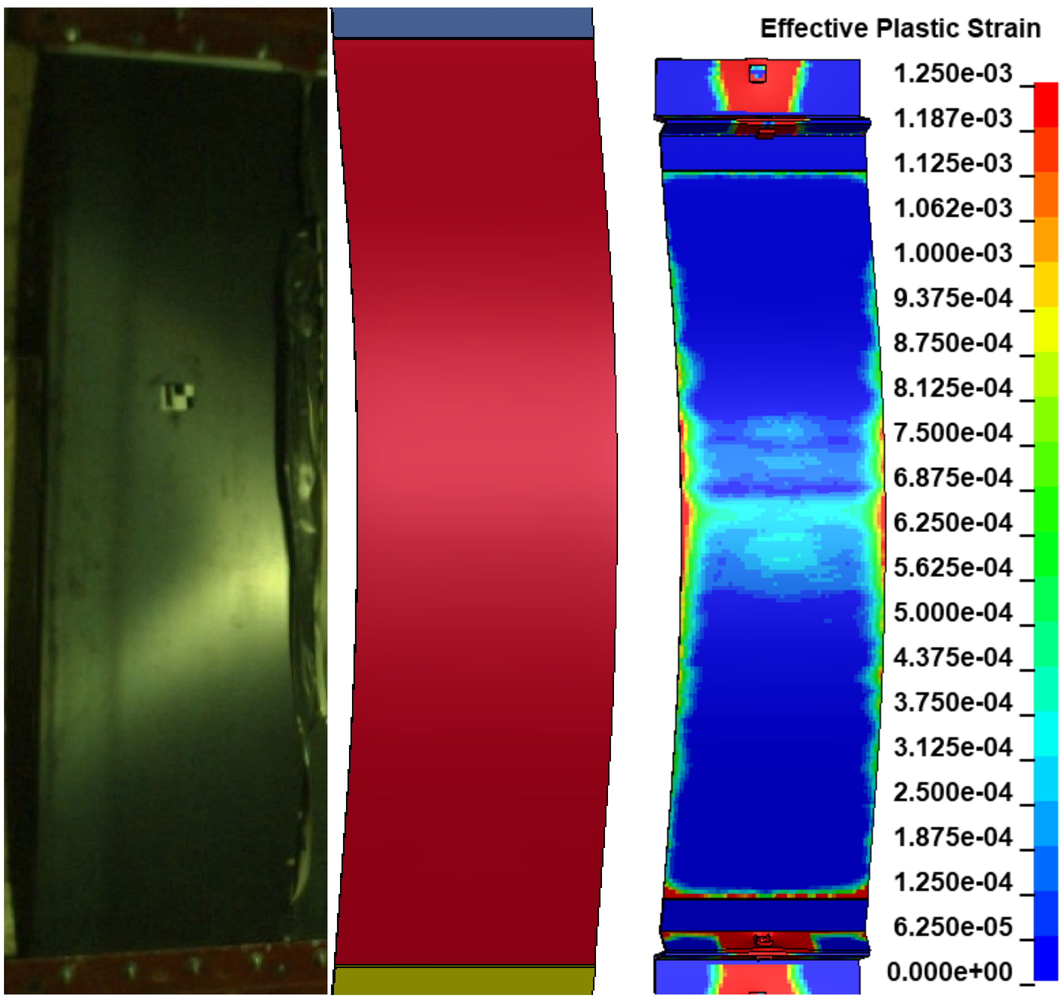

Figure 124: Shock tube tested 3 mm thick steel sheet (left), and LS-Dyna modelled specimen (center, right) subjected to a blast load with the 244 kg TNT weight and 40 metre standoff distance, Z = 6.4 m/kg$^{1/3}$ (62 kPa and 485 kPa-ms)

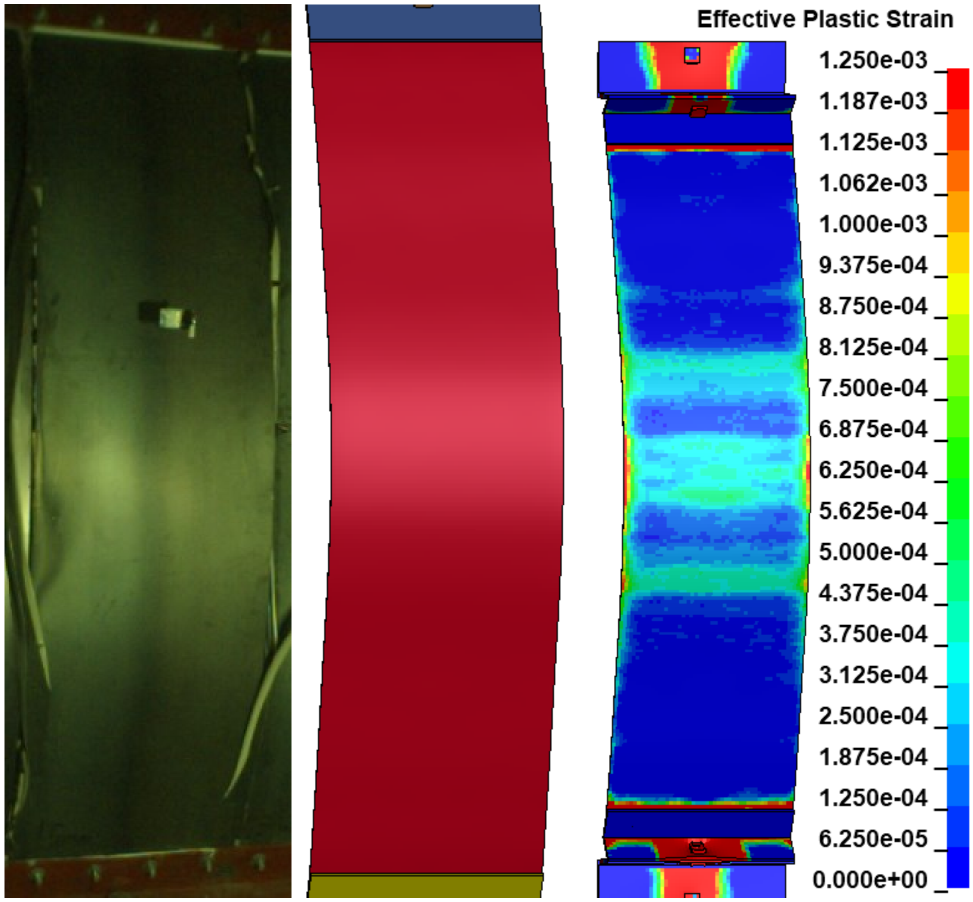

Figure 125: Shock tube tested 1.5 mm thick steel sheet (left), and LS-Dyna modelled specimen (center, right) subjected to a blast load with the 244 kg TNT weight and 40 metre standoff distance, Z = 6.4 m/kg$^{1/3}$ (62 kPa and 485 kPa-ms)

Table 15: Shock tube 5th Set of Specimens vs. LS-Dyna Models comparison for shot #2

	LS-Dyna Model 1	**Shock tube Specimen 1**	**LS-Dyna Model 2**	**Shock tube Specimen 2**
Initial Deformation, mm	0 mm	10 mm	0 mm	10 mm
Maximum Deformation, mm	317 mm	406 mm	342 mm	406 mm
Additional Deformation, mm	317 mm	396 mm	342 mm	396 mm
Equivalent Charge Weight (kg), Standoff Distance (m) (Reflected Pressure, Impulse)	244 kg, 40 m (62 kPa, 485 kPa-ms)	244 kg, 40 m (62 kPa, 485 kPa-ms)	244 kg, 40 m (62 kPa, 485 kPa-ms)	244 kg, 40 m (62 kPa, 485 kPa-ms)
Scaled Distance (m / kg$^{1/3}$)	6.4	6.4	6.4	6.4

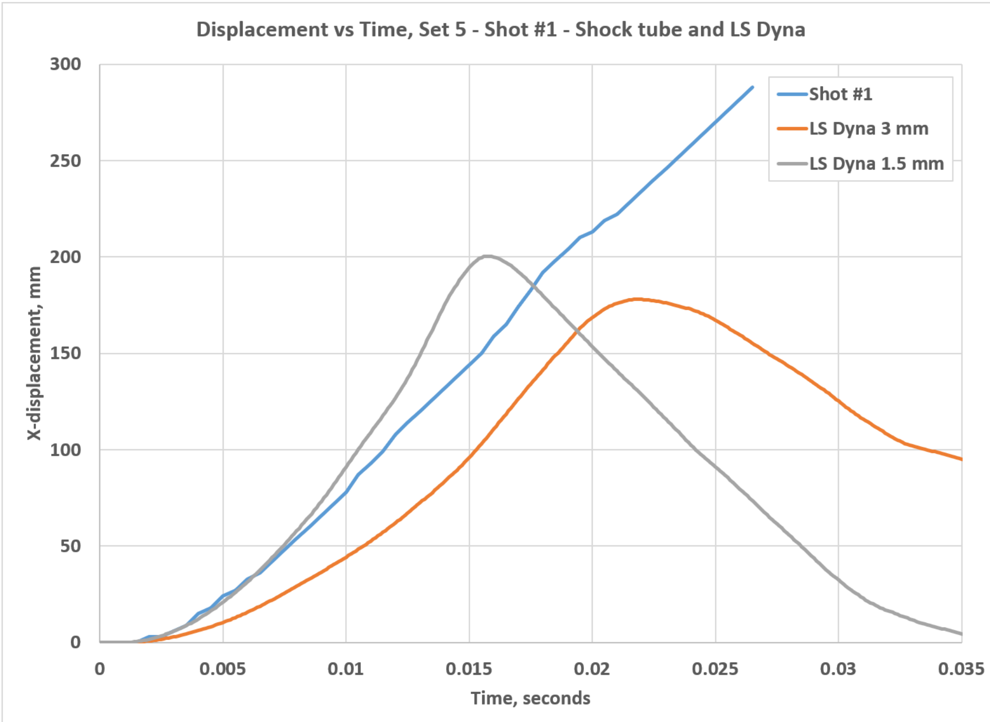

Figure 126: Displacement vs time curve of Shot #1, 138 kg at 51 m, Z = 9.8 m/kg$^{1/3}$ (32 kPa and 260 kPa-ms)

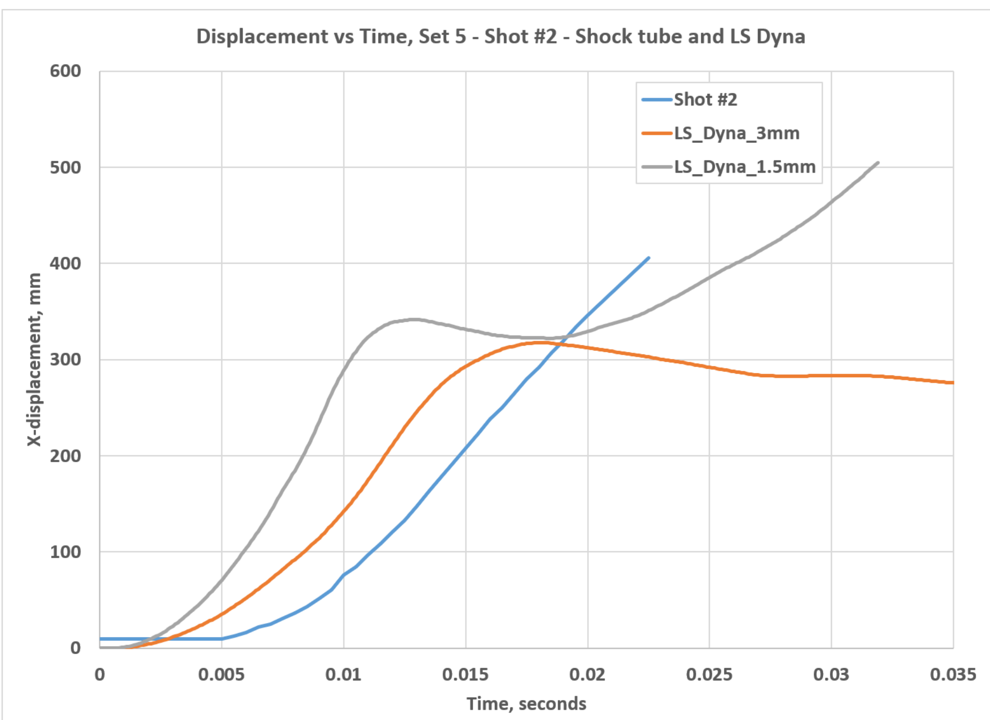

Figure 127: Displacement vs time curve of Shot #2, 244 kg at 40 m, Z = 6.4 m/kg$^{1/3}$ (62 kPa and 485 kPa-ms)

4.3 Parametric Finite Element Analysis Study

The parametric investigation aimed to include finite element analysis of selected specimens and load configurations that were not included in the shock tube test program. This was done by using the element models that had already been validated against test data. The parametric investigation facilitated the prediction of the behaviour of different configurations of panels under different blast loads. Furthermore, it also enabled the identification of panel properties that could be optimized to further enhance the performance of the panels and the wall systems. The details of the LS-Dyna models considered in the parametric investigation are provided in the preceding sections.

4.3.1 HSS Member with 3 mm steel sheet without ECC layers

This finite element model resembled the first set of test specimens, with the only difference being the absence of ECC layers. The intent was to observe the effect of ECC layers on the performance of the panels and the wall system. The same pressure time history that was applied to the first set of test specimens presented in the section **4.2.1 First Set of Specimens: Panels with HSS Members – 3mm Steel,** was also applied to this model to allow comparisons of results. The deformed shape of the LS-Dyna model without the ECC layer is shown side by side with the model with ECC-steel-ECC panel in **Figure 128**. Both models have the same deformation pattern.

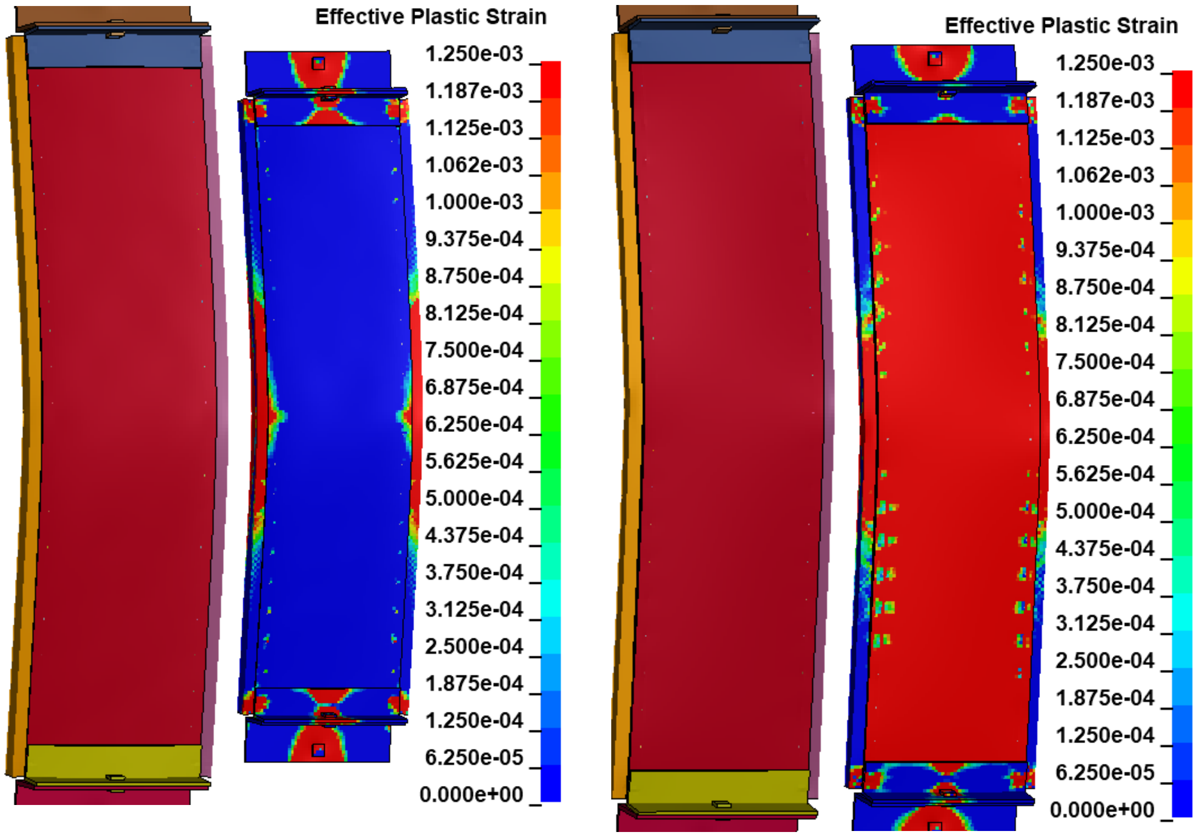

Figure 128: Deformed shape of LS-Dyna model with HSS member and 3 mm steel sheet without ECC layers (left), Set 1 specimen 3 mm steel sheet with ECC-Steel-ECC panel (right) under the blast effect of 1567 kg TNT at 64 m, Z = 5.5 m/kg$^{1/3}$ (82kPa, 1066 kPa-ms)

Table 16: Deformation results for shock tube Set 1 Specimen, LS-Dyna Model for Set 1, LS-Dyna Model without ECC

	Shock tube Specimen Set 1 – 3 mm with HSS	**LS-Dyna Model – ECC-Steel-ECC panel with HSS**	**LS-Dyna Model – 3 mm Steel Sheet with HSS**	**LS-Dyna Model – ECC-Steel-ECC panel with HSS**	**LS-Dyna Model – 3 mm Steel Sheet with HSS**
Initial Deformation, mm	54 mm	0 mm	0 mm	0 mm	0 mm
Maximum Deformation, mm	247 mm	175 mm	179 mm	75 mm	95 mm
Additional Deformation, mm	193 mm	175 mm	179 mm	75 mm	95 mm
Equivalent Charge Weight (kg) and Distance (m)	1567 kg, 64m (82kPa, 1066 kPa-ms)	1567 kg, 64m (82kPa, 1066 kPa-ms)	1567 kg, 64m (82kPa, 1066 kPa-ms)	162 kg, 30m (82kPa, 500 kPa-ms)	162 kg, 30m (82kPa, 500 kPa-ms)
Scaled Distance (m/kg$^{1/3}$)	5.5	5.5	5.5	5.5	5.5

The maximum deformation values of the specimen tested in the shock tube, the corresponding LS-Dyna model, and the LS-Dyna model without the ECC layers are shown below in **Table 16**. The model was first analyzed under a maximum reflected pressure of 82 kPa with a duration of 26 ms, with a corresponding impulse of 1066 kPa-ms, as in the case of the experiment. The results indicate that the maximum deformation of the steel-only model is only 3% higher than the maximum deformation of the ECC-Steel-ECC panel. The time to reach maximum deformation of the steel only panel was 24 ms, whereas for the ECC-Steel-ECC panel it was 30 ms. The steel only panel showed a reduction in the fundamental period of vibration. While the response obtained from the two models under a blast load with 26 ms duration is similar within this period range, the change in duration of loading may potentially generate a more significant effect. This shortening of the period could become a disadvantage when the blast duration is much shorter, as in the case of backpack bombs. This disadvantage stems from the reduced resistance requirement when the fundamental period of vibration of the system is much greater than the duration of the load. This phenomenon is summarized in **Figure 129** below from UFC 3-340-02, 2008. As the fundamental period of vibration (**T_N**) of a single degree of freedom system increases, the required ductility ratio (ultimate deformation over yield deformation, **X_m / X_E**) decreases for a constant resistance over load (**r_u / P**) ratio. In other words, for two systems with the same capacity (**r_u**) and ductility ratios (**X_m / X_E**), the one with a smaller load duration over period (**T / T_N**) resists higher loads. For example, for a system with a ductility ratio of 5 and a **T / T_N** ratio of 0.4, the **r_u / P** ratio is obtained from **Figure 129** to be approximately 0.35. If the load is 100 kN, the system should have a resistance of 35 kN to avoid failure. However, if the period was reduced by 25% and the **T / T_N** ratio becomes 0.5, the **r_u / P** ratio is read to be approximately 0.45. Hence, the resistance of the system should be 45 kN to avoid failure. In this example, a 25% shorter vibration period would require the panel resistance to increase by approximately 28%. Therefore, for shorter duration blasts, where the standoff distance is small, a reduced vibration period could be considered a disadvantage.

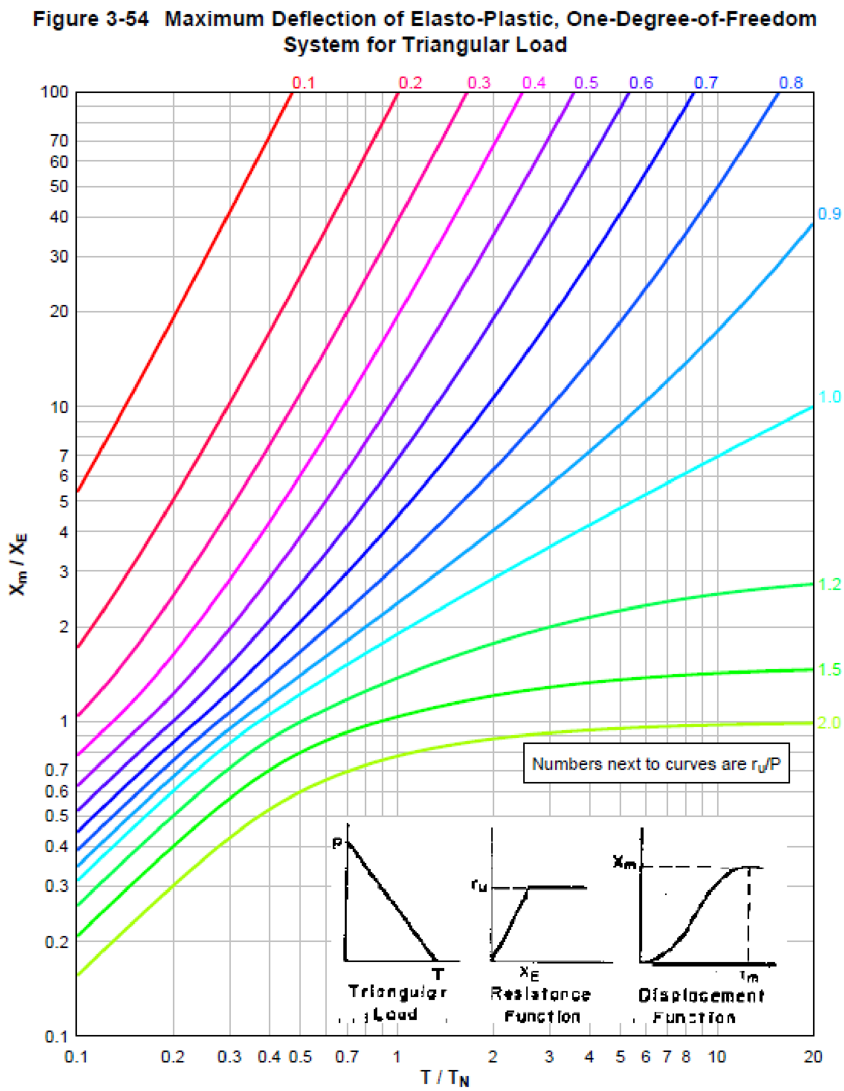

Figure 129: Required ductility ratio versus load duration to vibration period chart of elasto-plastic systems **(UFC 3-340-02, 2008)**

In order to illustrate the beneficial effects of a higher period of vibration for a short duration blasts, the LS-Dyna models for the HSS member with a 3 mm thick steel sheet were loaded with a shorter duration blast. This blast load had a peak reflected pressure of 82 kPa and a reflected impulse of

500 kPa-ms with a positive duration of 12 ms. This corresponded to a TNT weight of 162 kg and a standoff distance of 30 metres, and a scaled distance of 5.5 m/kg$^{1/3}$. The maximum deformation of the specimen with ECC had a maximum deformation of 75 mm, whereas the steel only specimen had a maximum deformation of 95 mm, illustrating the beneficial effect of an increased period of vibration for short duration blast loads.

Moreover, this numerical analysis does not consider the additional protection provided by the ECC layer against forced entry. The cementitious nature of the ECC layer has a blunting effect on drilling and cutting tools and would significantly delay cutting through the panel. Furthermore, the ECC layer provides effective protection against impact with a sledgehammer. This phenomenon was observed during the removal of the tested specimens from the shock tube (**Figure 69**).

4.3.2 Panel-only specimens with higher contact strength

This finite element model was based on the second set of specimens tested in the shock tube (**3.5.2 Second Set of Specimens**). The variation in this model was a higher contact strength of 2.75 MPa, such that delamination of ECC layers from the steel layer was prevented. This corresponded to a closer connector spacing of 55 mm. For this specific case, the same amount of normal stress capacity was included in the contact definition. This normal stress capacity of contact was assumed to represent connectors with a wide cap, which would provide resistance against the out-of-plane movement of the ECC layer. The lack of delamination represented a panel which remains fully composite even under higher blast loads.

The analysis of the LS-Dyna model indicated that the increased contact capacity has significantly improved the resistance of the panel under blast loads. Under the same load, the enhanced contact panel did not experience any delamination, and none of the elements reached the deletion strain, hence did not fail (**Figure 130**). The maximum deformation was calculated to be 298 mm, which is 1% more than the maximum deformation observed in the LS-Dyna model representing the second set of specimens with 100 mm connector spacing.

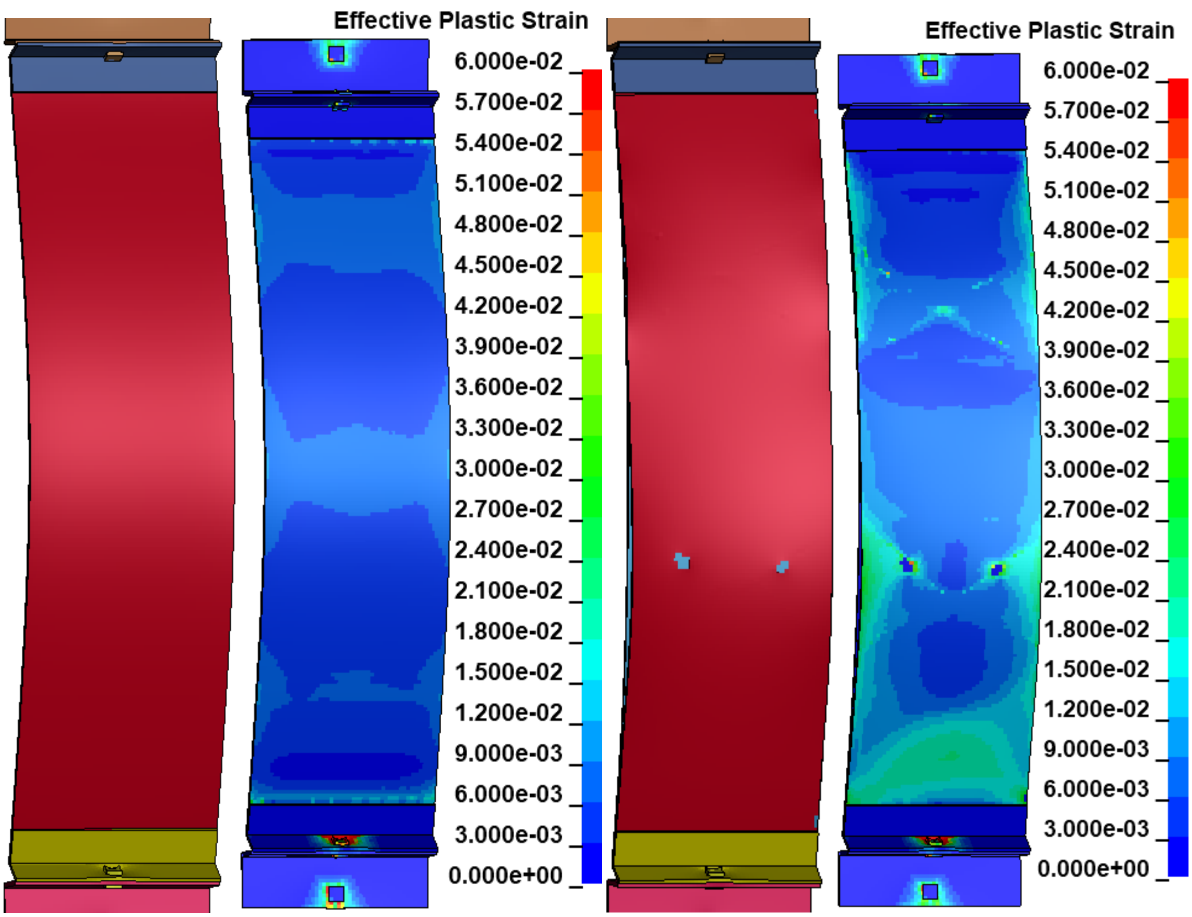

Figure 130: Deformed shape of LS-Dyna model with enhanced contact (left), Set 2 specimen representing 100 mm connector spacing (right) under the blast effect of 1417 kg TNT at 60 m, Z = 5.4 m/kg$^{1/3}$ (85 kPa and 1048 kPa-ms)

To demonstrate performance under higher blast loads, a second LS-Dyna model was prepared, in which the equivalent TNT weight was quadrupled to 5666 kg, keeping the same standoff distance, resulting in a maximum pressure of 239 kPa and a positive impulse of 2725 kPa-ms, corresponding to a scaled distance of 3.4 m/kg$^{1/3}$. Under this level of increased blast loading, the ECC layers failed at the supports as indicated by the erosion of the elements (**Figure 131**). However, delamination of ECC layers was not observed. The panel reached a maximum deformation of 489 mm.

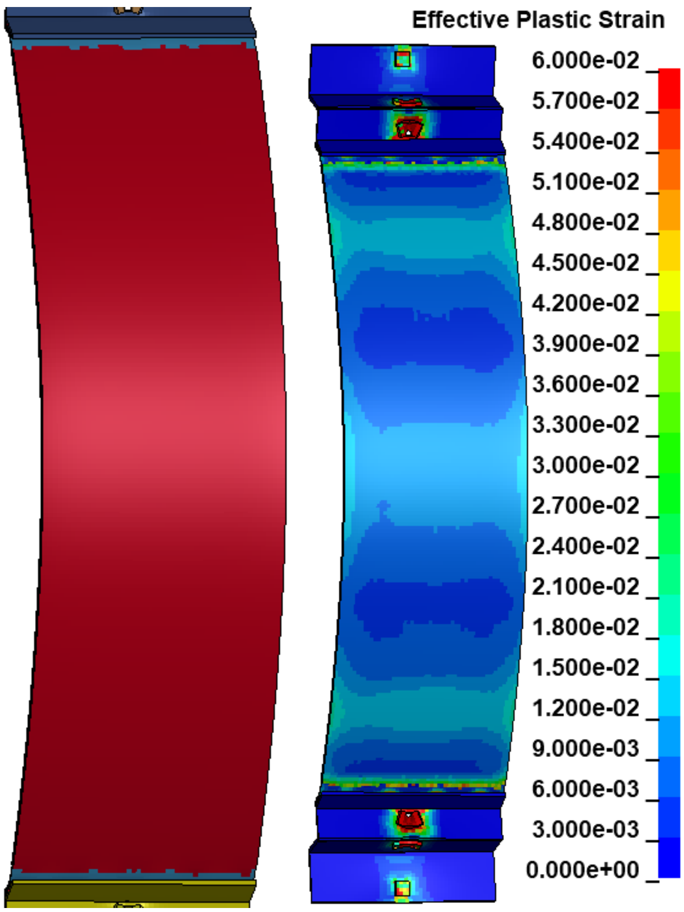

Figure 131: Deformed shape of the enhanced panel (left), deformed shape showing the effective plastic strain (right) under the blast effect of 5666 kg TNT at 60 m, Z = 3.4 m/kg$^{1/3}$ (239 kPa and 2725 kPa-ms)

The results from the LS-Dyna models for the standard contact specimen and the enhanced contact specimens are summarized in **Table 17**. The results clearly indicate that enhanced contact capacity increases the resistance of the panels. Enhanced contact capacity would potentially enable thicker layers of ECC to be used. Thicker layers of ECC would generate greater inertial forces, which may in turn cause delamination, which could be resisted by the higher contact capacity.

Table 17: LS-Dyna results for panel with 100 mm connector spacing and enhanced contact panels

	LS_Dyna Model for specimen with 100 mm connector spacing	LS-Dyna Model for enhanced contact specimen	LS-Dyna Model for enhanced contact specimen with quadrupled charge weight
Maximum Deformation, mm	295 mm (before rupture)	298 mm	489 mm
Equivalent Charge Weight (kg) and Distance (m)	1417 kg, 60 m (85 kPa, 1048 kPa-ms)	1417 kg, 60 m (85 kPa, 1048 kPa-ms)	5666 kg, 60 m (239 kPa, 2725 kPa-ms)
Scaled Distance (m / kg$^{1/3}$)	5.4	5.4	3.4

4.3.3 Panel-only specimens with 12 mm thick ECC layers

This specimen was modelled to observe the effects of using panels with thicker ECC layers, in this case, 12 mm thick, which resulted in a total specimen thickness of 27 mm. By increasing the thickness of ECC layers, the inertia forces associated with the dynamic loading were also increased. Therefore, when the contact formulation representing 100 mm connector spacing was used, the front ECC layer delaminated (**Figure 132**).

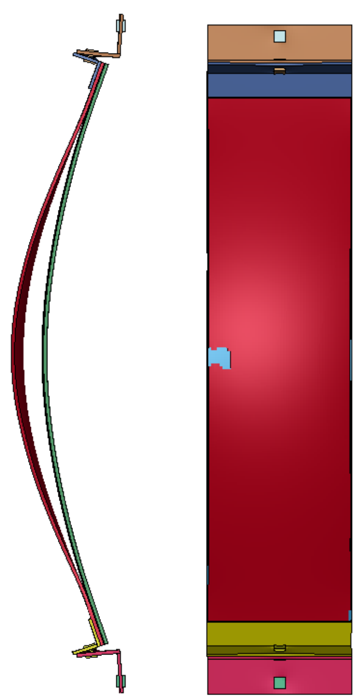

Figure 132: Deformed shape of the LS-Dyna model of the 27 mm thick specimen side (left) and front (right) using the contact formulation representing the 100 mm connector spacing, under 1417 kg TNT at 60 m blast load, Z = 5.4 m/kg$^{1/3}$ (85 kPa and 1048 kPa-ms)

In order to observe the behaviour of the model without delamination, a second model was prepared using the enhanced contact capacity between the ECC and steel layers. This increased contact capacity resisted the higher inertial forces and enabled the panel to deform in a ductile manner without delamination. This model was loaded with the blast pressures that were applied to the enhanced contact specimen mentioned in **4.3.2 Panel-only specimens with higher contact strength**, namely 1417 kg TNT at 60 m, Z = 5.4 m/kg$^{1/3}$ (85 kPa and 1,048 kPa-ms), and 5666 kg at 60 m, Z = 3.4 m/kg$^{1/3}$ (239 kPa and 2725 kPa-ms). The results indicated that the 27 mm thick, enhanced contact specimen had a smaller maximum deformation than that of the 15 mm thick enhanced contact specimen under the smaller blast due to 1417 kg TNT at 60 m, Z = 5.4 m/kg$^{1/3}$ (85 kPa and 1,048 kPa-ms). However, under the larger blast load due to 5666 kg TNT at 60 m, Z = 3.4 m/kg$^{1/3}$ (239 kPa and 2725 kPa-ms), the 27 mm thick, enhanced contact specimen failed by rupturing. The deformed shapes of both specimens are shown in **Figure 133** and **Figure 134**.

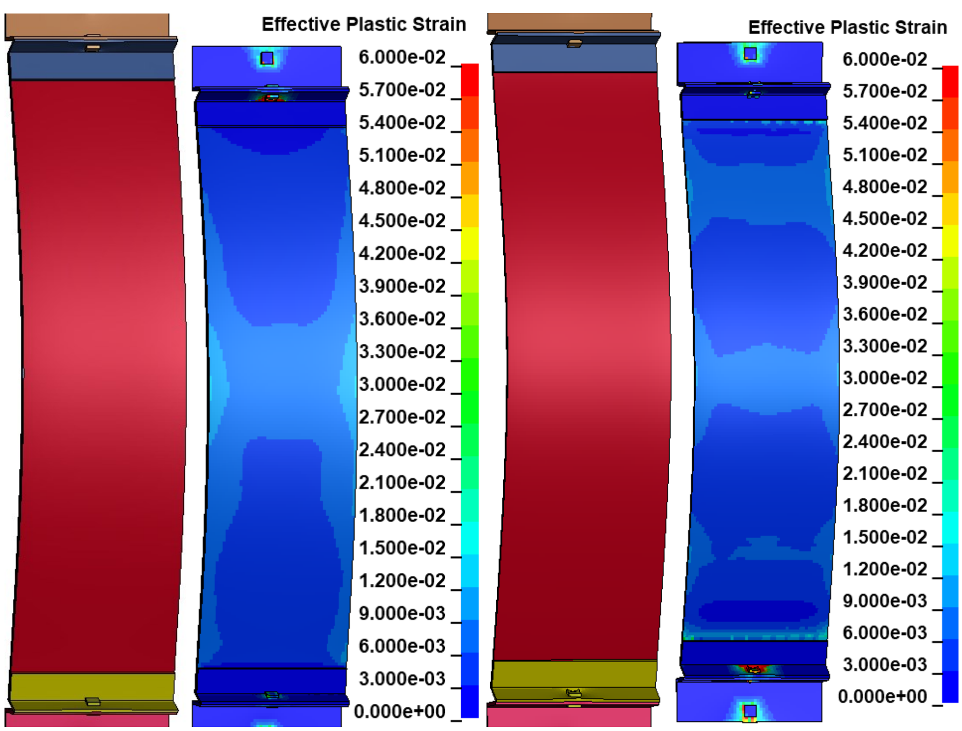

Figure 133: Deformed shape of the LS-Dyna models of enhanced contact 27 mm thick specimen (left) and enhanced contact 15 mm thick specimen (right) under 1417 kg TNT at 60 m blast load, Z = 5.4 m/kg$^{1/3}$ (85 kPa and 1,048 kPa-ms)

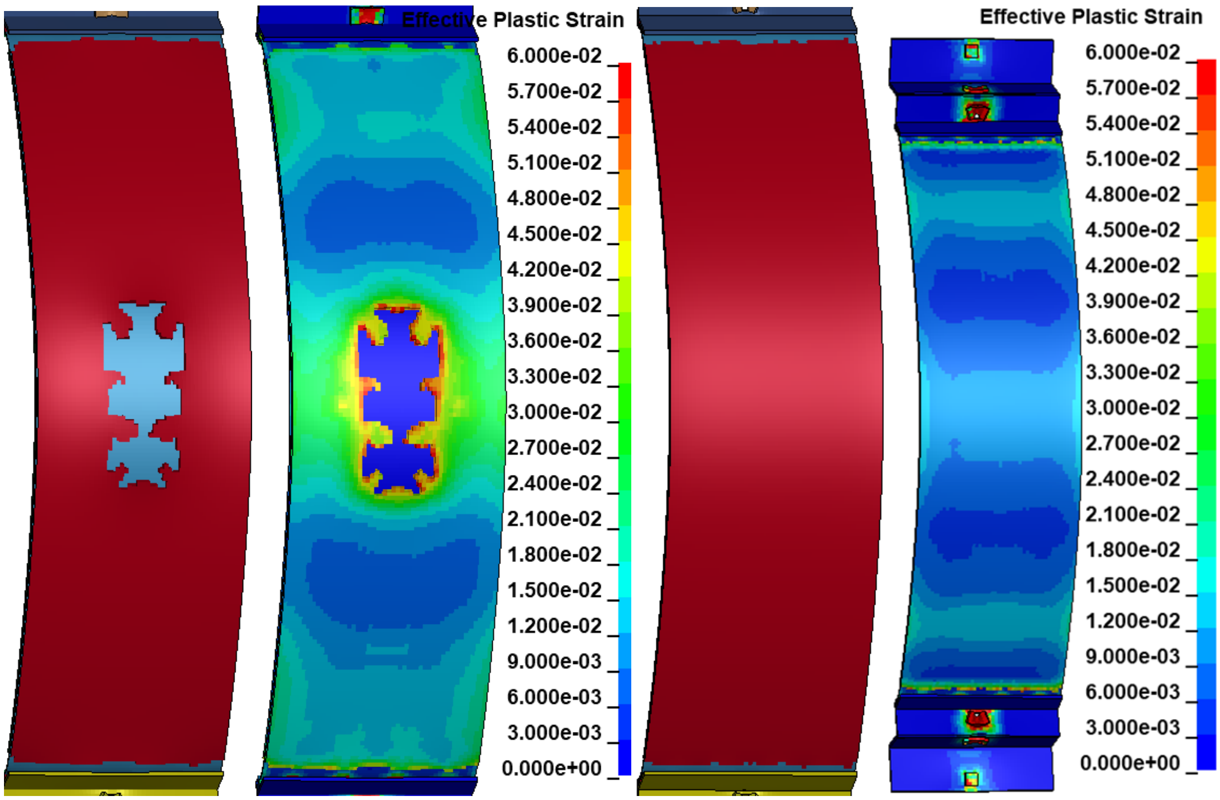

Figure 134: Deformed shape of the LS-Dyna models of enhanced contact 27 mm thick specimen (left) and enhanced contact 15 mm thick specimen (right) under 5666 kg TNT at 60 m blast load, Z = 3.4 m/kg$^{1/3}$ (239 kPa and 2725 kPa-ms)

The results of the 15 mm thick and 27 mm thick enhanced contact models clearly indicate that increasing the thickness of ECC layers decreases the maximum deformation when sufficient contact capacity prevents delamination. However, due to the increased inertia forces, the 27 mm thick panel has a smaller capacity than the 15 mm thick panel under higher pressure - long duration blast loads. These results are summarized in **Table 18** below.

Table 18: LS-Dyna Model results for 27 mm and 15 mm thick enhanced contact specimens exposed to blast loads from 1417 kg and 5666 kg TNT at 60 m

	15 mm thick enhanced contact specimen	**27 mm thick enhanced contact specimen**	**15 mm thick enhanced contact specimen**	**27 mm thick enhanced contact specimen**
Maximum Deformation, mm	298 mm	264 mm	489 mm	467 mm (before rupture)
Equivalent Charge Weight (kg) and Distance (m)	1417 kg, 60 m (85kPa, 1048 kPa-ms)	1417 kg, 60 m (85kPa, 1048 kPa-ms)	5666 kg, 60 m (239kPa, 2725 kPa-ms)	5666 kg, 60 m (239kPa, 2725 kPa-ms)
Scaled Distance (m / kg$^{1/3}$)	5.4	5.4	3.4	3.4

4.3.4 Partition Wall: Panel – HSS – Panel Specimens

This LS-Dyna model was developed to assess the performance of “partition walls” with HSS members for enhanced load resistance. This type of ECC-steel-ECC panels can be used as blast-resistant elements, replacing “drywall” panels. They can be particularly effective in creating blast-resistant enclosures within an existing building, such as security screening areas.

In this model, the same size HSS members (51 x 76 x 3.2 mm) as the ones used in the shock tube tests were employed with double panels, one covering each side of the HSS sections. The ECC-Steel-ECC panels were assumed to have a 3 mm thick steel plate, sandwiched between the ECC layers with 100 mm connector spacing. A rigid concrete slab was assumed to be located at the top and the bottom, with steel angles connected to the slabs via bolts. This connection was considered to be closer to a fixed connection as the use of double angles provided significantly more moment resistance compared to the single angle connection used in other specimens. The total thickness of the wall setup was 15 + 51 + 15 = 81 mm. The height of the wall setup was assumed to be 2080 mm for comparison with those tested in the shock tube. This height also allows comparison with the other models discussed earlier. The undeformed view of the model is shown in **Figure 135** below.

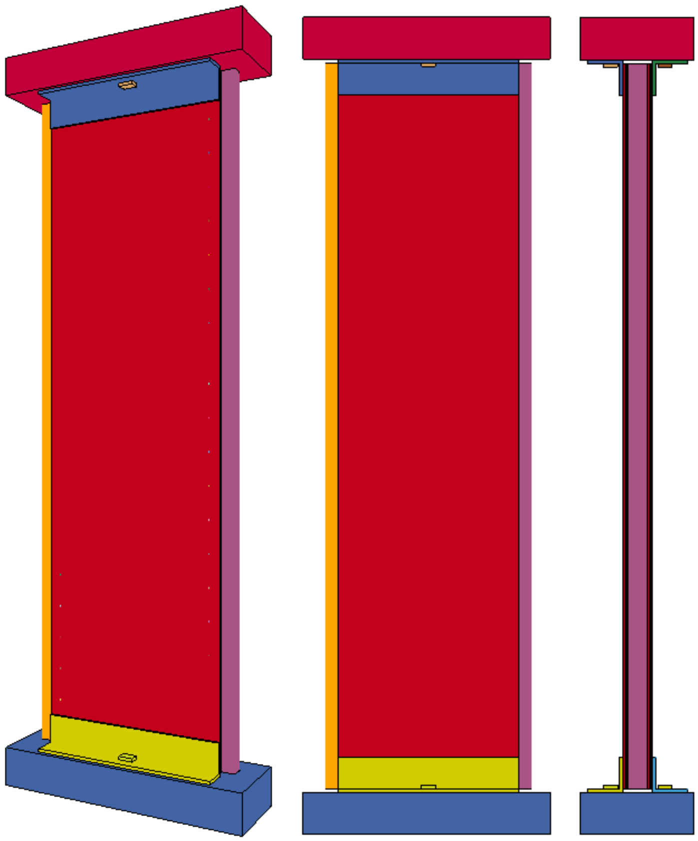

Figure 135: Undeformed view of the LS-Dyna model for the "Partition Wall" specimen

The additional support stiffness provided by the double angles and the panels covering both sides of the HSS members, similar to double-flanged steel sections, resulted in a partition wall with a significantly higher stiffness compared to those discussed earlier. As a result of the increased stiffness, the maximum deformation was observed to be much lower compared to the first set of shock tube specimens that consisted of a single panel and HSS members under the same blast load, 1567 kg of TNT at 64 metres, Z = 5.5 m/kg$^{1/3}$ (82 kPa and 1066 kPa-ms). The deformed shape and the effective plastic strain distribution of the partition wall type specimen are shown in **Figure 103**, with a maximum deformation of 50.2 mm at the front panel (protected side) and 59.4 mm at the back panel (blast side).

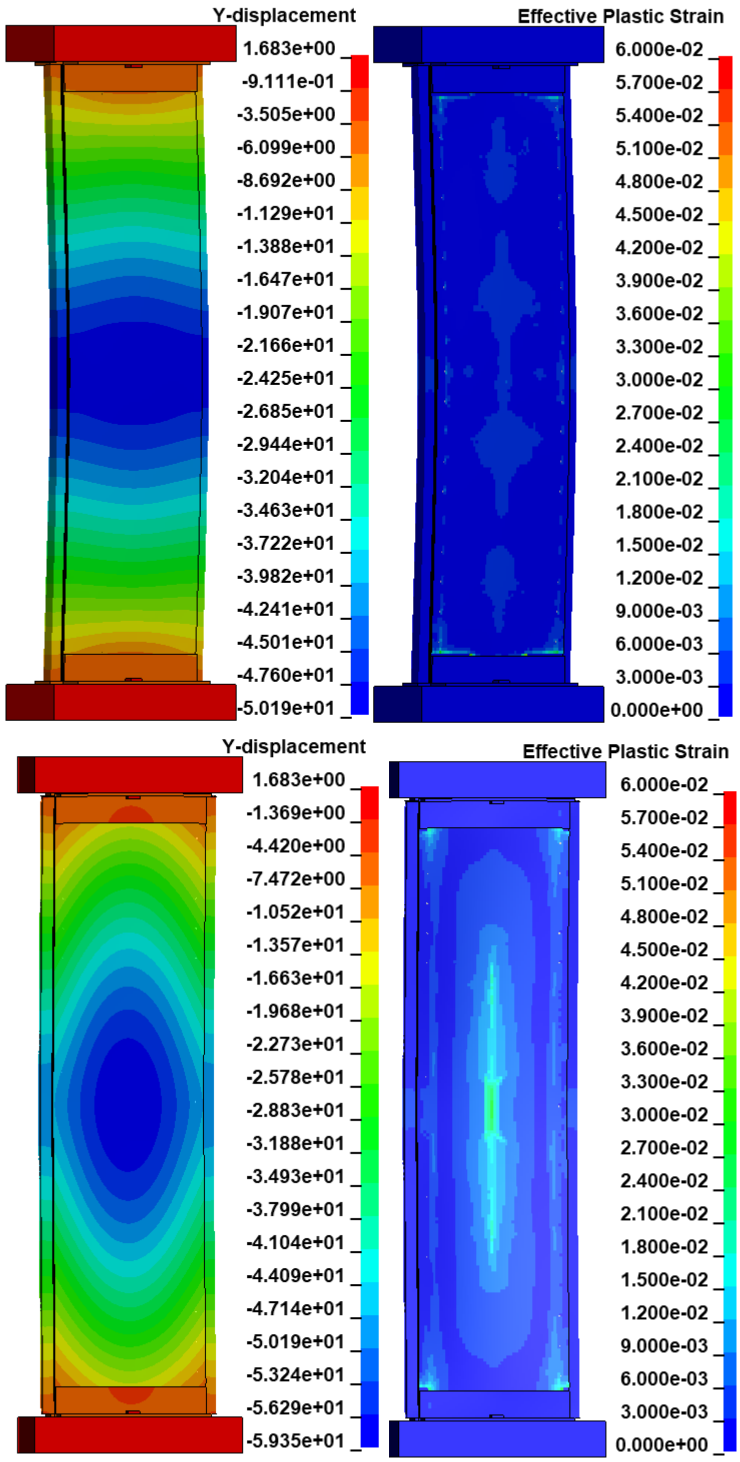

Figure 136: Deformed shape and plastic strain of the "Partition Wall" type specimen under the blast of 1567 kg TNT at 64 metres, Z = 5.5 m/kg$^{1/3}$ (82 kPa and 1066 kPa-ms). Protected side (top), blast side (bottom).

When used as interior building panels, as in the case of a security screening area, this type of wall panel would likely be exposed to smaller charge weights detonating within a closer distance. Therefore, the same model was also analyzed using a 10 kg charge weight at 5 metres from the wall, corresponding to a scaled distance of 2.3 m/kg$^{1/3}$. This blast load had a peak reflected pressure value of 674 kPa and a reflected impulse of 506 kPa-ms. The analysis results indicated that the specimen retained its integrity on the protected side and prevented fragmentation from occurring. The maximum deformation was obtained to be 53.4 mm on the protected side. The deformed shape of the specimen under 10 kg TNT and 5 metres is shown in **Figure 137**.

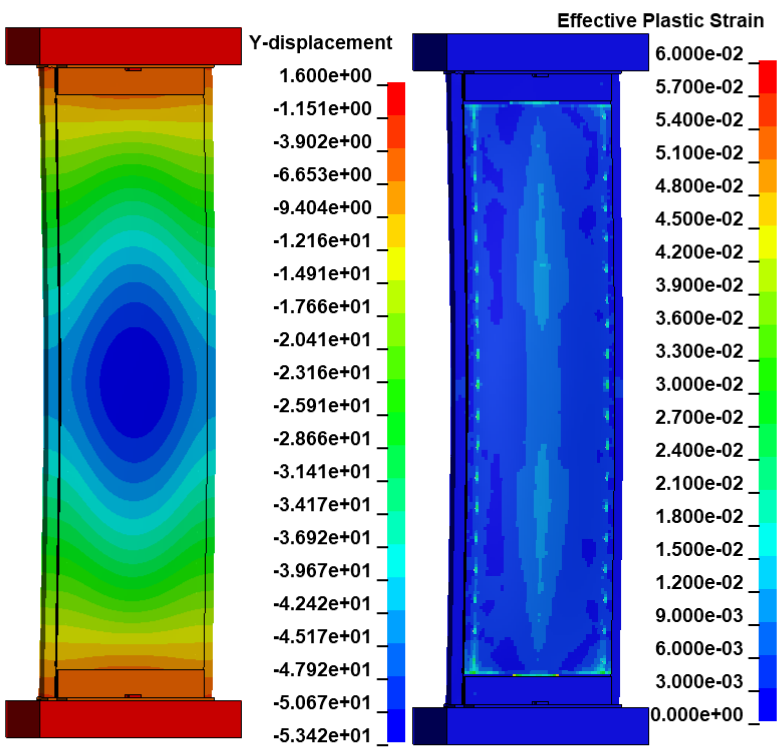

Figure 137: Deformed shape and plastic strain of the "Partition Wall" type specimen from the protected side under the blast of 10 kg TNT at 5 metres, Z = 2.3 m/kg$^{1/3}$ (674 kPa and 506 kPa-ms)

Due to the relatively small deformation of the specimen observed on the protected side, a third analysis was conducted under an increased blast load. This time, a charge weight of 15 kg at 5 metres, corresponding to a scaled distance of 2.0 m/kg$^{1/3}$ was used, which resulted in a peak reflected pressure of 1,011 kPa and a reflected impulse of 687 kPa-ms. This third blast load caused failure on the protected side, and delamination occurred. However, the simulation did not show fragmented particles becoming projectiles. The deformed shape obtained from this analysis is shown in **Figure 138**.

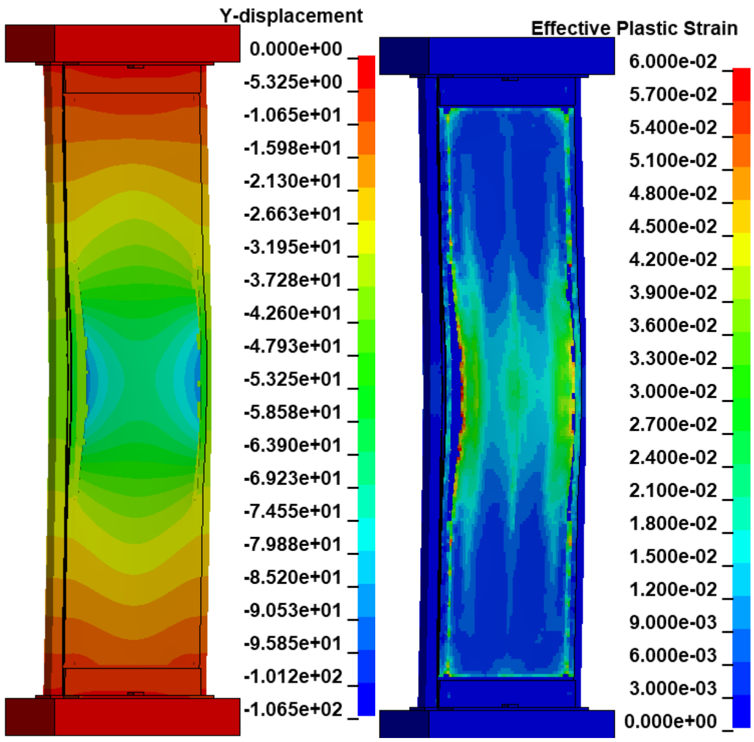

Figure 138: Deformed shape and plastic strain of the "Partition Wall" type specimen under the blast of 15 kg TNT at 5 metres, Z = 2.0 m/kg$^{1/3}$ (1,011 kPa and 687 kPa-ms). Protected side (top), blast side (bottom).

These results indicate that the “partition wall” type specimen was able to provide protection under the effect of both large charge weight and long standoff distance, as well as small charge weight and close standoff distance. The maximum deformation values obtained from the partition wall type specimens are summarized in **Table 19**.

Table 19: Summary of results for the "Partition Wall" type specimens

	1567 kg at 64 m (82 kPa, 1066 kPa-ms)	10 kg at 5 m (674 kPa, 506 kPa-ms)	15 kg at 5 m (1,011 kPa, 687 kPa-ms)
Front Panel (protected side) Maximum Deformation, mm	50.2 mm	53.4 mm	106.5 mm
Back Panel (blast side) Maximum Deformation, mm	59.4 mm	Crushed	Crushed
Scaled Distance, m / kg$^{1/3}$	5.5	2.3	2.0

4.3.5 Ballistic Protection Comparison

Two LS-Dyna models were prepared to simulate the effects of a ballistic bullet impact, either on a 3 mm thick steel sheet, or having an ECC-steel-ECC arrangement having an overall thickness of 6 + 3 + 6 = 15 mm. For computational efficiency, a quarter model, symmetric about the x and z axes, was used to represent the bullet and the target. The size of the quarter target was 50 mm by 50 mm, corresponding to a 100 mm by 100 mm plate or panel. The mesh was refined to a 0.5 mm size for a 20 mm by 20 mm area at the location of bullet impact, and it gradually increased towards the perimeter. Undeformed views from both models are shown in **Figure 139** and **Figure 140** below.

In addition to the contact-tiebreak algorithm used for other models mentioned above, an additional contact algorithm – eroding surface to surface – was used to model the contact between the bullet and the panel. This algorithm allows the contact to be preserved even after the elements are eroded due to damage. As the bullet moves through the plate, both the bullet and the plate experience high strains, and certain finite elements reach their failure strain. The eroding surface to surface algorithm allows the elements that are behind the eroded elements to experience the same contact forces.

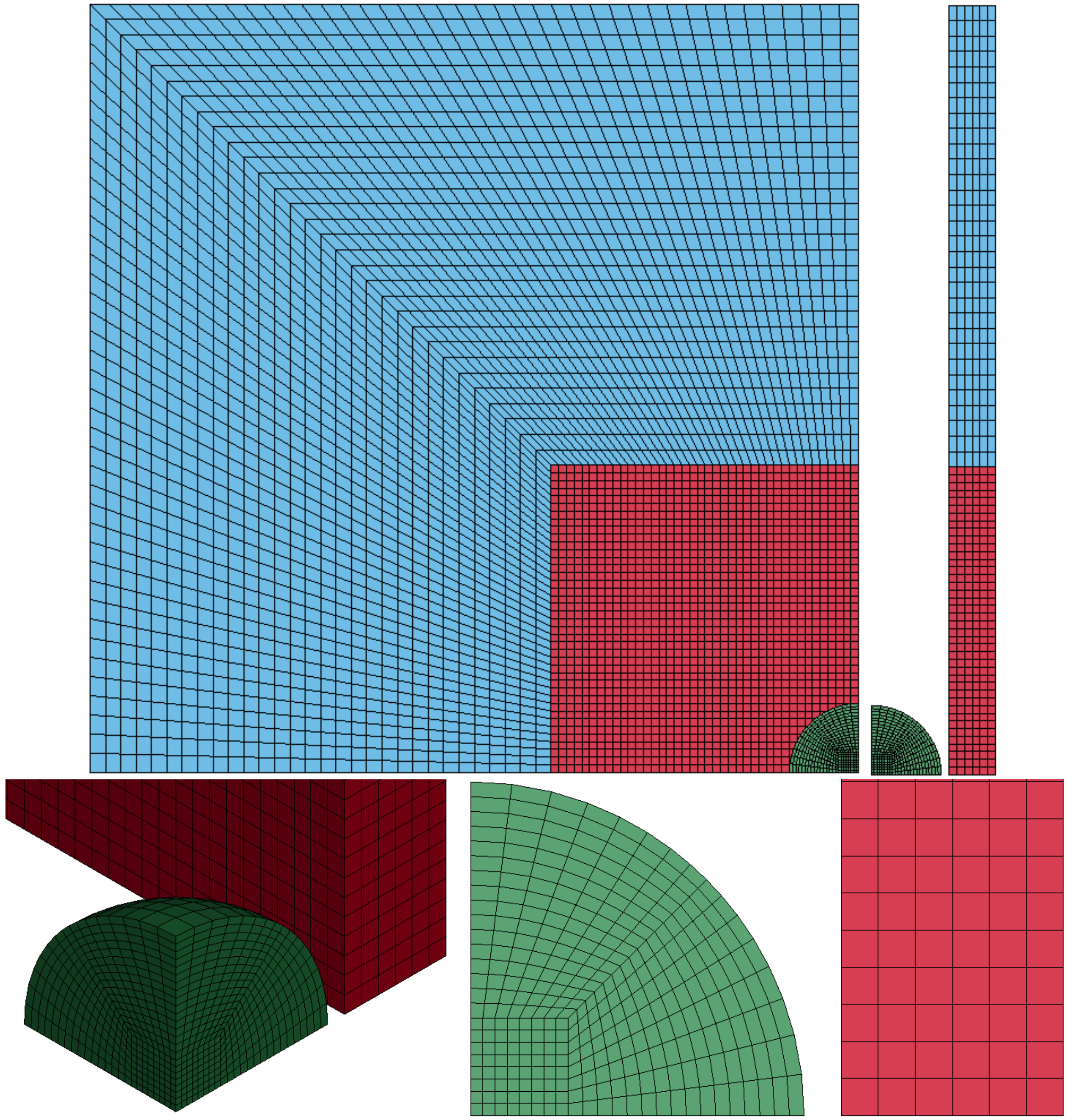

Figure 139: LS-Dyna model of a 9 mm bullet and a 3 mm thick steel plate

The bullet type used in these models was a 9 x 19 mm Parabellum round currently used by the Canadian Armed Forces. The bullet was modelled as a 1/8 of a sphere, where the surface impacting the plate was spherical. The mass of the full projectile was reported to be 8.5 grams, and in the LS-Dyna model, due to symmetry, the mass of the projectile was one-fourth of the full projectile. The initial speed of the bullet was 350 metres per second (1260 km/hr), and the kinetic energy of the bullet was 130.8 Joules.

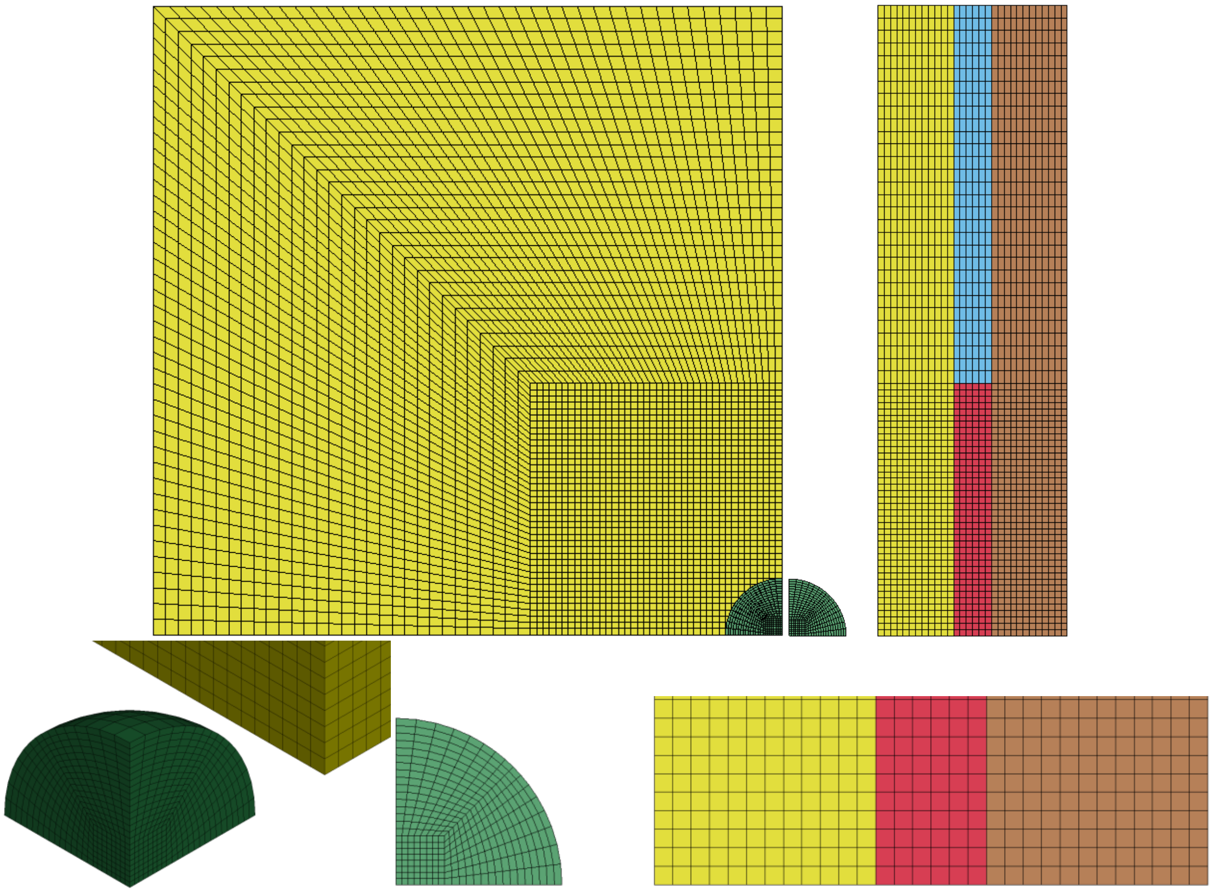

Figure 140: LS-Dyna model of a 9 mm bullet and a 15 mm thick ECC-steel-ECC panel

The results of the simulations indicate that the kinetic energy is reduced by 44% in the case of the steel plate only, and 62 % in the case of the ECC-steel-ECC panel. The change in kinetic energy during the simulations is shown in **Figure 141**. It is important to note that softening of the bullet due to increased temperature was not included in these simulations. Hence, the fragmentation of the bullet was not observed. The reduction in kinetic energy was considered to be an indicator of the blunting effect caused by the ECC layers. The deformed shape of the models is shown in **Figure 142**.

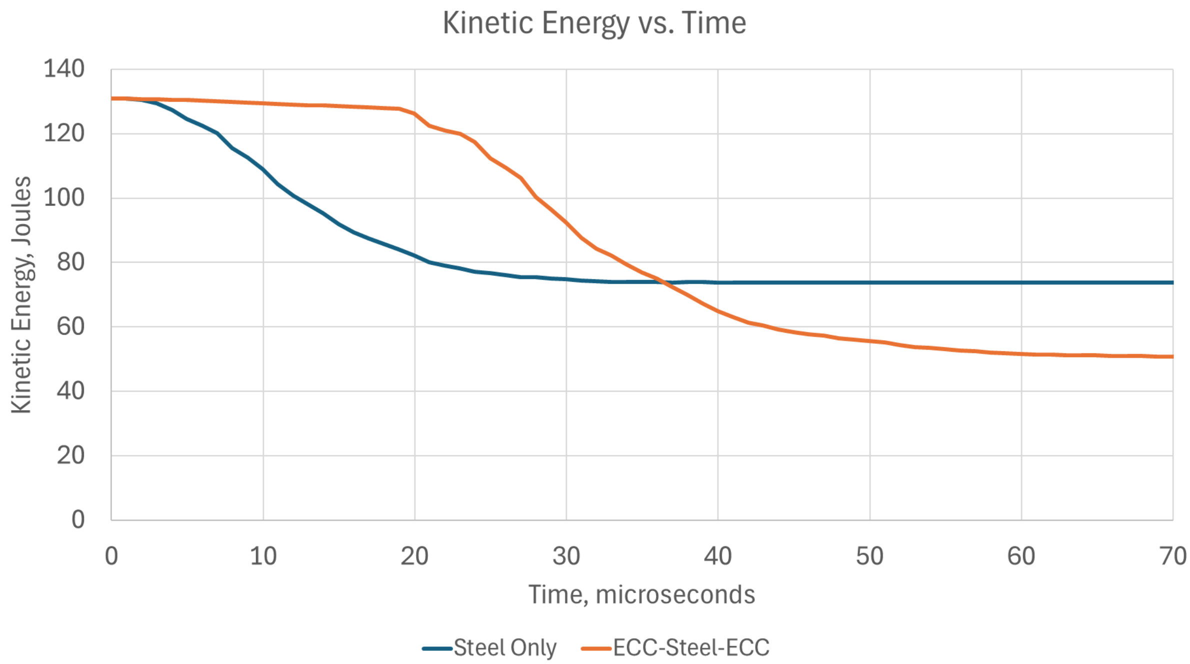

Figure 141: Change in kinetic energy

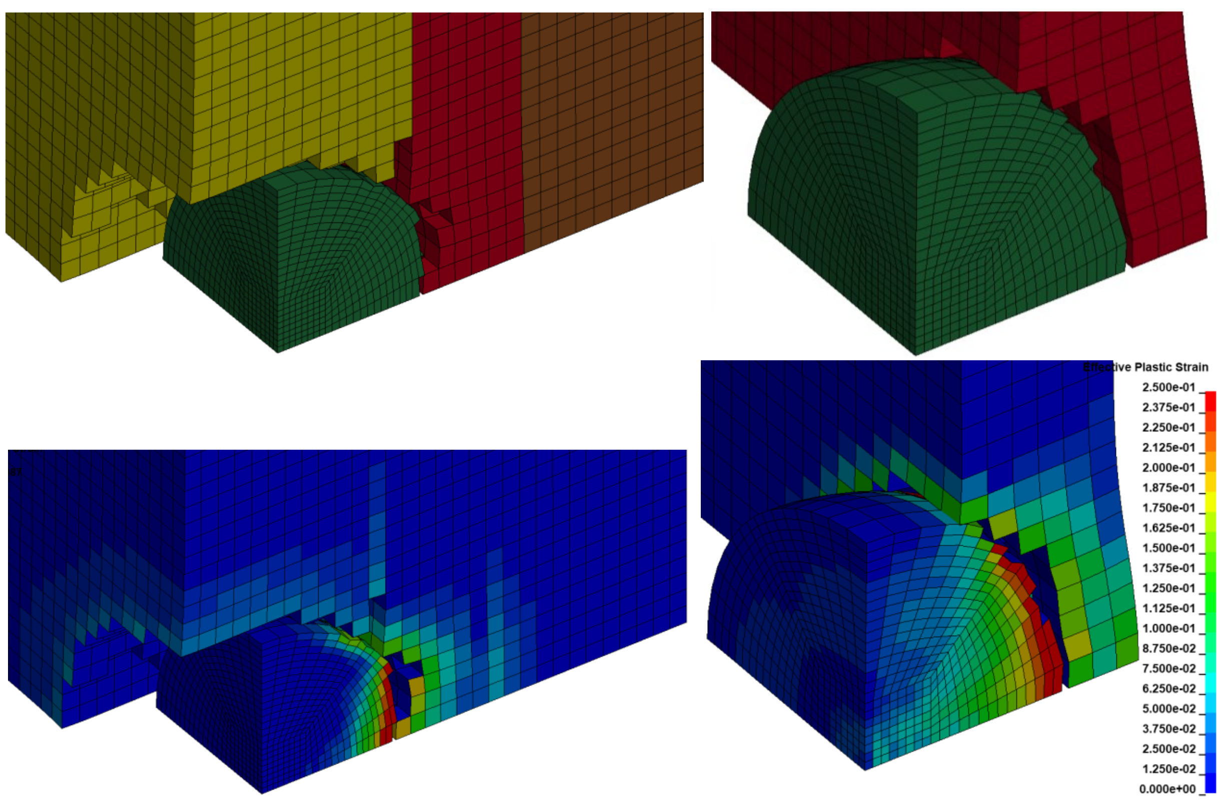

Figure 142: Bullet moving through ECC-Steel-ECC (left) and Steel (right) models

4.4 Single Degree of Freedom (SDOF) Approach

A single-degree-of-freedom (SDOF) analysis approach was used as a simple method for predicting panel/wall system behaviour under blast loads. This was done to establish the applicability of the SDOF analysis as a reliable design tool when appropriate resistance functions are developed. The SDOF approach relies on applying the blast loads on a single mass-spring system that represents the dynamic properties of the structural system via the transformation factors introduced by Biggs, (1964). In this analysis approach, the distributed mass of the structural system is condensed into a lumped mass with an attached spring that resists movement along the degree of freedom. The spring stiffness vs displacement relationship associated with this spring is called the resistance function. The analysis of an SDOF system with a known mass and an elasto-plastic resistance function under the effects of a triangular blast load is relatively simple and can be performed via publicly available charts. An example of such a chart is shown in **Figure 129** along with the corresponding calculations to determine the required resistance. For a nonlinear resistance function, the SDOF system analysis could be performed by numerical analysis using a spreadsheet or software. In the current research project, the numerical analysis was performed using RCBlast, developed by Eric Jacques (Jacques et al., 2013).

A critical step in using this SDOF approach is the determination of the resistance function. For the panel/wall element involved in this thesis, the resistance function was calculated using a flexural behaviour approach or a tensile behaviour approach, depending on the type of panel/wall system under investigation. For specimens that involved the use of HSS members, which had a relatively high flexural stiffness, the flexural behaviour approach was used to determine the resistance function. For panel-only specimens, which had a very low flexural stiffness, the tensile behaviour approach was used to determine the resistance function. The details of both approaches are described below.

4.4.1 Tension Behaviour of Panel-only Specimens

The ECC-steel-ECC panels have a very small flexural stiffness compared to their axial stiffness under tension loads. Due to this relatively low flexural stiffness, tension behaviour dominates their response to blast loads. As the panels are only supported at the top and bottom, and not the sides, their tension behaviour could be simplified to a cable. The details of this approach are explained in this section.

A cable with only axial stiffness supported at its ends deflects into a catenary curve under the influence of its own weight (Hibbeler, 2015). This catenary shape can then be used to calculate the tensile force and transverse deflection at any point along the cable. The maximum transverse deflection, or sag, occurs at the midpoint of the cable. Using the equation of the catenary, it is possible to calculate the total length of the catenary for a given value of sag. The length of the catenary increases with increasing values of “sag”. Therefore, if the cable has a high elongation capacity, it can tolerate higher values of sag or deflection.

Furthermore, as the sag increases, the inclination of the cable relative to the line connecting the supports also increases. As a result, the component of the tensile force in the cable that is opposing the out-of-plane load increases with increasing angle. Therefore, the cable is able to resist a higher transverse load with the same level of tension. This increased angle between the cable and the support line increases the “efficiency” of the cable by resisting a higher transverse load with the same amount of tension in the cable.

The equation relating sag and cable length is shown below. For a known value of axial strain, axial stress values can be calculated using the stress vs strain relationship of that material.

$$length(sag) = \frac{span}{2}\left[\sqrt{1+\left(\frac{4*sag}{span}\right)^2} + \frac{span}{4*sag}*\operatorname{asinh}\left(\frac{4*sag}{span}\right)\right] \qquad \textbf{Eq. 14}$$

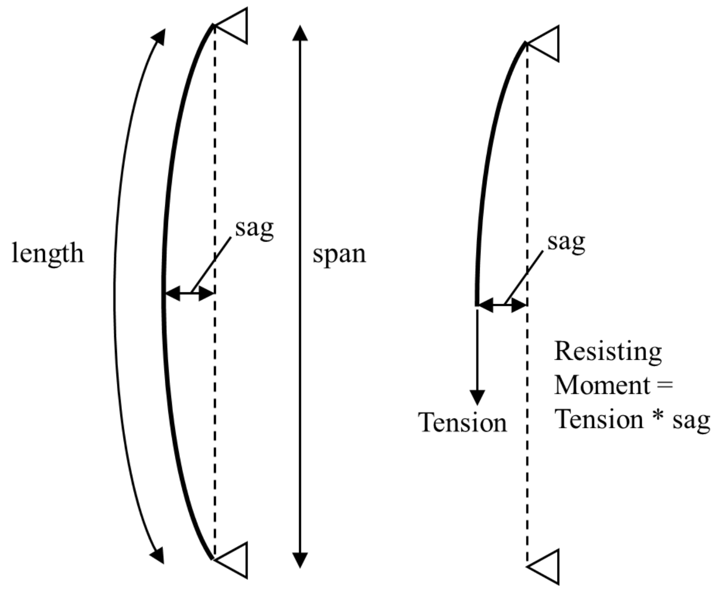

Figure 143: Span, length and sag of a cable with only axial stiffness

For an ECC-Steel-ECC panel with a 3 mm thick steel layer, the movement of the support angles has a significant effect on the resistance function. The support movements delay the yielding of the steel sheet and keep the resistance function value relatively small until yielding occurs. In the shock tube experiments, the primary factors contributing to the movement of the supports were observed to be the bending of the bolt connecting the two angles, the bending of the support angle and the bolt hole tolerances. Therefore, in the resistance function calculations, these factors were considered to calculate the support movement. The calculation steps for support movement are shown in **Appendix A**.

The calculation for the total force in the panel started by calculating the total length of the panel as a function of sag and then subtracting the movement of the supports to obtain the elongation of the panel. The average strain was calculated by dividing the elongation by the initial length of the panel. Stress for each material corresponding to the strain value was obtained from the stress-strain relationships, which are shown in **Figure 97** and **Figure 99**. The axial force for each material layer was calculated by multiplying the stress in each material by its corresponding area. Total force in the panel is obtained by the summation of the axial force in each layer.

Once the sag at the midpoint of the panel and the corresponding tension force at that point are known, the resisting moment is obtained by multiplying the tension force by the sag value. The resistance value is equal to the total uniformly distributed load along the length of the panel that would cause the resisting moment. The calculation of the resistance function by using the resisting moment is shown in **Eq. 15** below. The length, support movement, elongation, total force, moment, and resistance values corresponding to the amount of sag at the mid-height of the panel are shown in **Table 20**.

$$Moment = {w * L^2}/{8} \Rightarrow Resistance = w * L = Moment * 8 / L \qquad \textbf{Eq. 15}$$

Table 20: Sag, length, support movement and resistance function values for an ECC-steel-ECC panel

Sag	Length	Support Movement	Elongation	Total Force (kN)	Moment (kN*m)	Resistance (kN)
0	2000.0	0.0	7.97E-09	0.0	0.0	0.0
10	2000.1	0.1	1.30E-02	0.0	0.0	0.0
20	2000.5	0.5	2.59E-02	3.0	0.1	0.2
30	2001.2	1.2	3.89E-02	3.0	0.1	0.4
40	2002.1	2.1	5.19E-02	6.0	0.2	1.0
50	2003.3	3.3	6.48E-02	9.0	0.5	1.8
100	2013.3	13.1	1.30E-01	18.0	1.8	7.2
150	2029.6	29.4	1.94E-01	27.0	4.1	16.2
200	2052.1	51.9	2.59E-01	36.0	7.2	28.8
250	2080.5	80.1	3.24E-01	48.0	12.0	48.0
270	2093.3	93.5	3.50E-01	51.0	13.8	55.1
300	2114.2	93.5	2.12E+01	398.0	119.4	477.6
350	2153.0	93.5	6.00E+01	407.4	142.6	570.3
400	2196.5	93.5	1.03E+02	407.1	162.8	651.4

The resistance function of an ECC-steel-ECC panel with 3 mm thick steel was obtained as shown in **Figure 144** below.

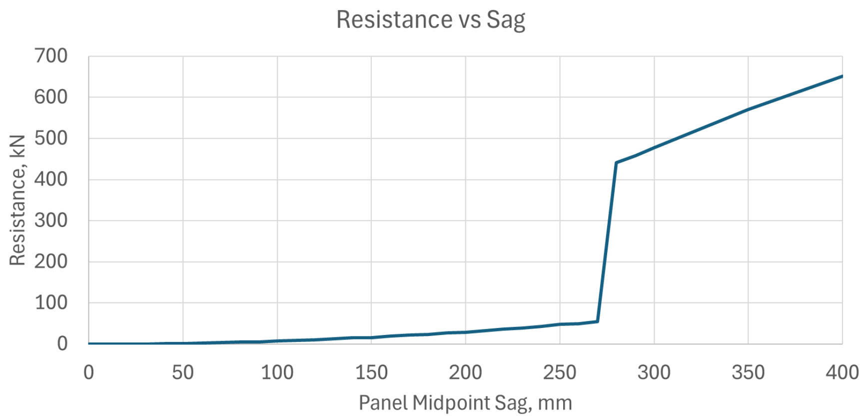

Figure 144: Resistance function of an ECC-steel-ECC panel with a 3 mm thick steel sheet

Once the resistance function was established, the SDOF analysis was performed using the RCBlast software. The displacement versus time relationship is shown in **Figure 145**. The maximum deformation was calculated to be 286 mm. This value is 3% less than 295 mm obtained from LS-Dyna and 15% more than the additional deformation of 249 mm measured in the third shot of the second set of shock tube specimens shown in **Table 12**. The time to reach the maximum deformation was 22 milliseconds in the SDOF analysis, which was obtained as 25 milliseconds in the LS-Dyna model, and measured as 26 milliseconds in the shock tube experiments.

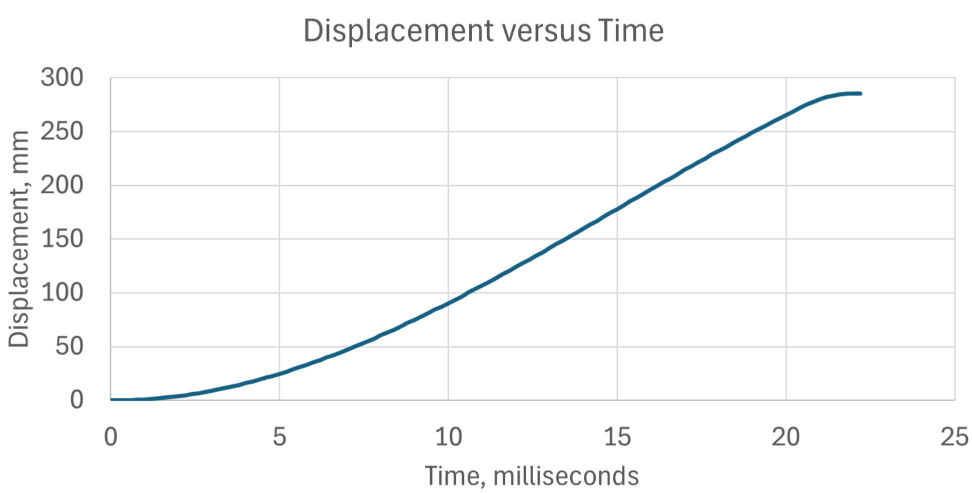

Figure 145: Displacement vs. Time obtained using RCBlast software

It was concluded that the maximum deformation value and the time to reach the maximum deformation were in good agreement with the experimental and finite element analysis results. Therefore, for tension-controlled specimens, this approach can be utilized as a sufficiently accurate alternative analysis method for use in design.

4.4.2 Flexure-only Behaviour of Panels

For panels that were used with HSS members, the governing behaviour was flexural. For these specimens, the flexural stiffness of the HSS members associated with the panels had a significant effect on the overall behaviour of the specimens. Therefore, for these specimens, the resistance function was obtained via flexural analysis. The flexural analysis of these specimens was performed using a spreadsheet incorporating sectional strain compatibility analysis. The spreadsheet performed sectional analysis by first slicing the total cross-section into 150 layers. For a given curvature, the strain value at each layer is calculated. Next, using the stress-strain relationship for the material defined in a layer, the corresponding stress is found. The stress is converted to force by using the area of the layer. Using iteration, the neutral axis location is calculated such that the sum of forces within the cross-section is zero. The moment capacity corresponding to the chosen curvature is calculated by adding the product of the force in each layer with its distance to the neutral axis. This process is completed for a range of curvature values to obtain a moment-curvature relationship. The moment-curvature relationship for a 76 x 51 x 3.2 mm HSS member connected to a 15 mm thick ECC-Steel-ECC layer with a 3 mm steel thickness specimen, as obtained from this spreadsheet, is shown in **Figure 146**. It is important to note that the effective width of the ECC-Steel-ECC portion of the cross-section was 500 mm (width of one panel), which corresponded to one quarter of the span. This cross-section was analogous to a T-section where the HSS is the stem and the panel is the flange.

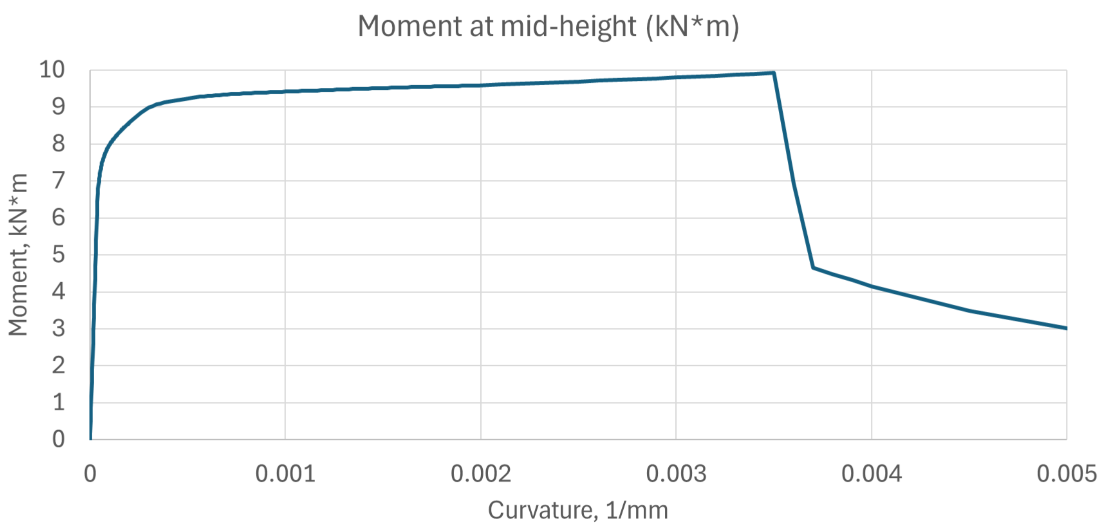

Figure 146: Moment-Curvature relationship for a 76 x 51 x 3.2 mm HSS member with ECC-Steel-ECC panel

The resistance function for the specimen is then obtained from the moment-curvature relationship by numerical integration. The specimen is analyzed as a simply supported beam, with the moment, curvature, slope, and deflection calculated at each 1 mm length. The resistance is calculated from the maximum moment, using **Eq. 15** shown above. The resistance-curvature and the resistance function (resistance-deformation) diagrams are shown in **Figure 147** and **Figure 148**.

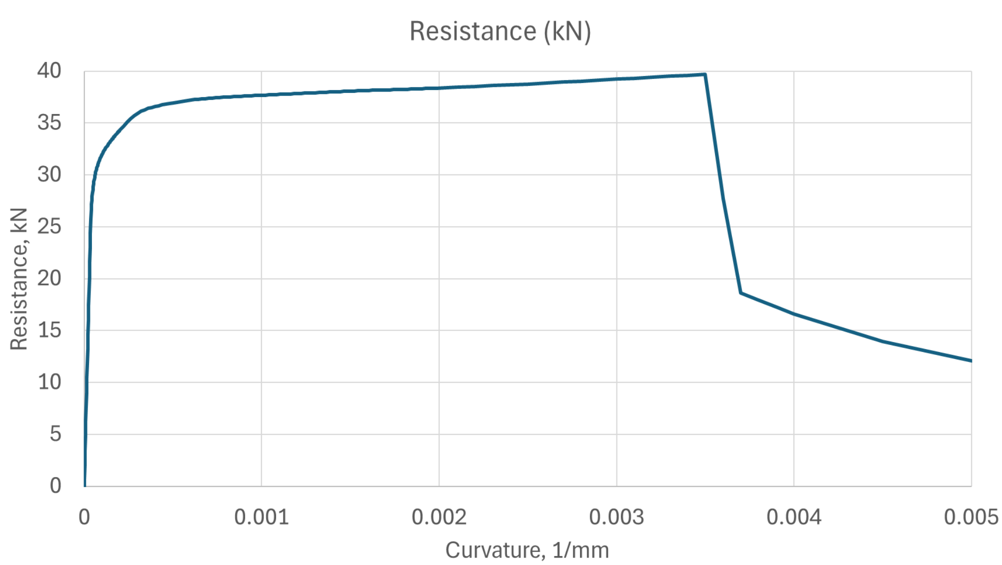

Figure 147: Resistance-Curvature diagram for 76x51x3.2 mm HSS and ECC-steel-ECC panel

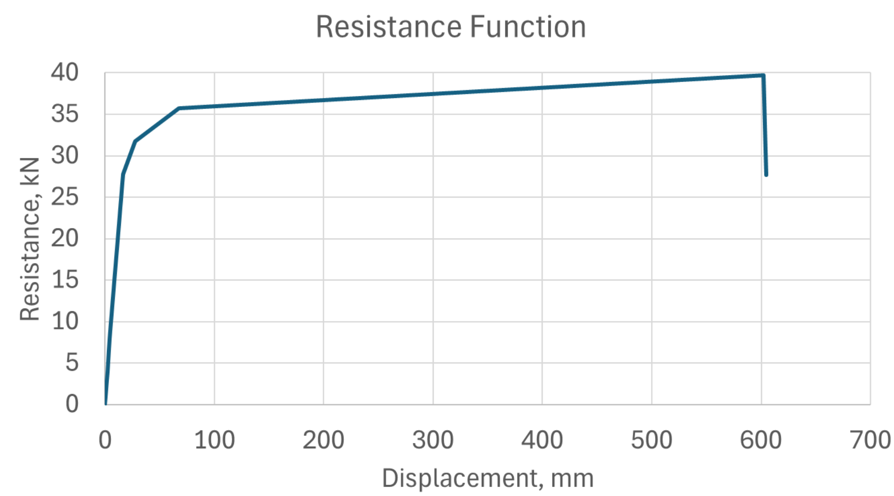

Figure 148: Resistance function for the 76x51x3.2 mm HSS and ECC-steel-ECC specimen

The resistance function was then used as an input for the RC Blast software to perform the SDOF analysis. The results of the SDOF analysis indicate that a maximum deformation of 211 mm is reached at 32 milliseconds after the blast (**Figure 149**). The maximum deformation value is 20% higher than the maximum deformation of 175 mm obtained in the LS-Dyna model, and 9% higher than 193 mm measured for the shock tube specimen, as reported in **Table 11**. Time to reach maximum deformation was obtained as 30 milliseconds for the LS-Dyna model and measured as 34 milliseconds for the shock tube specimen. Both of these values are considered to agree well with the shock tube specimen and LS-Dyna model results.

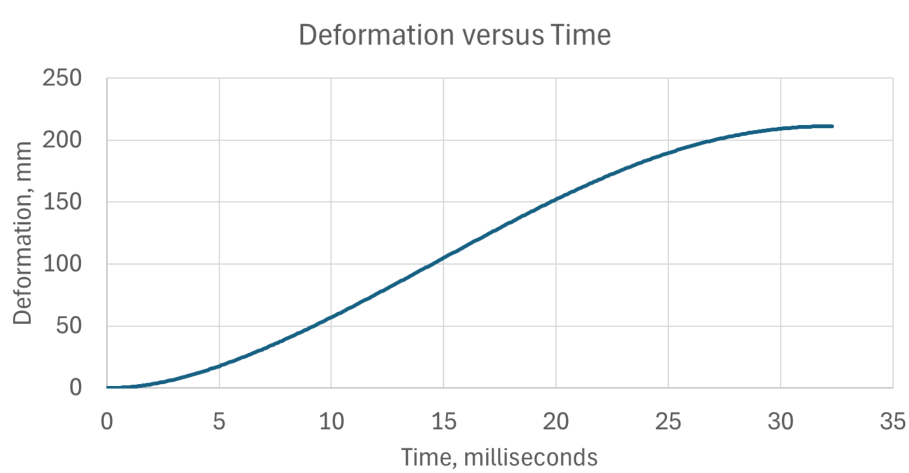

Figure 149: Deformation vs. Time relationship obtained from SDOF analysis

Chapter 5. Design Recommendations

This chapter presents design recommendations for the blast-resistant panels and wall systems developed as part of the current investigation. Design parameters covered in the experimental and numerical phases of research, although presented in earlier chapters, are discussed to assess their significance in terms of applications to practice. These observations led to the development of design recommendations and procedures for the two types of elements investigated. A more holistic consideration of all experimental and analytical data is presented below before developing the design recommendations.

5.1 Effects of Design Parameters

5.1.1 Steel Sheet Thickness

The significance of the interior steel layer used in panels was first investigated through shock tube tests. Further numerical research was conducted subsequently to generate additional data. Each 15 mm thick test panel had either a 1.5 mm or a 3.0 mm thick steel sheet between ECC layers. As the steel sheets were located at the center of the 15 mm thick panels, their contribution to the moment of inertia was limited. The ECC layers, which were the exterior layers, contributed more significantly to the flexural stiffness of panels. The uncracked moment of inertia of a 15 mm thick panel with 3.0 mm steel in the center was only 6% higher than that of a panel with 1.5 mm steel.

However, the effect of steel thickness was critical for the tension capacity of a panel. This was especially important for panel-only specimens, where tension-dominant behaviour was prevalent.

The second and third sets of specimens were panel-only specimens with either 3.0 mm or 1.5 mm steel sheets, respectively. The results shown in **Table 5** and **Table 6** indicate that specimens with 3.0 mm thick steel were able to withstand, on average, 35% higher pressure and 82% higher impulse. This enhanced performance of 3.0 mm thick steel was also observed in the LS-Dyna models presented in **Chapter 4. Analytical Investigation**.

5.1.2 ECC Layer Thickness

The shock tube specimens had ECC layers that were 6 mm and 6.75 mm thick, which were replicated in the LS-Dyna models used for validation. In addition to these thicknesses, two additional models were developed: one with a steel sheet and HSS only (0 mm ECC thickness), and the other with 12 mm thick ECC layers on either side of the steel sheet. These models were prepared in addition to the fifth set of test specimens, which did not have any ECC layer, and the panels consisted of either 1.5 mm or 3.0 mm thick steel sheets only.

The results indicate that specimens with no ECC layers result in the yielding of steel sheets under lower blast loads than those with ECC layers. Furthermore, the presence of ECC affects the dynamic properties of panels. The decrease in the period of vibration associated with the removal of ECC layers reduces the capacity of the panels against shorter duration blast loads, as explained in Section **4.3.1 HSS Member with 3 mm steel sheet without ECC layers** (**Figure 129**).

The effect of further increasing ECC thickness was studied numerically. Panels with increased ECC layer thickness, 12 mm on either side of a 3 mm thick steel (a total thickness of 27 mm), experienced premature delamination of ECC layers (**Figure 132**). This was due to the increased inertial forces generated by the increased mass of 12 mm thick ECC layers. However, this problem was resolved by reducing the connector spacing (using enhanced contact between the layers). This enhanced contact resulted in higher blast capacity and reduced deformations (**Figure 133**). However, when the blast load was increased with the use of quadrupled charge weight, the 27 mm thick enhanced contact specimen experienced failure, while the 15 mm thick enhanced contact specimen did not (**Figure 134** and **Table 18**).

Based on the above observations, it was concluded that increasing the ECC layer thickness does not necessarily increase the overall capacity of the panels unless the connector space is reduced and the composite action is improved. It is important to note that the asymmetrical ECC layer thickness was not investigated. A panel with a 6 mm thick ECC layer on the protected side and a 12 mm thick ECC layer on the blast side might prove to have increased resistance.

5.1.3 Connector Spacing

Two distinct layouts of connectors were used during the experiments to connect the ECC layers to the steel sheet. These included 100 mm and 200 mm spacings. The effect of these connectors on the composite action was more evident in the second and third sets of specimens, which were the panel-only specimens without the HSS sections. The specimens with 200 mm connector spacing experienced delamination of ECC under lower blast loads compared to those with 100 mm connector spacing. This is illustrated in **Figure 77** and **Figure 81**.

The effect of connector spacing was not as evident in specimens with HSS members, where the dominant behaviour was flexure. For the first set of specimens, failure occurred due to the flexural failure of HSS members, and the capacity of ECC-steel-ECC panels was not reached (**Figure 66** and **Figure 68**).

It is evident from the results of the shock tube experiments that an increased number of connectors increased the capacity of the panels via improving the composite action. This improved performance was also observed in the LS-Dyna models. It is concluded that an increased number of connectors with higher shear and out-of-plane resistance would be able to enhance the behaviour of the panels even further. This theoretical contact strength enhancement and its benefits were demonstrated in the LS-Dyna models shown in **Figure 130** and **Figure 131**. One of the unique properties of the ECC-steel-ECC panels was that all three layers worked together to form a composite section. Therefore, it was critical to capture this behaviour in the LS-Dyna models. The surface-to-surface tiebreak contact algorithm used in the models was verified repeatedly for different types of specimens by observing the matching failure profiles of shock tube and modelled specimens (**Figure 110** to **Figure 120**). The contact capacity values that were used, 0.55 MPa and 1.1 MPa for 200 mm and 100 mm connector spacing, respectively, enabled the model results to agree with the results of the shock tube experiments. The influence of the contact capacity on the overall model performance was significant. Due to this significant influence on the overall model performance, increased contact capacity models were included in the parametric finite element study, which indicated that the reduced connector spacing of 55 mm eliminated delamination completely.

The increased contact strength specimens used a contact capacity that was 2.5 times more than that of the 100 mm connector spacing specimens. This increased contact capacity was assumed to represent “T” shaped connectors, which have a widening head to provide out-of-plane resistance in addition to shear resistance. Therefore, the contact capacity was applied in both in-plane and out-of-plane directions.

The increase in capacity of these enhanced contact specimens was significant. The enhanced contact specimen did not fail under the same blast load that caused failure of the 100 mm connector spacing specimen. Moreover, the enhanced contact specimen did not show delamination under a blast load that was generated by a four times heavier weight of TNT (**Figure 131**). Under this more intense blast load, the enhanced contact specimen achieved an impressive 489 mm maximum deformation value (**Table 17**). Based on these results, it was concluded that increased connector capacity between the ECC and steel layers would increase the resistance of the panels against blast loads.

5.1.4 HSS Members

HSS members were used vertically to connect the panels for increased blast load resistance, leading to the development of blast-resistant wall systems. The HSS members were added vertically between the ECC-Steel-ECC panels. These wall elements primarily performed in a flexural mode of response. For the first and fourth sets of test specimens, where HSS members were used, flexural behaviour in the longitudinal direction was dominant. This behaviour was due to the flexural rigidity of the HSS being more than 20 times higher than that of the panels. As a result of this increased stiffness, wall specimens with HSS members experienced much smaller out-of-plane deformations compared to the panel-only specimens (**Table 4** and **Table 5**).

Furthermore, in the fourth set of specimens, where the ECC-steel-ECC panels were placed between two HSS members along the panel's vertical edges, the total flexural stiffness of the test specimens was increased by approximately 150 times compared to panel-only specimens. As a result of the increased stiffness in the vertical elements, the panels experienced some bending in the short direction. Due to the short span being one-fourth of the long span (500 mm versus 2000 mm), the overall stiffness of the panels was higher in the short direction. It is concluded that with sufficiently rigid HSS members acting as vertical supports, thus creating a much shorter span length, the panels would be able to resist much higher blast pressures, while transferring blast loads to the attached HSS elements.

The wall systems with HSS members were further extended to simulate typical partition walls in buildings with double panels connected by central HSS members, securing the panels along their vertical edges. A numerical model was created for this type of wall to investigate the performance of a wall construction layout that uses HSS members in the center and ECC-steel-ECC layer on either side. This wall layout was assumed to represent a typical partition wall, similar to those having wood or metal studs at the center, and gypsum drywall panels are connected on either side. The LS-Dyna model results indicated that this type of construction was very effective in resisting blast loads. This model was loaded with blasts caused by large TNT weight – large standoff distance (which are representative of the shock tube blasts), and by small TNT weight – small standoff distance (which are representative of backpack bombs). The results indicated that this wall type was able to resist the typical shock tube blast loads with small deflections and limited damage (**Figure 136**).

In addition, under the blast load due to a 10 kg TNT weight at 5 metres, which had a peak blast pressure of 674 kPa, the specimen did not experience any rupture or delamination on the protected side (**Figure 137**). Although delamination occurred under the blast load of 15 kg TNT at 5 metres, rupture was not observed on the protected side. It is important to note that this third blast had a peak reflected pressure of 1 MPa (**Figure 138**). Considering that the overall thickness of this wall specimen was 81 mm, and that the contact strength corresponding to 100 mm spacing was used in these specimens, it was concluded that this specimen type provided effective protection. This type of construction, with 15 mm thick ECC-steel-ECC panels connected to either side of HSS members with support angles connected to concrete slabs at the top and bottom, presents itself as a feasible option for protected enclosures in buildings.

5.1.5 Support Stiffness and Movement

During experimental research, it was consistently observed that the angles provided as top and bottom supports deformed under blast loads. This deformation and associated moment release provided additional flexibility to the overall behaviour of specimens. The importance of this support rotation was more pronounced for the panel-only specimens, where the tension membrane behaviour was dominant. For the panel-only specimens, the resisting moment is linearly proportional to the amount of sag at panel midspan (**Figure 143**). Therefore, releasing support fixity, which causes an increase in the midspan sag and promotes membrane action, increases the resistance of the panel-only specimens against blast loads.

Furthermore, the energy dissipated by the yielding of various support elements provides additional ductility. The support movement calculations provided in **Appendix A** show the parameters that affect the amount of rotational relaxation associated with forces that cause yielding in the support elements. Although variations in the rotational fixity of support members were not included in the experimental program, the use of spring washers on the bolts could further increase the deformation and energy dissipation capacity of the supports. Therefore, it is concluded that support movement provides benefits via three mechanisms: the first is an increase in the overall resistance of the panel; the second is additional energy dissipated through support elements; and the third is an increase in the vibration period of the overall structure.

5.1.6 Ballistic performance

The ballistic performance of ECC-steel-ECC composite panels was investigated as an additional benefit of including ECC layers, over and above those demonstrated for blast load resistance. The ballistic performance model was prepared to observe the effect of ECC layers in reducing the kinetic energy of a projectile. This model was used to compare the performance of a 3 mm thick steel sheet with that of a 15 mm thick ECC-steel-ECC panel under the impact of a 9 mm bullet representing a standard pistol round used by the Canadian Armed Forces.

The results of these models indicated that the reduction in kinetic energy of the projectiles were 44% and 62%, respectively, for the steel-only and ECC-steel-ECC panels. It is important to note that these models did not include the thermal modelling properties, which would mean that the lead projectile behaved in a more rigid manner than actual bullets. However, it was assumed that the models would allow comparison of post-impact kinetic energies. Based on the increased reduction of kinetic energy for the ECC-steel-ECC panels, the ballistic performance of the panels was concluded to be superior to steel-only plates.

5.2 Design Recommendations

A design procedure was developed for the application of both the ECC-steel-ECC panels and the wall systems that incorporate HSS elements. The first step involves the determination of design basis threat (DBT), as in any blast-resistant design procedure, which leads to the computation of the forcing function due to the blast loads. The subsequent stages involve sizing of the panels/walls and the connections to the substrate, depending on the application type, followed by an iterative design procedure, which involves dynamic analysis to establish strength and deformation capacities. Deformations lead to the limits for ductility ratios and/or support rotations, which are correlated with damage levels and the required levels of protection. Non-linear SDOF analysis was shown to provide sufficiently accurate analysis results for design purposes. If justified, the finite element method of analysis can be employed. If the member (panel of wall system) is found to be deficient or overdesigned, the member properties are revised, and another cycle of analysis is conducted as part of the iterative design procedure. The following step-by-step design procedure may be employed for each category of use.

Panels for blast hardening or use as a catchment system: ECC-steel-ECC panels are light elements that can be easily handled and installed. Their superior performance under blast loads stems from membrane resistance with sufficiently high tensile capacity. The composite behaviour obtained between ECC and steel layer is designed to develop high tensile resistance with high toughness, while the ECC, as a cement-based material, also provides resistance to ballistics and forced entry. The following are the steps that can be followed for design:

- Determine the required thickness for ECC and steel layers of the panel for the DBT at hand.
- Determine the connector spacing and size for full composite action following the empirical observations made in the current research project.
- Establish the resistance function for the membrane action for SDOF analysis, assuming fully composite behaviour.
- Design the end supports while potentially releasing rotational restraints to increase the sag under blast loads and associated increase in resistance to lateral loads while developing the membrane action.
- Conduct nonlinear SDOF dynamic analysis using the resistance function developed. If the results satisfy the performance level, i.e., meet the requirements for pre-determined levels of protection, complete the design. Otherwise, go back to the first step to revise the panel geometry and redesign the member.

Wall systems incorporating ECC-steel-ECC panels and HSS elements for enhanced blast resistance: The blast resistant wall systems developed are intended to function either as exterior façade elements (or to enhance existing façade elements), or to create blast-resistant space within a building (when used as partition walls). The HSS elements can increase the blast capacity significantly. These elements primarily respond in the flexure mode of deformations along the height, while the ECC-steel-ECC panels in between respond in the transverse direction (as one-way members) in flexure mode of deformations as they transfer the load to the HSS members. The panels were found to have sufficient flexural capacity in the transverse direction because of their inherently short spans with ECC external layers providing high tensile and compressive strengths. They are not expected to develop membrane action in the transverse direction (short direction), though they do have the capacity to function as tension elements if the geometric and loading conditions promote such behaviour. The steps to be followed for design are similar to those for the panel design, with differences arising from the behavioural mode of deformations, as itemized below:

- Determine the required size of HSS elements for blast loads associated with the DBT. The HSS can be a single element connecting the ECC-steel-ECC panels along the vertical edges or double HSS elements, one on either side of the panels. The HSS members may also be used with double panels, one panel connected to each side (threat and protected sides), forming a stud-wall system.
- Determine the connector spacing and size for full composite action of the panels and the connection details between the panels and the HSS elements to prevent delamination of the ECC and premature connection failure, respectively.

- Establish the resistance function for the HSS elements in flexure with the effective panel widths included in the analysis for use in SDOF analysis.
- Design the end supports with the required support conditions.
- Conduct nonlinear SDOF dynamic analysis. If the results satisfy the performance level, i.e., meet the requirements for pre-determined levels of protection, complete the design. Otherwise, go back to the first step to revise and redesign the member.

The methodology to obtain the resistance function and the displacement vs. time relationship for both tension-controlled and flexure-controlled elements was provided in the earlier sections. Once the resistance function is determined, the displacement versus time relationship is calculated using a numerical integration spreadsheet or software. In this research, RCBlast software was used to calculate the displacement vs. time relationship.

Pressure-Impulse (PI) Diagrams can also be generated for the elements under consideration if additional design tools are required for frequently used geometries. These diagrams are generated through SDOF analysis of members under different pressure and impulse combinations. The results having the same deformation quantity can be plotted for as many performance levels as required. For example, the elastic limit may be considered as one performance criterion for design, and the points corresponding to the elastic limit under different pressure-impulse combinations can be plotted as a P-I diagram. Different curves can be obtained, one for each performance level as represented by maximum displacement, ductility ratio or support rotation. P-I diagrams can be constructed conveniently using the software RCBlast, as illustrated in the Design Example given in the next section.

5.3 Design Example

A sample design is provided in this section, following the step-by-step design procedure outlined in the preceding section. A blast resistant partition wall is designed for a given DBT to satisfy the requirements of Medium Level of Protection (LOP) as per CSA S850-2026. The floor height is assumed to be 4.0 m, and the DBT is specified to be 10 kg of TNT at 5 metres.

First, the designer must decide the governing behaviour of the wall. In this case, the partition wall will behave primarily in flexure. The second step in the design process is to assume a design section. The wall height is 4 metres; therefore, a preliminary wall thickness of 200 mm – 1/20 of the wall height – is chosen. A typical HSS member size that could be used is 152 x 152 x 6 mm. On either side of the HSS member, 15 mm thick ECC-steel-ECC panels with 3 mm thick steel sheet will be used, resulting in a 182 mm thick wall. The spacing of the HSS is assumed to be 600 mm.

Next, the moment-curvature relationship of this wall is determined. For this purpose, a spreadsheet or software that can perform a numerical moment-curvature analysis by dividing the cross-section into numerous layers. The moment-curvature relationship for the wall is as shown in **Figure 150**.

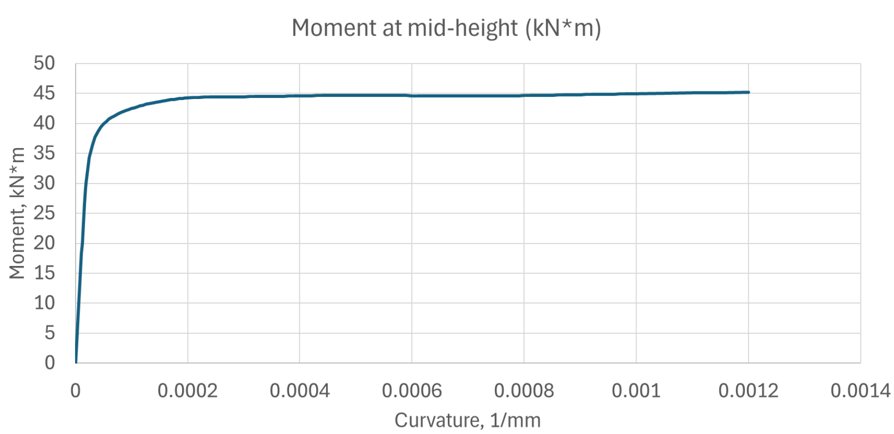

Figure 150: Moment-Curvature relationship for Panel-HSS-Panel section using 15 mm thick panels and HSS 152x152x6 mm

Using the moment-curvature relationship, the resistance function of the wall can be obtained via numerical integration using the following procedure.

1. Discretize the member along its span into sufficiently small increments. In this case, the 4-metre span was discretized at each 2 mm, creating 2000 points of integration. This was considered sufficiently small for numerical integration.
2. Define the potential plastic hinge locations. In this example, the length of the plastic hinge was assumed to be equal to the total section depth.
3. Calculate the moment at each point under a uniformly distributed load. Using the moment-curvature relationship obtained earlier, calculate the curvature value at each point. Once the curvature within the plastic hinge region reaches the yield curvature, the curvature at all integration points within the plastic hinge region shall be equal to the maximum curvature.
4. Calculate the slope at each integration point by summing the area under the curvature graph up to that point. It is necessary to consider the integration constant in the calculations, which should satisfy the condition that the slope at the mid-point of the span shall be equal to zero.
5. Calculate the deflection at each point by summing the area under the slope curve. The deflection at the supports should be zero, which shall be used as a condition to calculate the integration constant.
6. Calculate the resistance corresponding to the moment by multiplying the uniformly distributed load by the member span.
7. Repeat from step 3 by increasing the moment until reaching the ultimate moment corresponding to the ultimate curvature.

The resistance value is then plotted against the corresponding deflection. The resistance function for this example is shown in **Figure 151**.

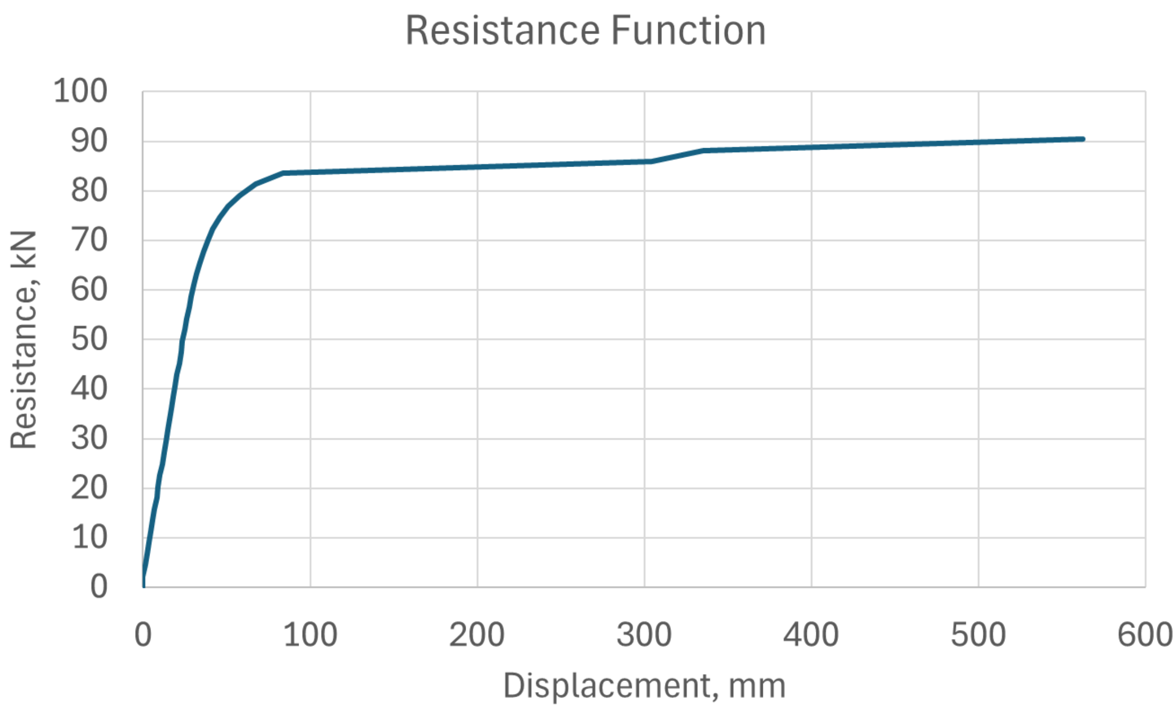

Figure 151: Resistance function of the Panel-HSS-Panel wall using 15 mm thick panels and HSS 152x152x6 mm

With the resistance function known, SDOF analysis is performed to obtain the deformation vs. time relationship under the design blast load of peak reflected pressure of 1011 kPa and peak reflected impulse of 687 kPa-ms. Using the RCBlast software, the deformation vs. time relationship is obtained as shown in **Figure 152**. The maximum deformation was calculated to be 106 mm at 21 milliseconds. This results in 3.0 degrees of support rotation, which corresponds to a medium level of protection as per CSA S850-2026.

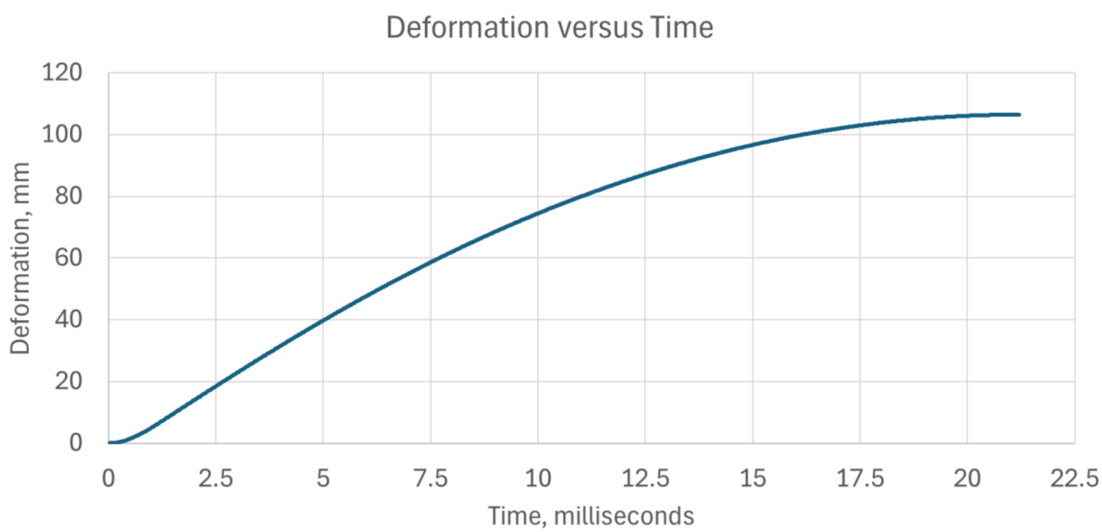

Figure 152: Deformation vs. Time relationship of the wall under 1011 kPa reflected pressure and 687 kPa-ms reflected impulse

Using the RCBlast software, pressure-impulse diagrams for this wall were created (**Figure 153**). Pressure-impulse diagrams are useful design tools that show the amount of deformation an SDOF system would develop under various combinations of pressure and impulse.

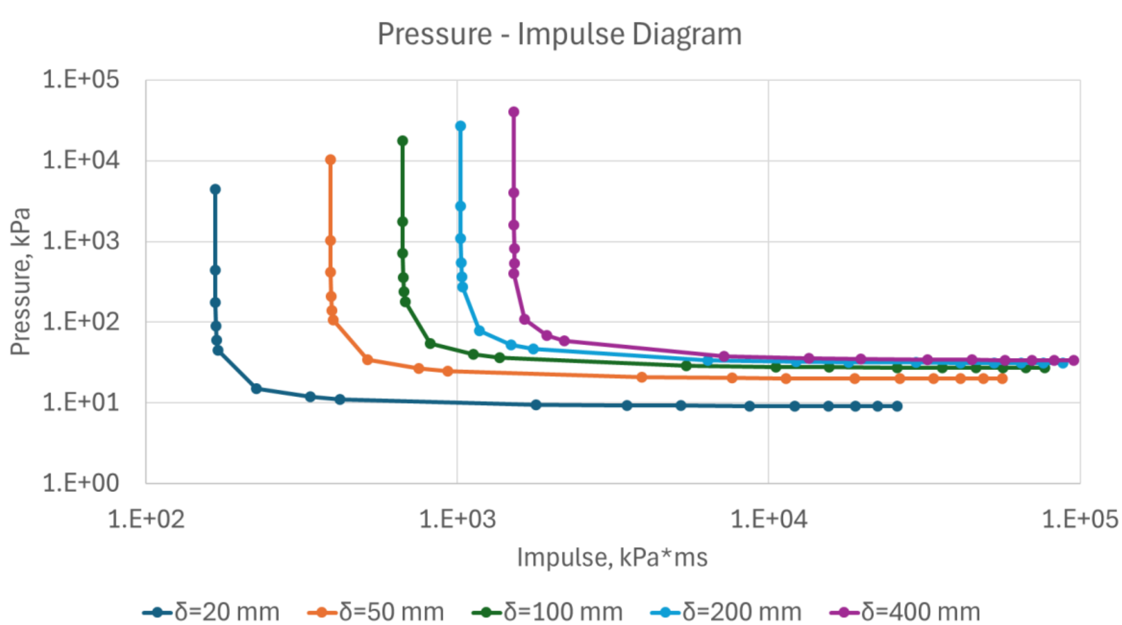

Figure 153: Pressure-Impulse diagram for the 4-metre-high wall

Chapter 6. Summary and Conclusion

6.1 Summary

The research presented in this thesis demonstrates that ECC-steel-ECC panels, especially when used in conjunction with HSS members, are capable of providing effective protection against blast loads while enabling easy installation and maintaining a relatively low weight.

In recent decades, explosion threats faced by civilian infrastructure have been more frequently caused by terrorist attacks than military ordnance. This means that the threats have charge weights ranging from a few kilograms in a backpack bomb to a few thousand kilograms in a minivan or truck bomb. An economically feasible protection option is needed to withstand these threats that could potentially target a large number of structures. The panels and wall systems developed in this thesis present such an option.

The panels are comprised of readily available materials: engineered cementitious composites (ECC) – a type of fibre-reinforced mortar that exhibits very high ductility under tensile loads – and steel sheets. The production of these 15 mm thick panels involves pouring ECC on either side of the steel sheet located at the center. A series of short connectors installed on steel sheets prior to the placement of ECC layers facilitates the composite behaviour of the panel.

The blast protection performance of these panels and wall systems was verified via a number of experiments and analytical studies. The blast simulation experiments were conducted at the Shock tube facility of the University of Ottawa. The shock tube could produce shockwaves with a peak reflected pressure of up to 100 kPa with a duration ranging between 5 and 50 milliseconds.

The specimens that were tested were placed at the 2,032 mm by 2,032 mm opening of the shock tube in various configurations. A total of 16 panel specimens that were 500 mm wide and 2082 mm tall were tested. Eight of these specimens had a 1.5 mm thick steel sheet, and the other eight had a 3 mm thick steel sheet at their center. Half of each group had connectors spaced at 100 mm, and the other half had connectors spaced at 200 mm.

The first set of specimens had a 76x51x3.2 mm HSS section between the panels on the blast side. These specimens behaved in a flexural-dominant manner and failed by the formation of plastic hinges at the mid-height of the HSS sections. The panels exhibited distributed tension cracking behaviour that is typical of ECC, but did not fail. These results proved that using panels in conjunction with HSS members provided a significant amount of protection against blast loads.

The second and third sets of specimens consisted of only panels. These specimens behaved in a tension-dominant manner, which resembled the catenary behaviour of cables. It was remarkable that, as a result of support movements and large deformation capabilities of the panels, these specimens resisted a similar level of blasts as the first set of specimens. Although the amount of damage was much higher than that of the specimens with HSS members, these sets of specimens proved that 15 mm thick ECC-steel-ECC panels had significant protection capabilities. Especially those with 3 mm thick steel in the middle and using 100 mm connector spacing.

The fourth set of specimens utilized HSS sections at the back and front of the panels. This application represented a case where the flexural stiffness of HSS members between the panels was much higher. These specimens exhibited flexural-dominant behaviour and deformed less than the other specimens. Due to the increased stiffness of the vertical HSS members, the panels experienced bending in both short and long spans. This double-axis bending behaviour proved that increasing the flexural stiffness of supporting members would provide a reserve capacity for the panels.

The fifth and final specimens tested in the shock tube were 1.5 mm and 3 mm thick steel sheets by themselves. Without the ECC layers, these members were extremely slender and failed due to buckling under lower intensity blast loads compared to the ECC-steel-ECC panels. These specimens proved that ECC layers were necessary for the optimum behaviour of the panels.

Following the promising performance of the panels and wall systems in the shock tube experiments, a comprehensive analytical study using finite element analysis software LS-Dyna was performed. This analytical study began with first verifying the modelling parameters by comparing the simulated experiment results with the actual shock tube experiment results. At this stage, it was observed that the LS-Dyna model simulations agreed well with the shock tube experiments, and that these models could be used to predict the behaviour of various panels not included in the shock tube experimental program.

The analytical parametric study using LS-Dyna utilized the verified model parameters and used them to predict the behaviour of specimens with different properties. These variations included changing the ECC layer thickness, increasing the interlayer contact strength, and utilizing multiple panels with HSS members. An additional simulation of ballistic projectile penetration resistance was also performed. The results of these parametric studies provided some important insights into how the performance of the panels could be improved.

A critical finding was that increasing the interlayer contact strength between the ECC and steel layers significantly enhanced the performance of the panels. By preventing the separation of the ECC layers from the steel sheets, the composite section was able to achieve higher deformation values and resist higher blast loads. Another finding of this parametric study was that installing a panel on both the blast side and the protected side of an HSS member, similar to a stud wall layout, resulted in the highest blast protection provided by the modelled specimens. This partition wall type specimen exhibited a relatively small amount of deformation under a 1 MPa of reflected pressure.

Using the data obtained from the shock tube experiments and the LS-Dyna models, a nonlinear single-degree-of-freedom analysis and design approach was developed. This approach mainly relied on spreadsheets and publicly available software to perform numerical integration calculations. The results of the SDOF approach were verified with the shock tube experiment and LS-Dyna model results. This approach was also used to design a partition wall type specimen as an example.

6.2 Conclusions

The following conclusions can be drawn from the combined experimental and numerical research conducted:

- The ECC-Steel-ECC composite panels, developed as part of the current investigation, provide significant resistance to blast loads, developing flexural response followed by membrane action, the magnitudes of which depend on the panel size. The panels can be used to strengthen non-structural building components, as well as structural elements, while offering easy installation and functionality for hardening existing elements.
- ECC, with its tensile strength and high tensile strain capacity, is an ideal material for use in blast engineering, providing significant inelastic deformability, ductility, and energy dissipation capacity, demonstrating excellent performance in the membrane mode of

deformations, especially when combined with steel sheets. ECC cover over steel sheets provides additional advantages stemming from their resistance to forced entry and increased ballistic rating while providing stability to the steel sheets.

- The blast-resistant wall systems consisting of ECC-Steel-ECC panels with attached HSS sections primarily respond in the flexure mode of deformations and provide significantly higher resistance to blast loads when compared with the use of panels alone. HSS sections spanning between floor slabs and/or supporting structural elements transfer blast loads acting on the panels to the attached structural elements, thereby increasing strength and performance against blast loads.
- Dynamic inelastic analysis of panels and wall systems under blast loads using LS-Dyna software with appropriate material constitutive and contact models can generate experimentally observed behaviour accurately. Such analysis has the advantage of modelling the support conditions, capturing support behaviour and its effects on potential softening and related dynamic characteristics of panels and wall systems during response.
- Single-degree-of-freedom dynamic inelastic analysis provides sufficiently accurate results for design purposes when used with appropriate resistance functions that account for nonlinear flexural and membrane behaviour. The resistance functions can be developed by assuming fully composite action between the ECC and steel layers when empirically established 100 mm connector spacing is provided for the material thicknesses considered.
- The design procedure developed based on the observations made during the experimental phase of research, combined with the results of the numerical parametric study, provides step-by-step guidelines for application in practice.

6.3 Limitations and Recommendations for Future Research

It is important to note that there were certain limitations to the experimental and finite element work that was performed as part of this research. These limitations, stemming from the scope of research and the blast simulator used, provide opportunities for future research.

The panels were not tested under the effects of real explosives. As practical and useful as the shock tube is, it does not simulate the fireball generated during actual detonations and the resulting thermal effects. Furthermore, the maximum peak reflected pressure that the shock tube used is approximately 100 kPa. This amount is not adequate to simulate shockwaves caused by explosives with high charge weights and those detonated at short standoff distances. Especially important are the effects of contact explosions that may result in material failure (spalling, scabbing, breaching), which could not be observed within the scope of the experimental research. It is anticipated that the use of ECC over the internal steel sheet could not only improve resistance to forced entry and ballistic attacks but also improve performance under contact or close-in explosions. Therefore, testing of specimens under live explosives with closer standoff distances would enable the observation of their performance under higher reflected pressures while incorporating the effects of close-in/contact explosions.

The pressure-impulse limitations of the shock tube used, while sufficiently high to permit large-scale testing of samples for application in practice, were not sufficient to test larger sizes or full-scale panels/wall systems. The large-scale samples tested were sufficient as proof of concept for developing the panels and wall systems, but further testing using larger or full-scale specimens is recommended as future research using a higher capacity blast simulator or live testing. Similarly, the scope did not include other variations in panel/wall design, such as the use of ECC only on the protective side or the use of panels on both sides of vertical HSS studs for enhanced performance. Future research using these variations in design, as well as different support conditions, is recommended for both experimental and numerical investigations.

Further limitations of results observed during the shock tube tests include the test setup and the manner in which the specimens were prepared. Steel angles used for supporting elements were used multiple times. These angles underwent some permanent deformation as a result of multiple shots, whereas in an ideal scenario, they would not have experienced any deformation. Although the effect of these deformations is assumed to be small, future experiments might consider using a new set of support elements for each test or using reinforced, rigid support members.

Another limitation of the experimental results is the type of connectors used to connect the steel sheets and ECC layers. In this research, self-drilling steel screws were used as connectors. These screws had relatively thick heads, limiting the amount of ECC paste that could be deposited between the steel sheet and the screw head. The use of headed studs with 6 mm length, which are more frequently used by the automotive industry, would be a more effective alternative. These studs could be welded on the steel surface using a stud gun, increasing the speed of installation, thereby making it feasible to install these connectors with a much smaller spacing. Furthermore, special production headed studs with a wide "T" shape would allow more ECC paste to be placed between the head and the steel sheet, thus increasing the interlayer contact strength.

Finally, a multi-core LS-Dyna solver would enable the solution of models with more than a million elements in a relatively short amount of time. Using the model parameters validated in this research, subsequent research projects could develop models with a higher element count and solve these models using supercomputing laboratory facilities.

Chapter 7. Bibliography

Alameer, A., & Saatcioglu, M. (2023). Blast-Resistant Window Anchors. II: Numerical Investigation. *Journal of Performance of Constructed Facilities*, *37*(2), 04023004. https://doi.org/10.1061/JPCFEV.CFENG-3899

Algassem, O., Li, Y., & Aoude, H. (2017). Influence of steel fibers on the shear and flexural performance of high-strength concrete beams tested under blast loads. *IOP Conference Series: Materials Science and Engineering*, *246*, 012032. https://doi.org/10.1088/1757-899X/246/1/012032

Alsayed, S. H., Elsanadedy, H. M., Al-Zaheri, Z. M., Al-Salloum, Y. A., & Abbas, H. (2016). Blast response of GFRP-strengthened infill masonry walls. *Construction and Building Materials*, *115*, 438–451. https://doi.org/10.1016/j.conbuildmat.2016.04.053

American Society of Civil Engineers. (2022). *ASCE 59-22 Blast Protection of Buildings*. American Society of Civil Engineers. https://doi.org/10.1061/9780784415719

Bangash, M. Y. H., & Bangash, T. (2006). *Explosion-resistant buildings: Design, analysis and case studies*. Springer.

Biggs, J. M. (1964). *Introduction to structural dynamics.* McGraw-Hill,.

Burrell, R. P., Aoude, H., & Saatcioglu, M. (2015). Response of SFRC Columns under Blast Loads. *Journal of Structural Engineering*, *141*(9), 04014209. https://doi.org/10.1061/(ASCE)ST.1943-541X.0001186

Canadian Standard Association. (2012). *CSA S806:12 Design and construction of building structures with fibre-reinforced polymers*. CSA Group.

Canadian Standard Association. (2014). *CSA G40.20-13/G40.21-13 General requirements for rolled or welded structural quality steel/Structural quality steel*. CSA Group.

Canadian Standard Association. (2023). *CSA S850:23: Design and assessment of buildings subjected to blast loads*. CSA Group.

Canadian Standard Association. (2024a). *CSA A23.3:24 Design of concrete structures*. CSA Group.

Canadian Standard Association. (2024b). *CSA O86:24 Engineering design in wood*. CSA Group.

Canadian Standard Association. (2024c). *CSA S16:24 Design and construction of steel structures*. CSA Group.

Carriere, M., Heffernan, P. J., Wight, R. G., & Braimah, A. (2009). Behaviour of steel reinforced polymer (SRP) strengthened RC members under blast loadThis paper is one of a selection of papers in the Special Issue on Blast Engineering. *Canadian Journal of Civil Engineering*, *36*(8), 1356–1365. https://doi.org/10.1139/L09-053

Cavili, B., & Rebentrost, M. (2006). Ductal – A High-Performance Material for Resistance to Blasts and Impacts. *Australian Journal of Structural Engineering*, *7*(1), 37–45. https://doi.org/10.1080/13287982.2006.11464962

Ciornei, L., & Saatcioglu, M. (2022). Protection of Historic Stone Masonry Walls Against Blast Loads. In I. Vayas & F. M. Mazzolani (Eds.), *Protection of Historical Constructions* (Vol.

209, pp. 500–511). Springer International Publishing. https://doi.org/10.1007/978-3-030-90788-4_40

Drdlová, M., Popovič, M., & Koutný, O. (2018). Blast resistance of hybrid fibre reinforced concrete containing polyvinyl alcohol, polypropylene and steel fibres with various shape parameters. *The European Physical Journal Special Topics*, *227*(1–2), 111–126. https://doi.org/10.1140/epjst/e2018-00061-y

Dusenberry, D. O. (Ed.). (2010). *Handbook for blast-resistant design of buildings*. J. Wiley.

FEMA P-439B. (2010). *Blast-Resistant Benefits of Seismic Design*. https://www.fema.gov/sites/default/files/2020-07/fema_p_439b.pdf

FEMA-426/BIPS-06. (2011). *Reference Manual to Mitigate Potential Terrorist Attacks Against Buildings*. https://www.dhs.gov/xlibrary/assets/st/st-bips-06.pdf

FEMA-428/BIPS-07. (2012). *Primer to Design Safe School Projects in Case of Terrorist Attacks and School Shootings*. https://www.dhs.gov/xlibrary/assets/st/bips07_428_schools.pdf

FEMA/BIPS 05. (2011). *Preventing Structures from Collapsing to Limit Damage to Adjacent Structures and Additional Loss of Life when Explosives Devices Impact Highly Populated Urban CentersPreventing Structures from Collapsing*. https://www.dhs.gov/xlibrary/assets/preventing-structures-from-collapsing-062011.pdf

Forni, D., Chiaia, B., & Cadoni, E. (2016). Strain rate behaviour in tension of S355 steel: Base for progressive collapse analysis. *Engineering Structures*, *119*, 164–173. https://doi.org/10.1016/j.engstruct.2016.04.013

Giovino, G., Olmati, P., Garbati, S., & Bontempi, F. (2014). Blast Resistance Assessment of Concrete Wall Panels: Experimental and Numerical Investigations. *International Journal of Protective Structures*, *5*(3), 349–366. https://doi.org/10.1260/2041-4196.5.3.349

Hammoud, A., Yan, J., Li, Y., & Aoude, H. (2021). Blast behavior of columns built with high-strength concrete and Grade 690 MPa high-strength reinforcement. *Canadian Journal of Civil Engineering*, *48*(11), 1422–1439. https://doi.org/10.1139/cjce-2019-0554

Hibbeler, R. C. (2015). *Structural analysis* (9th ed). Pearson Prentice Hall.

Jackson, C. M., Jacques, E., & Saatcioglu, M. (2022). Blast retrofit of one-way reinforced concrete members using externally bonded FRP and FRP anchorage. *International Journal of Protective Structures*, *13*(2), 209–235. https://doi.org/10.1177/20414196221087347

Jacques, E. (2013). *Software for Blast Load Calculation [Unpublished research report, CVG 6308 – Effective Design of Buildings, University of Ottawa]. Http://www.ericjacques.com/.*

Jacques, E., Lloyd, A., Braimah, A., Saatcioglu, M., Doudak, G., & Abdelalim, O. (2014). Influence of high strain-rates on the dynamic flexural material properties of spruce–pine–fir wood studs. *Canadian Journal of Civil Engineering*, *41*(1), 56–64. https://doi.org/10.1139/cjce-2013-0141

Jacques, E., Lloyd, A., & Saatcioglu, M. (2013). Predicting reinforced concrete response to blast loads. *Canadian Journal of Civil Engineering*, *40*(5), 427–444. https://doi.org/10.1139/L2012-014

Kadhom, B. (2016). *Blast Performance of Reinforced Concrete Columns Protected by FRP Laminates*. Université d'Ottawa / University of Ottawa.

King, K. W., Wawclawczyk, J. H., & Ozbey, C. (2009). Retrofit strategies to protect structures from blast loadingThis article is one of a selection of papers published in the Special Issue on Blast Engineering. *Canadian Journal of Civil Engineering*, *36*(8), 1345–1355. https://doi.org/10.1139/L08-058

Krauthammer, T. (2008). *Modern Protective Structures* (0 ed.). CRC Press. https://doi.org/10.1201/9781420015423

Lacroix, D. N., & Doudak, G. (2018). Experimental and Analytical Investigation of FRP Retrofitted Glued-Laminated Beams Subjected to Simulated Blast Loading. *Journal of Structural Engineering*, *144*(7), 04018089. https://doi.org/10.1061/(ASCE)ST.1943-541X.0002084

Lepech, M. D., & Li, V. C. (2008). Large-Scale Processing of Engineered Cementitious Composites. *ACI Materials Journal*, *105*(4). https://doi.org/10.14359/19897

Li, V. C. (2009). Damage Tolerant ECC for Integrity of Structures under Extreme Loads. *Structures Congress 2009*, 1–10. https://doi.org/10.1061/41031(341)242

Li, V. C. (2019). *Engineered Cementitious Composites (ECC): Bendable Concrete for Sustainable and Resilient Infrastructure*. Springer Berlin Heidelberg. https://doi.org/10.1007/978-3-662-58438-5

Li, Z., Chen, L., Fang, Q., Chen, W., Hao, H., Zhu, R., & Zheng, K. (2019). Experimental and numerical study on CFRP strip strengthened clay brick masonry walls subjected to vented gas explosions. *International Journal of Impact Engineering*, *129*, 66–79. https://doi.org/10.1016/j.ijimpeng.2019.02.013

Lim, J. Y., Goh, C. Y. M., Kang, K. W., Li, J., & Wu, C. (2025). Structural response of steel-concrete composite panels to near field simultaneous blast and fragmentation loading. *International Journal of Impact Engineering*, *195*, 105142. https://doi.org/10.1016/j.ijimpeng.2024.105142

LSTC. (2025a). *LS-DYNA Keyword User's Manual*.

LSTC. (2025b). *LS-DYNA Theory Manual*.

Malvar, L. J. (1998). Review of Static and Dynamic Properties of Steel Reinforcing Bars. *ACI Materials Journal*, *95*(5). https://doi.org/10.14359/403

McGrath, A., & Doudak, G. (2021). Investigating the response of bolted timber connections subjected to blast loads. *Engineering Structures*, *236*, 112112. https://doi.org/10.1016/j.engstruct.2021.112112

Naito, C., Beacraft, M., Hoemann, J., Shull, J., Salim, H., & Bewick, B. (2014). Blast Performance of Single-Span Precast Concrete Sandwich Wall Panels. *Journal of Structural Engineering*, *140*(12), 04014096. https://doi.org/10.1061/(ASCE)ST.1943-541X.0001020

Nam, J., Kim, H., & Kim, G. (2017). Experimental Investigation on the Blast Resistance of Fiber-Reinforced Cementitious Composite Panels Subjected to Contact Explosions.

International Journal of Concrete Structures and Materials, *11*(1), 29–43. https://doi.org/10.1007/s40069-016-0179-y

Park, P., Jones, R., Castillo, L., Vallangca, M., & Cantu, F. (2020). *Engineered Cementitious Composites (ECC) for Applications in Texas (0-7030-1)*.

Ranade, R., Li, V. C., Stults, M. D., Rushing, T. S., Roth, J., & Heard, W. F. (2013). Micromechanics of High-Strength, High-Ductility Concrete. *ACI Materials Journal*, *110*((4)), 375–385.

Saatcioglu, M., Ozbakkaloglu, T., Naumoski, N., & Lloyd, A. (2009). Response of earthquake-resistant reinforced-concrete buildings to blast loading. *Canadian Journal of Civil Engineering*, *36*(8), 1378–1390. https://doi.org/10.1139/L09-089

SBEDS Methodology Manual, U. S. A. C. of E. (2008). *Methodology Manual for the Single-Degree-of-Freedom Blast Effects Design Spreadsheets (SBEDS)*.

Sherif, M., Othman, H., Marzouk, H., & Aoude, H. (2023). An experimentally validated numerical analysis of UHP-FRC subjected to blast loading. *International Journal of Protective Structures*, *14*(4), 527–548. https://doi.org/10.1177/20414196221120512

Smith, P. D., & Hetherington, J. G. (1994). *Blast and ballistic loading of structures*. Butterworth-Heinemann.

Sun, M., Chen, Y., Zhu, J., Sun, T., Shui, Z., Ling, G., & Zhong, H. (2018). Effect of Modified Polyvinyl Alcohol Fibers on the Mechanical Behavior of Engineered Cementitious Composites. *Materials*, *12*(1), 37. https://doi.org/10.3390/ma12010037

Task Committee on Blast-Resistant Design. (2025). *Design of Blast-Resistant Buildings in Energy and Industrial Facilities* (L. Magenes, Ed.; Third Edition). American Society of Civil Engineers. https://doi.org/10.1061/9780784485897

Turk, K., & Nehdi, M. L. (2021). Flexural toughness of sustainable ECC with high-volume substitution of cement and silica sand. *Construction and Building Materials*, *270*, 121438. https://doi.org/10.1016/j.conbuildmat.2020.121438

UFC 3-340-02. (2008). *Structures to Resist the Effects of Accidental Explosions*. https://www.wbdg.org/FFC/DOD/UFC/ufc_3_340_02_2008_c2.pdf

Viau, C., & Doudak, G. (2016). Investigating the behaviour of typical and designed wall-to-floor connections in light-frame wood stud wall structures subjected to blast loading. *Canadian Journal of Civil Engineering*, *43*(6), 562–572. https://doi.org/10.1139/cjce-2015-0452

Yang, E.-H., & Li, V. C. (2012). Tailoring engineered cementitious composites for impact resistance. *Cement and Concrete Research*, *42*(8), 1066–1071. https://doi.org/10.1016/j.cemconres.2012.04.006

Yu, K.-Q., Yu, J.-T., Dai, J.-G., Lu, Z.-D., & Shah, S. P. (2019). Corrigendum to "Development of ultra-high performance engineered cementitious composites using polyethylene (PE) fibers" [Constr. Build. Mater. 158 (2018) 217–227]. *Construction and Building Materials*, *216*, 698. https://doi.org/10.1016/j.conbuildmat.2019.05.089

Appendices

Appendix A

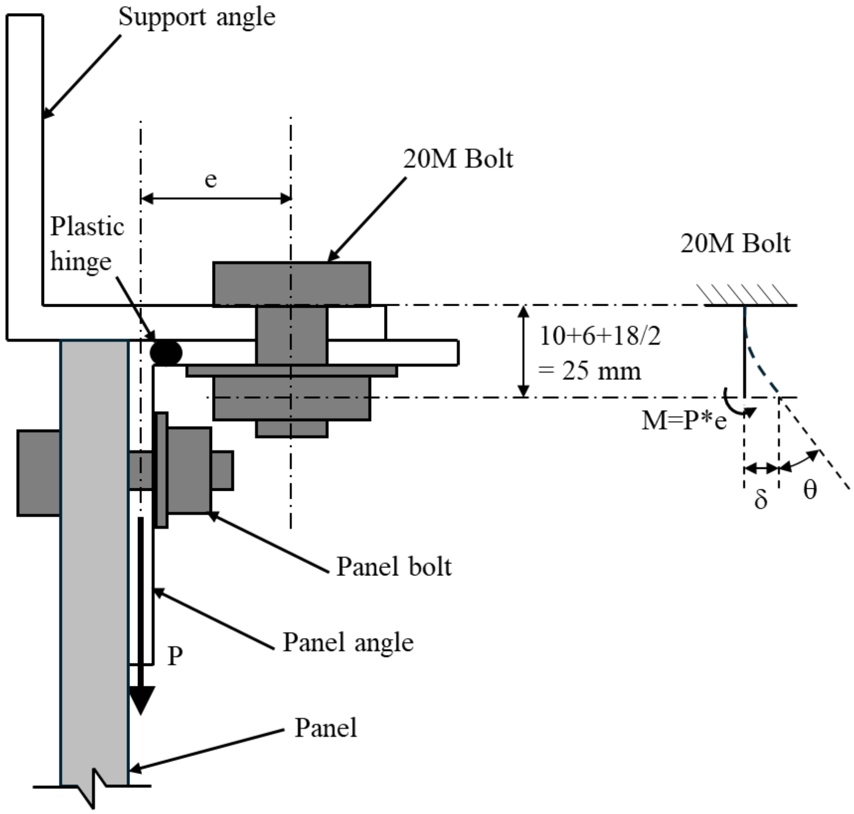

Support Movement Calculations

Bolt Bending

$d_{bolt} = 20mm$

$d_{hole} = 25mm$

$A_{bolt} = 314mm^2$

$E_{st} = 200GPa$

$f_{y\_bolt} = 400MPa$

$f_{u\_bolt} = 500MPa$

$$I_{bolt} = \frac{\pi}{4} \cdot \left(\frac{d_{bolt}}{2}\right)^4 = 7854\,mm^4$$

$$S_{bolt} = \frac{I_{bolt}}{d_{bolt}} \cdot 2 = 785\,mm^3$$

$$I_{bolt} = \frac{\pi}{4}\cdot\left(\frac{d_{bolt}}{2}\right)^4 = 7854\,mm^4$$ $$S_{bolt} = \frac{I_{bolt}}{d_{bolt}}\cdot 2 = 785\,mm^3$$

$$T_{u\_bolt\_nom} = A_{bolt}\cdot f_{u\_bolt} = 157\,kN$$ Nominal tension capacity of the bolt

$$M_{y\_bolt} = f_{y\_bolt}\cdot S_{bolt} = 314\,kN\cdot mm$$ Nominal yield moment of the bolt

$$e_{bolt} = 43mm$$ Distance from the center of angle to the center of the bolt

$$P_y = \frac{M_{y\_bolt}}{e_{bolt}} = 7.3\,kN$$ Tension force acting on the vertical leg of the angle that initiates yielding of the bolt

$$t_{angle\_panel} = 6mm$$ $$t_{angle\_support} = 10mm$$

$$t_{nut} = 18mm$$ Thickness of a 20M nut

$$L_{bolt} = t_{angle\_panel} + t_{angle\_support} + \frac{t_{nut}}{2} = 25\,mm$$ Bending length of the bolt

$$\theta_{bolt\_y} = \frac{P_y\cdot e_{bolt}\cdot L_{bolt}}{E_{st}\cdot I_{bolt}} = 5\times 10^{-3}\,rad$$ Tip rotation of the bolt due to P_y

$$\phi_{bolt\_u} = \frac{0.2}{d_{bolt}}\cdot 2 = 0.02\,\frac{1}{mm}$$ Ultimate curvature of the bolt assuming an ultimate strain of 0.2 for the bolt

$$\theta_{bolt\_u} = \phi_{bolt\_u}\cdot L_{bolt} = 0.5\,rad$$ Tip rotation of the bolt when the entire length of the bolt reaches ultimate curvature

$$sm_{bolt\_rtn} = \theta_{bolt\_u}\cdot e_{bolt} = 21.5\,mm$$ Separation between angles - *support movement* - when the bolt reaches its ultimate rotation capacity

Angle Deformation

$b_{effective} = e_{bolt} \cdot 5 = 215\,mm$

Effective width of angle resisting bending. Assumed 1 to 2.5 slope

$I_{angle\_panel} = \frac{1}{12} \cdot b_{effective} \cdot t_{angle\_panel}^{3} = 3870\,mm^{4}$

$f_{y\_angle} = 250MPa$

$M_{y\_angle} = \frac{f_{y\_angle} \cdot I_{angle\_panel}}{0.5 \cdot t_{angle\_panel}} = 322.5\,kN \cdot mm$

$P_{y\_angle} = \frac{M_{y\_angle}}{d_{bolt}} = 16.125\,kN$

Tension force on the angle vertical leg that initiates local yielding

$L_{hinge} = t_{angle\_panel} = 6\,mm$

Plastic hinge length. Assumed to be equal to angle leg thickness

$\phi_{ult\_hinge} = \frac{0.2}{t_{angle\_panel}} \cdot 2 = 0.067 \frac{1}{mm}$

Ultimate curvature of the hinge assuming an ultimate strain of 0.2 for the angle

$\theta_{hinge} = \phi_{ult\_hinge} \cdot L_{hinge} = 0.4\,rad$

Total rotation of the hinge

$\delta_{angle\_bending} = \frac{P_{y\_angle} \cdot e_{bolt}^{3}}{3 \cdot E_{st} \cdot I_{angle\_panel}} = 0.6\,mm$

Deflection caused by the bending of the horizontal leg of the angle

$\delta_{hinge\_ult} = \theta_{hinge} \cdot e_{bolt} = 17.2\,mm$

Deflection caused by the hinge rotating up to its ultimate rotation capacity

$sm_{angle\_bending} = \delta_{angle\_bending} + \delta_{hinge\_ult} = 17.8\,mm$

Bolt Movement within Hole Tolerances

$d_{tol\_panel} = 2mm$ Hole tolerance in the vertical leg of the angle connected to the panel

$d_{tol\_support} = 10mm$ Hole tolerance in the vertical leg of the angle connected to the shocktube. Elongated holes were used to facilitate installation.

$d_{tol\_shocktube} = 3mm$ Hole tolerance in the shocktube

$$sm_{hole\_tolerance} = \frac{d_{tol\_panel} + d_{tol\_support} + d_{tol\_shocktube}}{2}$$

$sm_{hole\_tolerance} = 7.5\,mm$ Half of the hole tolerances are considered for support movement assuming the bolts were initially centered

$$sm_{total} = \left(sm_{bolt\_rtn} + sm_{angle\_bending} + sm_{hole\_tolerance}\right)\cdot 2$$

$sm_{total} = 93.5\,mm$ Support movement occurs at the top and bottom supports, hence multiplied by 2.